INVERSE DESIGN OF SELF-ASSEMBLING COLLOIDS VIA LANDSCAPE ENGINEERING

BY

ANDREW WILSON LONG

DISSERTATION

Submitted in partial fulfillment of the requirements
for the degree of Doctor of Philosophy in Materials Science and Engineering
in the Graduate College of the
University of Illinois at Urbana-Champaign, 2017

Urbana, Illinois

Doctoral Committee:

Assistant Professor Andrew L. Ferguson, Director of Research
Professor Kenneth S. Schweizer
Professor Lee DeVille
Assistant Professor Christopher M. Evans

Abstract

This dissertation applies machine learning to the study of colloidal self-assembly to provide insights on the microscopic mechanisms driving assembly phenomena and drive towards a design framework capable of rationally manipulating the free energy landscape for self-assembly to derive building blocks that preferentially form into a target aggregate structure. The methodologies derived within are applicable to a wide class of self-assembly systems, both simulated and experimental, enabling a new frontier in the computer-aided design of self-assembling materials.

The first portion of this dissertation focuses on the development of the many-body diffusion map and its application to the study of self-assembly. Diffusion map dimensionality reduction has shown great promise in the study of the low-dimensional folding landscapes inherent to protein folding. We extend this technique to handle multi-body systems via a graph-based distance measure that treats aggregate structure as a bonding network. In comparison to other techniques that utilize pathway engineering or heuristics, diffusion mapping of self-assembly systems is shown to systematically infer the low-dimensional manifold on which self-assembly occurs, detailing the structural pathway information and providing a framework for computation of both thermodynamic (*what* will form) and kinetic (*how* will it form) properties in a unified framework.

We study this machine learning algorithm on the self-assembly and self-organization of three systems. In the first study we apply many-body diffusion maps to a double ring patchy colloid model shown to form discrete polyhedral aggregates by varying the angles of the different patchy rings. Our method is able to validate previous studies showing that

self-assembly of icosahedral aggregates occurs along two competing assembly-pathways, and we use this self-assembly landscape to suggest patch-interaction design criteria for robust icosahedral assembly. In a second study, we apply our many-body diffusion map approach to particle-tracking experiments of Janus colloid self-assembly. This was to our knowledge the first attempt at machine learning collective order parameters and deriving assembly landscapes directly from experimental particle tracking data. Here we demonstrate the ability of our many-body diffusion map to provide insights on the affect experimental controls have on the self-assembly process, proving in line with our physical interpretation and extending to predict experimental systems to improve the yield or specificity of a targeted region of the self-assembly space. In our third study, we apply the diffusion map to the self-organization of a digital colloid, a discrete colloidal cluster capable of storing information by adopting certain configurations. Here we extract the important kinetic and thermodynamic information driving transitions between colloidal bit states, deriving the engineering design tradeoff between information stability and the energy required to write information.

The second portion of this dissertation focuses on novel improvements to the sampling of diffusion map spaces to project free energy surfaces in the low-dimensional self-assembly landscape. The first part of this section proposes a novel extension of the diffusion map, so-called landmark diffusion maps, to enable the accurate and rapid embedding of out-of-sample points into a diffusion map landscape. Using this technique, we then propose a landscape engineering framework capable of manipulating the underlying free energy landscape for self-assembly to rationally design building blocks that aggregate into a desired structure. We use this design platform to study the self-assembly of the double ringed patchy colloid model, improving upon the expert-designed icosahedral building block's assembly rate by 76%, and then demonstrate that our technique can rapidly converge to new objective functions in the optimization of an octahedral forming patchy colloid.

To my parents, who have only ever wanted me to be happy.

Acknowledgments

First I would like to thank Andy Ferguson for being the most compassionate advisor I can imagine. Having gone through a host of medical issues in my time in graduate school, you have been forever behind me with the simple goal of wanting me to be well. It's striking how much we have both changed over these last 5 years, from sitting in your office for the first time during my visit weekend to forming a full research group that has begun to tackle a host of truly exciting problems. It's funny to imagine that this work is nearly the complete story of our chat during a random week in March of 2012. I've been truly lucky to work with you these past years, and I'm grateful for everything you've done for me.

The rest of the faculty at the University of Illinois have been equally gracious in directing me through my graduate life. I would like to thank Dallas Trinkle and Steve Granick for pushing me to see the forest for the trees. As Steve put it during my qualifying exams, "You're a great mathematician, but stop and think for a second." I hope that I've been able to follow that message in my time here. Additionally I'd like to thank Kenneth Schweizer for showing a true passion in his teaching and research that has inspired me in following my own path.

Working as part of the Ferguson research group has been a true honor. To Greg, Rachael, Bryce, Jiang, and Wei, spending time in the office was always exciting. Whether it was debugging silly errors or working out problems on the board, it was fun to be in a room with people who would drop everything for a chance to help each other. As to my undergraduate mentees, Bridgette and Suraj, you were outstanding scientists and I hope all the best for your futures.

To the materials science graduate community at Illinois, I am eternally indebted. There are too many of you to whom I owe so much, your support was instrumental in my continued pursuance of a Ph.D. degree. In particular I'd like to thank Kaitlin for being my true friend for the past 5 years, being constantly available to help in any way you could. To Eric and Joseph who have lived with me the past few years, I'm grateful for your constant presence in the event someone had a bad day and needed to blow off some steam. To Julia and Lucas, you have constantly offered your home and your warmth in times where I've been struggling. There are so many others that I could write a full second dissertation on the meaning you have to me.

Finally, to my parents. I am truly lucky to have loving and caring parents who have wanted nothing more from me than to do something I love and to find happiness. Not a day goes by where I don't think of you both and I would not be the person I am today without you.

Table of Contents

List of Tables

List of Figures

List of Abbreviations

BayesWHAM	Bayesian approach for the Weighted Histogram Analysis Method
CMA-ES	covariance matrix adaptation evolutionary strategy
CMOS	complementary metal-oxide-semiconductor
DC	digital colloid
DMap	diffusion map
EMD	earth mover's distance
FES	free energy surface
FIRE	fast inertial relaxation engine
FRET	Förster resonant energy transfer
GPU	graphics processing unit
HMC	hybrid Monte Carlo
HOOMD-blue	Highly Optimized Object-oriented Molecular Dynamics package
ITO	indium tin oxide
L-dMap	landmark diffusion map
L-Isomap	landmark Isomap
LJ	Lennard Jones potential
LLE	local linear embedding
MFPT	mean first passage time
MD	molecular dynamics
MC	Monte Carlo

NGA	Network Graph Analysis method
NP	nondeterministic polynomial time
NVE	microcanonical ensemble
NVT	canonical ensemble
PCA	principal component analysis
PST	pruned spanning tree selection
rICEP	reverse induced-charge electrophoresis
RMS	root-mean-squared
RMSD	root-mean-squared deviation
SPC	simple point charge model of water
SVM	support vector machine
TPM	3-methacryloxypropyl trimethoxysilane
TraPPE	Transferable Potentials for Phase Equilibria
WCA	Weeks-Chandler-Anderson potential
VMD	Visual Molecular Dynamics package

List of Symbols

Latin Alphabet:

$\mathbf{B}$	IsoRank score matrix
$\tilde{\mathbf{C}}$	diagonal multiplicity matrix
c_i	landmark multiplicity
dt^*	dimensionless timestep
F	Helmholtz free energy
$\hat{F}$	effective Helmholtz free energy
F^*	dimensionless Helmholtz free energy
f_{budding}	fraction of budding pathway character
f_{monomer}	fraction of monomeric-addition pathway character
$\mathbf{G}$	cluster bonding network
$\mathbf{G}'$	topology-augmented bonding network
$\mathbf{H}$	permutation matrix
$\mathbf{I}$	identity matrix
k_B	Boltzmann's constant
$\mathcal{L}$	library of configurations
$\mathbf{M}$	Markov matrix
$\tilde{\mathbf{M}}$	landmark reduced Markov matrix
m_i	mass of species i
$\mathcal{O}$	big-O notation for computational complexity
$\mathcal{N}$	normal distribution

$\hat{P}$	histogram approximation to probability distribution
Q_l	Steinhardt bond orientation order parameter of degree l
$\mathbf{R}$	interparticle distance matrix
$\mathbf{R}'$	topology-augmented interparticle distance matrix
$\mathcal{R}^K$	K-dimensional real space data set
S	speedup from landmarking
S_i	set of data inside landmark point's Voronoi space
T^*	dimensionless temperature
t^*	dimensionless time
U_{AB}	potential energy between particles A and B
u_{ij}	dipolar energy between species i and j
Y_{lm}	spherical harmonic of degree l and order m
Z	root-mean squared normalized percentage error from landmarking
$\otimes$	tensor product

Greek Alphabet:

α	complex polarizability
$\{\alpha_i^j\}$	landmark perturbations on eigenvector space
β	Boltzmann factor, equal to $1/k_BT$
Γ	escape rate for digital colloid transitions
$\delta\lambda_i$	landmark perturbation on ith eigenvalue
ϵ	Gaussian soft-thresholding bandwidth
ϵ_i	Lennard Jones interaction strength for species i
ϵ_0	vacuum permittivity
κ_i	strength of harmonic constraint in the ith dimension
λ_i	ith eigenvalue

Λ	ratio of central particle to halo particle diameters
Λ_0	initial diameter ratio for randomization
Λ_{sc}	spherical code diameter ratio for digital colloids
Λ_{T}	transition diameter ratio threshold
Λ_{U}	unlocked diameter ratio threshold
$\vec{\xi}$	k-dimensional vector in diffusion map space
ρ	density
σ	Lennard Jones length parameter
σ_i	Lennard jones length parameter for species i
Υ_N	rotational symmetry
ϕ	volume fraction
ϕ_i	patchy ring polar angle for species i
χ	thresholded interparticle distance matrix
ψ_i	ith right eigenvector
Ψ	complete set of right eigenvectors
$\tilde{\mathbf{\Psi}}$	landmark reduced right eigenvectors

Chapter 1

Introduction and background

1.1 Self-assembly for next generation materials

Self-assembly, the spontaneous organization of building blocks into hierarchical structures, is a prominent formation mechanism for biological systems, driving the growth of lipid membranes [1, 2], viral capsids [3, 4], fibrils [5], and potentially even the precursors of RNA that form the building blocks of life [6]. The spontaneous nature of self-assembly allows for the undirected fabrication of these structures, using the intrinsic geometric and chemical properties of the building blocks to guide the assembly of complex aggregates with a high degree of specificity. This specificity in self-assembly has made it a highly sought after fabrication technique for the "bottom-up" construction of novel materials [7–9]. Self-assembly has been used extensively across materials applications, from biomimetic vesicles for targeted drug delivery [10, 11] and cell penetrating peptides [12–14], to sensing with protein reactive dye nanoparticles [15] and ZnO gas sensors [16], and to optoelectronic devices like organic solar cells [17, 18] and photonic crystals [19]. This diversity of applications has led to an intense interest in understanding the microscopic mechanisms guiding the self-assembly process, and on the development of design rules and frameworks to improve the development of new self-assembly systems.

Colloidal self-assembly has proven a welcome test-bed for methodological development on the understanding and design of self-assembly processes. Advances in colloidal surface patterning and fabrication [11, 20, 21] enable a wealth of possible particle interactions and geometries. These colloidal systems can be used as coarse representations of peptide systems,

such as in the use of hemispherically patterned Janus colloids to create tubes, micelles, vesicles, and lattice structures [22–26], using the two hemispheric moieties to mimic a lipid-like structure. Colloidal shape can equally be modified to study the effect of building block geometry on aggregate morphology, such as in micellar-forming dumbbell colloids [27], "Mickey Mouse" colloids forming tubules [28], and colloidal molecules with controllable bond angles [29, 30]. This variability in colloid chemistry and structure makes them ideal for probing the relationship between building block features and assembly behavior.

Despite the intense interest in harnessing colloidal self-assembly, there is still a lack of fundamental understanding on the mechanisms driving the self-assembly process [20, 31]. Experimental studies to determine the impact of building block properties on observed terminal aggregates are typically costly and time-intensive [20, 32], and are often unable to fully elicit a detailed understanding of the microscopic mechanisms and driving forces promoting or frustrating assembly behavior [3, 33]. Computer simulations provide a complementary solution to traditional experimentation [34–36], and have shown success in producing "phase maps", linking terminal aggregate structures to properties of the building blocks [20, 22, 31]. These computational work offers great insight into the design of programmable building blocks that reverse engineer the self-assembly process, however these models rely on a purely thermodynamic model for self-assembly, matching building block properties to the most stable structure. A complete model of self-assembly must also characterize the structural steps leading to transitions between assembled aggregates, giving quantitative insight into the mechanisms that drive assembly and providing key information underpinning the kinetic accessibility and thermodynamic stability of different aggregate morphologies.

Identifying and extracting these assembly pathways and kinetic details from models of self-assembly has remained a difficult challenge. Typical methods require proxy measures of assembly, such as oligomer size distributions [35, 37], supported by visual trajectory inspection [36] to infer these pathways driving assembly, however these techniques are often frustrated by the collective motions inherent to self-assembly [36, 38], making visual in-

spection difficult and masking kinetic information used in these coarse descriptors for the self-assembly process.

A key challenge to the design of self-assembly systems then is the identification of good descriptors capturing both the kinetics and thermodynamics of self-assembly [38, 39]. Developing these descriptors would enable the systematic inference of microscopic assembly mechanisms governing self-assembly and the development of design principles for "pathway engineering", capable of steering self-assembly toward desired aggregates. Similar to the successful "new view" of protein folding [40–42], self-assembly can be thought of as occurring on a complex and highly textured landscape, the topology of which determines the stability of different aggregate states and assembly pathways. Several works have established the value of these landscapes in guiding building block design by pathway engineering [33, 35, 43, 44], however these still suffer from a lack of good collective variables in which to describe the collective structural rearrangements governing assembly dynamics, frustrating the development of landscapes that encode both the thermodynamics and kinetic features of assembly. In order to develop a more unified understanding of the self-assembly problem, it is illuminating to look at the recent advances made in the realm of modeling protein folding via machine learning.

1.2 Machine learning in soft-matter systems

One of the great advances in the treatment of molecular systems is the so-called "new view" of protein folding, where the dynamics of molecular motion are treated as transitions over an energy landscape describing the relative stability and locality of molecular conformations [40]. This landscape, defined over the conformational space of the molecule, provides a unified framework to describe the thermodynamics and kinetics of folding, encoding thermodynamics in the peaks and wells, hills and valleys of the rugged energy landscape, and kinetics in the proximity between states in conformational space, whereby proximal states are transi-

tioned between more quickly than those further apart. This depiction of the protein folding problem has led to a rapid explosion in techniques to identify and sample energy landscapes for proteins, a non-trivial task due to the high-dimensional nature of protein conformations. Given a protein with N-atoms, conformations exists as points in a 3N-dimensional space, describing the (x, y, z) coordinates of each atom. As early as the 1950s, chain dynamics were not treated as motions in this 3N-space; instead, the real-space degrees of freedom of a polymer chain were coupled together into a set of harmonic modes and corresponding relaxation timescales, such as those proposed by Rouse [45] and Zimm [46] in their models of polymer viscoelasticity. The basis for this reduction seems apparent, by shifting one atom in a chain, the local environment of the surrounding chains will feel and react to that motion, leading to coupled motions between neighboring atoms, and extending over the full length of the chain over a series of differing relaxation timescales. Further by treating these fluctuations over an internal reference frame, the relative motions of atoms do not depend on trivial chain translations and rotations. This reduction of the polymer dynamics to a series of relaxation modes will motivate much of the subsequent work on modeling polymer conformations.

The Rouse-Zimm approach proposed specific forms on the low-dimensional descriptors for the polymer dynamics based on harmonic chains, however alternative descriptors could be defined. Dimensionality reduction is a primary branch of the field of machine learning seeking to find low-dimensional order parameters in high-dimensional data that encapsulate the highest degree of information content. Instead of proposing a specific form, linear and nonlinear combinations of the system degrees of freedom may be utilized to derive a set of collective order parameters capturing key details from the high dimensional space. Much work has been done in the field of applying dimensionality reduction to protein folding, from linear techniques such as principal component analysis (PCA) [47–49] to nonlinear techniques such as SketchMap [50], IsoMap [51–53], local linear embedding (LLE) [54], and diffusion maps (DMaps) [55–58].

Diffusion maps [59–61] in particular have shown great promise in reducing the complex

nature of polymer dynamics to a few low-dimensional descriptors. By computing similarities between different chain conformations, the diffusion map provides a small set of diffusive relaxation modes and timescales describing the conformational phase space over which the long-time polymer dynamics are restrained, with fast decoupled motions being slaved orthogonally to these slow modes in a Mori-Zwanzig type operator formalism [56, 62]. The diffusion map thus defines an automated framework for the inference of this set of low-dimensional descriptors, provided that a measure of similarity between chain conformations can be defined. Typically, a rotationally and translationally minimized root-mean-squared deviation (RMSD) is employed, taking out the extraneous degrees of freedom due to localization and rotation of a polymer chain in comparing between different conformations [56, 63].

This framework, while successful in the case of a single molecule, has proven difficult to extend to many-body systems where indistinguishability and oligomer size differences between aggregate clusters play prominent roles in defining the structural morphology. Previous studies to identify low-dimensional representations of the self-assembly configurational space have relied on static numbers of particles to provide a consistent basis [64], or relied on shape descriptors [65] or cluster size-descriptors as a proxy for the configurational space of aggregate [35] in which to construct free energy landscapes. Shape descriptors have been employed in characterizing crystalline aggregates [64, 66], however thermal noise in self-assembly will lead to many defective states non-conforming to a particular crystalline architecture resulting in poor classification of aggregates and further exacerbated by a similarity metric to compare between shape descriptors [67]. In the case of projecting free energy landscapes onto a cluster size distribution, the deviations in structures of a particular size are collapsed into a single grouping, removing any morphological details for the aggregate and limiting the ability to directly extract the mechanisms driving cluster formation [35, 43]. Alternative strategies have been developed for "pathway engineering" via approximation of the partition function for self-assembly [33, 68] enabling a thermodynamic treatment for the transitions between aggregation states, however this technique still suffers from a lack

of good collective variables in which to describe the collective structural rearrangements governing assembly dynamics, frustrating the development of landscapes that encode both the thermodynamics and kinetic features of assembly. This problem of representation and comparison between self-assembled aggregates has remained one of the key difficulties in the application of machine learning to self-assembly systems for building block design.

1.3 Outline for this dissertation

The focus of this research has been on tackling the many-body challenge which has previously stymied the application of machine learning technique to self-assembly. In Chapter 2, we describe the diffusion map in detail along with our novel distance measure based on graph alignment techniques, allowing for direct comparison between self-assembled aggregate structures. This advancement allows for the treatment of self-assembly in analogy with the new view of protein folding as a rugged energy landscape over the self-assembly conformational space. Using this algorithm, we present in Chapter 3 a study on the simulated formation of polyhedra from a patchy colloid model to provide insight on temperature dependent assembly mechanisms, leading to a set of design rules to improve the formation of hollow capsids. In Chapter 4, we utilize this technique to analyze the experimental self-assembly of metallodielectric Janus colloids to identify assembly pathways and the relative stabilities of different colloidal aggregates, highlighting the effectiveness of this technique as a bridge between the experimental and computational realms. To further exemplify the usefulness of this many-body diffusion map approach, we demonstrate in Chapter 5 the identification of the key engineering design boundary for the stability of a class of soft information storage elements known as "digital colloids".

Owing to the computational complexity of our graph-based distance measure and quadratic scaling of the diffusion map with the number of observations, large scale uses of the diffusion map quickly become computationally intractable. In Chapter 6, we describe this computa-

tional challenge and propose landmark diffusion maps (L-dMaps) as an efficient methodology to rapidly improve the runtime performance of diffusion maps for large datasets while retaining high manifold embedding accuracy. This advancement opens the door for diffusion maps to be employed in a variety of time-sensitive or computationally demanding applications that were previously inaccessible.

Harnessing L-dMaps, we propose in Chapter 7 a "landscape engineering" framework capable of manipulating building block architecture to assemble a target aggregate structure, demonstrating its effectiveness in the design of patchy colloids to form polyhedral capsids. By optimizing the underlying free energy landscape for self-assembly, this framework allows for the systematic design of colloidal building blocks capable of enhancing the yield and specificity of self-assembling systems.

Chapters 2-7 are based in full or in part on the following publications:

- Andrew W. Long and Andrew L. Ferguson, "Nonlinear machine learning of patchy colloid self-assembly mechanisms and pathways", *Journal of Physical Chemistry B*, **118**, 15, 4228-4244 (2014). [**Chapter 2, Chapter 3**]

- Andrew W. Long, Jie Zhang, Steve Granick, and Andrew L. Ferguson, "Machine learning assembly landscapes from particle tracking data", *Soft Matter*, **11**, 8141-8153 (2015). [**Chapter 4**]

- Andrew W. Long, Carolyn L. Phillips, Eric Jankowksi and Andrew L. Ferguson, "Nonlinear machine learning and design of reconfigurable digital colloids", *Soft Matter*, **12**, 7119-7135 (2016). [**Chapter 5**]

- Andrew W. Long and Andrew L. Ferguson, "Landmark diffusion maps (L-dMaps): Accelerated manifold learning out-of-sample extension", *Applied and Computational Harmonics Analysis* (accepted 2017) [`https://arxiv.org/abs/1706.09396`] [**Chapter 2, Chapter 6**]

- Andrew W. Long and Andrew L. Ferguson, "Rational design of patchy colloids via landscape engineering", (in preparation 2017). [**Chapter 7**]

Extension of the techniques presented in this dissertation to the field of classifying structures in colloidal crystallization is given in:

- Wesley F. Reinhart, Andrew W. Long, Michael P. Howard, Andrew L. Ferguson, and Athanassios Z. Panagiotopoulos, "Machine learning for autonomous crystal structure identification", *Soft Matter*, **13**, 4733-4745 (2017).

Chapter 2

Machine learning of self-assembling materials

Nonlinear machine learning has been previously applied to molecular simulation trajectories to identify the pathways by which polymers collapse and proteins fold [52, 55, 69–72], to define order parameters for the crystallization of colloidal clusters with a constant number of particles [64], and characterize the binding of ligands to DNA [58, 73]. In contrast to simpler linear techniques, such as PCA [47, 74], nonlinear manifold learning techniques are basis free, requiring only a pairwise distance measure between clusters and allowing us to circumvent the absence of a spatially invariant basis set with which to describe many-body self-assembly phenomena [56]. Application of nonlinear techniques to the study of generalized self-assembly has, however, been frustrated by difficulties in defining a structurally and kinetically meaningful measure of the pairwise similarity of clusters containing differing numbers of identical particles.

In this chapter, we introduce the nonlinear diffusion map dimensionality reduction technique [56, 59, 75, 76] and confront the challenges in applying this technique to self-assembly by deriving graph-based distance measures to compare between many-body clusters. Using the diffusion map on self-assembly systems enables the identification of the fundamental underlying collective modes governing the long-time dynamics of patchy particle self-assembly. In analogy to the Mori-Zwanzig projection operator formalism [60, 62], this algorithm as-

This chapter is based on work presented in:

Andrew W. Long and Andrew L. Ferguson, "Nonlinear machine learning of patchy colloid self-assembly mechanisms and pathways", *Journal of Physical Chemistry B*, **118**, 15, 4228-4244 (2014).

Andrew W. Long and Andrew L. Ferguson, "Landmark diffusion maps (L-dMaps): Accelerated manifold learning out-of-sample extension", *Applied and Computational Harmonic Analysis* (accepted 2017).

sumes that the underlying dynamical modes for the system can be described by a (small) number of slow modes governing the long-time dynamical evolution of the system, to which the remaining fast modes are slaved and couple as effective noise. Projection of the simulation trajectories into this kinetically meaningful "slow subspace" reveals the structural progression by which the system assembles into its terminal aggregates, naturally uncovering the underlying assembly pathways and mechanisms.

2.1 Diffusion map dimensionality reduction

The diffusion map is a nonlinear dimensionality reduction technique that discovers low-dimensional manifolds within high-dimensional datasets by performing harmonic analysis of a random walk constructed over the data to identify nonlinear collective variables containing the predominance of the variance in the data [59, 60, 75, 76]. The first step in applying diffusion maps is to compute a measure of similarity between the N high-dimensional data points to construct the N-by-N pairwise distance matrix $\mathbf{d}$ with elements,

$$d_{ij} = ||\vec{x}_i - \vec{x}_j||, \tag{2.1}$$

where $||.||$ is an appropriate distance metric for the system under consideration (e.g. Euclidean, Hamming, earth mover's distance (EMD), rotationally and translational aligned root mean squared deviation (RMSD)). These distances are then used to define a random walk over the data by defining hopping probabilities A_{ij} from point i to point j as proportional to the convolution of d_{ij} with a Gaussian kernel,

$$A_{ij} = \exp\left(-\frac{d_{ij}^2}{2\epsilon}\right), \tag{2.2}$$

where ϵ is a soft-thresholding bandwidth that limits transitions between points within an $\sqrt{\epsilon}$ neighborhood. Systematic procedures exist to select appropriate values of ϵ for a particular

dataset [55, 77]. Forming the diagonal matrix $\mathbf{D}$ containing the row sums of the $\mathbf{A}$ matrix,

$$D_{ii} = \sum_{j=1}^{N} A_{ij}, \tag{2.3}$$

we normalize the hopping probabilities to obtain the Markov matrix $\mathbf{M}$,

$$\mathbf{M} = \mathbf{D}^{-1}\mathbf{A}, \tag{2.4}$$

describing a discrete diffusion process over the data. Although other choices of kernels are possible, the symmetric Gaussian kernel is the infinitesimal generator of a diffusion process such that the Markov matrix is related to the normalized graph Laplacian,

$$\mathbf{L} = \mathbf{I} - \mathbf{M}, \tag{2.5}$$

where $\mathbf{I}$ is the identity matrix, and in the limit of $N \to \infty$ and $\epsilon \to 0$ the matrix $\mathbf{L}$ converges to a backwards Fokker-Planck operator describing a continuous diffusion process over the high-dimensional data in the presence of a potential well [55, 59, 61, 75].

Diagonalizing $\mathbf{M}$ by solving the N-by-N eigenvalue problem,

$$\mathbf{M}\mathbf{\Psi} = \mathbf{\Psi}\mathbf{\Lambda} \tag{2.6}$$

where $\mathbf{\Lambda}$ is a diagonal matrix holding the eigenvalues $\{\lambda_i\}_{i=1}^{N}$ in non-ascending order and $\mathbf{\Psi} = \{\vec{\psi}_i\}_{i=1}^{N}$ is a matrix of right column eigenvectors corresponding, respectively, to the implied time scales and relaxation modes of the random walk [59, 75]. By the Markov property the top pair $\{\lambda_1 = 1, \vec{\psi}_1 = \vec{1}\}$ are trivial, and the steady state probability distribution over the high-dimensional point cloud is given by the top left eigenvector $\vec{\phi}_1 = \mathrm{diag}(\mathbf{D})$ [55]. The graph Laplacian $\mathbf{L}$ and Markov matrix $\mathbf{M}$ share left $\mathbf{\Phi}$ and right $\mathbf{\Psi}$ biorthogonal eigenvectors, and the eigenvalues of $\mathbf{L}$ are related to those of $\mathbf{M}$ as $\lambda_i^L = 1 - \lambda_i$ [55]. Accordingly, the

leading eigenvectors of $\mathbf{M}$ are the slowest relaxing modes of the diffusion process described by the graph Laplacian $\mathbf{L}$ [75].

A gap in the eigenvalue spectrum exposes a separation of time scales between slow and fast relaxation modes, informing an embedding into the slow collective modes of the discrete diffusion process that excludes the remaining quickly relaxing fast degrees of freedom [61]. Identifying this gap at λ_{k+1} informs an embedding into the top k non-trivial eigenvectors,

$$\vec{x}_i \rightarrow \{\vec{\psi}_2(i), \vec{\psi}_3(i), \ldots, \vec{\psi}_{k+1}(i)\}. \tag{2.7}$$

This diffusion mapping can be interpreted as a nonlinear projection of the high-dimensional data in $\mathcal{R}^K$ onto a low-dimensional "intrinsic manifold" in $\mathcal{R}^k$ discovered within the data where $k < K$. The diffusion map determines both the dimensionality k of the intrinsic manifold and good collective order parameters $\{\vec{\psi}_l\}_{l=2}^{k+1}$ with which to parameterize it. As described above, the overall complexity of manifold discovery and projection via diffusion maps is $\mathcal{O}(N^2)$, where efficient diagonalization routines typically leave this calculation dominated by calculation of pairwise distances.

2.1.1 Nyström embedding for out-of-sample extension

The Nyström extension presents a means to embed new data points outside the original N used to define the low-dimensional nonlinear embedding by approximate interpolation of the new data point within the low-dimensional manifold [78–82]. This operation proceeds by computing the distances of the new point to the N existing points defining the manifold $d_{\text{new},j} = ||\vec{x}_{\text{new}} - \vec{x}_j||$, and using these values to compute $A_{\text{new},j} = \exp\left(-\frac{d^2_{\text{new},j}}{2\epsilon}\right)$ and augment the $\mathbf{M}$ matrix with an additional row $M_{\text{new},j} = \left(\sum_{j=1}^{N} A_{\text{new},j}\right)^{-1} A_{\text{new},j}$ [81, 82]. The projected coordinates of the new point onto the k-dimensional intrinsic manifold defined by

the top $l = 2 \ldots (k+1)$ non-trivial eigenvectors of $\mathbf{M}$ are then given by,

$$\vec{\psi}_l(\text{new}) = \frac{1}{\lambda_l} \sum_{j=1}^{N} M_{\text{new},j} \vec{\psi}_l(j). \tag{2.8}$$

The computational complexity for the Nyström projection of a single new data point is $\mathcal{O}(N)$, requiring N distance calculations in the original K-dimensional space and then projection onto the k-dimensional manifold. Projections are exact for points in the original dataset, accurate for the interpolation of new points within the kernel bandwidth $\sqrt{\epsilon}$ of the intrinsic manifold defined by the N original points, but poor for extrapolations to points residing beyond this distance away from the manifold [56, 82, 83].

2.2 Distance measures for self-assembly systems

In order to apply diffusion maps to data mine assembly pathways from our self-assembly trajectories (cf. Section 2.1), we require a method to quantify the structural similarity of clusters as a proxy measure for their kinetic proximity [56, 76]. A variety of distance metrics are possible [59, 81, 84, 85], but an appropriate choice must properly treat the many-body nature of the system in which clusters comprise variable numbers of identical particles. Firstly, an N particle cluster can be described by $N!$ equivalent relabelings of the indistinguishable and interchangeable constituent particles, requiring that the measure explicitly confront this multiplicity in defining cluster similarities. Secondly, each cluster can have an arbitrary number of particles in an arbitrary configuration, making quantitative comparisons between clusters more complex as compared to clusters containing the same number of particles [64]. The use of a real space Euclidean distance metric is frustrated by the absence of a spatially invariant basis with which to describe arbitrary cluster configurations containing arbitrary numbers of particles. Simple metrics comparing cluster size or degree of connectivity discard information on the internal cluster structure. More advanced metrics

based on shape matching have been developed [86], but these methods also effectively coarse grain the underlying bonding network, discarding information on the local bonding structure of the cluster in favor of cluster symmetries and archetypal structures. In principle, the earth mover's distance (EMD) [87] could be applied to define pairwise cluster similarities, but the particle "democracy" requires an exhaustive consideration of all $N!$ particle labelings, making the problem computationally intractable for large clusters [81, 88].

We overcome the technical challenges arising from the lack of a invariant basis and particle fungibility by abstracting the cluster matching problem into a graph matching problem [33, 89], where scalar measures of graph similarity between graphical representations of cluster pairs serve as a good proxy measures for their structural similarity. This approach eliminates the difficulty of comparing dissimilarly sized clusters and circumvents the absence of a spatially invariant real-space basis by representing the cluster in a transformed graph space. Finding the optimal alignment of two graphs, the subgraph isomorphism problem, remains in general an NP-complete problem [85, 90, 91], requiring the evaluation of all possible $N!$ permutations for N node graphs, although for particular graph structures, such as planar graphs, it has been shown to be strongly polynomial [92]. While an exhaustive search is possible for small cluster sizes, this computation is intractable for large cluster graphs. For example, exhaustive comparison of two unique 12 particle clusters would require $12! = 479,001,600$ separate calculations to guarantee recovery of the optimal pairwise alignment. Due to the large number of unique clusters produced in our self-assembly studies, we instead appeal to an approximate greedy solution using an adaptation of the spectral graph matching algorithm IsoRank [85]. Owing to its usefulness in this work, we provide a brief description of the IsoRank algorithm, and then present the two primary greedy algorithms employed in this study.

2.2.1 IsoRank nodal similarity

The IsoRank algorithm, presented in Ref. [85], was developed to provide a global matching framework in the alignment of protein-protein interaction graphs. The procedure starts by construction of the binary adjacency matrix $\mathbf{G}_i$ defining the graph representing the pairwise bonding in cluster i. $\mathbf{G}_i(p,q) = 1$ indicates that our distance criterion has defined a bond between particles p and q in the cluster, whereas $\mathbf{G}_i(p,q) = 0$ indicates that no bond exists between these particles.

IsoRank provides a measure of nodal similarity between two network graphs, yielding a measure of the proximity between node p in graph $\mathbf{G}_i$ and node q in $\mathbf{G}_j$. It works by formation of the tensor product between graphs, $\mathbf{K} = \mathbf{G}_i \otimes \mathbf{G}_j$, and then row-normalizing to generate a random walk over the tensor (or Kronecker) product graph $\mathbf{D}_{ii} = \sum_j \mathbf{K}_{ij}$, $\mathbf{M} = \mathbf{D}^{-1}\mathbf{K}$. Eigendecomposition of the random walk described by the M matrix yields the steady state solution describing the distribution of a walker along the nodes in the tensor product graph. Recasting this solution from column form to matrix-form yields a score $\mathbf{B}(p,q)$ that defines the similarity between node p in $\mathbf{G}_i$ and node q in $\mathbf{G}_j$.

Further improvements in the construction of this heuristic can be made. Construction of the tensor product can be a time consuming process, as for graphs of size $N \times N$ and $M \times M$, the tensor product is of size $(N \times M) \times (N \times M)$. Formulating and solving the eigenvalue problem is equally time consuming due to this drastic increase in size. Owing to the properties of tensor products, we can avoid construction of the full tensor product and instead solve reduced eigendecompositions for random walks on the individual graphs to reconstruct the tensor product's eigenvector [93]. This advance provides a large reduction in the complexity of computing IsoRank heuristics.

2.2.2 Simultaneous traversal matching

The IsoRank algorithm was derived for the alignment of protein-protein interaction graphs. The highly sparse nature of these graphs enables rapid solution of the graph matching procedure via the Hungarian algorithm [94]. In highly connected graphs, this method breaks down, owing to an inability to preserve the underlying bonding network in the matching procedure. Here we propose a matching algorithm using a simultaneous breadth-first traversal of the two graphs' bonding networks using IsoRank score as a heuristic to strictly preserve the bonding architecture. Having defined our two graphs, $\mathbf{G}_i$ and $\mathbf{G}_j$, and our nodal score $\mathbf{B}$, we start by choosing the node pairing with the highest similarity score. In the event that more than one node pair has the same score, one pairing is selected at random. The assignment process then proceeds by considering as candidates for the next pairing only those nodes in each graph that are connected to the most recently paired node in each graph that we refer to as the "central node". This choice preserves connectivity information in the matching procedure, ensuring that new node pairs are connected to the previously assigned networks. The pairing within this candidate set possessing the maximum similarity score is selected next. In the event of ties we select the node pair possessing the maximum degree of edges linking to previously assigned nodes, thereby favoring matches within the densest segments of each graph first. If ties still persist, one pairing is selected at random. Each node pairing made is added to a queue, and after the central node pair is exhausted of unassigned neighbors, the nodes in the pairing at the head of the queue are made the central nodes in each graph. This process is iteratively repeated until all node pairings are made.

This operation defines a permutation matrix, $\mathbf{H}$, that rearranges the rows and columns of $\mathbf{G}_i$ such that the transformation $\mathbf{G}_i' = \mathbf{H}\mathbf{G}_i\mathbf{H}^T$ represents the best discovered global alignment of $\mathbf{G}_i$ and $\mathbf{G}_j$. In the event that we are matching graphs $\mathbf{G}_i, \mathbf{G}_j$ of differing sizes N_i, N_j, where without loss of generality $N_i < N_j$, we augment the smaller graph with $|N_j - N_i|$ additional rows and columns of zeros to represent the missing particles relative

to the larger cluster. The addition of these "ghost" particles, and comparison against these particles reflect the absence of these contacts within the smaller cluster.

Our modification drastically improves the performance of the matching for a set number of attempted greedy assignments as compared to a Hungarian algorithm approach, and we observe empirically superior and more robust alignment performance compared to the original IsoRank implementation. Nevertheless, we observe that our modified algorithm remains fundamentally greedy in nature, and as an NP-complete problem [85, 90], guaranteed recovery of the optimal global alignment would require enumeration over all possible alignments. For clusters containing more than a handful of particles, exhaustive enumeration quickly becomes computationally intractable.

2.2.3 Tree-based matrix alignment

In the previously section we proposed a strategy for the matching of graphs via breadth first traversal of the graph structures. In this section we describe a matching procedure that works via a depth-first traversal over the permutation space, offering a systematic means of defining the size of the search space over which to look for an optimal alignment, allowing for greater control of the trade-off between accuracy and computational efficiency in graph matching. Further, it has shown empirically to serve better in the alignment of pairwise distance matrices over Hungarian or simultaneous traversal, while not necessarily preserving the strict connectivity information as in simultaneous matching. This procedure works by constructing a tree with branching factor k, a simple example of which is given in Figure 2.1. We start by generation of the IsoRank matrix as described above. We identify the top k scores in the IsoRank matrix, corresponding to the k node pairs that we wish to investigate. For each node pair selected, we construct a branch of the tree where we eliminate that node pair from future matches, having already assigned it to the proposed permutation matrix.

We traverse this tree in a depth-wise manner, iterating from the initial root node to a leaf node whereby we have matched all nodes from graph $\mathbf{G}_i$ to nodes in $\mathbf{G}_j$. We use a

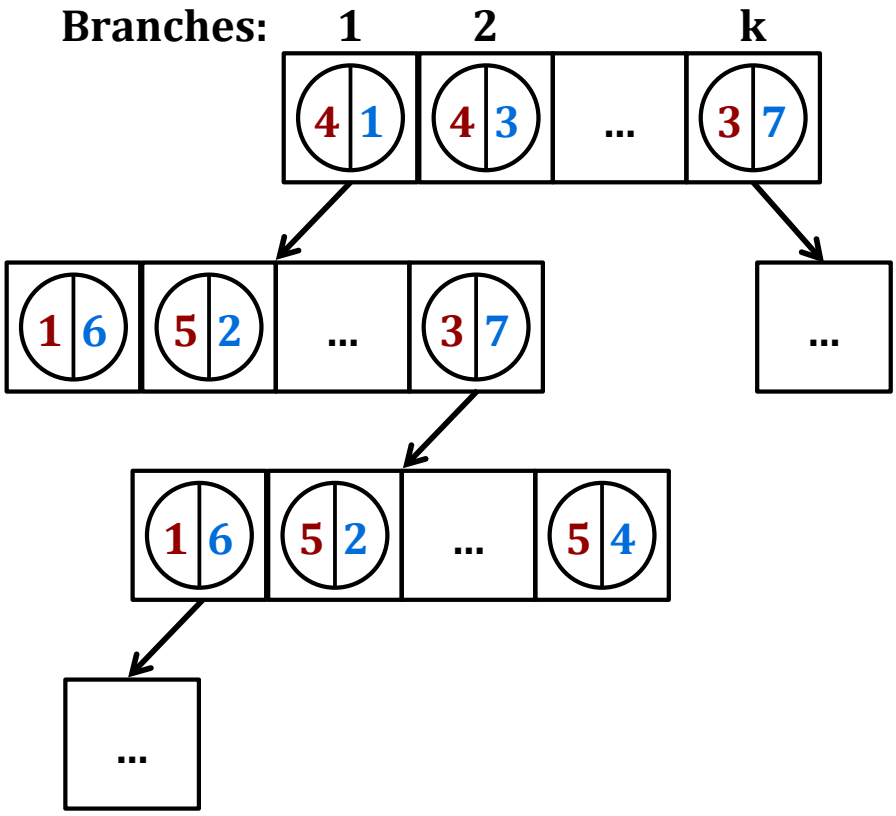

Figure 2.1: Example representation of the nodal permutation tree structure traversed to find a pseudo-optimal alignment between cluster bonding matrices. At each layer of the tree, we generate k subbranches constituting the top k node pairs by IsoRank score that have not been previously assigned in the tree hierarchy.

similar augmenting procedure as discussed for the simultaneous traversal algorithm to deal with cases of unequal graph sizes. Upon reaching a leaf node, we are able to construct the full permutation **H** corresponding to this path in the tree. We measure the distance between graphs induced by this permutation, and pop back up the tree to follow the next branch, continuing this procedure of moving up and down paths in this tree until we have exhaustively sampled all leaf nodes or have yielded a perfect match. This depth-first strategy allows us to realize additional computational savings through an early exist strategy in which we discard from contention any subbranches that possess a greater graph distance

tan the current minimum computed distance without having to traverse all the way down to the leaf node. This approach has proved to be an extremely efficient strategy in all of our tests and is generally applicable to graph matching problems in a variety of fields. A C++ implementation is hosted for free public download at `https://github.com/awlong/DiffusionMap`.

2.2.4 Graphical distances

Having defined our bonding matrices, $\mathbf{G}_i$ and $\mathbf{G}_j$, and permutation matrix $\mathbf{H}$ through the procedures described above, we are interested in computing the distance between the two graph structures. The exact form for this distance is context dependent, and particular specializations are discussed in subsequent chapters. The primary notion however is that we seek to compute the aligned distance between cluster topologies. We compute the inter-particle distance matrix between all particles in cluster i, $\mathbf{R}_i$. Using our nodal permutation, we transform this distance matrix into the basis of our transformed bonding network as $\mathbf{R}_i' = \mathbf{H}\mathbf{R}_i\mathbf{H}^T$. We then define the similarity of the two clusters by summing over the absolute differences of corresponding interparticle distances between the two clusters

$$d_{ij} = \sum_{p=1}^{N} \sum_{q=p+1}^{N} \|R_i'(p,q) - R_j(p,q)\| \tag{2.9}$$

where $\mathbf{d}$ is the (symmetric) matrix of cluster pairwise distances, $R_i'(p,q)$ is the distance between particles p and q in the transformed basis of cluster i, $R_j(p,q)$ is the distance between particles p and q in cluster j, and $N = \max(N_i, N_j)$, where N_i is the number of particles in cluster i. This distance metric encapsulates both the local deviations in bonding as particles fluctuate around their equilibrium separation and the global differences between clusters with different bonding architectures.

2.3 Many-body diffusion maps

By applying diffusion maps to our many-body distance measure, we are able to infer the low-dimensional intrinsic manifold driving self-assembly behavior. As discussed in Ref. [55], the leading eigenvectors of the **M** matrix correspond to the slow collective modes of the system under two relatively mild assumptions: (i) the system dynamics are well-modeled by a diffusion process, and (ii) that our pairwise similarity measure between clusters is a good measure of short-time diffusive motions. *A priori*, we anticipate that interactions between the patchy colloids will lead to cooperative couplings between the system degrees of freedom and the emergence of a small number of slow collective modes governing the long-time self-assembly behavior. The presence of a gap in the eigenvalue spectrum of the **M** matrix provides *post hoc* substantiation of this conjecture. A separation of time scales suggests that the system dynamics may be modeled under the Mori-Zwanzig formalism as a set of coupled stochastic differential equations in the slow collective modes, to which the remaining fast degrees of freedom couple as effective noise. Such a description suggests that the system may be modeled as a diffusive process, satisfying the first assumption.

Our measure of pairwise cluster similarities by graph matching captures both global differences resulting from addition/removal of particles from the cluster, and local differences stemming from bond length fluctuations, furnishing a measure of the "structural remodeling" required to transform one cluster into another. Small values of this measure are therefore expected to reflect short-time changes in the cluster structure resulting from fluctuations in interparticle distances and/or number of particles in the cluster. Accordingly, we expect our cluster similarity metric to satisfy the second assumption by serving as a good measure of short time diffusive evolution of the cluster structure.

Under these two assumptions, not only do the leading eigenvectors correspond to the slow collective modes, but Euclidean distances between clusters in the embedding prescribed by Equation 2.7 approximate "diffusion distances" in real space, where the diffusion distance

can be interpreted as the ease with which one cluster may transform into another [55, 75, 76]. By including all $(N-1)$ non-trivial eigenvectors in the embedding this correspondence becomes exact [76]. Together, these two properties imbue the diffusion map with its capacity to project simulation trajectories into dynamically meaningful low-dimensional embeddings that map out the long-time evolution of the system, and, as a corollary, reveal the underlying self-assembly pathways and mechanisms. A number of nonlinear manifold learning techniques exist, including Isomap [53], local linear embedding (LLE) [54], and Laplacian eigenmaps [95], but it is this attractive feature of diffusion maps that lead us to favor this approach.

Chapter 3

Machine learning of patchy colloid assembly

Determination of assembly pathways describing the sequence of structural steps leading to the formation of a terminal aggregate provides a powerful means to infer the structural mechanisms underpinning assembly [33]. Wilber *et al.* [35, 43] observed the self-assembly of patchy particles into icosahedral aggregates to proceed by two distinct assembly paths. At high temperatures, aggregates formed through step-wise addition of monomers, whereas at low temperatures, the particles flocculated into a disordered liquid phase from which near complete icosahedral clusters periodically "bud off". The authors identified these two pathways by visual inspection of simulation trajectories supported by tracking of the cluster size distribution. This approach to assembly pathway inference, however, cannot reveal the full microscopic mechanistic details of the process. A systematic approach to assembly pathway inference developed by Jankowski and Glotzer [33, 68] discovers metastable structures by computing approximate partition functions and identifies assembly pathways by constructing a directed network over these states. The great strength of this approach is that it recovers thermodynamic assembly pathways independently of system dynamics, but by the same token cannot capture the thermodynamically *and* kinetically meaningful assembly pathways within a single unified framework.

In this chapter, we present a new approach to systematically infer self-assembly pathways by nonlinear machine learning of molecular simulation trajectories. By mimicking the true

This chapter is adapted with permission from the American Chemical Society (Copyright 2014) from work presented in:

Andrew W. Long and Andrew L. Ferguson, "Nonlinear machine learning of patchy colloid self-assembly mechanisms and pathways", *Journal of Physical Chemistry B*, **118**, 15, 4228-4244 (2014).

building block dynamics within the simulations, we naturally recover assembly pathways that reflect both the thermodynamics (*what* can assemble?) and kinetics (*how* does it assemble?) of the process. As we discuss below, the nonlinear machine learning technique described in Chapter 2 employed in this work – many-body diffusion maps [56, 75] – circumvents the technical difficulties that plague the application of linear approaches such as principal components analysis (PCA) [47], and recovers kinetically meaningful order parameters that characterize the collective structural rearrangements driving the long-time evolution of the assembly process [56]. We demonstrate our approach in an application to Brownian dynamics simulations of the self-assembly of anisotropic patchy particles into polyhedral aggregates as a well-characterized test system [9, 35, 43]. Our approach is directly extensible to systems with arbitrary dynamics and arbitrary particle geometries and chemistries. We anticipate that the systematized recovery of self-assembly pathways and mechanisms will provide a deeper understanding of self-assembly processes of scientific and technological importance, and ultimately help to guide rational building block design for the fabrication of materials with desirable structural and functional properties.

3.1 Materials and methods

3.1.1 Patchy colloid model

We model anisotropic "patchy particles" using the model of Zhang & Glotzer [9] in which each particle comprises a large sphere decorated by smaller attractive surface patches arranged in two coaxial annular rings. This model has been used previously to study the reversible self-assembly of a range of aggregates including tetrahedral, octahedral, and icosahedral clusters [9]. The patchy particle is composed of three subspecies, denoted A, B, and C, that together comprise a rigid body (Figure 3.1). All patchy particle visualizations were generated using VMD [96]. The larger A-spheres represent a spherical colloidal particle. The smaller B- and C-spheres that adorn the A-sphere mediate the anisotropic interparticle

interactions. The B-spheres compose the ring closest to the equator of the A-sphere, while the C-spheres make up the ring closer to the pole. B-B interactions and C-C interactions between spheres in different particles are attractive, serving as anisotropic "sticky patches". We can alter the relative geometry of our patchy particles by varying the polar angle of the B and C rings. Following Zhang and Glotzer [9], we bias the assembly of particular polyhedra by placing the sticky patches such that they optimally contact in the geometry of an idealized aggregate. We are interested in two simple, but non-trivial, target structures upon which to test and validate our methodology: tetrahedral aggregates as a simple test case for the assembly of small polyhedral clusters, and icosahedral aggregates as a toy model for viral capsid formation that has been well-characterized by Wilber *et al.* [35, 43]. To favor icosahedral clusters we place 14 B-spheres at a polar angle of 70.6°, and 11 spheres C-spheres at a polar angle 49.0°. To favor tetrahedral cluster formations, we place 11 B-spheres at a polar angle of 46.8°, and 6 C-spheres at a polar angle of 24.9°.

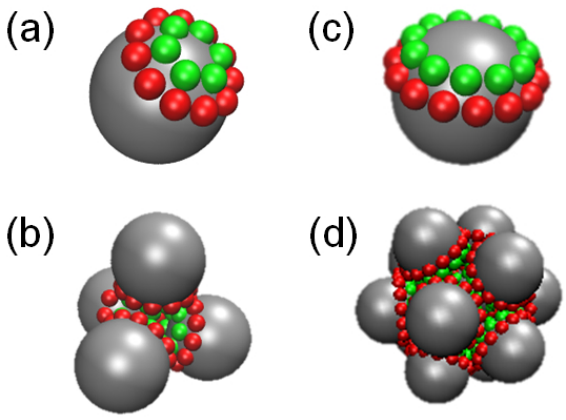

Figure 3.1: Rigid body double ring patchy particles employed in this study [9]. (a) and (b) correspond to the structure of the tetrahedral monomer and the idealized tetrahedral cluster, and (c) and (d) represent the icosahedral monomer and idealized icosahedral cluster. A-spheres are gray, B-spheres red, and C-spheres green.

We treat the patchy particles as rigid bodies neglecting all intraparticle interactions, and model interparticle interactions using potentials previously implemented by Glotzer and coworkers [9, 34]. Interparticle B-B and C-C interactions are modeled by a Lennard Jones

potential

$$U_{LJ}^{ii}(r) = 4\varepsilon_i \left[\left(\frac{\sigma_i}{r} \right)^{12} - \left(\frac{\sigma_i}{r} \right)^{6} \right] \tag{3.1}$$

where σ_i is the diameter of particle i, ϵ_i is the potential well depth for particle type i, and r is the interparticle separation. A-X, where X $\in$ {A,B,C}, and B-C interactions occur through a surface shifted Weeks-Chandler-Andersen (WCA) potential to account for excluded volume of the A spheres [97]

$$U_{WCA}^{ij}(r) = \begin{cases} 4\varepsilon_{ij} \left[\left(\frac{\sigma}{r-\Delta_{ij}} \right)^{12} - \left(\frac{\sigma}{r-\Delta_{ij}} \right)^{6} \right] + \varepsilon_{ij}, & r < 2^{(1/6)}\sigma + \Delta_{ij} \\ 0, & r \geq 2^{(1/6)}\sigma + \Delta_{ij} \end{cases} \tag{3.2}$$

where $\varepsilon_{ij} = \sqrt{\varepsilon_i \varepsilon_j}$ is defined according to the Berthelot combining rule [98], $\Delta_{ij} = (\sigma_i + \sigma_j)/2 - \sigma$, and σ is a parameter for the shifted Lennard Jones potential given by HOOMD-blue [99]. We perform our simulations in dimensionless units such that $\sigma = \sigma_B = \sigma_C = 1$, $\sigma_A = 5$, $\varepsilon = \varepsilon_A = \varepsilon_B = \varepsilon_C = 1$, and $m = m_A = m_B = m_C = 1$ where m_i is the mass of sphere i. The reduced temperature is defined as $T^* = k_B T/\epsilon$, and reduced time as $t^* = t/\sqrt{m\sigma^2/\epsilon}$. We note that for this choice of parameters, $\Delta_{AA} = 4$, $\Delta_{AB} = \Delta_{AC} = 2$, and $\Delta_{BC} = 0$, which effectively prohibits A-A overlaps, assuring that the patchy particles interact primarily by specific B-B, C-C, and B-C interactions on the surface of the A spheres.

3.1.2 Brownian dynamics simulations

Simulations were conducted using the HOOMD-blue GPU-accelerated molecular dynamics code [99] using a rigid-body Brownian dynamics integrator to implicitly model solvent effects on the motion of colloidal patchy particles in suspension [100]. The code is available at: `http://codeblue.umich.edu/hoomd-blue`. The equations of motion were numerically integrated using a symplectic, microcanonical scheme for rigid bodies developed by Miller *et al.* [101], in which drag and random forces are applied to each particle according to

the fluctuation-dissipation relation at the specified system temperature. Periodic boundary conditions in a cubic box were implemented in all dimensions.

All simulations are initialized and performed in the following manner. First, a random initial configuration was generated by placing 120 patchy particles on a square lattice and evolving this system at high temperature ($T^* = 1.0$) with only WCA interactions active. The initial volume fraction of the box is $\phi = 0.05$, and the box dimensions are shrunk, scaling the particle positions with the box size, to reach the target volume fraction of $\phi = 0.20$ over 10^4 time steps with $dt^* = 10^{-4}$. Our choice of target volume fraction is identical to that employed by Zhang and Glotzer [9] and corresponds to a particle number density of $1.8 \times 10^{-3}\sigma^{-3}$. Once the box has reached its terminal size, an additional 10^6 time steps with $dt^* = 10^{-3}$ are conducted to randomize the starting configuration. To investigate the effect of temperature on icosahedral cluster formation, we perform three independent simulations at each of nine dimensionless temperatures $T^* = \{0.55, 0.60, 0.65, 0.70, 0.75, 0.80, 0.85, 0.90, 0.95\}$ for 3×10^6 time steps with $dt^* = 5 \times 10^{-3}$. For temperatures $T^* \leq 0.5$, the simulations become kinetically arrested in a large disordered aggregate comprising all particles in the box. For temperatures $T^* > 0.95$, we observe a monomeric vapor of particles with transient formation of small clusters. The simulation duration was sufficiently long to observe the formation of complete icosahedra at all temperatures. Assembly of the icosahedra was effectively irreversible on the time scale of our simulations, with disassembly of complete icosahedral aggregates never observed. In the case of tetrahedral cluster formation, we perform three independent simulations at each of eight dimensionless temperatures $T^* = \{0.2, 0.3, 0.4, 0.5, 0.6, 0.7, 0.8, 0.9\}$ for 2×10^6 time steps with $dt^* = 5 \times 10^{-3}$. For temperatures $T^* < 0.2$, the system condenses into a disordered liquid comprising all particles in the system.

To define a mapping of our dimensionless simulations to real units, we may specify (for example) σ_A =1 μm, ρ_A = 1 g/cm^3, and $\epsilon = 1 k_\mathrm{B}T$ at T = 298 K. This maps our reduced temperature $T^* = 1.0$ to a real temperature of T = 298 K, and the dimensionless simulation time step of $dt^* = 5 \times 10^{-3}$ to a real time step of $dt = 0.36$ μs. Our simulations of tetrahedral

cluster assembly therefore correspond to a run time of $t = 0.7$ s and a temperature range of $T = 60 - 268$ K, and of icosahedral cluster assembly to $t = 1.1$ s and $T = 164 - 283$ K.

3.1.3 Cluster determination

Over the course of a simulation, snapshots of the system are saved every 10^4 time steps. To identify clusters of particles, we abstract each snapshot into interaction graphs describing the connectivity between particles in the system, where vertices and edges represent the patchy particles and the bonds between these particles, respectively [89]. A simple distance criterion is used to establish the existence of a bond in our simulation, whereby if two attractive B- or C-spheres on distinct patchy particles are within a distance of 1.5σ, the particles are considered bonded. We have verified that our results are robust to variations in the distance threshold over the range 1.125–1.875σ. We identify the strongly connected subgraphs corresponding to distinct clusters in each snapshot using Tarjan's algorithm [102].

3.1.4 Many-body diffusion mapping

We describe in detail the many-body diffusion map procedure in Chapter 2. Here we describe the key methodological details unique to this study, namely the functional form for the distance between particle clusters. Given two clusters with corresponding bonding matrices $\mathbf{G}_i, \mathbf{G}_j$ and pairwise distance matrices $\mathbf{R}_i, \mathbf{R}_j$, we utilize the simultaneous traversal matching procedure from Section 2.2.2 to construct the pseudo-optimal aligning permutation $\mathbf{H}$. Using this permutation, we transform the bonding and distance matrices $\mathbf{G}_i, \mathbf{R}_i$ into the transformed basis $\mathbf{G}'_i = \mathbf{H}\mathbf{G}_i\mathbf{H}^T$, $\mathbf{R}'_i = \mathbf{H}\mathbf{R}_i\mathbf{H}^T$. We define the similarity between two clusters by summing over the absolute differences of corresponding interparticle distances between the two clusters

$$d_{ij} = \sum_{p=1}^{N} \sum_{q=p+1}^{N} |R'_i(p,q)G'_i(p,q) - R_j(p,q)G_j(p,q)| \tag{3.3}$$

where $\mathbf{d}$ is the (symmetric) matrix of cluster pairwise distances, $R_i'(p,q)$ is the distance between particles p and q in the transformed basis of cluster i, $G_i'(p,q)$ is the corresponding element of the binary adjacency matrix in the transformed basis, $R_j(p,q)$ is the distance between particles p and q in cluster j, $G_j(p,q)$ is the corresponding element of the binary adjacency matrix, and $N = \max(N_i, N_j)$, where N_i is the number of particles in cluster i. Multiplying the distances by the corresponding element of the binary adjacency matrix assures that only particle pairs between which a bond has been defined participate in the sum.

Having constructed our pairwise distance matrix $\mathbf{d}$, we apply diffusion map dimensionality reduction (Equations 2.2, 2.3, and 2.6) to extract the low-dimensional landscape for self-assembly. The "diffusion mapping" is the embedding of the i^{th} cluster into this low-dimensional space by projecting it into the i^{th} component of the top k non-trivial eigenvectors,

$$\mathbf{x}(i) \rightarrow (\Psi_2(i), \Psi_3(i), ..., \Psi_{k+1}(i)) \tag{3.4}$$

This low-dimensional manifold describes the collective motions driving self-assembly, with each eigenvector corresponding to a particular dynamical mode. As described in the following sections, the systems in this work each exhibited a gap in the eigenvalue spectrum at either k=2 or 3 (Figures 3.3 and 3.8).

3.1.5 Physical order parameters

Despite the attractive properties of diffusion map embeddings, it is a well-known deficiency of diffusion maps (and of nonlinear dimensionality reduction methodologies in general) that the approach does not also provide a direct physical interpretation of the slow collective modes approximated by the leading eigenvectors of the $\mathbf{M}$ matrix [56]. Thus while order parameters furnished by the diffusion map are good descriptors of the slow collective modes, assigning physical meaning to these modes is a non-trivial task [55, 69]. In this work,

we derive physical interpretability by correlating each eigenvector with candidate physical variables to furnish physical "bridge" variables to help physically interpret the diffusion map embeddings [55].

As described below, we identified the the Steinhardt bond orientation order parameters, $\{Q_l\}$, [103] as good bridge variables, and which have been used extensively in the analysis of Lennard Jones cluster formations [65] and in nucleation theory [104, 105]. Q_l represents the l^{th} order sum of rotationally invariant spherical harmonics, given by,

$$Q_l = \left[\frac{4\pi}{2l+1} \sum_{m=-l}^{l} |\bar{Q}_{lm}|^2| \right]^{\frac{1}{2}}, \tag{3.5}$$

where $\bar{Q}_{lm}$ is defined as,

$$\bar{Q}_{lm} = \frac{1}{N_b} \sum_{\vec{r_b}} Y_{lm}(\theta(\vec{r_b}), \phi(\vec{r_b})), \tag{3.6}$$

where $\vec{r_b}$ is the vector connecting the cluster center of mass to a bond midpoint, θ and ϕ are the polar and azimuthal angles corresponding to this vector $\vec{r_b}$, Y_{lm} is the spherical harmonic of degree l and order m, N_b is the number of bonds in the cluster, and the sum over $\vec{r_b}$ runs over all N_b vectors. By projecting cluster orientations onto rotationally invariant combinations of spherical harmonics these order parameters effectively measure the degree of angular ordering of the particles around the cluster center of mass.

In Section 3.2.3, we discuss the effectiveness of these order parameters in characterizing the coordinates furnished by the diffusion map for the self-assembly of icosahedral clusters. It is conceivable that other physical variables exist that might show improved correlation with the diffusion map coordinates – for example, structural order parameters corresponding to the bulk crystal phases – and we observe that systematic procedures exist to screen pools of candidate variables to identify such physical variables [106, 107]. We note, however, that while the identification of such correspondences can provide a wealth of physical insight into the self-assembly process, the inherently many-body and often complex nature of the self-assembly process means that we may not expect simple physical interpretations of the

underlying collective modes identified by the diffusion map.

3.2 Results and discussion

3.2.1 Tetrahedral cluster formation

Following the protocols described in Section 3.1, we simulated the self-assembly of our tetrahedral forming patchy particles at temperatures $T^* = \{0.2,\ 0.3,\ 0.4,\ 0.5,\ 0.6,\ 0.7,\ 0.8,\ 0.9\}$ from which we identified a total of 63,335 clusters belonging to 427 unique geometry classes. For clusters belonging to the same geometry class, the mean distance between them is 2.87 ± 0.02, while for clusters belonging to different classes, the mean minimum distance is 7.37 ± 0.11. This shows that our distance metric is able to effectively capture bonding differences both within and between the different cluster geometries. Differences between clusters within the same geometry class correspond to fluctuations around the equilibrium bond distances, while distances between clusters in different geometry classes also arise from the addition or removal of bonds within the cluster.

The structure of each cluster observed in our simulation is defined in real space by the (relative) position and orientation of all particles in the cluster. The low-dimensional embedding constructed by the diffusion map projects these configurations onto a manifold in which the various clusters are separated according to their structural similarity. Simulations at different temperatures are expected to explore different regions of configurational phase space since high-temperature systems can access higher energy configurations and jump energy barriers that low-temperature systems cannot. (Indeed, due to finite sampling and sensitive dependence on initial conditions, simulations at the same temperature initialized with distinct starting configurations are also expected to explore different configurational ensembles.)

Since the manifold constructed by the diffusion map is a function of the configurations from which it is constructed, in order to compare the low-dimensional embeddings of differ-

ent simulations in the same basis set, it is necessary to construct a single composite manifold from the configurations aggregated from all simulation trajectories. Constructing a different manifold for each simulation trajectory would prohibit comparisons across simulations since the basis sets (i.e., the eigenvectors, $\{\Psi_i\}$, spanning each embedding) are constructed from different structural ensembles, and therefore differ between embeddings. The various regions of the composite manifold explored by different simulations can then be identified by considering only those data points corresponding to those runs. In this manner, the regions of the composite manifold explored by simulations at high and low temperatures can be identified. Since the volume of thermally accessible phase space increases with temperature, we anticipate that at equilibrium the range of structures explored by low-temperature simulations will constitute a subset of those sampled at high temperatures. As a corollary, we expect the volume of the composite manifold sampled by a simulation at low temperature to be a subvolume of that explored at a high temperature.

We applied the diffusion map to the complete ensemble of 63,335 clusters identified at all eight temperatures to construct a single composite diffusion map embedding of the self-assembly process. Following Singer et al. [77], we determine an appropriate bandwidth of the Gaussian kernel used to soft-threshold the pairwise cluster distances matrix by constructing a log-log plot of the element sum of the soft-thresholded cluster pairwise distances matrix, $\mathbf{A}$, against the kernel bandwidth, ϵ. The log-log plot for the tetrahedral patchy particles considering all 63,276 post-deislanding clusters identified in simulations at all eight temperatures is presented in Figure 3.2. This system exhibits a double-sigmoid character, indicative of diffusion processes at two different length scales. At kernel bandwidths below the intermediate plateau, the bandwidth is sufficiently large for each cluster to "see" neighbors within their own geometry class, which possess the same internal bonding structure, but different bond lengths. For ϵ values above the intermediate plateau, the bandwidth is sufficiently large for clusters to "see" clusters outside their own geometry class, and the data becomes globally connected. It is imperative that we select a bandwidth in the latter regime

to assure that we model one global diffusion process, rather than an ensemble of disjoint processes, to synthesize a single unified diffusion map embedding of the data. Empirically, we find that selecting relatively large ϵ values within the upper plateau is necessary to attain global connectivity within our data, with insufficient kernel bandwidths producing highly disconnected diffusion map embeddings. For the case of tetrahedral patchy particles, we selected $\epsilon = \exp(10)$ as the soft-thresholding bandwidth.

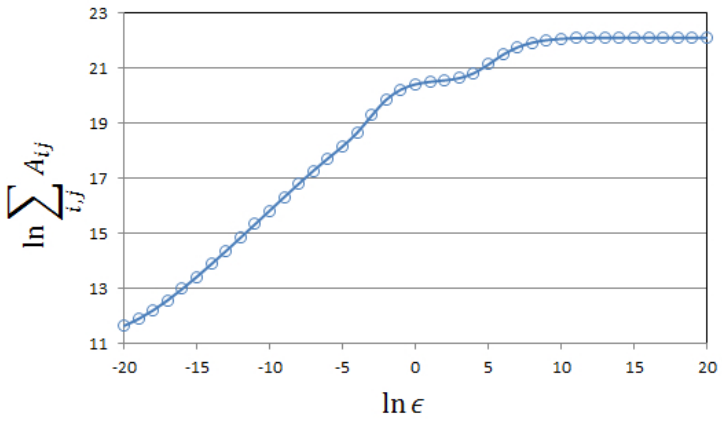

Figure 3.2: Log-log plot of the sum of the pairwise similarity matrix, $\sum_{i,j} A_{ij}$, as a function of soft-thresholding bandwidth used in Gaussian kernel for similarities computed between all realized clusters in tetrahedral simulations.

Using the L-method [108], we identified a gap in the diffusion map eigenvalue spectrum after the third non-trivial eigenvalue (Figure 3.3), motivating the construction of three-dimensional embeddings. Upon embedding into the three non-trivial eigenvectors with eigenvalues above the spectral gap, a small number of 59 clusters were identified as outliers separated from the rest of the data in the low-dimensional projection. From the correspondence of real space diffusion distances with diffusion map Euclidean distances, these clusters may be interpreted as rarely visited configurations to which no well-sampled dynamic pathway exists to the bulk of the data, possibly due to the presence of high free energy barriers. Following the "deislanding" procedure detailed in Ref. [69], we removed these outlying clusters from our cluster ensemble and recomputed the diffusion map embedding over the

remaining 63,276 clusters.

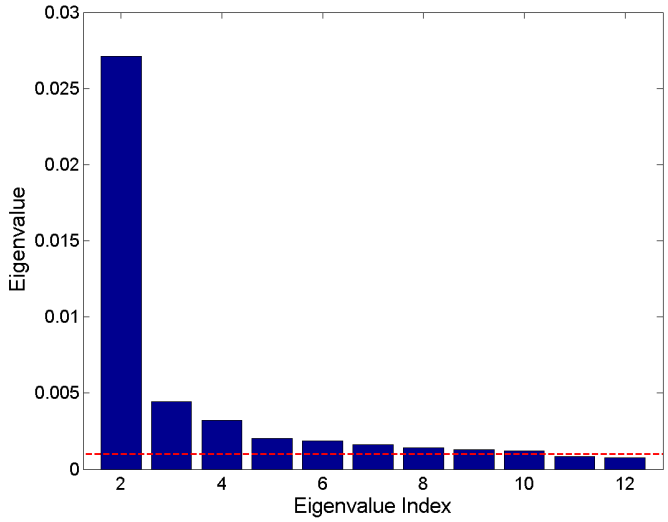

Figure 3.3: Diffusion map eigenvalue spectrum for the tetrahedral patchy particle system. The trivial unit eigenvalue, λ_1, has been omitted for clarity. The noise floor identified by a permutation test is indicated by a horizontal broken line. A spectral gap after the third non-trivial eigenvalue, λ_4, was identified using the L-method, motivating a k=3 dimensional diffusion map embedding of this system.

We present our diffusion map embedding in 3.4. Each point corresponds to a single cluster colored according to the number of particles it contains. Visualizations of representative cluster geometries along the manifold have been overlaid to reveal the assembly pathways resolved by this low dimensional embedding. Our approach systematically infers the progression of cluster arrangements that lead from free monomers to self-assembled tetrahedral aggregates. Further, we can see the formation of diverse structures from the desired tetrahedral formation, such as hexahedra, and two divergent assembly pathways leading to the formation of two morphologically distinct particle chains. The chain visible to the right of the image corresponds to a stack of interlocking dimers and tetrahedral tetramers, while that towards the bottom is composed of a stack of interlocking trigonal planar trimers. The chain length is limited only by the number of particles present in the simulation box.

To more easily visualize the assembly pathways revealed by the diffusion map, in Figure

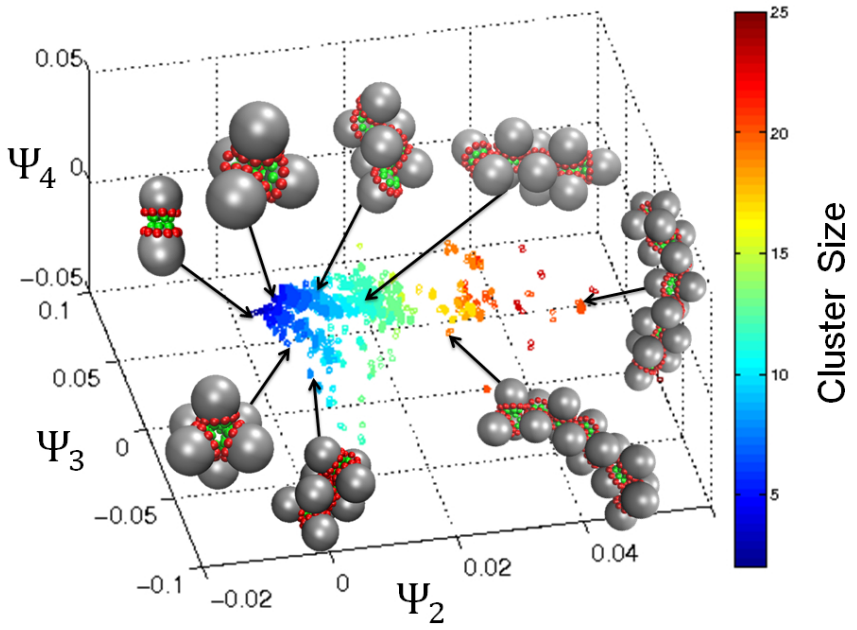

Figure 3.4: Three-dimensional embedding of the tetrahedral self-assembly process in the top three eigenvectors, $[\Psi_2, \Psi_3, \Psi_4]$, furnished by the diffusion map. Each point corresponds to one of 63,276 clusters observed in Brownian dynamics simulations at one of eight temperatures, $T^* = \{0.2, 0.3, 0.4, 0.5, 0.6, 0.7, 0.8, 0.9\}$. Particular clusters have been selected for visualization to illustrate the structural evolution along the assembly pathways. Points have been colored according to cluster size.

3.5 we have projected our three dimensional embedding into the two-dimensional planes parametrized by $[\Psi_2, \Psi_3]$ and $[\Psi_2, \Psi_4]$. By collapsing onto the $[\Psi_2, \Psi_3]$ plane (Figure 3.5a), we can discern some variation in the assembly pathways leading to the two chains, but the variability with respect to Ψ_3 is insufficient to clearly separate the two assembly pathways. In contrast, the two distinct routes can be clearly discerned in the embedding in $[\Psi_2, \Psi_4]$ in Figure 3.5b. The top pathway corresponds to the formation of the stacked interlocking dimers and tetrahedral tetramers, while the bottom pathway yields the stacked interlocking trigonal planar trimers. Visualization of representative clusters along the pathway extracted by the diffusion map reveals the assembly mechanism along each path. In the upper pathway, monomers first condense into dimers and tetrahedral tetramers, which then form dimer-dimer and tetramer-dimer pairs that condense monomers and dimers from the bulk into

an extending chain. This appears to enable structural rearrangement into relative particle positions that maximize the overlap of attractive patches. The bottom pathway, on the other hand, proceeds exclusively by the condensation of free trimers, and yields a more dense interlocking structure. Although the patches on the particle surfaces were placed to favor assembly of the idealized tetrahedral cluster, we see that (depending on temperature, cf. Figure 3.6) this may only represent an intermediate, rather than terminal, aggregation state due to these chain condensation processes.

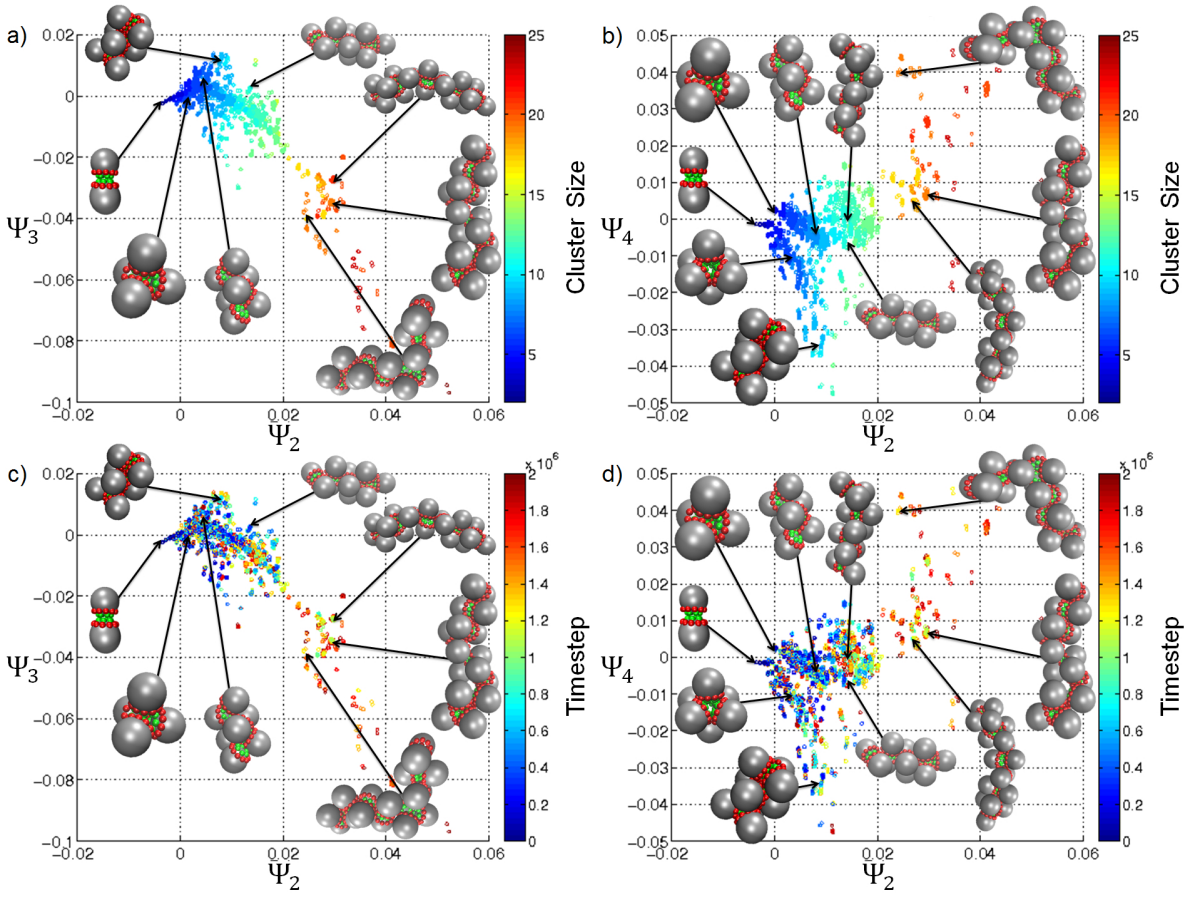

Figure 3.5: Two-dimensional embedding of the tetrahedral self-assembly process into (a,c) [Ψ_2,Ψ_3], and (b,d) [Ψ_2,Ψ_4]. Each point corresponds to one of 63,276 clusters observed in Brownian dynamics simulations at one of eight temperatures, $T^* = \{0.2, 0.3, 0.4, 0.5, 0.6, 0.7, 0.8, 0.9\}$. Particular clusters have been selected for visualization to illustrate the structural evolution along the assembly pathways. Points in panels (a) and (b) have been colored according to cluster size, and in panels (c) and (d) according to the simulation time at which the cluster was observed.

In Figure 3.6a, we reproduce Figure 3.5b, and in panels b–i restrict the embeddings to only those points harvested at each of the eight temperatures considered. By modulating the temperature, or equivalently modifying the interaction strength, we observe that we can selectively activate or deactivate the pathways for formation of chain-like aggregates. At high temperature (low interaction strength), $0.7 \leq T^* \leq 0.9$, interparticle interactions are sufficient to stabilize clusters containing up to only eight particles. The system exists as an ensemble of small dispersed clusters, with tetrahedral clusters dominating. Upon lowering the temperature (increasing the interaction strength) to $0.5 \leq T^* \leq 0.6$, the bottom assembly pathway to chains of stacked trigonal planar trimers becomes active. In this temperature regime, dimers and trimers readily form. Collision of two trimers induces a structural relaxation that leads the trimers to interlock, permitting partial overlap of the attractive patches and energetic stabilization of the aggregate. Further elongation of the interlocking chain can occur through the addition of free trimers, as well as monomers and dimers. Coalescence of monomers at the chain end caps the chain by forming an effective tetrahedral aggregate at the terminus. Similarly, interaction of the chain terminus with dimers can induce the dimer to decompose, with one partner serving as the end cap while the other is released back into the bulk. Capped trimers chains are able to continue growing through the addition of a monomer that binds to the tetrahedral terminus, serving as a bridging site for further aggregation.

Upon lowering the temperature further (increasing the interaction strength), $0.2 \leq T^* \leq 0.4$, assembly of chains of interlocking dimers and tetrahedral tetramers becomes favorable, and begins to compete with the assembly of trimer chains. In this regime, bonding between monomers is effectively irreversible, and dimers quickly form from free monomers. The collision of a dimer with another dimer or larger aggregate leads to condensation, where the dimer reorients to an interlocking position that maximizes attractive patch overlap in the aggregate. The formation of tetrahedra can still occur in this low temperature setting, but they are readily condensed into the interlocking chain structures.

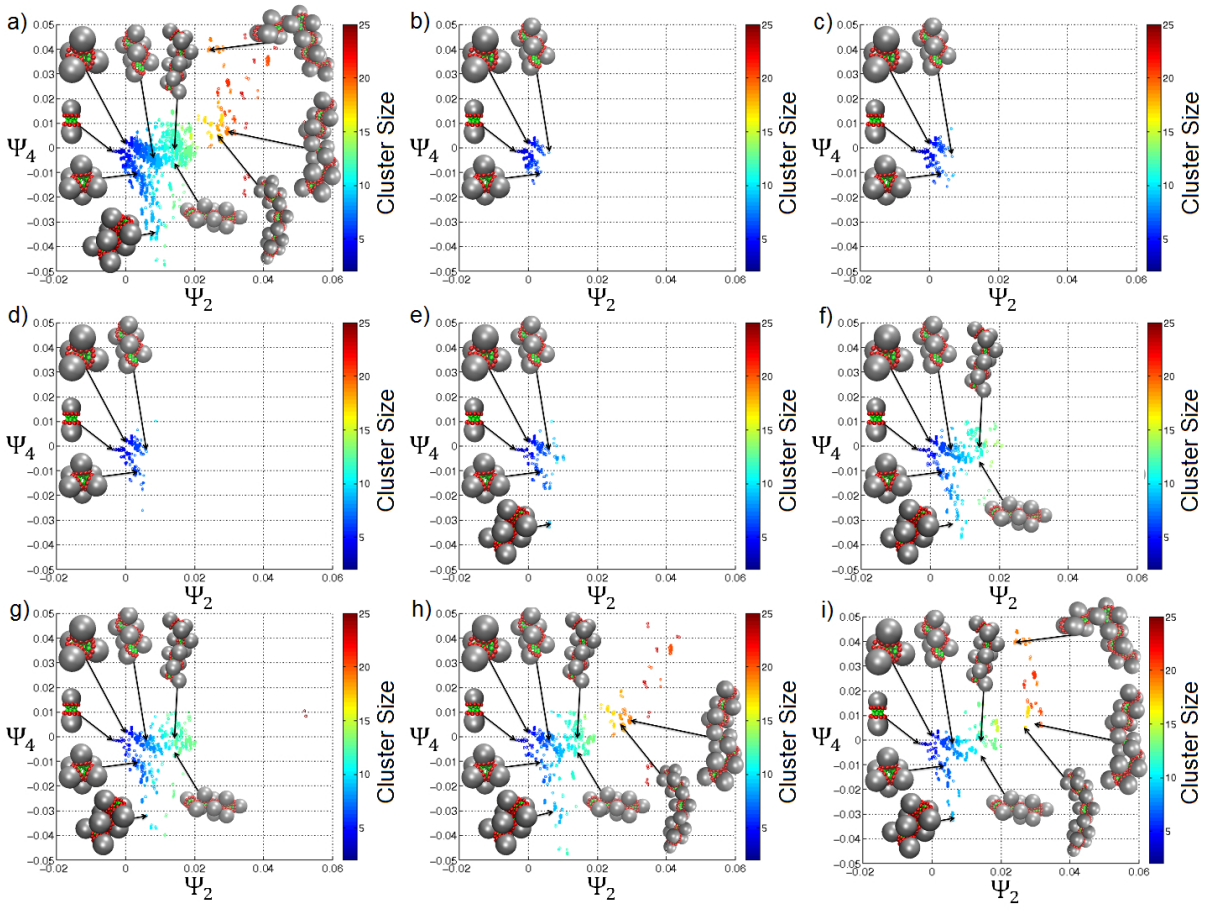

Figure 3.6: Two-dimensional embedding of the tetrahedral self-assembly process into $[\Psi_2,\Psi_4]$ at (a) all eight temperatures $T^* = \{0.2, 0.3, 0.4, 0.5, 0.6, 0.7, 0.8, 0.9\}$, (b) $T^* = 0.9$, (c) $T^* = 0.8$, (d) $T^* = 0.7$, (e) $T^* = 0.6$, (f) $T^* = 0.5$, (g) $T^* = 0.4$, (h) $T^* = 0.3$, and (i) $T^* = 0.2$. Points are colored according to cluster size, and particular clusters selected for visualization.

By embedding our simulation trajectories using diffusion maps, we have systematically identified two distinct assembly pathways and mechanisms leading to the formation of long chains of particles. Although we designed the anisotropic interactions of our patchy particle to favor the assembly of idealized tetrahedral clusters, we only observe formation of tetrahedral aggregates as one component of a mixture of small (N<8) clusters at high temperatures (weak interaction strengths), $0.7 \leq T^* \leq 0.9$, or in addition to long chains of stacked dimers and tetrahedral clusters at lower temperatures (stronger interaction strengths), $0.2 \leq T^* \leq 0.4$. At intermediate temperatures, $0.5 \leq T^* \leq 0.6$, tetrahedral

clusters appear metastable relative to long chains of interlocking trigonal planar trimers. These findings demonstrate the rich range of cluster morphologies and assembly mechanisms that can be accessed by manipulating the interparticle interaction strength. However, modification of interaction strength alone is insufficient to uniquely favor the assembly of tetrahedral clusters over all competing aggregates, indicating that particle redesign by adjusting placement of the anisotropic interaction patches will be necessary to achieve this goal. We anticipate that placing the annular rings closer to the particle poles will better mask the patches within the tetrahedral cluster, discouraging the formation of extended chains. Placing the rings too close to the pole, however, will likely favor dimers over tetramers.

We note that the simulations conducted in this work – particularly at the lower temperatures considered – are intrinsically non-equilibrium, in which we simulate the irreversible assembly of large aggregates. Accordingly, while the assembly pathways unveiled by the diffusion map reveal the underlying kinetic mechanisms by which self-assembly proceeds, the simulation snapshots are not drawn from an equilibrium distribution, and therefore each cluster is not represented in proportion to its Boltzmann factor. As a result, the density of points in the diffusion map embeddings cannot be related to the underlying equilibrium probability distribution, and it is not possible to infer the relative prevalences of the observed clusters and/or compute empirical free energy surfaces over the embeddings [55, 56]. The assembly pathways revealed in the present work may be viewed as the progression of the self-assembly process along the low-lying valleys of the underlying free energy surface. In Chapter 7 we describe a procedure to conduct biased sampling directly in the order parameters furnished by the diffusion map (i.e., $[\Psi_2,\Psi_3,\Psi_4]$) to recover the global topography of the free energy landscape parameterized by these kinetically meaningful variables [109, 110].

3.2.2 Icosahedral cluster formation

Identification of different assembly mechanisms

Following the same protocol as above, we conducted simulations of our icosahedral forming patchy particles at each of nine different temperatures $T^* = \{0.55, 0.60, 0.65, 0.70, 0.75, 0.80, 0.85, 0.90, 0.95\}$. We identify from these simulations a total of 48,010 clusters belonging to 1365 unique geometry classes. The mean distance between clusters in the same geometry class is 3.06 ± 0.03, whereas the mean minimum distance between different geometries is 10.08 ± 0.24, again showing that our distance metric is able to effectively resolve in-class and out-of-class distances. The diffusion map was applied to the pairwise similarities between all 48,010 structures to produce low-dimensional embeddings of the icosahedral self-assembly process. The soft-thresholding bandwidth was selected using the approach of Coifman *et al.* [77] (Figure 3.7), and a gap in the eigenvalue spectrum after the second non-trivial eigenvalue (Figure 3.8) motivated us to construct the diffusion map embeddings into the top two non-trivial eigenvectors presented in 3.9.

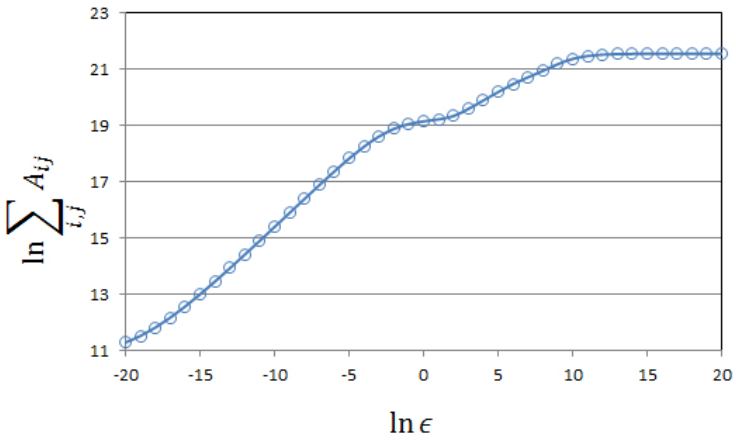

Figure 3.7: Log-log plot of the sum of the pairwise similarity matrix, $\sum_{i,j} A_{ij}$, as a function of soft-thresholding bandwidth used in Gaussian kernel for similarities computed between all realized clusters in icosahedral simulations.

The diffusion map embedding reveals two distinct assembly pathways leading to the same

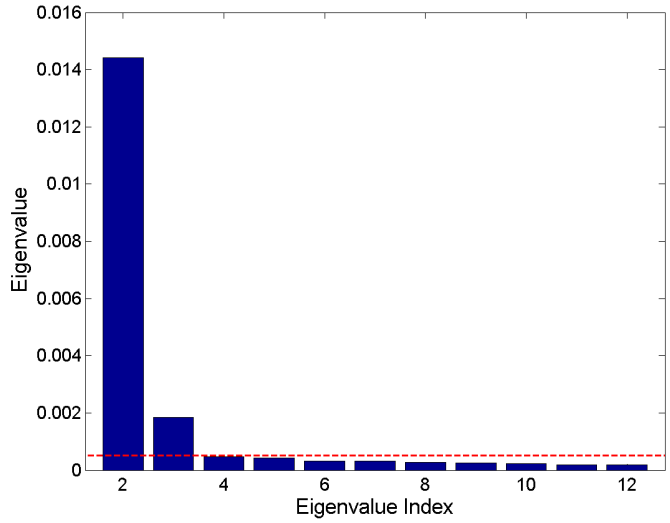

Figure 3.8: Diffusion map eigenvalue spectrum for the icosahedral patchy particle system. The trivial unit eigenvalue, λ_1, has been omitted for clarity. The noise floor identified by a permutation test is indicated by a horizontal broken line. A spectral gap after the third non-trivial eigenvalue, λ_4, was identified using the L-method. Since λ_4 resides below the noise floor, this led us to define the spectral gap at the last non-trivial eigenvalue above the noise floor, λ_3, motivating a k=2 dimensional diffusion map embedding of this system.

terminal icosahedral aggregates. This is qualitatively different from the tetrahedral system, in which we inferred two divergent assembly pathways leading to two morphologically distinct chains. Furthermore, the length of the extended chains of tetrahedral building blocks was limited only by the number of particles in the simulation, whereas the icosahedral building blocks produce self-limiting, finite-sized icosahedral aggregates.

We demonstrate the impact of temperature upon assembly by extracting points from the composite embedding corresponding to only those clusters observed at each of the nine temperatures, and color points according to cluster size (Figure 3.10), mean number of bonds per particle in the cluster (Figure 3.11), and simulation time step (Figure 3.12). At high temperatures, $T^* = 0.95$ (Figure 3.10b), there is no pathway from dimers to icosahedral structures as the thermal energy is on the order of the interaction strength between patchy particles, resulting in a gas of monomers, dimers, and other small aggregates.

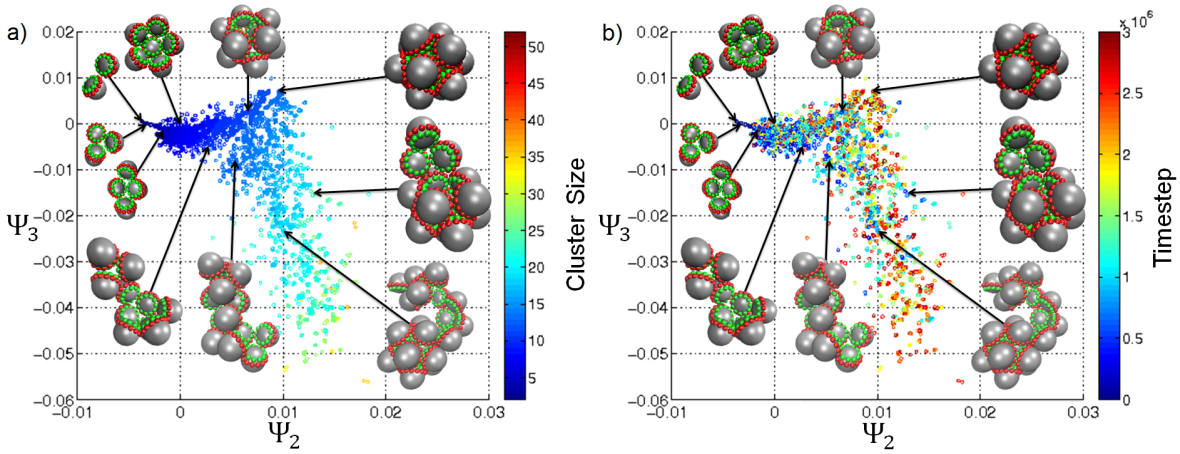

Figure 3.9: Two-dimensional embedding of the icosahedral self-assembly process in the top two eigenvectors, $[\Psi_2, \Psi_3]$, furnished by the diffusion map. Each point corresponds to one of 48,010 clusters observed in Brownian dynamics simulations at one of nine temperatures, $T^* = \{0.55,\ 0.60,\ 0.65,\ 0.70,\ 0.75,\ 0.80,\ 0.85,\ 0.90,\ 0.95\}$. Particular clusters have been selected for visualization to illustrate the structural evolution along the assembly pathways. Points in panel (a) have been colored according to cluster size, and in panel (b) according to the simulation timestep at which the cluster was observed.

As the temperature decreases (interaction strength increases), $0.85 \leq T^* \leq 0.90$ (Figures 3.10c-d), a path emerges whereby dimers can transform into icosahedra by monomeric addition in which the mean number of bonds per particle increases towards the five nearest neighbors of each particle in the terminal icosahedral cluster (Figures 3.11c-d). Thus this high-temperature assembly mechanism proceeds in a stepwise fashion, with free monomers accreting onto a partially formed aggregate in the structural configuration of a partially formed icosahedral cluster. This high-temperature mechanism is identical to that previously reported by Wilber *et al.* [35, 43] by visual inspection of assembly trajectories supported by tracking of particle size distributions.

As the temperature is lowered to $T^* = 0.80$ (Figure 3.10e), we observe the formation of large ($N > 12$) disordered aggregates that do not lie on the monomeric addition assembly pathway. At still lower temperatures (stronger interaction strengths), $0.65 \leq T^* \leq 0.75$ (Figures 3.10f-h), this ensemble of liquid-like aggregates expands, opening up a second assembly

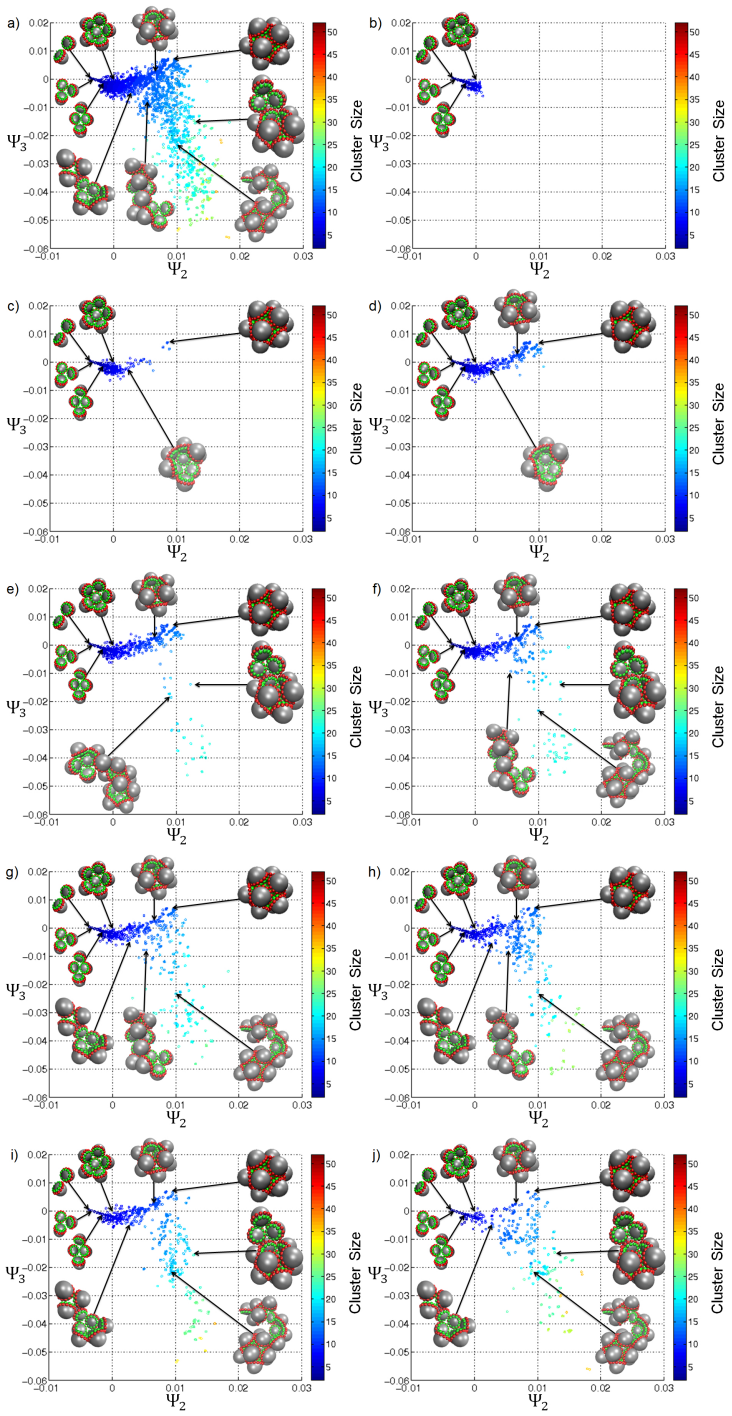

Figure 3.10: Two-dimensional embedding of the icosahedral self-assembly process into $[\Psi_2,\Psi_3]$ at (a) all nine temperatures $T^* = \{0.55, 0.60, 0.65, 0.70, 0.75, 0.80, 0.85, 0.90, 0.95\}$, (b) $T^* = 0.95$, (c) $T^* = 0.90$, (d) $T^* = 0.85$, (e) $T^* = 0.80$, (f) $T^* = 0.75$, (g) $T^* = 0.70$, (h) $T^* = 0.65$, (i) $T^* = 0.60$, and (j) $T^* = 0.55$. Points are colored according to cluster size, and particular clusters selected for visualization.

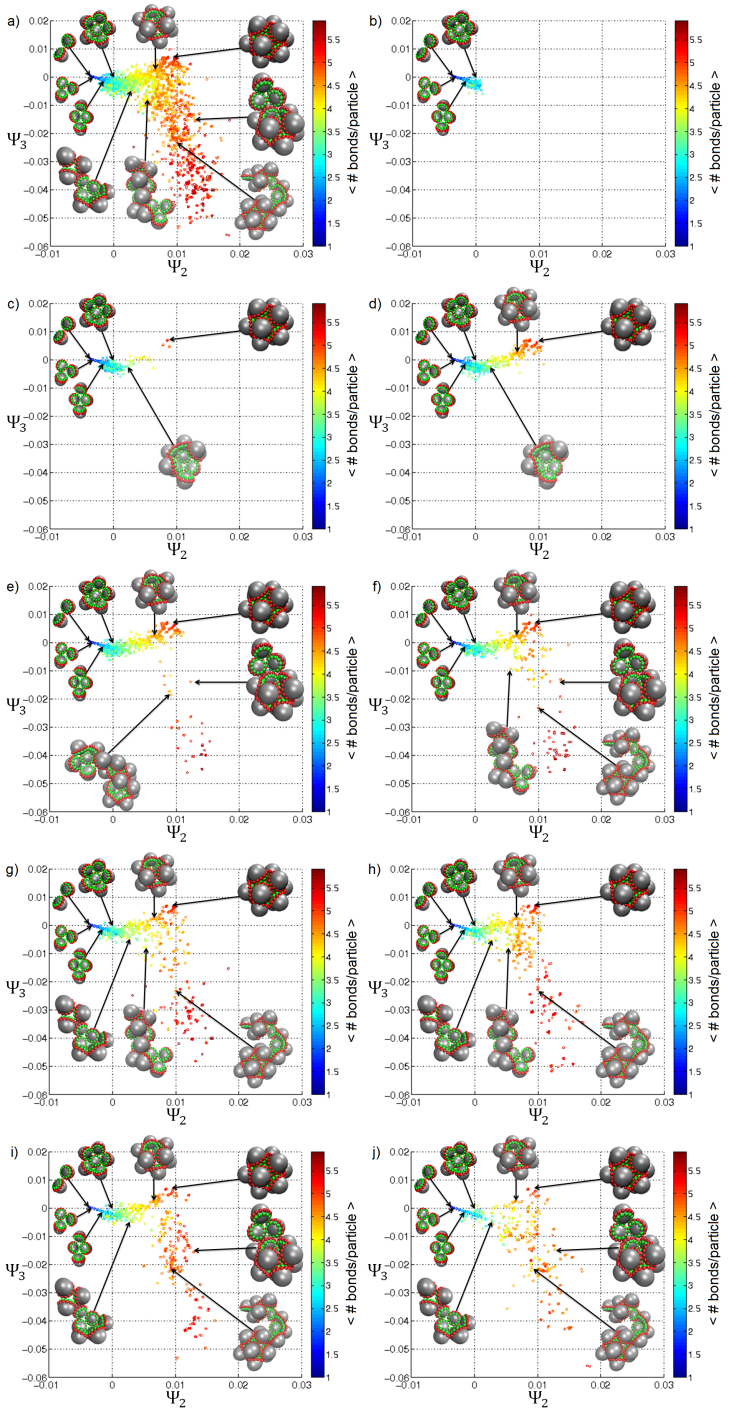

Figure 3.11: Two-dimensional embedding of the icosahedral self-assembly process into $[\Psi_2,\Psi_3]$ at (a) all nine temperatures $T^* = \{0.55, 0.60, 0.65, 0.70, 0.75, 0.80, 0.85, 0.90, 0.95\}$, (b) $T^* = 0.95$, (c) $T^* = 0.90$, (d) $T^* = 0.85$, (e) $T^* = 0.80$, (f) $T^* = 0.75$, (g) $T^* = 0.70$, (h) $T^* = 0.65$, (i) $T^* = 0.60$, and (j) $T^* = 0.55$. Points are colored according to the mean number of bonds per particle in the cluster, and particular clusters selected for visualization.

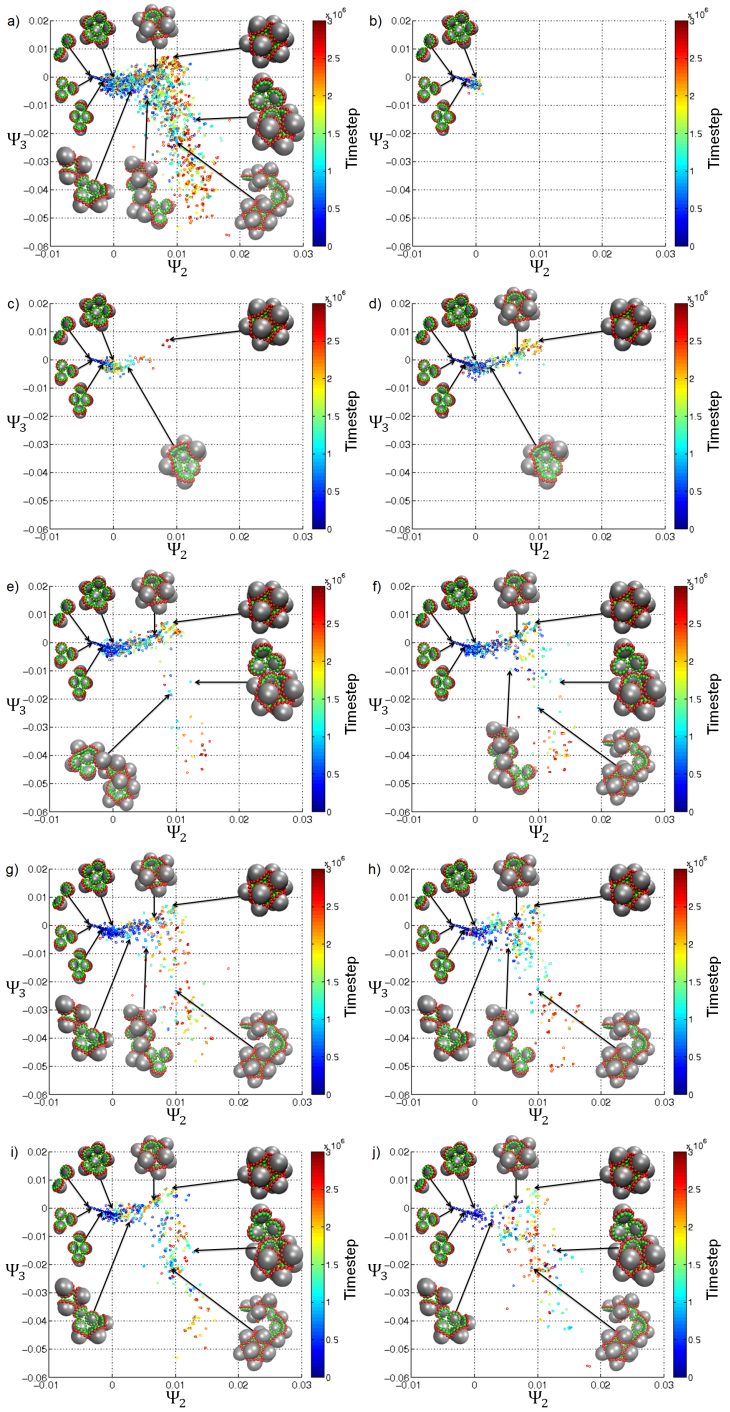

Figure 3.12: Two-dimensional embedding of the icosahedral self-assembly process into $[\Psi_2,\Psi_3]$ at (a) all nine temperatures $T^* = \{0.55, 0.60, 0.65, 0.70, 0.75, 0.80, 0.85, 0.90, 0.95\}$, (b) $T^* = 0.95$, (c) $T^* = 0.90$, (d) $T^* = 0.85$, (e) $T^* = 0.80$, (f) $T^* = 0.75$, (g) $T^* = 0.70$, (h) $T^* = 0.65$, (i) $T^* = 0.60$, and (j) $T^* = 0.55$. Points are colored according to the simulation time at which the cluster was observed, and particular clusters selected for visualization.

pathway to the terminal icosahedra, wherein complete icosahedral, or near-icosahedral, clusters periodically detach from the disordered liquid phase. This second assembly mechanism becomes more prevalent as the temperature decreases, lowering the fraction of clusters that assemble by monomeric addition (cf. Figure 3.14), eventually dominating the monomeric pathway at low temperatures, $0.55 \leq T^* \leq 0.60$ (Figure 3.10i-j). This low-temperature icosahedral assembly mechanism is precisely the "budding" mechanism previously described by Wilber *et al.* [35, 43].

The mechanistic difference between the budding and monomeric addition pathways is clearly illustrated in Figures 3.11g-j. Along the upper monomeric addition route, the average number of bonds per particle increases monotonically towards the five nearest neighbors of the terminal icosahedron, whereas along the lower budding pathway, the particles assemble into disordered clusters within which internal structural rearrangements periodically yield sub-clusters possessing $\sim$5 bonds per particle that subsequently detach into the terminal icosahedral aggregates.

We have employed diffusion maps to systematically reveal and resolve two distinct assembly pathways – monomeric addition, and budding from a disordered liquid – for the assembly of terminal icosahedral clusters. Unlike the tetrahedral system, the idealized icosahedral aggregate that inspired placement of our anisotropic interaction patches does represent the low-temperature stable terminal aggregate at temperatures $T^* > 0.5$. At lower temperatures, the system collapses into a disordered liquid that is kinetically trapped on the time scale of our simulations. Further, by modulating temperature (interaction strength) we can control the mechanism by which the icosahedra assemble: monomeric addition at high temperatures, and budding at low temperatures (cf. Figures 3.14). The two competing assembly pathways identified by our approach are in good agreement with those previously reported by Wilber *et al.* [35, 43], providing strong validation that our methodology can perform automated extraction of assembly pathways and mechanisms that were previously only deducible by visual inspection of assembly trajectories.

Pathway propensity

The embeddings in Figures 3.10-3.12 reveal two distinct assembly pathways but do not inform the relative assembly fluxes through each pathway at each temperature. Since assembled icosahedra are never observed to disassemble, the icosahedral state represents a sink state, and by tracing the assembly of each icosahedron backwards in time, we can infer the pathway along which it passed in the low-dimensional assembly landscape, and therefore by which of the two mechanisms it assembled. This calculation quantifies the relative assembly fluxes along each path as a function of temperature.

To determine the relative probabilities with which each icosahedron assembles by monomeric addition or liquid budding, we first must classify each cluster in our embedding as belonging to one of these two pathways. We use a support vector machine (SVM) classifier with a radial basis function kernel to compute a nonlinear surface – the separatrix – separating the two classes in the two-dimensional embedding in $[\Psi_2,\Psi_3]$ (3.9a). We construct this surface by first generating a uniform 100×100 square grid of points over the two-dimensional diffusion map embedding spanning $\Psi_2 = [-0.004, 0.023]$ and $\Psi_3 = [-0.056, 0.009]$. Each point in the grid is classified as belonging to the monomeric assembly or liquid budding mechanism by majority vote of a distance weighted five-nearest neighbor classifier comprising training points drawn from a high-temperature simulation at $T^* = 0.90$ in which we define all points to belong to the monomeric addition pathway (Figure 3.10c), and a low-temperature simulation at $T^* = 0.55$ in which we define all points to belong to the budding pathway (Figure 3.10j). We then compute the separatrix by training a two-class SVM classifier over the classified 100×100 grid using a radial basis function kernel with Gaussian bandwidth of 1.0 and box constraint for the soft margin of 1.0. We elect to apply the SVM to the classified grid trained on the high and low temperature data, rather than to the raw data itself, to smooth out the large deviations in density of the point cloud in our embedding (Figure 3.13) and synthesize a more robust and smooth classification surface. Our attempts to train an SVM on the raw

data produced a classifier that was unable to effectively distinguish the two assembly mechanisms since it was disproportionately biased to generate a classification surface within the high density region of points localized within ($\Psi_2 \approx [-0.005, 0.005], \Psi_3 \approx [-0.008, 0.002]$), effectively ignoring the sparsely populated region ($\Psi_2 \approx [0.005, 0.017], \Psi_3 \approx [-0.05, -0.01]$). Finally, we use this separatrix to classify all of the clusters observed at all temperatures, by specifying those residing below the separatrix to belong to the budding path, and those above to monomeric addition (Figure 3.13). Our classifier maintains the general demarcation between the two pathways described in the previous section, and enables computation of the relative flux through each pathway by unambiguously assigning each cluster to one of the two assembly pathways.

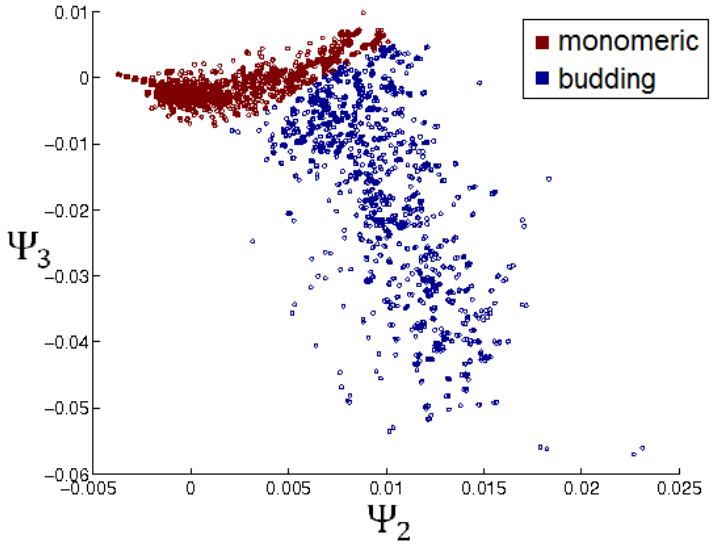

Figure 3.13: SVM classification of the [Ψ_2,Ψ_3] diffusion map embeddings of the 48,010 clusters harvested at all nine temperatures as belonging to the monomeric addition (red) or budding (blue) assembly pathway.

For each temperature trajectory, we identify each terminal icosahedron and trace the constituent particles back through all intermediate clusters leading to assembly. For each

trace we define the fraction of budding character of the corresponding icosahedron as

$$f_{\text{budding}} = \frac{\sum_{i=1}^{N_{\text{trace}}} \text{size}(i)\text{class}(i)}{\sum_{i=1}^{N_{\text{trace}}} \text{size}(i)}, \tag{3.7}$$

and the fraction of monomeric addition character as

$$f_{\text{monomer}} = 1 - f_{\text{budding}}, \tag{3.8}$$

where size(i) is the number of particles in the i^{th} cluster in the trace, class(i) is 1 if the i^{th} cluster belongs to the budding class and 0 if it belongs to the monomeric addition class, and N_{trace} is the number of clusters constituting the trace that ultimately coalesces into the terminal icosahedral aggregate. For icosahedra that form predominantly through budding, f_{budding} will be close to 1, whereas for those that form principally through monomeric addition it will be close to 0.

In Figure 3.14a we present the mean and standard deviation of the budding and monomeric addition character averaged over all icosahedra formed at each temperature. At high temperatures, $T^* > 0.65$, the monomeric addition pathway dominates the budding pathway, whereas at low temperatures, $T^* < 0.65$, this trend inverts. At $T^* \approx 0.65$, both pathways are equally active. The monomeric addition pathway does not completely shut off in the low temperature limit, however, as the formation of large liquid aggregates initially proceeds by the formation of small clusters by monomeric addition that subsequently coalesce into the large unstructured aggregates.

In Figure 3.14b we show the number of icosahedra observed to assemble in each of the three independent simulations at each temperature. From this plot it is apparent that the temperature of maximum flux is $T^*_{max} \approx$ 0.75-0.80. Interestingly, in this temperature window both assembly pathways are active, with the monomeric route more populated than the budding. The existence of a temperature optimum can be understood as a complex

interplay of assembly thermodynamics (high temperatures disfavor the formation of large aggregates, cf. Figure 3.10b), kinetics (high temperatures lead to faster rates, and low temperatures to kinetic trapping in a disordered liquid), and the topography of the free energy surface (at high temperatures ($T^* \geq 0.85$) only the monomeric addition pathway is effectively open, whereas at lower temperatures both the monomeric addition and budding routes are available).

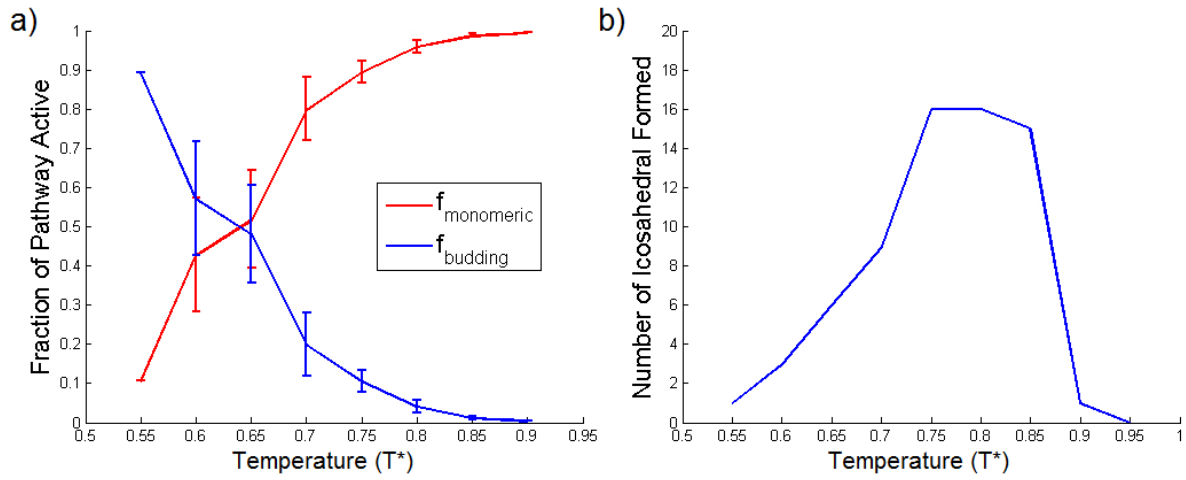

Figure 3.14: Icosahedral assembly fluxes. (a) Mean budding (red) and monomeric addition (blue) character of the icosahedral clusters observed to assemble at each temperature. Error bars represent the standard deviation in the icosahedral character averaged over all assembled icosahedra. (b) Total number of icosahedra assembled in the three independent simulations at each temperature.

3.2.3 Physical interpretation of diffusion map coordinates

As previously observed here and elsewhere [56], a limitation of the diffusion map approach is that order parameters describing the low-dimensional embedding (i.e., $\{\Psi_i\}$) come with no *a priori* physical interpretability. To provide *post hoc* understanding of the physical correspondence of these order parameters, we correlated Ψ_2 and Ψ_3 with candidate physical variables to identify two physical "bridge" variables showing strong correlation with each of these collective order parameters. In Figure 3.15, we color the combined temperature two-

dimensional embeddings by the eighth and tenth order Steinhardt bond orientation order parameters, Q_8 and Q_{10} [103].

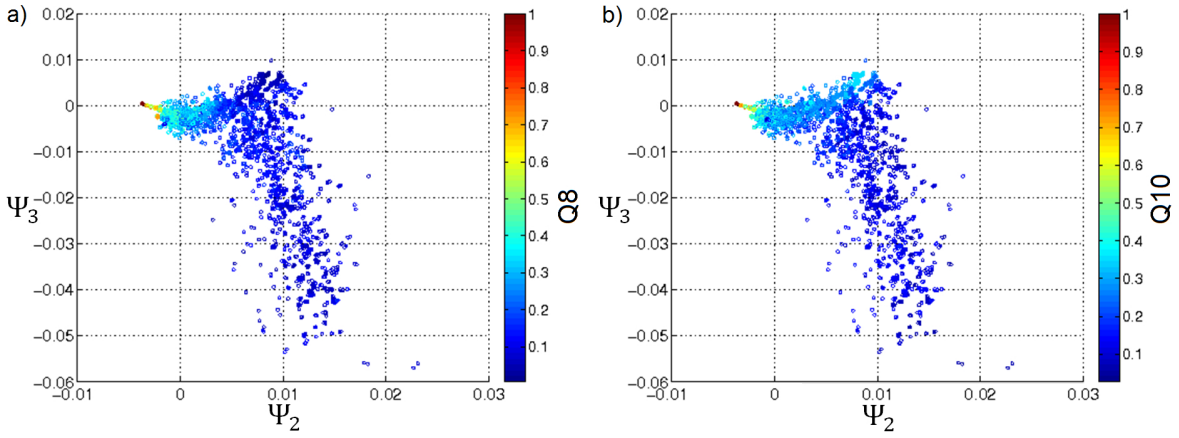

Figure 3.15: Two-dimensional embedding into [Ψ_2,Ψ_3] of the 48,010 clusters harvested at all nine temperatures colored by (a) Q_8 and (b) Q_{10}.

Q_8 approaches zero for clusters with icosahedral symmetry, enabling this variable to delineate between liquid or open structures and the closed compact icosahedral clusters (Figure 3.15a). Ψ_2 exhibits strong correlation with Q_8 as measured by the Pearson correlation coefficient, $\rho(\Psi_2, Q_8) = -0.874$, with Q_8 falling from unity for dimers to zero for the terminal icosahedral aggregates. In particular, this parameter is capable of tracking the formation of icosahedral clusters along the monomeric assembly pathway, but cannot distinguish between icosahedral and near-icosahedral aggregates with $Q_8 < 0.1$ and the disordered liquid phase.

Q_{10} is unity for dimers, approximately 0.363 for idealized icosahedra, and decreases towards zero as clusters become larger and more disordered. Accordingly, Q_{10} is a good variable by which to distinguish the liquid budding mechanism from monomeric assembly as illustrated in Figure 3.15b. Q_{10} therefore approximately tracks deviations in Ψ_3, but the correlation is rather weak, with a Pearson correlation coefficient of $\rho(\Psi_3, Q_{10}) = 0.156$. Despite searching a variety of candidate variables (including principal moments of the gyration tensor, cluster size, mean number of bonds per particle in a cluster, Q_4, Q_6, Q_8, Q_{10}, and

Q_{12}) we were unable to find a physical variable possessing stronger correlation with Ψ_3.

Our failure to find a physical variable strongly correlated with Ψ_3 underscores the difficulty in assigning simple physical interpretations to the diffusion map variables [56, 69]. While systematic procedures exist to search pools of candidate variables, the variable combinations so formed can often themselves be so complex as to obscure the underlying physical meaning [106, 107]. Furthermore, the diffusion map order parameters are themselves typically complex nonlinear collective variables, making the existence of a simple physical correspondence far from certain [55, 56, 69]. While of unquestionable value in offering physical insight into the low-dimensional diffusion map embedding, the identity of diffusion map order parameters as good descriptors of the slow collective modes is independent of their physical interpretation [56, 59, 75, 76], and the embeddings retain their validity and utility in the absence of this understanding. Furthermore, the Nyström extension [56, 80, 81, 109] enables direct embedding of new data points into the diffusion map embedding without possessing this physical correspondence, which facilitates efficient incorporation of new data and permits biased sampling directly in the diffusion map order parameters [109].

3.3 Conclusions

We have introduced a new approach to systematically infer self-assembly pathways and mechanisms from molecular simulations that is capable of identifying both *what* terminal aggregates are produced and *how* they are formed. Our approach is based on the nonlinear manifold learning approach known as the diffusion map [55, 59, 75, 81], which we have previously used to identify the folding mechanisms of hydrocarbon chains and peptides [55, 69]. The key innovation of this work is the extension of this approach to treat many-body phenomena, in which identical building blocks spontaneously assemble into structured terminal aggregates. In developing this generalization, we confronted a key technical challenge in defining structural similarities between clusters containing different numbers of identical

particles in different configurations using graph matching techniques [85, 89]. Our approach systematically identifies collective order parameters describing the long-time assembly dynamics of the system, furnishing a kinetically meaningful low-dimensional subspace in which to project simulation trajectories to reveal the underlying self-assembly pathways and mechanisms.

We have demonstrated our approach in applications to the self-assembly of anisotropic patchy particles with architectures designed to favor the assembly of tetrahedral and icosahedral clusters. Application of our approach to Brownian dynamics simulations of the self-assembly of icosahedral clusters reveals assembly to proceed by two distinct mechanisms: monomeric addition, and budding from a disordered liquid. Both of these mechanisms were previously reported by Wilber *et al.* from viewing simulation trajectories and tracking of cluster size distribution [35, 43], validating the capacity of our approach to systematically extract assembly mechanisms that were previously only discernible by visual inspection. Furthermore, by resolving the assembly pathways within a low-dimensional projection, our approach enabled us to explicitly compute the flux along each path and quantify their relative propensities as a function of temperature (interaction strength).

In an application to the particles designed to assemble tetrahedral clusters, our approach revealed the existence of two distinct assembly pathways to two distinct terminal aggregates: (i) chains of stacked interlocking dimers and tetramers, and (ii) chains of stacked interlocking trigonal planar trimers. Our approach revealed these chains to form by the condensation mechanism. While both pathways are active at low temperatures (strong particle interactions), we have shown that the trimer chain can be favored over the dimer/tetramer chain by elevating the temperature (decreasing the interaction strength). Despite designing our building block to favor the formation of tetrahedral clusters, we do not observe these structures to be uniquely favored at any temperature (interaction strength) suggesting that stabilization of tetrahedral clusters will require redesign on the anisotropic interactions. We observe that conducting and interpreting simulations of self-assembly presents a powerful

approach to unveil the rich thermodynamic and kinetic features of the multi-body assembly as a function of building block architecture, and that naïve building block design considering only the desired aggregate is insufficient to guarantee its stability and/or accessibility [33, 68, 111].

These applications of our approach illustrate its capacity to systematically identify assembly pathways and mechanisms from molecular simulations, and provide fundamental insight into the assembly process. Furthermore, our approach furnishes a framework to quantify how assembly conditions (e.g., temperature, pressure) or building block design (e.g., interaction strength and anisotropy, particle size and architecture) impact both the stable terminal aggregates, and the mechanisms by which they assemble. Our exploration of the effect of temperature represents an exploration of the impact of one design variable (interaction strength), and future work may consider the placement of the annular rings, as well as the role of hydrodynamic interactions, system size, and polydispersity in the building block architecture.

Chapter 4

Inferring assembly pathways from particle-tracking data

In this chapter, we apply the many-body diffusion map approach to infer self-assembly landscapes from experimental particle tracking data, and quantify how these landscapes change as a function of experimental conditions. To the best of our knowledge, this represents the first time that collective order parameters and assembly landscapes have been inferred directly from experimental data.

The particular system we consider is the nonequilibrium self-assembly of Janus colloids, micron sized spheres whose hemispheres possess different surface chemistries [23, 112, 113]. These highly tunable building blocks can be induced to self-assemble diverse aggregate structures on experimentally measurable time scales, presenting an ideal system to study the effect of particle anisotropy and experimental conditions on the assembly of clusters, chains, helices, sheets, discs, and tubes [23–26, 114, 115]. In particular, we are interested in the nonequilibrium self-assembly of metallodielectric Janus particles under an applied AC electric field [116, 117]. The oscillating field induces a differential dipole moment between metallic and dielectric hemispheres leading to anisotropic interactions between colloids and induced motions through reverse induced-charge electrophoresis (rICEP). An attractive feature of our data-driven machine learning approach to discover collective order parameters and assembly roadmaps is that it requires no knowledge of the underlying physics of the system. Accordingly, we can infer empirical assembly roadmaps directly from experimental data without a

This chapter is based on work presented in:

Andrew W. Long, Jie Zhang, Steve Granick, and Andrew L. Ferguson, "Machine learning assembly landscapes from particle tracking data", *Soft Matter*, **11**, 8141-8153 (2015).

complete understanding of the underlying physics, and the pathways and collective dynamics discovered by our analysis can inform improved understanding of the system.

The structure of this chapter is as follows. In Section 4.1, we describe the experimental details of the Janus particle synthesis and self-assembly, and the computational details of the machine learning algorithm. In Section 4.2, we describe the application of our approach to nonequilibrium self-assembly of two metallodielectric Janus particle systems: (i) the templated assembly of Janus pinwheels and other branched structures directed by passive linker particles, and (ii) the spontaneous self-assembly of long Janus particle chains and loops. In each case we demonstrate that our approach reveals the underlying self-assembly pathways, and furnishes quantitative design rules linking the attainable terminal aggregates to the AC frequency, electric field strength, and salt concentration. In Section 4.3 we present our conclusions and outlook for future work. The experimental work detailed in this chapter was conducted by our collaborators Jie Zhang (UIUC) and Prof. Steve Granick (Ulsan).

4.1 Materials and methods

4.1.1 Janus particle tracking experiments

Janus particles are synthesized by depositing 20 nm of titanium and then 20 nm of SiO_2 vertically on a submonolayer of 3μm silica particles (Tokuyama) using an electron-beam evaporator. After washing with isopropyl alcohol and deionized water, Janus particles are sonicated down from the substrate to deionized water. For the templated assembly experiments with binary mixtures of Janus and "linker" particles, Janus particles and untreated silica particles are mixed in a 10:1 ratio. NaCl stock solution is added to the particle suspension to prepare 0.01 mM and 0.1 mM NaCl solutions, respectively. The particle suspensions are sandwiched between two ITO coated coverslips (SPI Supplies) separated by a 120 μm-thick spacer (GraceBio SecureSeal) with a 9 mm hole in the center to confine the fluid. An AC electric field is applied to the sample cell using a function generator (Agilent 33522A).

The sample cell is imaged with a 40× air objective on an inverted microscope (Axiovert 200). Microscopic images and videos are taken with a CMOS camera (Edmund Optics 5012M GigE). A schematic of our experimental setup is given in Figure 4.1a. Representative movies of the templated and homogenous self-assembly experiments are presented in the supplemental information of Ref. [118].

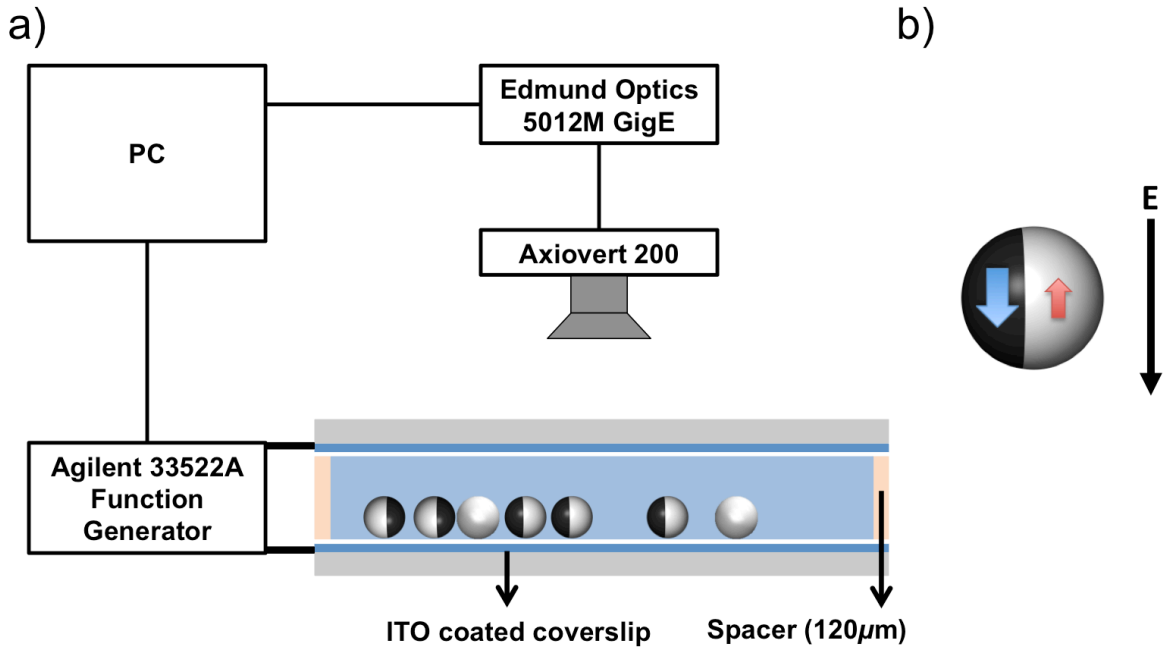

Figure 4.1: Janus particle self-assembly under an applied AC electric field. (a) Schematic of the Janus particle tracking experimental setup comprising both Janus particles and passive linker particles. (b) Under an applied electric field, the Janus interface aligns parallel with the field direction and a dipole moment is induced in the metallic (left) and dielectric (right) hemispheres of the Janus particle. The magnitude of the dipole moment is greater in the metallic hemisphere due to an increased polarizability of the thin metallic layer, and aligns with the direction of the applied field. The dipole moment of the dielectric hemisphere aligns antiparallel with the applied field.

Particle positions are determined using a circular Hough transform [119], providing the 2D coordinates of all particle centers in a given image or video frame. We use these positions to identify the distinct particle clusters in a frame. First, we define particles as being "bonded" to one another if their center of mass separation is less than $r_{\text{cutoff}} = 1.15D$, where D=3 μm is the particle diameter, to form a complete binary interaction graph at a particular

instance in time, $\mathbf{K}$, where $\mathbf{K}(p,q) = 1$ if particles p and q are bonded and $\mathbf{K}(p,q) = 0$ if not bonded. Using Tarjan's algorithm, [102] we identify distinct subgraphs, $\mathbf{G}$, defining connected clusters of particles within the complete graph. We aggregate all of these clusters from the video frames across all of our experimental trajectories to form a library of clusters $\{\mathbf{G}_i\}$. We have verified that our results are robust to choices of bonding cutoffs in the range $[1.10D, 1.25D]$.

4.1.2 Janus particle self-assembly

Under the influence of the perpendicular AC electric field, the Janus particles align their interface parallel to the field and an induced dipole moment develops in each hemisphere as illustrated in Figure 4.1b. The net interaction between two Janus particles, A and B, at a separation, r, and relative orientation of the particle directors normal to the Janus interface, θ, is the sum of the four distinct dipole-dipole interactions between each of the two dipoles, i, in particle A and the two dipoles, j, in particle B,

$$U_{AB}(r,\theta) = \sum_{i,j} u_{ij}(r_{ij}(r,\theta)), \qquad u_{\mathrm{ij}}(r_{ij}) = \frac{\mathrm{Re}\left(\alpha_{\mathrm{i}}\alpha_{\mathrm{j}}\right) E_0^2 \left(1 - 3\cos^3\beta\right)}{4\pi\epsilon r_{ij}^3}, \tag{4.1}$$

where where $i = \{\mathrm{metal}_A, \mathrm{dielectric}_A\}$, $j = \{\mathrm{metal}_B, \mathrm{dielectric}_B\}$, $r_{ij}(r,\theta)$ is the orientation and separation dependent dipole-dipole separation, α_k is the complex polarizability of the Janus hemisphere composed of material k, E_0 is the electric field strength, β is the angle of the interface ($\beta = \pi/2$ for a Janus particle), and ϵ is the permittivity of the solution. The differing polarizability of the metallic and dielectric hemispheres gives rise to an orientation-dependent attractive or repulsive interaction between particles. To calculate the induced dipole of a dielectric particle coated with metal on one hemisphere, we assume the induced dipole moment of each hemisphere is half of a spherical particle of the same diameter and material. For a spherical colloidal particle, the complex polarizability is computed as $\alpha = 4\pi\epsilon_0\epsilon_s K R^3$, where K the complex dipole coefficient. K is sensitive to the electric

field frequency, particle surface charge and ionic strength in the solution. We compute the complex dipole coefficient of a metallic sphere using the analytical solution in Ref. [120], considering the effect of the protective SiO_2 coating in reducing the electric field outside the metal coating. For a negatively charged silica sphere, we employ the approximate analytical solution in Ref. [121].

Above a particular transition frequency of the applied electric field, this difference in polarization across the Janus interface also leads to particle motion by reverse induced charge electrophoresis (rICEP) perpendicular to the field in the direction of the metallic hemisphere [122]. We empirically quantify the ballistic velocities from a quadratic fit of particle mean squared displacements at short times using the particle tracking algorithm developed by Crocker and Grier [123].

4.1.3 Machine learning of assembly roadmaps

The particle tracking data recorded during the self-assembly experiments described in Section 4.1.1 contains all of the information on the self-assembly mechanisms and terminal aggregates attainable under different experimental conditions, but it is exceedingly challenging to resolve these mechanisms and terminal states by visual inspection alone [114]. Visualization can be supported by tracking cluster size distributions [35, 43], or tracking the evolution of the evolving clusters using canonical shape descriptors [86], but such intuitive, coarse-grained descriptors are typically not coincident with the emergent collective order parameters that govern assembly.

The difficulty in parsing the particle tracking data is largely a question of dimensionality. The orientation and location of a single Janus particle in the plane oriented parallel to the external electric field is given by three numbers specifying its 2D location and its rotational orientation. The assembly trajectory for a collection of N Janus particles residing in the plane, resides in a $3N$-dimensional phase space. For even a modest number of particles, it is extremely challenging to identify within this high-dimensional space the underlying assembly

pathways and accessible aggregates that lie buried within this data. Despite existing in this high-dimensional phase space, self-assembly is an inherently multi-body process that depends on cooperative interparticle interactions. This coupling of building block degrees of freedom generally results in a separation of time scales, such that the long time evolution of the system is governed by a relatively small number of collective modes [60, 62]. Extracting these slow collective modes permits construction of a low-dimensional subspace capturing the important dynamical features of self-assembly, and the existence of such low-dimensional subspaces – frequently of dimensionality as low as 2-3 – has been borne out in molecular simulations of polymer dynamics, protein folding, and colloidal self-assembly [55, 69, 70, 124, 125].

Nonlinear learning offers a means to systematically extract this low-dimensional subspace – the so-called *intrinsic manifold* [55] – from the high-dimensional data, and in doing so reveal the important collective modes, assembly pathways, and accessible aggregates. In contrast to linear techniques (e.g., principal components analysis [47]), nonlinear approaches are more powerful and flexible in determining the potentially nonlinear combinations of the particle degrees of freedom comprising the collective modes [56, 69, 70]. We apply the many-body diffusion map approach presented in Chapter 2 to infer assembly pathways and the accessible terminal aggregates directly from experimental data. Below we detail the specific form of the distance measure employed and how to construct free energy landscape over the diffusion map space. We note that our methodology requires neither that the number nor identity of particles remain constant in each frame of the trajectory, and the interaction potentials between particles need not be known. Rather the approach is a data-driven one that infers a low-dimensional description of the assembly process from empirical observations of the diversity of structural aggregates within the system.

Cluster distance metric

We start by compiling a library of all clusters observed in our particle tracking trajectories using the procedure described in Section 4.1.1. Each distinct cluster observed in the particle

tracking movies is represented by its underlying bonding network, yielding a binary adjacency matrix $\mathbf{G}$ where $\mathbf{G}(p,q) = 1$ denotes the presence, and $\mathbf{G}(p,q) = 0$ the absence of a bond between particles p and q. We then compute distances between all pairs of graphs in our library, $(\mathbf{G}_i, \mathbf{G}_j)$, using graph matching to identify the pseudo-optimal permutation, $\mathbf{H}$, of particle labels between these two clusters such that the adjacency matrices are maximally similar. Mathematically this corresponds to finding the $\mathbf{H}$ that minimizes the Frobenius norm between $\mathbf{G}_i' = \mathbf{H}\mathbf{G}_i\mathbf{H}^T$ and $\mathbf{G}_j$, For clusters with different numbers of particles, the smaller graph is augmented by a number of rows and columns of zero to bring it up to the same size as the larger when computing alignment. Due to the planar structure of these graphs this optimization is strongly polynomial, requiring an approximate solution algorithm for even moderately sized networks [91, 126]. We adopt the simultaneous traversal matching algorithm using an IsoRank heuristic [85] that preserves local bond connectivity as detailed in Section 2.2.2.

Given the optimal particle label permutation between two graphs, we define their dissimilarity based on the separation between analogous pairs of bonded particles. For each cluster we construct the matrix $\boldsymbol{\chi}$, where $\boldsymbol{\chi}(p,q)$ is the real space distance between particles p and q if $\boldsymbol{\chi}(p,q) < r_{\text{cutoff}}$, and is zero otherwise. We define the structural dissimilarity of clusters i and j as,

$$\mathbf{d}_{ij} = \sum_{p} \sum_{q>p} ||\boldsymbol{\chi}_i'(p,q) - \boldsymbol{\chi}_j(p,q)||, \tag{4.2}$$

where $\boldsymbol{\chi}_j$ contains the distances between the bonded particles in cluster j, and $\boldsymbol{\chi}_i'$ the distances between the corresponding particles in cluster i under the permutation defined by $\mathbf{H}$. Ghost particles are added as necessary to bring the clusters to equal size, which corresponds to the addition of a number of imaginary non-bonded particles to the smaller cluster [125]. In the case of the templated assembly of Janus pinwheels directed by passive linker particles, $\boldsymbol{\chi}$ corresponds to distances between particle centers. In the homogeneous self-assembly of

Janus particles into chains and loops it corresponds to the distance between metallic face centers – the midpoint between the particle center and metallic surface normal to the Janus interface – which provides information on relative particle orientations that is critical in distinguishing different loop and chain architectures.

The distance metric $\mathbf{d}_{ij}$ provides a good measure of the structural dissimilarity of clusters that encapsulates both the breaking and forming of bonds between different cluster sizes and architectures, and deviations in bond lengths within a single architecture [125]. We observe that the definition of structural distances based on graph matching of the underlying networks surmounts the difficulties associated with the absence of a spatially invariant real space basis in which to compare clusters of different numbers of indistinguishable particles translating and rotating through space.

Effective free energy landscapes

By collecting histograms over the embeddings we construct effective free energy landscapes describing the relative probabilities of the various cluster architectures in the experimental trajectories. We construct these landscapes using the standard relationship from (equilibrium) statistical mechanics, $\beta\hat{F}(\vec{\xi}) = -\ln\hat{P}(\vec{\xi}) + C$, where $\beta = 1/k_BT$ is the inverse temperature, k_B is Boltzmann's constant, T is the absolute temperature, $\vec{\xi}$ is a k-dimensional vector specifying a point on the intrinsic manifold spanned by the vectors $(\vec{\Psi}_2, \vec{\Psi}_3, ..., \vec{\Psi}_{k+1})$, $\hat{P}(\vec{\xi})$ is a histogram approximation to the probability density of single particles on the manifold at $\vec{\xi}$, weighting each point in the manifold by the number of particles belonging to the corresponding cluster, $\hat{F}(\vec{\xi})$ is an effective per particle free energy at $\vec{\xi}$, and C is an arbitrary constant that we specify such that the free energy of an isolated monomer defines the zero of free energy. Since the experimental self-assembly trajectories were conducted in the presence of an external driving force (the oscillating AC electric field), they are inherently out of equilibrium, and therefore $\hat{F}$ cannot be interpreted as a true thermodynamic free energy, but rather an *effective* free energy that is best interpreted as a convenient represen-

tation of the likelihood to find a particle in a particular cluster architecture. By computing these effective free energy landscapes upper different conditions – salt concentration, electric field strength, AC frequency – we use these effective free energy landscapes, along with the dynamic interpretability of the diffusion map embeddings, to link experimental control parameters to changes in the relative propensities of different cluster architectures and mechanistic pathways over the assembly landscape.

4.2 Results and discussion

4.2.1 Templated Janus "pinwheel" assembly

Mixtures of metallodielectric Janus particles with passive dielectric particles in a 10:1 ratio were subjected to AC frequencies of 70 kHz - 11 MHz and applied AC field strengths of 250-833 V/cm at a salt concentration of [NaCl] = 0.1 mM (cf. Section 4.1.1). A total of 28 experiments were conducted over this range at the particular field strengths and frequencies listed in Table 4.1. At each set of conditions, the system was allowed to attain steady state with respect to the applied AC field by waiting for the particle velocity distribution to stabilize, typically occurring approximately 8 seconds after initial application of the field. The transient portion of each particle tracking trajectory was rejected from our analysis such that the aggregates and assembly pathways extracted by our analysis correspond to those produced by the dynamical assembly and disassembly of clusters at steady state.

Within the ensemble of particle trajectories from all 28 experiments, we identified a total of 3,403,918 clusters (including free monomers) belonging to 21,708 distinct cluster architectures. Since the size of the matrices used to perform the diffusion mapping scale quadratically with cluster number, we make the analysis computationally tractable by retaining a random subset of cluster from each unique cluster architecture to generate a reduced ensemble of 60,926 clusters. We apply diffusion maps using a kernel bandwidth of $\epsilon = \exp(10)$ determined using the approach in Ref. [77]. We note that particle identity – Janus or linker – is

	Field Strength (V/cm)					
Frequency (kHz)	250	417	500	583	750	833
70	0	0	0	0	0	1
100	1	3	1	1	1	5
150	0	0	0	0	0	1
200	0	0	0	0	0	3
300	0	1	0	0	0	1
600	0	0	0	1	0	2
1000	0	0	1	0	0	1
5000	0	0	0	0	0	1
7000	0	0	0	0	0	1
9000	0	0	0	0	0	1
11000	0	0	0	0	0	1

Table 4.1: Number of experiments performed for a self-assembling system of active metallodielectric Janus particles with passive linker particles at a salt condition of 0.1mM NaCl

not easily identifiable in these experiments, and as such our diffusion map analysis operates purely on the geometric cluster architectures rather than the type of particles constituting these clusters. We employ the L-method [108] to identify a gap in the eigenvalue spectrum after λ_3 (Figure 4.2), implying an effective dimensionality of two and motivating the construction of two-dimensional diffusion map embeddings in the top two non-trivial eigenvectors $\{\vec{\Psi}_2, \vec{\Psi}_3\}$. To preserve the experimentally observed cluster distribution, we project into the diffusion map embedding the remaining $(3,403,918 - 60,926) = 3,342,992$ clusters using the Nyström extension [80, 81, 109]. By analyzing all systems simultaneously, we construct a single composite diffusion map defining a common basis within which to compare the distribution of clusters at different experimental conditions by restricting the ensemble to the clusters extracted from particular experimental trajectories.

We present the two-dimensional composite diffusion map in Figure 4.3. Each point corresponds to a particular cluster observed in one of the experimental particle tracking trajectories. To assist in visual discrimination of different cluster architectures, we color each point according to the the average path length between pairs of particles in the cluster bonding network as a coarse-grained measure of cluster size and connectivity. We also

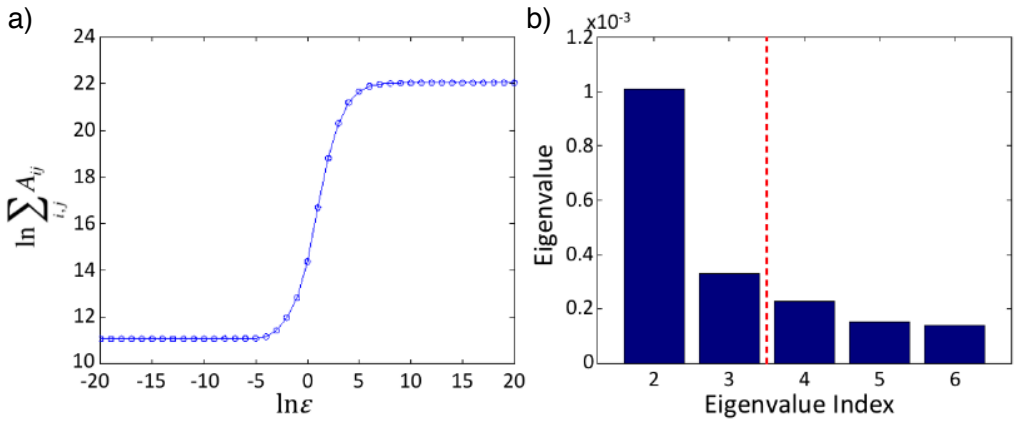

Figure 4.2: Specification of diffusion map bandwidth and effective dimensionality for the self-assembly of the mixture of active Janus particles and passive linker particles. (a) Specification of the diffusion map Gaussian kernel bandwidth using the approach in Ref. [77]. A log-log plot of the sum of the elements of the pairwise similarity matrix, $\sum_{i,j} A_{ij}$, as a function of Gaussian kernel bandwidth, ϵ, exhibits a sigmoid shape. The lower plateau defines ϵ values for which the discrete Markov chain is effectively disconnected prohibiting the construction of a unified diffusion map embedding. The upper plateau defines ϵ values for which the Markov chain is fully connected, precluding discrimination between local and non-local hops, and therefore fast and slow time scales. Accordingly, an appropriate bandwidth should be selected from the linear region. In practice, we find better results from selections near the intersection of the linear region and the upper plateau, motivating our choice of $\epsilon = \exp(10)$. (b) Diffusion map eigenvalue spectrum omitting the trivial unit eigenvalue, $\lambda_1 = 1$, for viewing clarity. Application of the L-method of Salvador and Chan [108] identifies the first "knee" (i.e., discontinuity) in the eigenvalue spectrum between λ_3 and λ_4, implying a spectral gap after the second non-trivial eigenvalue and an effective dimensionality of $k = 2$. This motivated us to construct diffusion map embeddings into the top two non-trivial eigenvectors (Ψ_2, Ψ_3).

visualize representative clusters to illustrate the cluster architectures populating different regions of the intrinsic manifold constituting the assembly landscape. The landscape reveals four distinct quadrants defining different aggregation states. The lower left quadrant is populated primarily by free monomers residing at ($\Psi_2 \approx -0.135$, $\Psi_3 \approx -0.185$) and possessing an average path length of zero. Tracing a pathway up to the upper left quadrant corresponds to the formation of relatively small, dense cluster architectures residing in the vicinity of ($\Psi_2 \approx -0.135$, $\Psi_3 \approx -0.165$) and possessing a small average path length (high network connectivity). The assembly pathway linking the monomers to the lower right quad-

rant corresponds to the formation of spinning "pinwheels" in the vicinity of ($\Psi_2 \approx -0.120$, $\Psi_3 \approx -0.180$) and possessing long average path lengths (low network connectivity) reflecting the presence of three chains bound to a central linker particle. Finally, the assembly pathway leading to the upper right quadrant corresponds to the assembly of "archipelago" type structures in the region of ($\Psi_2 \approx -0.125$, $\Psi_3 \approx -0.160$), corresponding to clusters with locally dense packings connected by spanning chains.

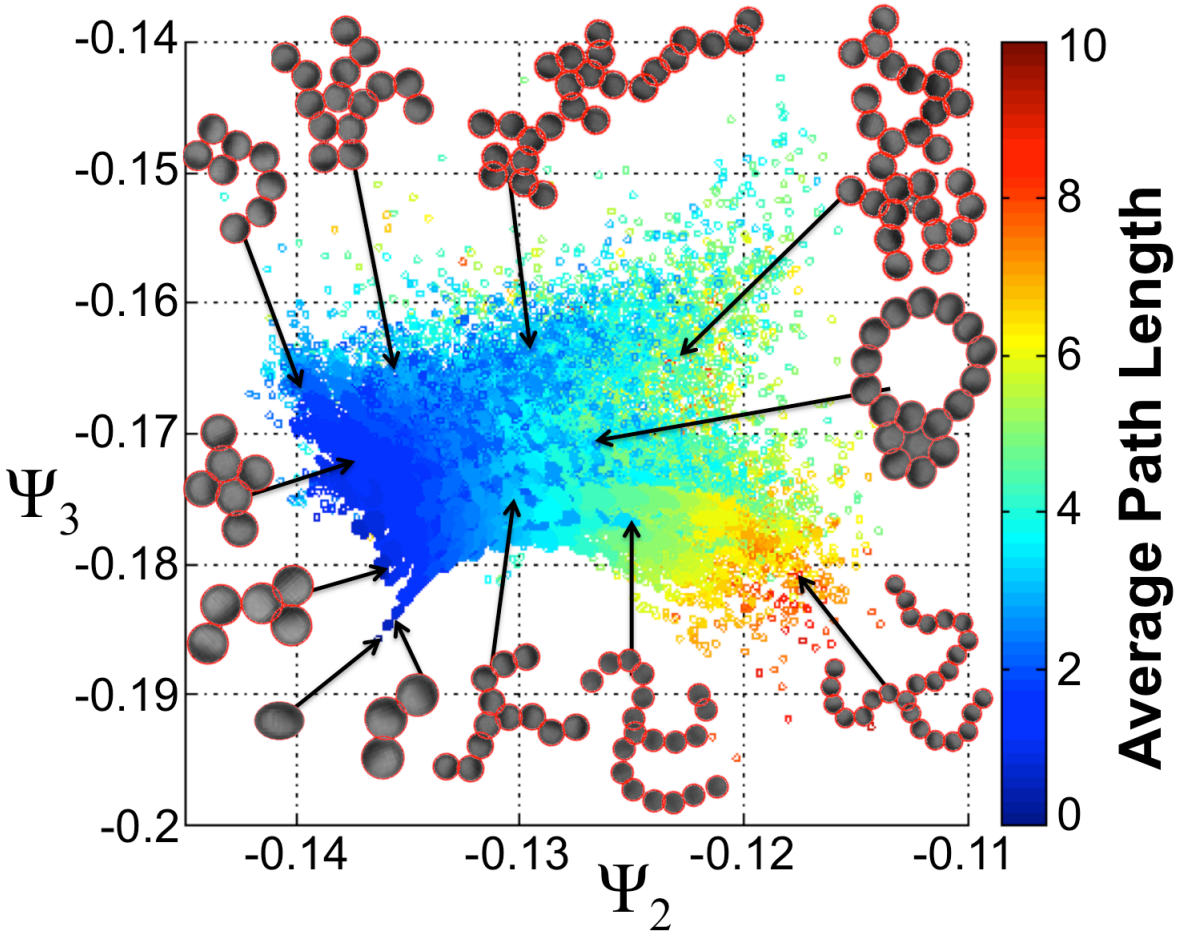

Figure 4.3: Composite diffusion map embedding for the self-assembly of a mixture of active Janus particles with passive linker particles in the top two collective modes [Ψ_2, Ψ_3] furnished by the diffusion map. Each point represents one of the 3,403,918 clusters observed in the 28 experiments conducted over a range of AC frequencies and electric field strengths (cf. Table S1). To aid in visualization, points are colored by the average path length between pairs of particles in the cluster bonding network, and representative aggregates superposed onto the manifold.

By restricting the clusters projected into the composite diffusion map embedding to those observed under particular range experimental conditions, we can determine the impact of experimentally controllable variables on the self-assembly behavior. Due to the wide range of AC frequencies investigated in this work, we bin the frequency distribution into two classes: low (70-300 kHz) and high (0.6-5 MHz). We reject the very high frequency regime (7-11 MHz) from this analysis due to poor characterization of the field strength arising from the capacitive behavior of the experimental setup. Similarly, we bin electric field strengths into two classes, low (250-500 V/cm) and high (583-833 V/cm). By binning our data, we accumulate more data within each class and improve the statistical robustness of our analysis, but elect to restrict our investigation to the high electric field strength regime due to relatively poor sampling under low electric field conditions (constituting just 9% of all observed particles combined over both frequency regimes). In Figure 4.4a,b, we present the intrinsic manifold corresponding to each of the two frequency bins at high electric field strengths of 583-833 V/cm.

In Figure 4.4c,d, we present the analogous effective free energy landscapes, $\hat{F}(\Psi_2, \Psi_3)$, illustrating the relative probability of observing a single particle in a particular cluster configuration. Since each frequency bin contains data from multiple experimental trajectories, we average the probability distributions, $\hat{P}(\Psi_2, \Psi_3)$, extracted from each individual run, then compute the effective free energy as described in Section 4.1.3. Bootstrap estimates reveal the the uncertainty in any bin of the effective free energy landscape to be less than 0.3 $k_B T$, with the largest errors occurring in regions of high effective free energy (Figure 4.5). At low frequencies (Figure 4.4c), the dominant low effective free energy pathway connects free monomers to local effective free energy minima in the lower right quadrant at ($\Psi_2 \approx -0.120$, $\Psi_3 \approx -0.180$) containing pinwheels of characteristic size $N \sim 16$. The dense cluster architectures in the upper left quadrant and archipelago structures in the upper right quadrant are relatively disfavored, residing at higher effective free energies. We quantify the relative prevalence of the various cluster architectures by reporting on the figure the mass fraction

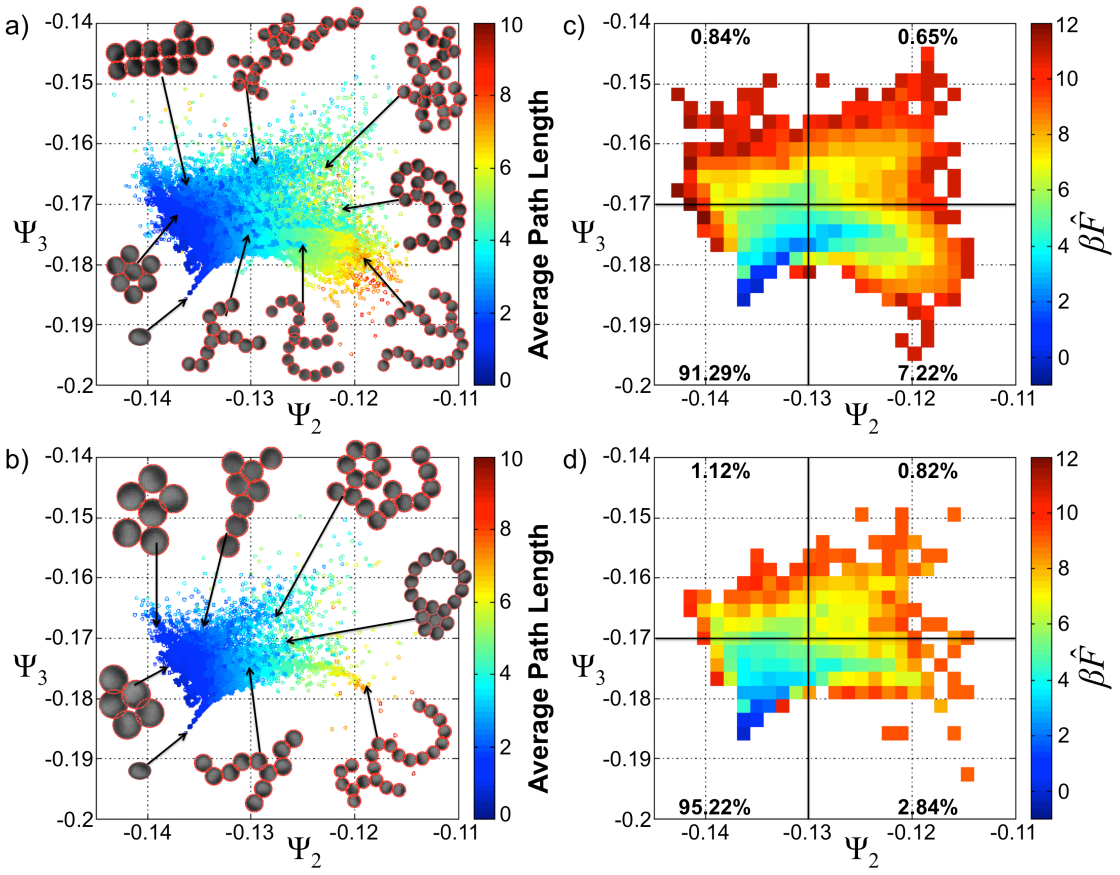

Figure 4.4: Restriction of the composite diffusion map intrinsic manifold for the self-assembly of a mixture of active Janus particles with passive linker particles in Figure 4.3 to the cluster ensembles extracted at (a) low (70-300 kHz) and (b) high (600 kHz - 5 MHz) AC frequencies, f, at electric field strengths, E, of 583-833 V/cm. Points are colored by the average path length between pairs of particles in the cluster bonding network, and representative clusters superposed onto the manifolds. Effective free energy landscapes in the (c) low, and (d) high frequency regimes. The four percentages listed on panels (c) and (d) denote the mass fraction of particles residing within that quadrant.

of clusters projected into each quadrant of the landscape. At high frequencies (Figure 4.4d), the size of the intrinsic manifold shrinks, reflecting the disappearance of the larger aggregates of size $N \gtrsim 12$ residing around the periphery of the landscape under these conditions. The topography of the effective free energy surface becomes flatter, attenuating the depth of the local minima within the pinwheel architectures. Similarly by considering the mass fraction of particles existing in the different assembly regimes as we shift from low to high

AC frequencies, we see an increase in fraction of particle mass for small clusters (91 to 95%), a substantial reduction in mass fraction of pinwheels (7 to 3%), and small increases in the mass fraction of archipelago (0.7 to 0.8%) and dense cluster architectures (0.8 to 1.1%).

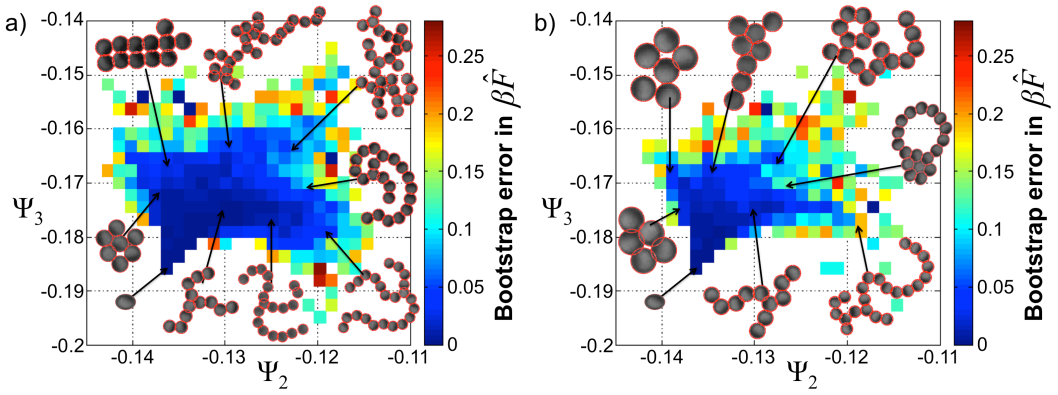

Figure 4.5: Estimated uncertainties in effective free energy surfaces for the self-assembly of a mixture of active Janus particles with passive linker particles presented in Figure 4.4c,d estimated by 10 bootstrap resamples at high field strength E (583-833 V/cm) and (a) low AC frequency f (70-300 kHz) and (b) high AC frequency (600 kHz-5MHz).

The nonequilibrium self-assembly is governed by a balance of hydrodynamics, dipole-dipole interactions, and rICEP motion. The decrease in volume of the intrinsic manifold at high frequencies discovered by the diffusion map is consistent with the frequency dependence of the Janus hemisphere polarizabilities and particle velocity under induced rICEP motion. We illustrate in Figure 4.6a the frequency dependence of the real portion of the product of the hemisphere polarizabilities (cf. Equation 4.1), and thus the relative magnitude of the different dipolar interactions between particles at [NaCl] = 0.1 mM. In the low frequency regime, $f \leq 300$ kHz, the metal-metal and metal-dielectric dipolar interactions are attractive, giving rise to more variety in energetically favorable configurations and enabling a larger volume of the intrinsic manifold to be explored. Upon increasing the frequency, metal-metal interactions become repulsive, limiting the possible structures that can be formed, favoring primarily head-to-tail configurations, and shrinking the manifold. In Figure 4.6b, we present the frequency dependence of the ballistic velocity of a Janus particle moving under rICEP.

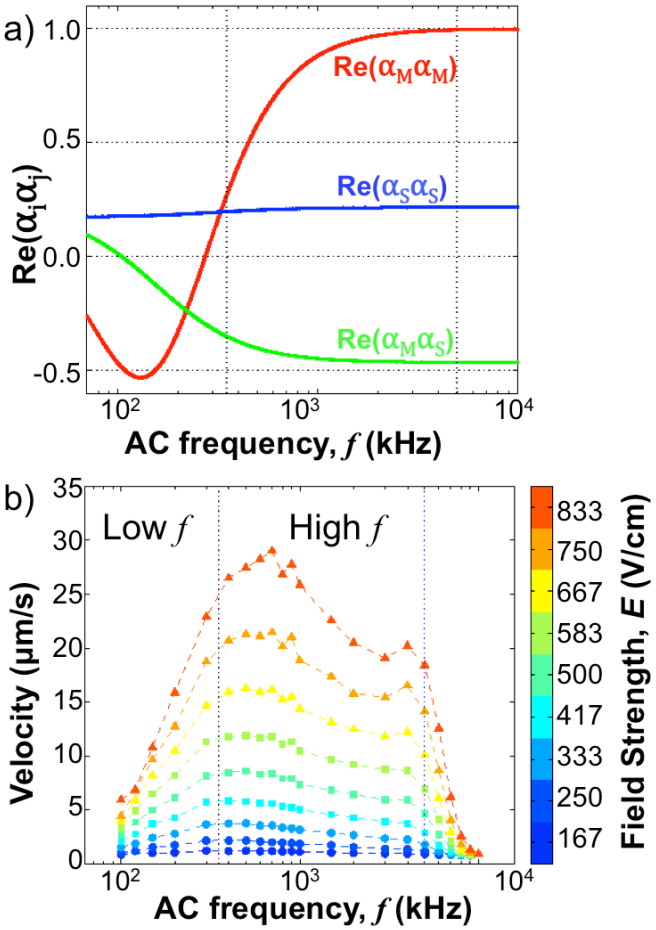

Figure 4.6: Dependence of particle polarization and rICEP velocity upon AC frequency, f, at [NaCl] = 0.1 mM. (a) Frequency dependent real portion of the product of polarizabilities of metal-metal (red), metal-silica (green), and silica-silica (blue) interactions (cf. Equation 4.1). (b) Ballistic velocity profile for Janus particles under dilute particle concentrations in a 0.1 mM NaCl solution as a function of AC frequency, f, at different electric field strengths, E. Consistent with the binning of the field strengths in the main text, circles correspond to low (167-333 V/cm), squares to intermediate (417-583 V/cm), and triangles to high (667-833 V/cm) field strengths. The vertical lines delineate the low (70-300 kHz) and high (400 kHz - 5 MHz) frequency regimes.

These data show the particle velocity to increase steeply between the low and high frequency regimes. The velocity peaks at ∼500 kHz, then decreases steadily to ∼4 MHz, beyond which there is a precipitous drop-off due to capacitive breakdown in our experimental system. We suggest that the combination of an increase in metal-metal repulsions and elevated particle

velocity at high frequency serves to inhibit the formation of large clusters, as metal-silica attachments are disfavored and chain-like structures such as pinwheels shear off weakly bonded particles.

In sum, by applying our machine learning algorithm to experimental particle tracking data, we have extracted a two-dimensional assembly landscape revealing the presence of three distinct families of aggregates. We have also determined how the landscape changes as a function of the frequency of the applied AC electric field and quantified the relative prevalence of the different cluster architectures and assembly pathways in good agreement with the physical understanding of the frequency response of the interparticle attractions and velocity. The assembly landscape provides quantitative insight into the relative prevalence of different cluster architectures, and provides a roadmap to tune experimental conditions to favor the assembly of desired aggregates. Specifically, low AC frequencies (70-300 kHz) preferentially favor the assembly of three-armed pinwheels of $\sim$16 particles, whereas high frequencies (600 kHz - 5 MHz) inhibit the formation of large clusters of $N \gtrsim 12$ particles.

4.2.2 Tunable Janus chain formation

We studied the self-assembly of homogeneous ensembles of metallodielectric Janus particles in the absence of inert silica linker particles over AC frequencies of 70 kHz - 11 MHz, electric field strengths of 167-833 V/cm, and NaCl concentrations of 0.01 mM and 0.1 mM. A total of 537 experiments were conducted over this full parameter space, with specific conditions considered listed in Table 4.2 and Table 4.3 for [NaCl] = 0.01 mM and [NaCl] = 0.1 mM, respectively. The transient portion of each particle tracking trajectory was rejected such that the assembly dynamics of each system was studied at steady state. Analysis of all 537 experiments revealed a total of 739,246 clusters (including free monomers) belonging to 338 distinct architectures. A small number of clusters comprising more than 25 particles were very rarely observed, constituting just under 0.04% of the observed structures and appearing as extreme outliers in our diffusion map embeddings. It is known that the presence of rare

observations disconnected from the bulk of the data can compromise the resolution of the diffusion map embedding, [69] in this case causing us to lose discriminatory power to resolve architectures and pathways at small cluster sizes of $N \lesssim 20$. Accordingly we followed our previously described "deislanding" approach to eliminate these rarely observed cluster aggregates from our analysis [69]. We applied diffusion maps to a subsampled ensemble of 34,151 clusters over the unique cluster architectures, employing a kernel bandwidth of $\epsilon = \exp(5.5)$ [77]. A gap in the eigenvalue spectrum after λ_3 (Figure 4.7), led us to construct two-dimensional diffusion map embeddings in $\{\vec{\Psi}_2, \vec{\Psi}_3\}$ [108]. The remaining $(739,246 - 34,151) = 705,095$ were projected into the embedding using the Nyström extension.

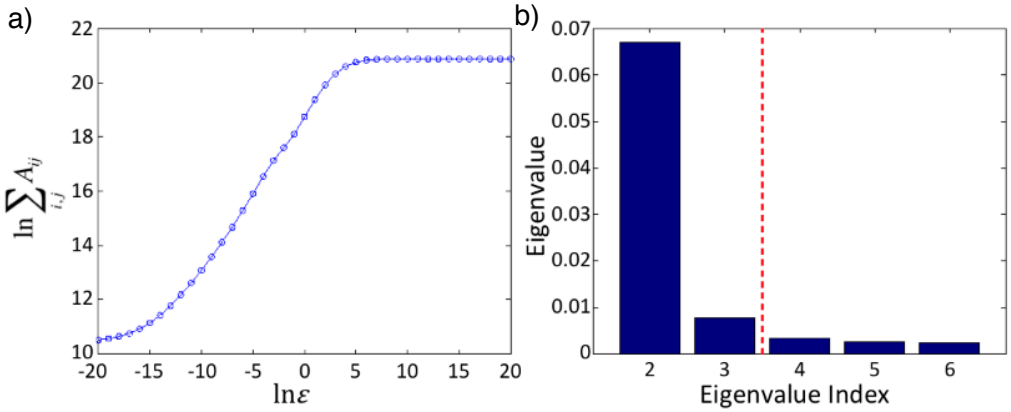

Figure 4.7: Specification of diffusion map bandwidth and effective dimensionality for the self-assembly of active Janus particles. (a) Specification of the diffusion map Gaussian kernel bandwidth using the approach in Ref. [77]. We selected a value of $\epsilon = \exp(5.5)$. (b) Diffusion map eigenvalue spectrum omitting the trivial unit eigenvalue, $\lambda_1 = 1$, for viewing clarity. Application of the L-method of Salvador and Chan [108] identifies the first "knee" (i.e., discontinuity) in the eigenvalue spectrum between λ_3 and λ_4, implying a spectral gap after the second non-trivial eigenvalue and an effective dimensionality of $k = 2$. This motivated us to construct diffusion map embeddings into the top two non-trivial eigenvectors (Ψ_2, Ψ_3).

We present in Figure 4.8 the two-dimensional composite diffusion map embedding with points colored by cluster size. Our analysis reveals a quasi one-dimensional assembly landscape. Advancing left to right along the principal axis of the manifold corresponds to the aggregation of progressively longer one-dimensional chains of Janus particles. Excursions perpendicular to the manifold correspond to the synthesis of Janus rings formed by a chain

0.01mM	Electric Field Strength E (V/cm)								
Frequency f (kHz)	167	250	333	417	500	583	667	750	833
50	0	1	1	1	1	1	1	1	1
100	1	1	1	1	1	1	1	1	1
120	0	0	0	0	0	0	0	0	0
150	0	0	0	0	0	0	0	0	0
200	1	1	1	1	1	1	1	1	1
300	0	1	1	1	1	1	1	1	1
400	0	0	0	1	0	0	0	0	1
500	1	1	1	1	1	1	1	1	1
600	1	1	1	1	1	1	1	1	1
700	1	1	1	1	1	1	1	1	1
800	1	1	1	1	1	1	1	1	1
900	1	1	1	1	1	1	1	1	1
1000	1	1	1	1	1	1	1	1	1
1500	1	1	1	1	1	1	1	1	1
2000	1	1	1	1	1	1	1	1	1
2500	1	1	1	1	1	1	1	1	1
3000	1	1	1	1	1	1	1	1	1
4000	0	1	1	1	1	1	1	1	1
5000	0	0	0	1	0	0	0	0	1
6000	1	1	1	1	1	1	1	1	1
7000	0	0	0	1	0	0	0	0	1
8000	1	1	1	1	1	1	1	1	1
9000	0	0	0	0	0	0	0	0	1
10000	0	0	0	0	0	0	0	0	0

Table 4.2: Number of experiments performed for a homogeneous self-assembling system of active metallodielectric Janus particles at a salt condition of 0.01mM NaCl

wrapping back on itself to "bite" its own tail, ejecting the excess particles that are pinched off in the formation of the ring. (We provide an illustration of this interesting process over the manifold in Figure 4.9, showing the fragmentation of a 12-mer chain in this manner to form a 6-mer ring and a 6-mer chain.) Progressing further still from the manifold leads to a sparsely populated outer corona comprising of branched clusters typically formed by the collision of linear chains.

To quantify the impact of electric field strength, AC frequency, and salt concentration upon the self-assembly process, we again binned the experimental data into different regimes:

0.1mM	Electric Field Strength E (V/cm)								
Frequency f (kHz)	167	250	333	417	500	583	667	750	833
50	0	0	0	0	0	0	0	0	0
100	1	1	1	1	1	1	1	1	1
120	0	1	1	1	1	1	1	1	1
150	1	1	1	1	1	1	1	1	1
200	1	1	1	1	1	1	1	1	1
300	1	1	1	1	1	1	1	1	1
400	1	1	1	1	1	1	1	1	1
500	1	1	1	1	1	1	1	1	1
600	1	1	1	1	1	1	1	1	1
700	1	1	1	1	1	1	1	1	1
800	1	1	1	1	1	1	1	1	1
900	1	1	1	1	1	1	1	1	1
1000	1	1	1	1	1	1	1	1	1
1500	1	1	1	1	1	1	1	1	1
2000	1	1	1	1	1	1	1	1	1
2500	0	0	0	0	0	0	0	0	0
3000	1	1	1	1	1	1	1	1	1
4000	1	1	1	1	1	1	1	1	1
5000	1	1	1	1	1	1	1	1	1
6000	1	1	1	1	1	1	1	1	1
7000	1	1	1	1	1	1	1	1	1
8000	1	1	1	1	1	1	1	1	1
9000	1	1	1	1	1	1	1	1	1
10000	0	0	0	0	0	0	0	0	1

Table 4.3: Number of experiments performed for a homogeneous self-assembling system of active metallodielectric Janus particles at a salt condition of 0.1mM NaCl

(i) low (50-300 kHz), intermediate (400-800 kHz), high (900 kHz - 3 MHz) AC frequency, f, (ii) low (167-333 V/cm), intermediate (417-583 V/cm), and high (667-833 V/cm) electric field strength, E, and (iii) low (0.01 mM) and high (0.1 mM) NaCl concentration, [NaCl]. We again neglect trends in the very high frequency regime due to capacitive effects in our experimental setup precluding accurate control of the field strength. We present in Figure 4.10 the effective free energy landscapes in the nine different E-f regimes at low salt concentration. At high salt concentrations, we observe dramatically suppressed assembly behavior due to increased electrostatic screening from counter-ions in the solution, only observing

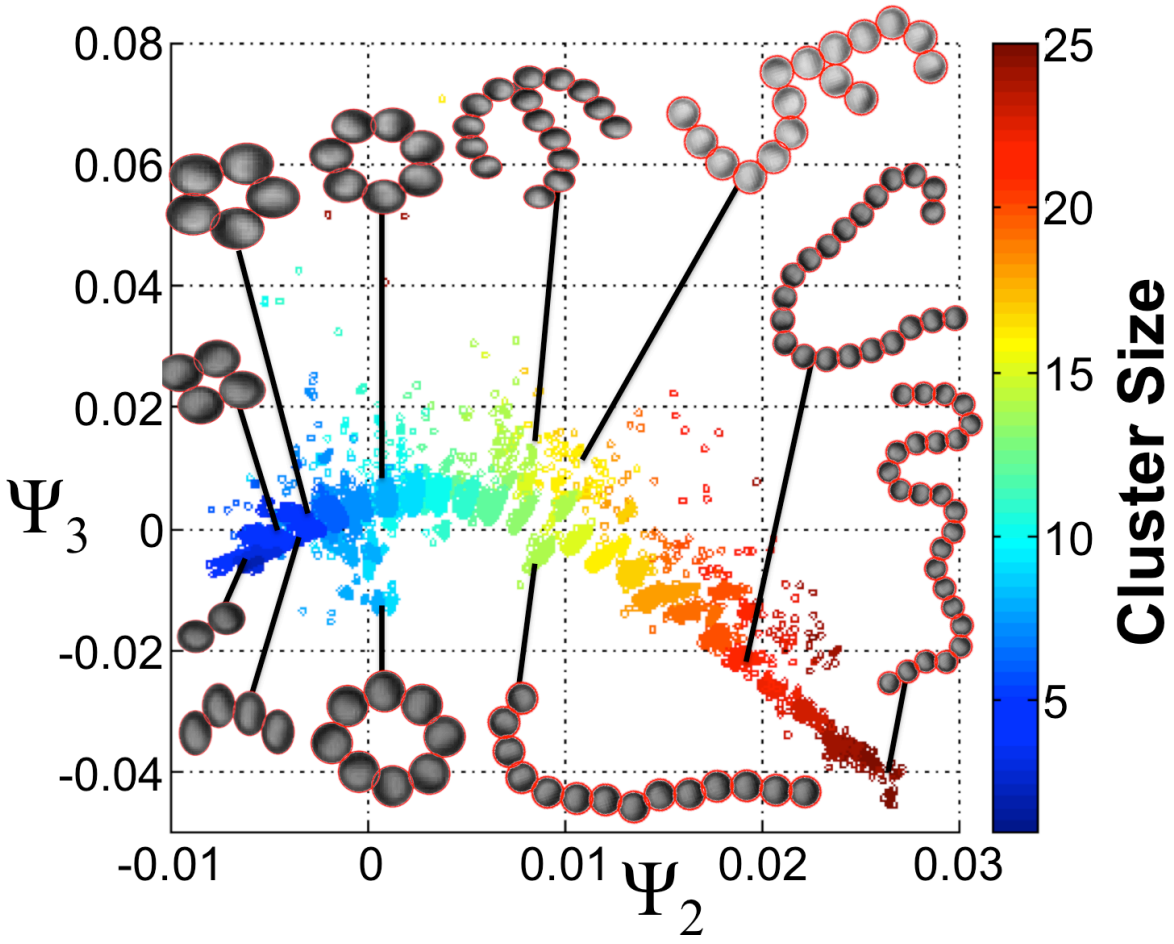

Figure 4.8: Composite diffusion map embedding for the self-assembly of active Janus particles in the top two collective modes $[\Psi_2, \Psi_3]$ furnished by the diffusion map. Each point represents one of the 739,246 clusters observed in the 537 experiments conducted over a range of AC frequencies, electric field strengths, and NaCl concentrations (cf. Tables 4.2 and 4.3). To aid in visualization, points are colored by the number of particles in the cluster, and representative aggregates superposed onto the manifold.

significant aggregation in the high frequency regime where the induced dipoles are largest (cf. Figure 4.6a). Accordingly, we relegate the [NaCl] = 0.1 mM data to Figure 4.13, and all subsequent discussions pertain to [NaCl] = 0.01 mM unless otherwise noted.

From Figure 4.10, we can readily infer how varying the frequency and field strength affects assembly. At low frequencies, self-assembly is limited to predominantly monomers and transient small aggregate formations. Higher frequencies stabilize the formation of

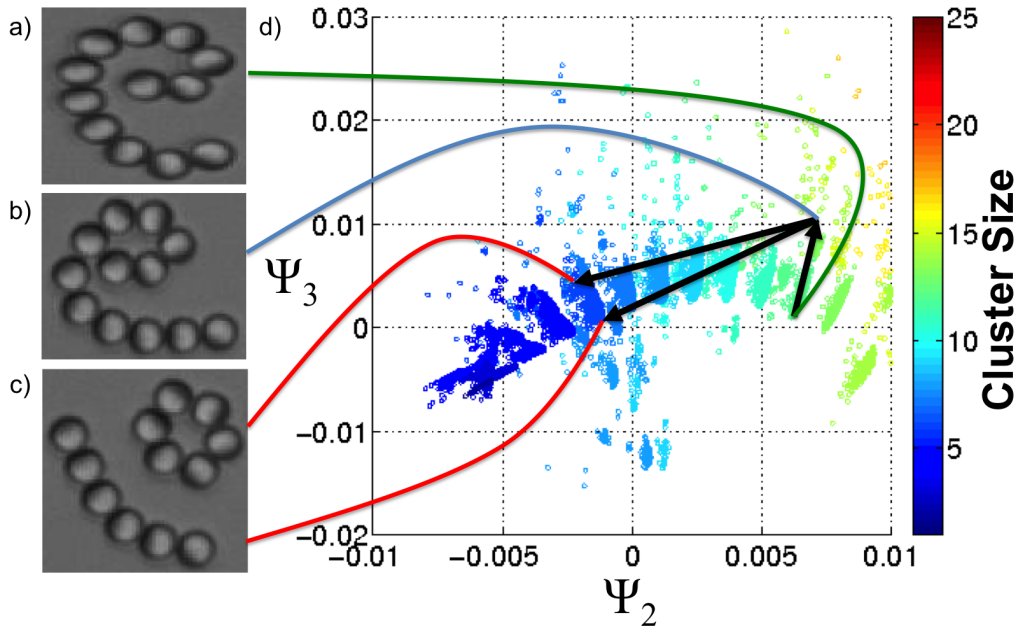

Figure 4.9: An example of a ring formation event extracted from the particle tracking trajectory for the self-assembly of active Janus particles at E=583.3 V/cm, f=1.5 MHz, [NaCl] = 0.01mM traced over the composite intrinsic manifold discovered by the diffusion map (Figure 4.8). (a) A linear 12-mer chain progressing under rICEP coils back upon itself. (b) The head of the chain collides with the middle of its own tail leading to the formation of a 6-mer ring and a residual 6-mer linear chain. (c) The ring and chain disaggregate leading to the formation of two new and distinct clusters. (d) The progression of the ring formation event superposed onto the composite intrinsic manifold. The coiling back of the 12-mer chain results in a local step over the manifold, followed by a non-local jump corresponding to the splitting of the 12-mer into two 6-mers. Internal cluster rearrangements and monomer addition or removal corresponds to local moves over the manifold, whereas large scale cluster aggregation or disaggregation events correspond to non-local jumps.

Janus chains of varying sizes, with low field strengths producing chains of ∼8 particles while intermediate and high field strengths generate chains of size ∼10-15 particles. At high frequency, a larger range of structures are stabilized in the intermediate and high field regimes, corresponding to chains of ∼20-25 particles, as well as ring and branched structures of various sizes.

By partitioning the quasi-one dimensional assembly process into the different regions indicated in Figure 4.11, we quantify the mass fraction of different chain (regions I, III, IV)

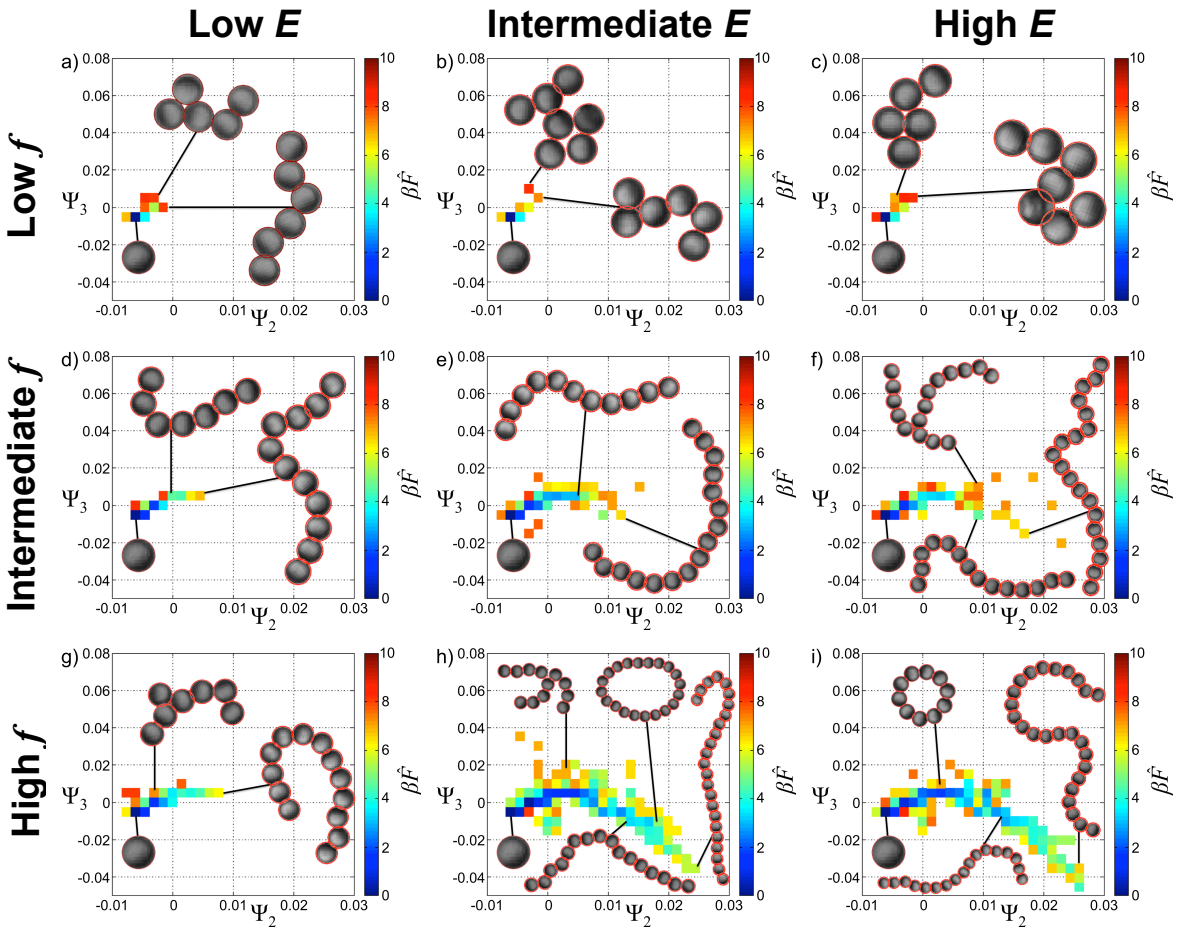

Figure 4.10: Effective free energy landscapes for the self-assembly of active Janus particles at low (0.01 mM) NaCl concentration at different applied AC electric field strengths, E, and frequencies, f. Columns partition the electric field strength into low (167-333 V/cm), intermediate (417-583 V/cm), and high (667-833 V/cm) regimes. Rows split the AC frequency of the applied field into low (50-300 kHz), intermediate (400-800 kHz), and high (900 kHz - 3 MHz) regimes.

and non-chain (regions II, IV, VI) aggregates to guide the design of experimental conditions to favor the assembly of desired aggregates. For example, if we are only concerned with maximizing the yield of intermediate length chains (region III), we should assemble the particles at high f – intermediate E to maximize the mass of the system residing in this region at 36.6%, with 6.0% residing in the non-chain regions II/IV/VI. If instead we wished to form intermediate length chains, but also limit formation of non-chain structures, we could shift to intermediate f – intermediate E (17.5% in region III, 1.9% in II/IV/VI), high

f – low E (9.1%, 0.5%), or intermediate f – low E (3.7%, 0.3%) depending on our tolerance for non-chain aggregates.

By studying the changes to the assembly landscape as a function of the experimental conditions, we can relate these changes to the underlying particle behaviors. We first consider the dependence of assembly behavior upon AC frequency. From Figure 4.10, we observe that larger clusters form at higher frequencies. This behavior can be understood from the dependencies upon AC frequency of the polarizability and velocity of Janus particles at [NaCl] = 0.01 mM presented in Figure 4.12a. The real portions of the product of the hemisphere polarizabilities are a weakly increasing function of frequency below 300 kHz, remaining effectively constant over the intermediate and high frequency range (cf. Equation 4.1). Only the metal-dielectric interactions are favorable, consistent with the observation of primarily chain-like aggregates. The particle velocity, however, is highest in the low frequency regime, dropping sharply within the intermediate and high frequency regimes Figure 4.12b. Particles in the low frequency regime therefore experience weaker interparticle attractions and higher kinetic energies, restricting self-assembly to predominantly monomers and dimers. We observe the assembly of heavier aggregates at intermediate and high frequencies due to an increase in attractive potential between particles and a decrease in particle velocity.

We now consider the dependence of assembly behavior upon electric field strength. From Figures 4.10 and 4.11, the assembly landscape shows that increasing field strength beyond the low field strength regime leads to the formation of larger clusters at intermediate and high AC frequencies. At low frequencies, only small aggregate sizes are observed independent of field strength. By Equation 4.1, the interparticle attraction increases as the square of the electric field strength, E^2. Similarly from Figure 4.12c, particle velocities also scale approximately as E^2. We observe a critical field strength for the assembly of aggregates of size $N \gtrsim 8$ residing between the low and intermediate field strength regimes. We suggest that this may be due to weak interparticle interactions and low particle velocities resulting in a reduced likelihood for the particles to come into contact range and bind. At intermediate and high

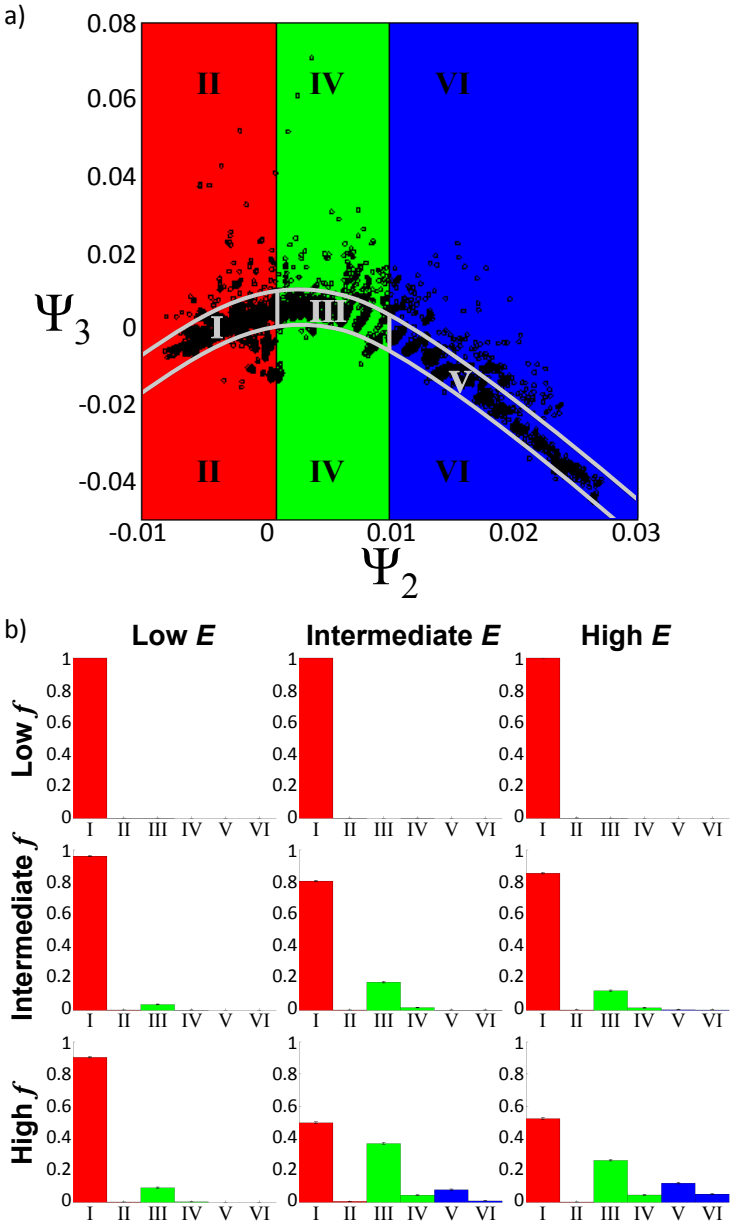

Figure 4.11: Mass fraction of different chain architectures as a function of electric field strength and AC frequency for the self-assembly of active Janus particles. (a) Partitioning of diffusion map space into 6 distinct regimes corresponding to small (I,II), medium (III,IV), and large (V,VI) clusters, inside (I,III,V) and outside (II,IV,VI) of the linear chain envelope. (b) Fraction of system mass located inside these 6 distinct regions of self-assembly as a function of experimental conditions. Columns partition the electric field strength, E, into low (167-333 V/cm), intermediate (417-583 V/cm), and high (667-833 V/cm) regimes. Rows split the AC frequency of the applied field into low (50-300 kHz), intermediate (400-800 kHz), and high (900 kHz - 3 MHz) regimes.

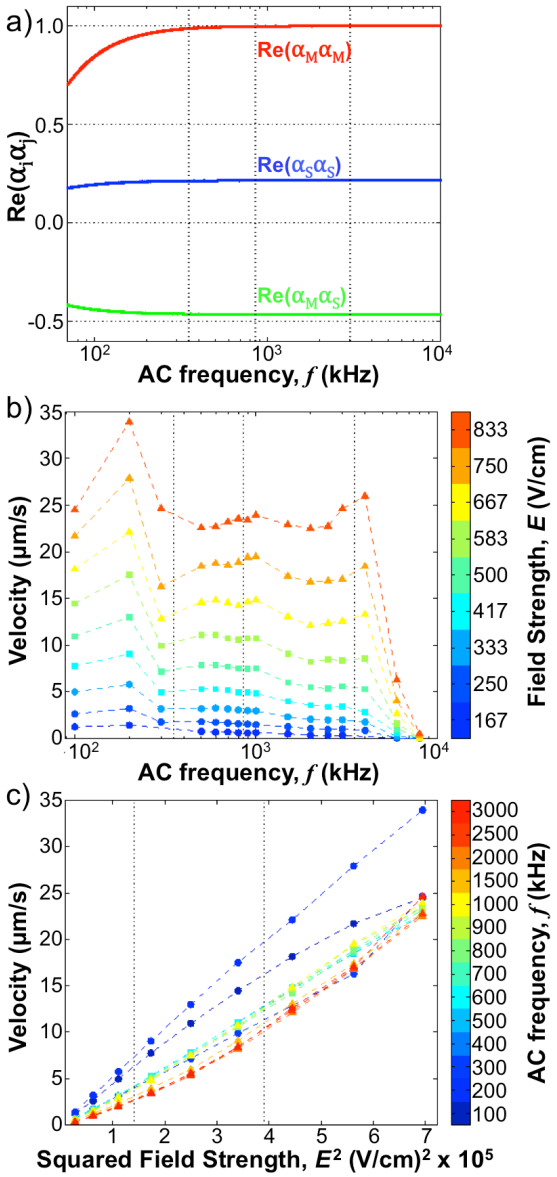

Figure 4.12: Dependence of rICEP particle velocity upon AC frequency and electric field strength at [NaCl] = 0.01 mM. (a) Real portion of product of hemispheric polarizabilities as a function of AC frequency, f (c.f. Equation 4.1). (b) Dependence of Janus particle ballistic velocities as a function of AC frequency, f, at different electric field strengths, E. Consistent with the binning of the field strengths in the main text, circles correspond to low (167-333 V/cm), squares to intermediate (417-583 V/cm), and triangles to high (667-833 V/cm) field strengths. The vertical lines selected to separate the low (70-300 kHz), intermediate (400-800 kHz), and high (900 kHz - 3 MHz) frequency regimes. (c) Dependence of Janus particle ballistic velocities as a function of squared electric field strengths, E^2, at different AC frequencies, f. Consistent with the binning of the field strengths in the main text, circles correspond to low (70-300 kHz), squares to intermediate (400-800 kHz), and circles to high (900 kHz - 3 MHz) frequency regimes. The vertical lines selected to separate the low (167-333 V/cm), intermediate (417-583 V/cm), and high (667-833 V/cm) field strengths.

frequencies, shifting from intermediate to high field strengths yields a small increase in the stability of larger aggregate structures. Although assembly behavior is heavily suppressed under the high salt conditions, we observe a similar trend at [NaCl] = 0.1 mM in the high frequency regime (Figure 4.13). The observation of markedly larger aggregates at high field strengths demonstrates that despite similar E^2 scaling of velocity and attraction, the balance of these two effects results in an elevated aggregation propensity at larger values of E. We are quick to note that more detailed analysis and understanding of rICEP and electrohydrodynamic motion, may be necessary to fully account for the observed trends [122, 127, 128]. Nevertheless, a complete understanding of the physics underpinning the system behavior is not required by our data-driven approach, which can inform understanding of assembly by empirically quantifying assembly behaviors from particle tracking data.

In sum, we have used our machine learning framework to construct two-dimensional embeddings capturing the self-assembly of metallodielectric Janus particles, and mapped the regions of configuration space accessible under various salt concentrations, AC frequencies, and electric field strengths. The manifolds generated provide new insights for our understanding of self-assembly in this system, and provide a roadmap showing how to control assembly behavior by manipulating experimental conditions. Low AC frequencies suppress assembly at all field strengths and salt concentrations, resulting in essentially only free monomers. To produce chain aggregates, we can move into the intermediate frequency regime, where for low salt conditions we can generate chains spanning from ∼8 particles under a low applied field to ∼10-15 particles in the intermediate and high field strength regimes. Finally, moving into the high frequency regime, where form diverse architectures including rings and ramified structures, as well as chains in excess of ∼20 particles.

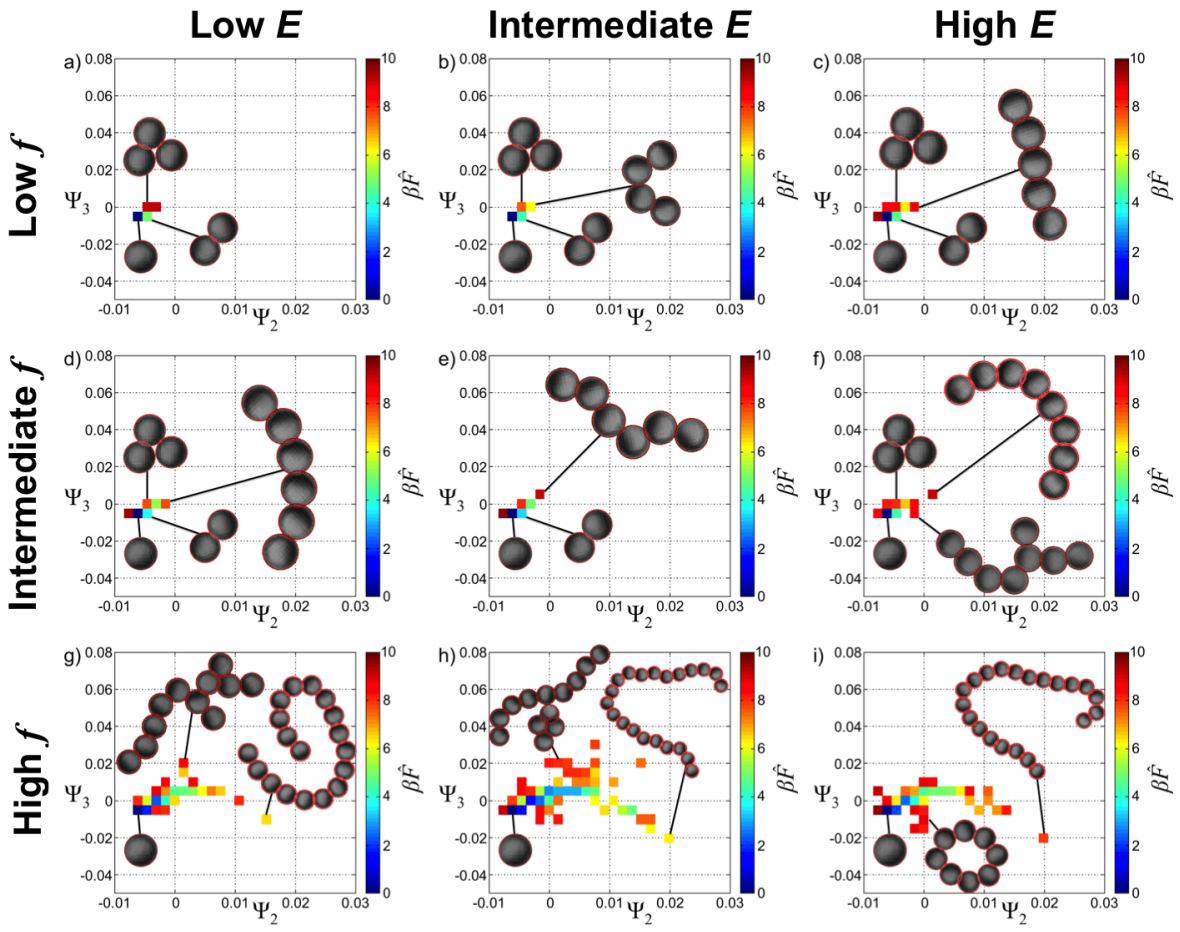

Figure 4.13: Effective free energy landscapes at high (0.1 mM) NaCl concentration at different applied AC electric field strengths, E, and frequencies, f. Columns partition the electric field strength into low (167-333 V/cm), intermediate (417-583 V/cm), and high (667-833 V/cm) regimes. Rows split the AC frequency of the applied field into low (50-300 kHz), intermediate (400-800 kHz), and high (900 kHz - 3 MHz) regimes. Assembly is arrested under low and intermediate frequencies under these salt conditions, with high frequency behavior analogous to the low salt system.

4.3 Conclusions

We have presented an approach to infer low-dimensional roadmaps of self-assembly by analyzing experimental particle tracking trajectories using diffusion maps. The variables spanning the low-dimensional embeddings discovered by the diffusion map correspond to the slow collective modes governing the long-time dynamics of assembly, and reveal the range of accessible aggregates and assembly pathways without requiring prior knowledge of the

underlying physics governing particle aggregation or motion. The effective free energy landscapes constructed over these embeddings reveal the relative prevalence and stability of different cluster architectures. By recovering these landscapes under different experimental conditions, we can quantify the impact of experimentally controllable parameters on the topography of the free energy surface. The findings from this data-driven approach may be compared and rationalized with existing theoretical and experimental understanding of the system, or used to help infer the properties of novel or poorly characterized systems. Furthermore, these landscapes furnish quantitative understanding of the system response to externally imposed conditions, and can guide the tuning of these conditions to favor desired cluster architectures.

We have demonstrated our methodology in applications to the nonequilibrium assembly of Janus particles subjected to an oscillating electric field that drives interparticle attractions and self-propelled particle motion. In an application to the templated assembly of active Janus particles and passive linker particles, our approach revealed the existence of an effectively two-dimensional embedding comprising three different assembly routes leading to dense disordered clusters, three-armed pinwheels, and extended archipelago topologies. We then demonstrated that the relative stability of these various architectures could be tuned by manipulating the AC frequency of the applied field, and showed that this behavior was in good accord with the physical understanding of the particle response to the AC field. In a second application to homogeneous ensembles of active Janus particles, our method discovered a quasi one-dimensional projection mapping the range of accessible cluster architectures. The principal axis of the manifold traced the assembly of progressively longer linear chains of Janus particles, with departures perpendicular to the manifold corresponding to the formation of rings and branched chains of particles. We quantified the relative stability of the various aggregates as a function of electric field strength, AC frequency, and salt concentration, showing how these three control parameters can be simultaneously manipulated to favor the assembly of clusters of desired size and architecture. By relating these empirical

findings to our understanding of the underlying particle physics, we found good agreement for our model of assembly behavior as a function of these experimental controls.

By integrating experimental particle tracking technology with sophisticated machine learning tools, this work presents a new approach to infer assembly pathways and attainable aggregates directly from experimental data, providing insight into the interplay of different experimentally controllable parameters on assembly behavior, and informing the rational design of conditions favoring the assembly of desired structures. In Chapter 8, we build on this work to "close the feedback loop" to establish an iterative design process wherein the insights and design rules discovered by machine learning are used to inform rational redesign of particle properties to favor assembly of desired aggregates. We anticipate that with continued development this approach will improve our understanding and control of self-assembly processes, and help forge a powerful new pathway to rationally engineer novel self-assembling materials with desired structure and function.

Chapter 5

Characterizing bit-state transitions in digital colloids

Digital colloids [129], reconfigurable clusters of lock-and-key colloidal particles [130], have recently been proposed as a novel soft matter-based substrate for high-density information storage. A digital colloid comprises freely-rotating but tethered "halo" particles that are bound to the surface of a central particle (Figure 5.1). Information can be stored within distinguishable configurations of the halo particles around the central particle. These structures have been experimentally synthesized via depletion mediated binding of dimpled halo particles to the surface of a central spherical particle [129, 130], as well as through programmable DNA interactions [131]. These halo particles may be distinguished through a variety of labeling techniques [132], such as functionalization with complementary Förster Resonant Energy Transfer (FRET) pairs [133] or through binding of short oligonucleotides [129], thereby enabling the unique identification of distinct metastable halo particle configurations that mediate information storage and retrieval.

Storing information in micron-scale colloids has the potential to advance computing in unconventional environments. A prime example of which is DNA-based computing in solution, wherein arbitrary digital circuitry can be mapped onto reaction networks of DNA strands [135]. One practical limitation of DNA-based computing is the storage of information in the concentrations of DNA strands, which are essentially uniform throughout the computing volume. Digital colloids have potential as compartmentalized, high-density stor-

This chapter is based off work presented in:

Andrew W. Long, Carolyn L. Phillips, Eric Jankowksi and Andrew L. Ferguson, "Nonlinear machine learning and design of reconfigurable digital colloids", *Soft Matter*, **12**, 7119-7135 (2016).

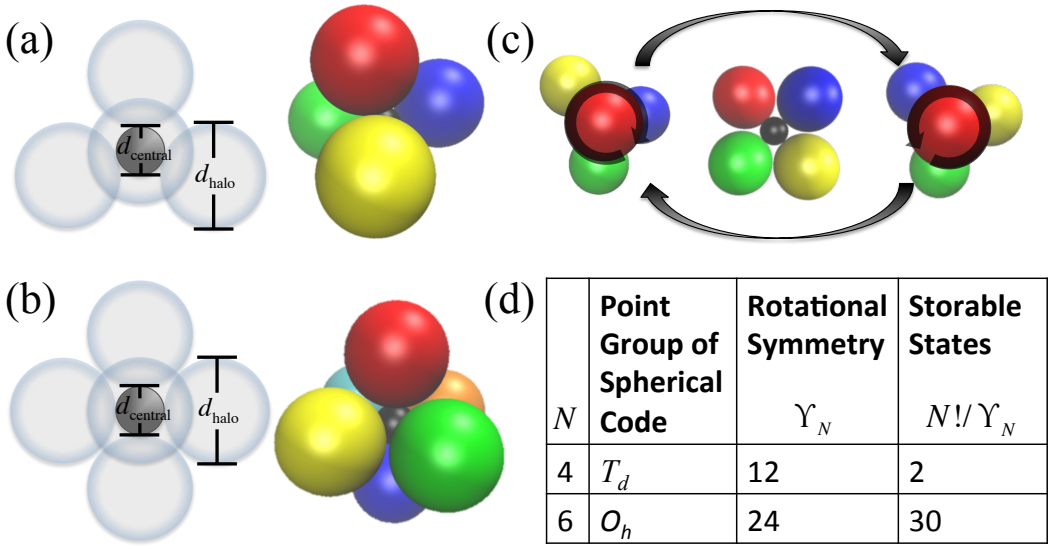

N	Point Group of Spherical Code	Rotational Symmetry Υ_N	Storable States $N!/\Upsilon_N$
4	T_d	12	2
6	O_h	24	30

Figure 5.1: Schematic of the digital colloid architecture with N distinguishable halo particles with diameter d_{halo} tethered to the surface of a central particle with diameter d_{central}. The diameters exist in a ratio $\Lambda = d_{\text{central}}/d_{\text{halo}}$. The *spherical code* structure defines the densest packing of halo particles around the central particle at the minimum diameter ratio Λ_{SC} for which the halo particles do not overlap [129], and defines the idealized structural arrangement of halo particles defining a distinguishable *bit state*. At $\Lambda = \Lambda_{\text{SC}}$, the halo particles of a (a) N=4 digital colloid define the vertices of a tetrahedron, and (b) an octahedron in a N=6 digital colloid. For $\Lambda_{\text{SC}} < \Lambda < \Lambda_{\text{T}}$ there is sufficient free volume for the halo particles to rattle around the stable spherical code structure, but not transition between different structures. Above a critical diameter ratio $\Lambda > \Lambda_{\text{T}} > \Lambda_{\text{SC}}$, there is sufficient free volume for the halo particles to cooperatively transition between different distinguishable configurations of the halo particles. (c) It is the availability of distinguishable bit states and transition pathways between them that makes it possible to store information within digital colloids. The N=4 digital colloid, for example, possesses two distinguishable tetrahedral bit states corresponding to left- and right-handed chiral arrangements. Transitions between these two chiral configurations mediated by a structural transition through a square planar arrangement of halo particles. (d) Table of the symmetry Υ_N and information storage capability of the N=4 and N=6 digital colloids. The more rotationally distinguishable bit states available the higher the information storage capacity. By using configurations for information storage, these digital colloids are capable of ultra-high information storage density. For example, N=6 digital colloids composed of 3-methacryloxypropyl trimethoxysilane (TPM) colloidal particles with density $\rho = 1.228$ g/cm^3 [134] and particle diameters of 1 μm possess an estimated memory density of 1.1 TB / g.

age elements that can diffuse throughout a computing volume, and which can in principle be reconfigured during computations. In order to realize the potential of digital colloids as unconventional computing elements, we require a fundamental understanding of the configurational transitions between storage states.

The number of distinguishable halo particle configurations in the digital colloid ground state determines the number of unique "bit states" of a cluster, and therefore its information storage capacity. For example, the halo particles of the N=4 digital colloid exist in a tetrahedral ground state, meaning – after the elimination of trivial rotational symmetries – it possesses exactly two distinguishable arrangements of the four halo particles (Figure 5.1c). These two available states mean that the N=4 colloid is a binary storage element that can encode exactly one bit of information. In general, the number of storable states is specified by the $N!$ halo particle permutations divided by the symmetry operator for the ground state configurational arrangement, Υ_N. The symmetry operator for an N-particle colloid is determined by the spherical code solution for the arrangement of the halo particles around the central particle [129, 136–139]. This arrangement is the solution to the Tammes problem [140] – a special case of the Thomson problem [141] – corresponding to the configuration of N halo particles that maximizes the minimum distance (or equivalently minimum angle) between the halo particle centers [136–139, 142]. This configuration determines both the point group of the packing structure and the multiplicity of the symmetry operator. Putatively optimal spherical code solutions up to N=130 are reported in Ref. [143]. The spherical code solution for N=4 is a tetrahedron (Figure 5.1a) and for N=6 an octahedron (Figure 5.1b) with corresponding point groups, rotational symmetries, and number of storable states listed in Figure 5.1d. The number of bit states that can be written in a digital colloid is given by the base-2 logarithm of the number of storable states, $\log_2(N!/\Upsilon_N)$. The information storage capacity of digital colloids increases as $O(\log_2(N!))$, making them ideal for high-density information storage [129]. For example, a single N=6 octahedral cluster is capable of storing 4.9 bits (0.613 bytes), and a N=12 icosahedral cluster 22.9 bits (2.87 bytes).

A key feature of these digital colloids is that the halo particles, although strongly tethered to the central particle, are free to move over the surface of the central particle. Defining the diameter ratio between the central and halo particles as $\Lambda = d_{\text{central}}/d_{\text{halo}}$, the spherical code solution imposes a minimum value Λ_{SC} for a given system of N halo particles, below which the N particles cannot bind to the surface without overlapping. For Λ above this value but below some threshold ratio, $\Lambda_{\text{SC}} \leq \Lambda < \Lambda_{\text{T}}$, each halo particle is confined within a cage composed of its neighbors, and the digital colloid is locked into a single bit state. This threshold ratio, Λ_{T}, is given by the minimum value of Λ needed for collective halo particle rearrangements to access the transition state, and has been previously computed for N=4-12 [129]. At $\Lambda \geq \Lambda_{\text{T}}$ there is sufficient free volume for the halo particles to transition between bit states and the digital colloid becomes unlocked. By actuating halo particle transitions between bit states, information can be written. By observing the halo particle bit state, information can be read.

Above the unlocking transition, the digital colloid is no longer confined to oscillate around the spherical code configuration, and can explore a rich and complex morphological landscape. The design of information storage elements with tailored free energy barriers sufficiently low to actuate the halo particle configuration (i.e., a low write free energy) but sufficiently high to prevent thermally-activated spontaneous bit state flips (i.e., low memory volatility) requires an accounting of the thermally accessible configurational state space, transition state free energy barriers, and mean first passage times as a function of N and Λ. Furthermore, designing reliable digital colloids requires an understanding of how sensitive bit transitions are to the manufacturing tolerances of their constituent parts.

The configurational state of a digital colloid exists in a $2N$-dimensional phase space defined by the azimuthal and polar coordinates of the N halo particles on the surface of the central sphere. Excluded volume and any other interactions between the halo particles means that their motions and locations are correlated, and these cooperative couplings are expected to define an emergent low-dimensional subspace to which the digital colloid

dynamics are effectively restrained [125]. This latent low-dimensional manifold supports the free energy surface containing the thermally-accessible system configurations, stable and metastable states, and transition pathways between them. Determining this landscape provides quantitative understanding of the system morphology, thermodynamics, and kinetics.

Dimensionality reduction techniques have demonstrated good success in recovering these low-dimensional manifolds for both single molecule [50, 57, 70] and many-body self-assembly [66, 118, 125] systems as shown in Chapters 3-4. Building upon these foundations, in this work we combine Brownian dynamics simulations, nonlinear machine learning, and first passage time analysis to quantify the stable and transition state morphologies and determine the transition mechanisms, free energy barriers, and transition rates for bit state switching for N=4 and N=6 digital colloids. We use this new quantitative understanding to computationally design addressable digital colloids with tailored kinetic stability and actuation free energies, providing a step towards the engineering of high-density digital colloid information storage media.

5.1 Materials and methods

We study the morphology, thermodynamics, and kinetics of digital colloids comprising N=4 and N=6 halo particles using Brownian dynamics simulations, nonlinear dimensionality reduction, and first passage time analysis.

5.1.1 Brownian dynamics simulations of digital colloids

Following the protocol previously detailed in Refs. [129, 136], we performed Brownian dynamics simulations of N=4 and N=6 digital colloids using the HOOMD-blue GPU-based molecular simulation package (`http://glotzerlab.engin.umich.edu/hoomd-blue/`) [99, 144, 145]. The spherical halo particles are constrained to glide over the surface of the spherical central particle using a radial restoring force perpendicular to the free particle

direction of motion. This restoring force provides a rigid constraint binding the halo particles to the central particle surface [129], implemented via the HOOMD `constrain.sphere` module (`http://hoomd-blue.readthedocs.io/en/stable/module-md-constrain.html`). The diameter of the central particle d_{central} regulates the geometric confinement of these halo particles, which is defined by the ratio of central to halo particle diameters, $\Lambda = d_{\text{central}}/d_{\text{halo}}$. The central particle is treated as static and inert, while halo particles i and j interact through a surface-shifted Weeks-Chandler-Anderson (WCA) pair potential to account for excluded volume interactions [97],

$$u(r_{ij}) = \begin{cases} 4\varepsilon \left[\left(\frac{\sigma}{r_{ij}-\Delta} \right)^{12} - \left(\frac{\sigma}{r_{ij}-\Delta} \right)^{6} \right] + \varepsilon, & r_{ij} < 2^{(1/6)}\sigma + \Delta \\ 0, & r_{ij} \geq 2^{(1/6)}\sigma + \Delta \end{cases} \tag{5.1}$$

where r_{ij} is the center of mass separation between the halo particles, ε is the interaction strength, σ is the size parameter, and the parameter $\Delta = 2\sigma$ shifts the WCA potential to an effective surface of the halo particles. We perform our simulations in a dimensionless gauge such that energy is measured in units of ε and distance in units of σ. The reduced temperature is defined as $T^* = k_B T/\epsilon$, and reduced time as $t^* = t/\sqrt{m\sigma^2/\epsilon}$ where m is the mass of a halo particle.

The surface-shifted WCA potential is a convenient computational approximation for particles possessing hard core interactions [146, 147], and can be mapped to a hard sphere fluid using a perturbative generalization of the Rowlinson scheme developed by Barker and Henderson [148–150]. Employing Equation 12 in Ref. [148], we determine an effective hard sphere diameter of the halo particles of $d_{\text{halo}} = 3.0785\sigma$. The central particle diameter is defined as $d_{\text{central}} = 2d_{\text{central-halo}} - d_{\text{halo}}$, where $d_{\text{central-halo}}$ is the constrained center of mass distance between the central and halo particles. This mapping of our WCA halo particles to effective hard spheres of diameter $d_{\text{halo}} = 3.0785\sigma$ enables us to calculate the spherical code diameter ratio Λ_{SC} and threshold diameter ratio Λ_{T} based on purely geometric considerations

[129, 136]. These hard sphere values do not hold precisely for our soft particles, but the steepness of the WCA potential and moderate temperatures employed in our calculations mean that they do behave as approximate hard spheres. Specifically, we observe no pair of halo particles i and j to approach closer than $r_{ij} = 2.95\sigma$ corresponding to a pairwise interaction energy $u(r_{ij}) = 2.96\epsilon$. The values of Λ_{SC} and Λ_{T} reported for each of the digital colloid architectures should therefore be interpreted as approximations based on the effective hard sphere mappings.

Simulations were performed at a reduced temperature of T^*=0.1and the Brownian dynamics (overdamped Langevin dynamics) equations of motion numerically integrated using velocity verlet in the NVE ensemble and a Langevin thermostat [144] with a time step of dt^*=10^{-3} [151]. Each simulation was initialized with $\Lambda_0 >> \Lambda_{\mathrm{T}} > \Lambda_{\mathrm{SC}}$ and the halo particles randomly distributed and free to move over unencumbered over the central particle surface. The central particle was then gradually shrunk to the desired value of Λ over the course of 1.1×10^5 time steps to allow the system to equilibrate before conducting a 10^9 time step production run.

To make contact between our dimensionless simulations and real units, we adopt a characteristic interaction strength of $\epsilon = 10\ k_BT$ at 298 K between micron-sized halo particles with $\sigma = 0.915\ \mu$m ($d_{\mathrm{halo}} = 2.82\ \mu$m) fabricated from 3-methacryloxypropyl trimethoxysilane (TPM) with density $\rho = 1.228$ g/cm^3 [134]. Under this choice the reduced temperature T^* = 0.1 maps to $T = 298$ K, the reduced time step $dt^* = 10^{-3}$ to $dt = 0.54\ \mu$s, and the reduced simulation time $t^* = 10^9 \times 10^{-3} = 10^6$ to $t = 540$ s.

5.1.2 Digital colloid dimensionality reduction

Simulations of the digital colloid dynamics provide all particle coordinates as a function of time, furnishing, in principle, all of the morphological, thermodynamic, and kinetic details governing transitions between different configurations of the distinguishable halo particles defining the information storage bit states. In practice, extracting this information from

the trajectories is challenging due to the high dimensionality of the system: a particular configuration of N halo particles rolling around the surface of a central particle exists as a point in a $2N$-dimensional phase space defined by the surface locations of each halo particle. For sufficiently small values of Λ the accessible phase space volume is, however, drastically reduced by excluded volume interactions that give rise to cooperative halo particle rearrangements [129]. These cooperative couplings are expected to yield a separation of time scales, wherein local caged oscillations within a stable bit state give rise to high-frequency motions, and transitions between bit states are rare events with slow characteristic time scales. We anticipate that these cooperative transition pathways correspond to a small number of slow collective modes of the halo particle dynamics [118, 125, 152]. Extracting these slow modes from the simulation trajectory reveals the multi-body transition pathways governing the digital colloid dynamics, and also presents kinetically meaningful collective coordinates in which to construct low-dimensional free energy surface mapping out the accessible morphologies, stable states, and dynamical transition pathways [51, 55–58, 70, 118, 125].

In this work, we apply the many-body diffusion map technique to Brownian dynamics simulations of digital colloids to extract the intrinsic manifold governing digital colloid morphology and transitions. We present a complete description of the diffusion map approach in Chapter 2, but we detail the system specific distance measure used in diffusion mapping below.

Microstate pairwise distances

The metastable bit states of the digital colloids are morphologically identical in that they correspond to the same configurational arrangement of halo particles around the central sphere [129]. Information storage is only possible insofar as all (or some) of the halo particles are distinguishable, thereby permitting unambiguous discrimination between all (or some) of the bit state configurations. In this work we consider all N halo particles to be distinguishable such that there are $N!$ relabelings cluster that are reduced by the rotational symmetry of

the bit state Υ_N to yield an information storage capacity of $\log_2(N!/\Upsilon_N)$ bits.

Our nonlinear dimensionality reduction algorithm requires as input a measure of similarity distances between different digital colloid configurations observed over the course of the simulation. When we measure the distance between different halo particle configurations, we assume the halo particles are indistinguishable, but retain the halo particle label information for *a posteriori* identification of the distinguishable bits states within the low-dimensional projection. By separating morphology and labeling when sampling the configurational phase space we achieve an important practical advantage. Since each of the $N!$ bit states are morphologically identical, treating the halo particles as indistinguishable allows for comprehensive sampling of the identical metastable basin of all bit states within relatively short simulation trajectories. In contrast, treating halo particles as distinguishable would result in the emergence of $(N!/\Upsilon_N)$ identical metastable free energy wells within the intrinsic manifold, many of which would be incompletely sampled, and some never sampled at all. For small digital colloids containing few states, this is unlikely to present difficulties, but for larger colloids containing hundreds of thousands of states, sampling the intrinsic manifold without this simplification presents a practical challenge.

For digital colloids comprising N halo particles we compile a library $\mathcal{L}(N, \{\Lambda\})$ of all digital colloid microstates observed in our simulation trajectories over a range of central to halo particle diameter ratios Λ. We compute χ the N-by-N pairwise distance matrix between all pairs of halo particles in a particular digital colloid microstate in $\mathcal{L}(N, \{\Lambda\})$. We normalize pairwise distances by the minimum distance between vertices in the idealized regular polyhedron with equispaced halo particle vertices for a given value of Λ. For a central to halo particle distance $d_{\text{central-halo}} = d_{\text{halo}}\left(\Lambda + 1\right)/2$, the edge length of the idealized tetrahedron in the N=4 system is $d'_{\text{halo-halo}} = \sqrt{8/3}d_{\text{central-halo}}$, and that of the idealized octahedron in the N=6 system is $d'_{\text{halo-halo}} = \sqrt{2}d_{\text{central-halo}}$. In each case, we define the normalized pairwise distance matrix $\chi' = \chi/d'_{\text{halo-halo}}$. By normalizing with respect to the ideal polyhedral edge length, we enable direct comparisons between digital colloid microstates across different Λ

values.

Using the χ' computed for each digital colloid microstate in $\mathcal{L}(N, \{\Lambda\})$, we can define a fast, rotationally invariant, graph-based measure of structural similarity between pairs of digital colloid microstates i and j,

$$\mathbf{d}_{ij} = \min_{\mathbf{H}} ||\chi'_i - \mathbf{H}^T \chi'_j \mathbf{H}||, \tag{5.2}$$

where $\mathbf{H}$ is a permutation matrix rearranging the rows and columns of χ'_j. That is, our measure is the minimum of the permuted entrywise $L_{1,1}$ norm between halo particle distance matrices. Minimizing over permutations is equivalent to minimizing over relabelings of halo particles. For the N=4 and N=6 systems considered in this work, the number of permutations is quite small, $N! = 24$ and $N! = 720$, permitting us to determine the minimum permuted distance by brute force enumeration. Exhaustive enumeration will become intractable for sufficiently large systems, and it will be necessary to resort to approximate graph matching approaches such as those we have previously employed in Ref. [125].

Diffusion maps

Using the diffusion map dimensionality reduction technique described in Chapter 2 yields a set of right eigenvectors $\{\vec{\Psi}_i\}$ and associated eigenvalues $\{0 \leqslant \lambda_i \leqslant 1\}$ with the trivial top pair $\vec{\Psi}_1 = \vec{1}$ and $\lambda_1 = 1$ [55]. These eigenvectors are discrete approximations to the eigenfunctions of the Fokker-Planck equation describing the time evolution of the probability density function over the data [59, 75], with eigenvalues corresponding to the frequency of these collective harmonic modes. Large eigenvalues correspond to the slow (e.g. long time) relaxation modes of the Markov process, and small eigenvalues correspond to fast modes. A gap in the eigenvalue spectrum corresponds to a separation of relaxation time scales, with collective modes above the gap corresponding to the slow subspace modes governing long time structural evolution to which the remaining fast modes are restrained [55, 60, 62]. We

employ the L-method of Salvador and Chan to systematically identify the location of this spectral gap [57, 108, 125].

Identifying a gap in the eigenvalue spectrum after $\lambda_{(k+1)}$ prompts construction of a low-dimensional landscape in the top k nontrivial eigenvectors furnished by the diffusion map $\{\vec{\Psi}_i\}_{i=2}^{k+1}$. The low-dimensional projection of the i^{th} microstate in our library $\mathcal{L}(N, \{\Lambda\})$ is specified by the "diffusion mapping" into the i^{th} component of these top k eigenvectors,

$$\text{microstate}_i \mapsto \left(\vec{\Psi}_2(i), \vec{\Psi}_3(i), ..., \vec{\Psi}_{k+1}(i)\right). \tag{5.3}$$

This projection defines the nonlinear dimensionality reduction from the $2N$-dimensional phase space of halo particle angular coordinates to the k-dimensional intrinsic manifold.

One of the primary limitations of the diffusion map, and nonlinear dimensionality reduction methods in general – with the exception of autoencoders [153] – is that the technique does not furnish a mapping for these collective variables to the input features of the original high dimensional data. While automated techniques exist to sieve and approximate these top eigenvectors from a candidate feature pool [106, 107], these algorithmic features can be so complex that attributing physical characteristics to these eigenvectors can still be exceedingly difficult. Further, there is no guarantee that a concise physical mapping exists for the nonlinear order parameters describing these many-body systems [56, 125]. To aid in physical interpretation, we correlate the diffusion map variables by physical "bridge" variables such as the polyhedral volume or the distance of a configuration from an idealized polyhedron.

5.1.3 Free energy surfaces

We construct free energy landscapes over the k-dimensional intrinsic landscape defined by the diffusion map embedding (Equation 5.3) for each digital colloid. The free energy landscape is constructed by collecting histograms over all microstates collected over the course of the simulation projected into the low-dimensional projection, and employing the statistical

mechanical relationship [154, 155],

$$F^*(\Lambda, \vec{\xi})/T^* = -\ln \hat{P}(\Lambda, \vec{\xi}) + C(\Lambda), \tag{5.4}$$

where Λ is the diameter ratio, $T^* = k_B T/\epsilon$ is the reduced temperature at which we conduct our simulations, $\vec{\xi}$ is a k-dimensional vector specifying a point on the k-dimensional intrinsic manifold defined by the diffusion map, $\hat{P}(\Lambda, \vec{\xi})$ is a histogram approximation to the probability density of digital colloid microstates at $\vec{\xi}$ for a specific value of Λ, $F^*(\Lambda, \vec{\xi})$ is the reduced free energy of the configurations at location $\vec{\xi}$ and diameter ratio Λ, and $C(\Lambda)$ is an arbitrary additive constant that may differ for each diameter ratio. At constant temperature and volume, $F^* = F/\epsilon$ is identifiable as the reduced Helmholtz free energy. In applying Equation 5.4 to estimate the equilibrium free energy surface from the empirical probability distribution computed from the Brownian dynamics trajectories, we assume that our simulations are sufficiently long to return converged estimates of the probability distribution over the low-dimensional manifold. Computing $F^* = F/\epsilon$ from our simulations at a reduced temperature $T^* = 0.1$, we identify $\beta F = \epsilon F^*/k_B T$. By converting these units to room temperature $T = \epsilon T^*/k_B = 298$ K, and a characteristic interaction energy of $\epsilon = 10\ k_B T$, we can calculate $\beta F = \epsilon F^*/k_B T = F^*/T^* = 10F^*$ in units of $k_B T$ at $T = 298$ K.

Importantly, although each histogram $\hat{P}(\Lambda, \vec{\xi})$ is constructed from an independent simulation trajectory performed at a different value of Λ, the diffusion map was constructed from a library of microstates $\mathcal{L}(N, \{\Lambda\})$ collected over all values of Λ. This permits each individual simulation trajectory to be projected into a shared intrinsic manifold spanned by the same nonlinear basis vectors $\{\vec{\Psi}_i\}_{i=2}^{k+1}$, and allowing us to quantify the impact of Λ upon the underlying free energy landscape of the digital colloid of fixed size N. We have previously referred to this approach as the composite diffusion map approach [57]. We choose the arbitrary constant $C(\Lambda)$ for each value of Λ so as to shift the global free energy minimum to zero (i.e., $C(\Lambda) : \min_{\vec{\xi}} F(\Lambda, \vec{\xi}) = 0$). Uncertainties in the free energy landscape were

computed by performing 10 bootstrap resamples (random resampling with replacement) of the data used to compile the histograms at each Λ.

5.1.4 Determining the digital colloid bit state

Up until now, the halo particles in the calculation have been treated as indistinguishable. To discern one bit state from another, we must now perform a *post hoc* accounting of the distinguishable states of each of the digital colloid microstructures projected into the intrinsic manifold. For the $N = 4$ and $N = 6$ digital colloids considered in this work, we employ a simple procedure to identify the distinguishable bit state of a given microstate based on the N-by-N halo particle adjacency matrix $\mathbf{G}$ and the halo particle positions. We compute the symmetric binary adjacency matrix $\mathbf{G}$ between the halo particles of any particular digital colloid configuration from the pairwise distances matrix χ by specifying a threshold separation of 110% of the halo particle separation in the idealized polyhedral configuration. Halo particles i and j closer than this distance are defined as bonded ($G_{ij} = 1$) and those at larger separations are not ($G_{ij} = 0$). Thus the adjacency matrix maps the set of all possible microstates to a finite set of structures by applying a proximity criterion between halo particles. We have verified that our results are robust to choices of cutoff over the range 105% to 130% of the ideal polyhedron halo particle separation. The symmetric binary adjacency matrix $\mathbf{G}$ cannot, however, distinguish between two states that rotationally distinguishable but related through a mirror reflection, and distinguishing between these states requires additional analyses described below.

N=4 bit states

The tetrahedral structure formed by the N=4 digital colloid belongs to the T_d point group, with rotational symmetry $\Upsilon_4 = 12$. Given the $N! = 24$ possible permutations of halo particle labelings, we have $N!/\Upsilon_N =$ 2rotationally distinguishable states that can be stored in the configuration of these halo particles, corresponding to the two chiral enantiomers of

the tetrahedral bit state. We distinguish the two bit states through their chirality (i.e., handedness) by computing the signed volume, V, of the parallelepiped connecting the halo particle centers of mass using the triple product. The sign of this volume, $\mathrm{sgn}(V)$, determines the handedness of the tetrahedron, allowing us to distinguish between left- and right-handed structures and discriminate between the two bit states.

N=6 bit states

The octahedral structure defined by the N=6 digital colloid belongs to the O_h point group with rotational symmetry $\Upsilon_6 = 24$, giving a total of $N!/\Upsilon_N = 30$ rotationally distinguishable bit states. These 30 bit states correspond to 15 possible unique permutations of the adjacency matrix of an octahedron, each of which has two distinct chiralities owing to a left- or right-handed arrangement of the halo particles occupying the mid-plane of the octahedron. To identify a digital colloid as belonging to a particular bit state, we first classify the structure as containing one of the 15 unique adjacency matrices. To distinguish the two chiral alternatives within each of these 15 matrix classes, we tag the particle corresponding to the first row of the adjacency matrix and specify that particle to reside at the top of the digital colloid (e.g., the red halo particle in Figure 5.1b). We then identify the three halo particles corresponding to the first three non-zero entries of the first row of the adjacency matrix as three neighboring particles residing in the mid-plane of the octahedron (e.g., the green, yellow, and orange particles in Figure 5.1b). The signed volume, V, of the parallelepiped connecting these four halo particle centers of mass distinguishes between a clockwise or counter-clockwise arrangement of halo particles in the mid-plane, permitting unambiguous identification of the right- and left-handed chiral bit states. By pairing the adjacency matrix and chirality information, the instantaneous configuration of an arbitrary sized digital colloid can be unambiguously assigned to one of its distinguishable bit states.

5.1.5 Bit state transition kinetics

Having determined the rotationally distinguishable bit state of each digital colloid microstructure following the approach detailed in Section 5.1.4, we can track transition events as changes in colloidal bit state over time. To quantify the transition kinetics and the dwell time (or volatility) of each bit state, we compute from our simulations the mean first passage time (MFPT) as the average duration for which a bit state is occupied before a transition occurs [62, 156]. The minimum first passage time identified in our simulation trajectories is 80-times larger that the sampling period, assuring that the identified transition events are "elementary transitions" in the sense that they correspond to a single structural rearrangement events. We define for each bit state a core region comprising an ensemble of configurations around the idealized bit state structure. The phase space between core regions comprises a "no man's land" belonging to none of the bit states. The digital colloid is considered to occupy a particular bit state when it passes into its corresponding core region, and to have left that bit state only when it passes into the core region of a new bit state. Transient excursions into the no man's land and then back into the same bit state core region are not considered transitions. The use of non-contiguous core regions separated by a no man's land leads to improved MFPT estimates by eliminating diffusive recrossing events of the separatrix between bit states that can artificially depress the MFPT estimate [157]. The particular definition of the core regions depends on the architecture of the digital colloid under consideration and is detailed in Section 5.2. Having defined the core regions we analyze our Brownian dynamics production run to extract for each of the $k = 1...K$ bit states all of the $i = 1...P(k)$ first passage times of the system out of that bit state $\{FPT_i^k\}_{i=1}^{P(k)}$. The MFPT for bit state k then follows straightforwardly as $MFPT^k = \frac{1}{P(k)} \sum_{i=1}^{P(k)} FPT_i^k$. Moreover, since the bit states are all structurally identical, we can average the estimate over all N equivalent bit state transitions $MFPT = \frac{1}{N} \sum_{k=1}^{K} \sum_{i=1}^{P(k)} FPT_i^k$. Similarly, we compute the variance of the first passage time as $\sigma^2 = \frac{1}{N} \sum_{k=1}^{K} \sum_{i=1}^{P(k)} \left(FPT_i^k - MFPT\right)^2$. Using the

central limit theorem, we estimate 95% confidence intervals from the sampling distribution of the MFPT as $\left[MFPT - 1.96\frac{\sigma}{\sqrt{N}}, MFPT + 1.96\frac{\sigma}{\sqrt{N}}\right]$.

The reciprocal of the MFPT is the escape rate $\Gamma = 1/\text{MFPT}$ [62], which, since all bit states for a particular digital colloid are structurally equivalent, is identical for all bit states. For the N=4 system, the escape rate is precisely equal to the transition rate between the two chiral bit states. For the N=6 case, the escape rate is equal to the transition rate from any particular bit state to any one of eight other rotationally distinguishable bit states accessible by a single halo particle rearrangement event (Figure 5.7). This quantification of mean first passage times and escape rates can be straightforwardly extended to digital colloids of arbitrary size.

As detailed in Section 5.1.1, we adopt experimentally relevant parameter values of $\epsilon = 10\ k_BT$ at 298 K, $\sigma = 0.915\ \mu$m, and $\rho = 1.228$ g/cm^3 [129, 134]. This maps our reduced time step $dt^* = 10^{-3}$ to $dt = 0.54\ \mu$s, and permits us to report the MFPT in seconds and the escape rate in inverse seconds.

5.2 Results and discussion

5.2.1 N=4 (2-state) digital colloids

Using the approach detailed in Section 5.1.1, we performed Brownian dynamics simulations of the tetrahedral N=4 digital colloid for $\Lambda = \{0.4000, 0.4142, 0.4400, 0.5000, 0.7500, 1.0000, 1.1256\}$. In each case we held the halo particle diameter fixed and varied the size of the central particle. These values of Λ span three regimes: (I) $(\Lambda_{\text{SC}} \approx 0.2247) \leq \Lambda < (\Lambda_{\text{T}} = 0.4142)$ where the central particle diameter is sufficiently small that the digital colloid bit state is effectively locked since the halo particles possess insufficient free volume to transition to a new bit state, (II) $(\Lambda_{\text{T}} = 0.4142) \leq \Lambda < (\Lambda_{\text{U}} = 0.5361)$ where the central particle is sufficiently large such that the cluster is unlocked and transitions between bit states are permitted, and (III) $\Lambda \geq (\Lambda_{\text{U}} = 0.5361)$ where the central particle is so large that bit state

transitions are effectively barrierless and the digital colloid remains in constant flux between states. $\Lambda_{\mathrm{SC}} \approx 0.2247$ is the minimum diameter ratio at which the halo particles can exist on the surface of the central particle without overlaps [129] under the effective hard sphere mapping with $d_{\mathrm{halo}} = 3.0785\sigma$. (As observed above, the soft WCA potential does admit a closer distance of approach but we never observe two halo particles to approach closer than 2.95σ over the course of any of our calculations.) The threshold $\Lambda_{\mathrm{T}} = 0.4142$ is the transition threshold diameter ratio below which bit state transitions are geometrically forbidden under the effective hard sphere mapping, and was previously computed from geometric considerations in Ref. [129]. The threshold $\Lambda_{\mathrm{U}} = 0.5361$ is defined by the value of Λ for which the free energy barrier height for bit state transitions falls to 1 $k_B T$ and the transition free energy barrier is comparable to the size of thermal fluctuations (cf. Figure 5.4a).

From each simulation we extract 2×10^6digital colloid microstates saved every 500 time steps, and aggregate these into a single composite library $\mathcal{L}(N = 4, \Lambda = \{0.4000, 0.4142, 0.4400, 0.5000, 0.7500, 1.0000, 1.1256\})$ comprising 1.4×10^7 microstates. Constructing diffusion maps over such a large number of microstates is computationally intractable, so we reduce the number of microstates used to construct the diffusion map embedding by subsampling the data. In principle, this could be done uniformly, but to ensure that we have good coverage of the structural conformations we instead take advantage of the vast number of redundant (i.e., nearly identical) microstates in our library. We identify from each simulation trajectory the set of unique adjacency matrices $\mathbf{G}$ and assign each conformation in the trajectory as belonging to one of these prototypical architectures. Aggregating the different architecture lists across all values of Λ yields a set of 34 prototypical architectures. To obtain good coverage over this range of structures, we sample 30 configurations from each architecture (when there are less than 30 configurations, we select all observed microstates) to define a representative set of 941 digital colloid microstates over the various values of Λ.

We then applied diffusion maps to these 941 microstates using the distance measure defined in Section 5.1.2 and procedure detailed in Chapter 2, employing a soft-thresholding

bandwidth of $\epsilon = \exp(3)$ determined via the method defined in Ref. [77]. Using the *L*-method [108], we identified a gap in the eigenvalue spectrum beyond λ_3, prompting the construction of a two-dimensional landscape in the top two non-trivial diffusion map eigenvectors (Ψ_2, Ψ_3). The remaining $(1.4 \times 10^7 - 941)$ configurations were projected into this two-dimensional intrinsic manifold using the Nyström extension [80, 81, 109]. By constructing a diffusion map over microstates collected from simulations spanning all values of Λ, we can project each simulation trajectory into a shared intrinsic manifold and quantify the impact of Λ upon the morphology, stability, and kinetics of the digital colloid within a unified low-dimensional basis [57].

Morphology and stability. We present in Figure 5.2a the reduced ensemble of digital colloid structures observed at the transition threshold value of $\Lambda_{\mathrm{T}} = 0.4142$ in the two dimensional intrinsic manifold spanned by (Ψ_2, Ψ_3). Each point in this manifold corresponds to a single digital colloid configuration observed in our simulation. To aid in visualization, we have superimposed onto the manifold renderings of representative snapshots visualized using VMD [96]. Given a particular labeling of the distinguishable halo particles (A – red, B – yellow, C – blue, D – green) illustrated in Figure 5.2c, we compute for each digital colloid microstate the vector triple product $V = \hat{AB} \cdot \left(\hat{AC} \times \hat{AD}\right)$ defining the signed volume of a parallelepiped connecting the halo particle centers of mass, where $\hat{XY}$ denotes the unit vector pointing from X to Y. By employing unit vectors, the magnitude of V is bounded on the interval [0,1] irrespective of Λ and can be interpreted as a measure of the deviation of the halo particle configuration from planarity: $|V| = 0$ corresponds to all halo particles residing in a single plane, and $|V| = \sqrt{2}/2$ to an idealized tetrahedral arrangement. The sign of V distinguishes the chirality of the two tetrahedral bit states: $V > 0$ corresponds to right-handed tetrahedra and $V < 0$ to left-handed configurations.

Coloring each point in Figure 5.2a by $|V|$ reveals a strong correlation between Ψ_3 and $|V|$, indicating that Ψ_3 was discovered by the diffusion map as a collective variable measuring the relative planarity of the halo particle configuration. The minimum value of $|V| = 0$ is

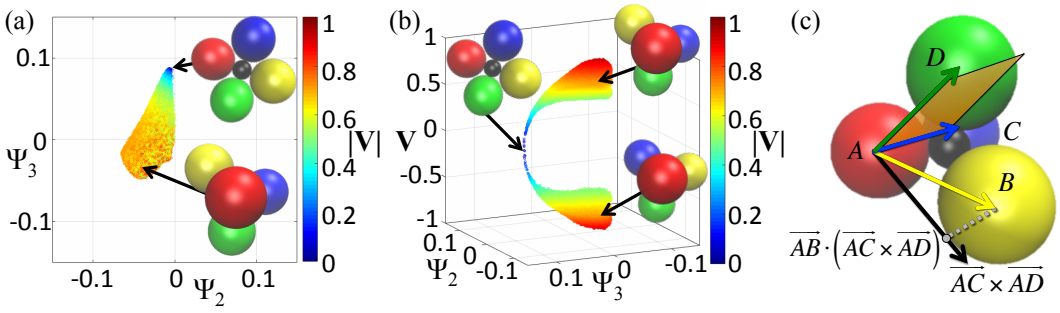

Figure 5.2: Diffusion map embeddings of the N=4 tetrahedral digital colloid at the unlocking threshold $\Lambda_{\mathrm{T}} = 0.4142$. (a) Embedding into the top two collective modes (Ψ_2, Ψ_3) furnished by the diffusion map. Each point represents one of the 2×10^6 microstates recorded over the course of this simulation trajectory. To assist in interpretation of the embedding, we present visualizations of representative microstates and color points by the absolute volume of the parallelepiped $|V| = |\vec{AB} \cdot \left(\vec{AC} \times \vec{AD}\right)|$ connecting the centers of mass of the halo particles. The magnitude of V provides a measure of the deviation of the halo particle configuration from planarity: $|V| = 0$ corresponds to all halo particles residing in a single plane, and $|V| = \sqrt{2}/2$ to an idealized tetrahedral arrangement. (b) Augmentation of the 2D intrinsic manifold in panel (a) with a third axis containing the signed volume of the parallelepiped V. The sign of V distinguishes the chirality of the two tetrahedral bit states: $V > 0$ corresponds to right-handed tetrahedra and $V < 0$ to left-handed configurations. (c) Graphical illustration of the triple product defining the signed parallelepiped volume $V = \vec{AB} \cdot \left(\vec{AC} \times \vec{AD}\right)$.

attained at the top of the tear-shaped intrinsic manifold in the region of $(\Psi_2 \approx 0.01, \Psi_3 \approx 0.085)$ where the digital colloid adopts a square planar geometry. The largest values of $|V| \approx \sqrt{2}/2$ are reached at $(\Psi_2 \approx -0.03, \Psi_3 \approx -0.04)$ where the digital colloid adopts approximately tetrahedral geometries. The square planar geometry defines the transition state for interconversions between bit states [129]. At the transition threshold value of $\Lambda_{\mathrm{T}} = 0.4142$ the transition state comprises essentially a single point within the intrinsic manifold since the free volume available to the halo particles at the transition state is so small as to admit essentially a unique square planar configuration. Contrariwise, since $(\Lambda_{\mathrm{T}} = 0.4142) > \Lambda_{\mathrm{SC}}$ the tetrahedral structures occupy a relatively larger volume at the bottom of the tear-shaped intrinsic manifold corresponding to a diversity of structures defining the metastable bit state rattling around the caged volume centered on the idealized tetrahedral

geometry.

As a result of our choice to construct diffusion map embeddings without regard to halo particle distinguishability (Section 5.1.2), the two rotationally distinguishable chiral bit states accessible to the N=4 digital colloid are collapsed together onto the intrinsic manifold in Figure 5.2a. In order to separate these two bit states we present in Figure 5.2b the diffusion map embedding augmented with a third axis containing the signed triple product $V = \vec{AB} \cdot \left(\vec{AC} \times \vec{AD} \right)$ as a measure of both microstate morphology and chiral bit state. This augmented embedding separates the two chiral bit states and makes clear their structural equivalence, with each occupying a topographically identical volume of the intrinsic manifold and connected by the square planar transition structure occupying the slim bottleneck at $V = 0$.

In Figure 5.3, we present the augmented diffusion map embeddings for all seven values of Λ. In each case we present both the low-dimensional diffusion map projection into (Ψ_2, Ψ_3, V) of the 2×10^6 microstates recorded over the course of this simulation trajectory, and the free energy surface over the intrinsic manifold $F(\Psi_2, \Psi_3, V)$ defined by collecting histograms over the embedding. As detailed in Section 5.1.3, by assuming a characteristic interaction strength between halo particles of $\epsilon = 10\ k_B T$ at 298 K (cf. Equation 5.1), we report βF as a dimensionless free energy measured in units of $k_B T$ at $T = 298$ K. In Movie S1 in the supplementary information to Ref. [158], we present rotating images of the images in Figure 5.3 that more clearly illustrate the shape and topography of the intrinsic manifolds and free energy surfaces.

For $(\Lambda = 0.4000) < (\Lambda_{\mathrm{T}} = 0.4142)$ (Figure 5.3a,b), structural transitions are effectively forbidden and the digital colloid is locked into the bit state in which it was initialized. The square planar transition state at $V = 0$ is effectively inaccessible due to excluded volume interactions and is never visited over the course of our simulations.

At $\Lambda = (\Lambda_{\mathrm{T}} = 0.4142)$ (Figure 5.3c,d), the digital colloid is at the unlocking threshold and is able to access the square planar transition state $|V| = 0$ and make transitions between

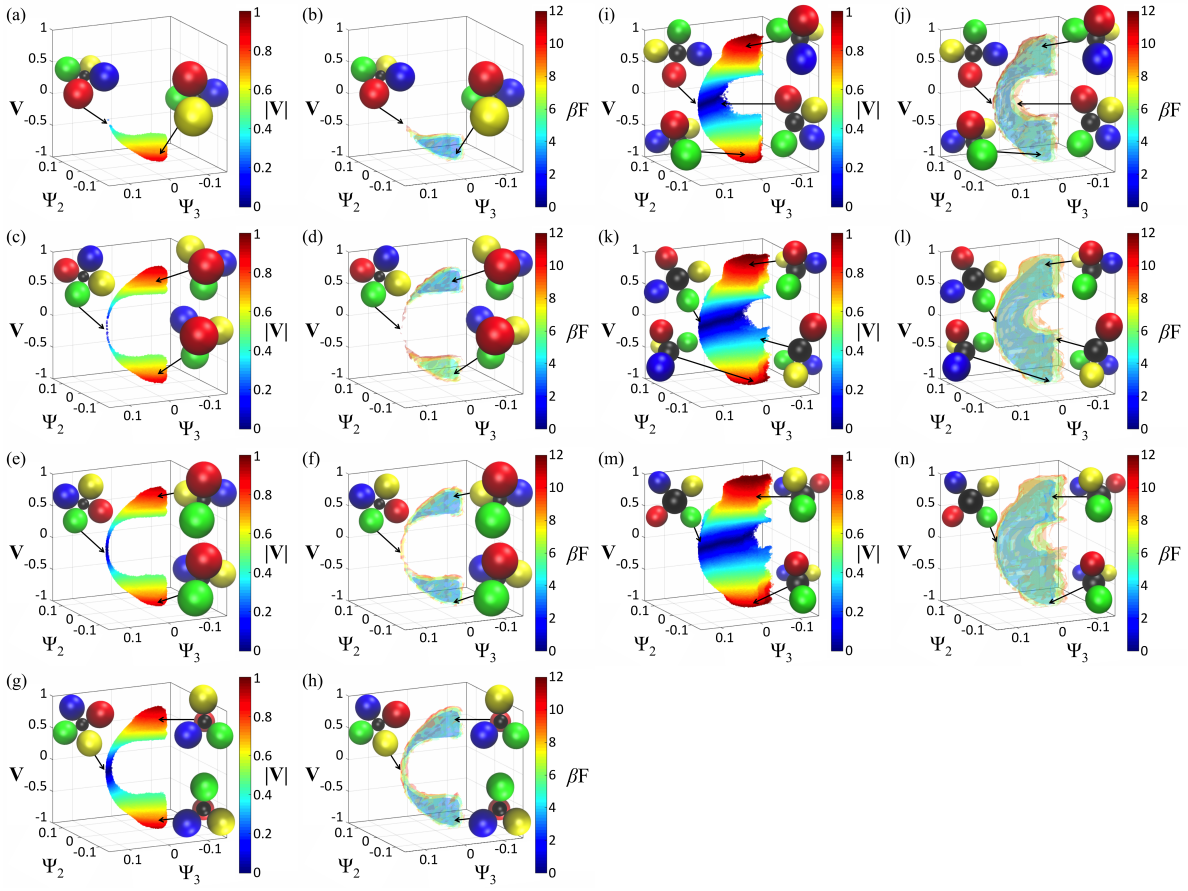

Figure 5.3: Diffusion map embeddings and the free energy surfaces they support of the N=4 tetrahedral digital colloid as a function of Λ. Embeddings are constructed in (Ψ_2, Ψ_3, V) where (Ψ_2, Ψ_3) are the top two non-trivial eigenvectors discovered by diffusion map corresponding to the slowest collective modes of the digital colloid dynamical rearrangements and V is the signed volume of a parallelepiped connecting the halo particle centers of mass (Figure 5.2c). The sign of V distinguishes the chirality of the two tetrahedral bit states: $V > 0$ corresponds to right-handed tetrahedra and $V < 0$ to left-handed configurations. The magnitude of V provides a measure of the deviation of the halo particle configuration from planarity: $|V| = 0$ corresponds to all halo particles residing in a single plane, and $|V| = \sqrt{2}/2$ to an idealized tetrahedral arrangement. In each pair of panels we present on the left the low-dimensional projection of the 2×10^6 microstates harvested from the Brownian dynamics simulation at a particular value of Λ into the intrinsic manifold, and on the right the free energy surface over the intrinsic manifold $F(\Psi_2, \Psi_3, V)$ computed by application of Equation 5.4 employing rectilinear histogram bins of size $[\Delta\Psi_2, \Delta\Psi_3, \Delta V] = [0.01, 0.01, 0.05]$. (a,b) $\Lambda = 0.4000$, (c,d) $\Lambda = 0.4142$, (e,f) $\Lambda = 0.4400$, (g,h) $\Lambda = 0.5000$, (i,j) $\Lambda = 0.7500$, (k,l) $\Lambda = 1.0000$, (m,n) $\Lambda = 1.1256$. Points in the diffusion map embeddings are colored by $|V|$. Isosurfaces are plotted at $\beta F = \{0, 2, 4, 6, 8, 10, 12\}$, with the arbitrary zero of free energy defined by the most populated voxel of the embedding. Representative microstates have been projected over the embeddings to illustrate the halo particle configurations in each region of the intrinsic manifold.

the two bit states. The transition bottleneck exists at the top of a high $\Delta(\beta F) = (9.07 \pm 0.23)$ free energy barrier. Accordingly, bit state transitions are an activated process and a rare event, and we observe only three bit state transitions over the course of the simulation. The structural equivalence of the two chiral bit states means that the topography of the free energy surface within each metastable basin should be identical. The observed differences in the empirical free energy values computed within the two basins is a consequence of kinetic trapping and rare transition events leading to poor sampling of the accessible phase space.

For $\Lambda > (\Lambda_{\mathrm{T}} = 0.4142)$ (Figure 5.3e-n), the volume of the transition state ensemble at $|V| = 0$ expands as the increased free volume available to the halo particles admits a greater diversity of square planar transition structures. There is a commensurate drop in the transition barrier to $\Delta(\beta F) = (5.15 \pm 0.07)$ at $\Lambda = 0.4400$, to $\Delta(\beta F) = (1.93 \pm 0.02)$ at $\Lambda = 0.5000$, before the transitions become essentially barrierless with $\Delta(\beta F) < 1$ for $\Lambda > (\Lambda_{\mathrm{U}} = 0.5361)$.

We present in Figure 5.4a the free energy barrier as a function of Λ. An exponential fit of the form $\Delta(\beta F) = C_0 \exp(-C_1 \Lambda)$ provides a good fit to the data, with best fit parameters $\{C_0 = (1.29 \pm 0.89) \times 10^4, C_1 = (17.65 \pm 1.55)\}$ and an adjusted $R^2 = 0.98$. Quantification of the free energy barrier for the transition provides a measure of the reversible work required to actuate a transition between bit states, or equivalently the size of a concerted thermal fluctuation necessary to induce a spontaneous transition. This stands as one of the key variables for the design of stable but addressable information storage elements.

To ascertain the change in the phase space volume and structural morphologies of the transition state as a function of Λ, we present in Figure 5.4b a superposition of 2D (Ψ_2, Ψ_3) sections through the 3D free energy landscapes at $V = 0$, where the halo particles occupy planar configurations at the transition between the two chiral bit states. The broadening of the transition region bottleneck with increasing Λ is a result of the increased free volume available to the halo particles moving over the surface of increasingly large central particles, permitting access to a greater diversity of planar transition structures and a commensurate

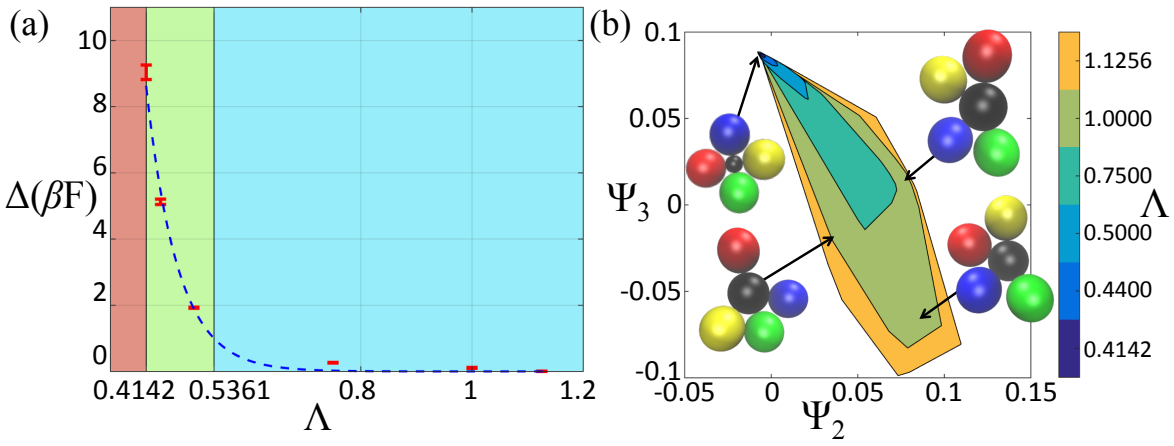

Figure 5.4: Free energy barriers for bit state transitions and cross sections of the transition region from the N=4 free energy surfaces in Figure 5.3 as a function of Λ. (a) Free energy barrier height $\Delta(\beta F)$ computed as the free energy difference between the global minimum of the free energy surface and the minimum free energy within the transition state region defined by $V \in [-0.1, 0.1]$. Error bars correspond to 95% confidence bounds computed by 10 rounds of bootstrapping. The blue dashed-line corresponds to an exponential of the form $\Delta(\beta F) = C_0 \exp(-C_1 \Lambda)$ with parameters $\{C_0 = (1.29 \pm 0.89) \times 10^4,\ C_1 = (17.65 \pm 1.55)\}$ and an adjusted $R^2 = 0.98$. Best fit parameters were computed by weighted least squares regression in which we confronted the observed heteroskedasticity in the data by weighting each free energy measurement in inverse proportion to its variance [159]. The colored regions distinguish the different regimes of Λ: $(\Lambda_{\mathrm{SC}} \approx 0.2247) \leq \Lambda < (\Lambda_{\mathrm{T}} = 0.4142)$ (red, locked), $(\Lambda_{\mathrm{T}} = 0.4142) \leq \Lambda < (\Lambda_{\mathrm{U}} = 0.5361)$ (green, unlocked), and $\Lambda \geq (\Lambda_{\mathrm{U}} = 0.5361)$ (blue, barrierless transitions).$\Lambda_{\mathrm{T}} = 0.4142$ defines the unlocking transition at which there is sufficient free volume for the halo particles to transition between bit states through the square planar transition state. $\Lambda_{\mathrm{U}} = 0.5361$ defines the transition to effectively unconstrained barrierless transitions between bit states where $\Delta(\beta F) = 1$. (b) Sections through the 3D free energy surfaces in $F(\Psi_2, \Psi_3, V)$ constructed from the subset of approximately planar halo particle configurations with $V \in [-0.1, 0.1]$. At $\Lambda_{\mathrm{T}} = 0.4142$ the cluster is at the transition threshold and there exists an essentially unique square planar transition state. With increasing Λ the increased free volume available to the halo particles permits access to a greater diversity of planar configurations including trapezoidal and kite geometries. This increase in the phase space volume of the transition region leads to a commensurate decrease in the transition state free energy barrier due to reduced energetic and entropic barriers.

reduction in the free energy barrier between the two bit states.

Kinetics. The depression of the transition state free energy with increasing Λ leads to more frequently observed transitions between the two chiral bit states. To quantify the transition rate as a function of Λ we report in Figure 5.5 the mean first passage time (MFPT) computed from each simulation as the average duration for which a bit state is occupied before a transition occurs [62, 156]. MFPT calculations were conducted for $\Lambda = \{0.4142$, 0.4200, 0.4300, 0.4400, 0.4500, 0.4750, 0.5000, 0.5100, 0.5200, 0.5300, 0.5400, 0.5500, 0.6000, 0.6500, 0.7000, 0.7500, 1.000, 1.1256$\}$. To mitigate the impact of possible recrossing events at the summit of the free energy barrier leading to artificially depressed MFPT estimates, we define a core regions within each bit state separated by a no man's land [157]. We define the core region of the right-handed bit state to be the region of the intrinsic manifold for which $V > 0.5$, and that of the left-handed bit state to be the region for which $V < -0.5$. The digital colloid is defined to enter a particular bit state the first time it passes into the corresponding core region, and is defined to have transitioned out of that bit state only when it passes into the core region of a new bit state. Excursions into the interstitial no man's land (i.e., $-0.5 \leqslant V \leqslant 0.5$) followed by re-entry into the core region of the same bit state are not considered transition events.

We present in Figure 5.5 the calculated MFPT as a function of Λ and associated error bars delimiting 95% confidence intervals. A shifted exponential of the form $\ln(\text{MFPT}) = B_0 \exp(-B_1 \Lambda) + B_2$ provides a good fit to the data, with best fit parameters $\{B_0 = (2.03 \pm 0.91) \times 10^3$, $B_1 = (14.08 \pm 0.92)$, $B_2 = (-2.53 \pm 0.04)\}$ and an adjusted $R^2 = 0.97$.

For $\Lambda < (\Lambda_{\text{T}} = 0.4142)$, the cluster is effectively locked and the MFPT is undefined since transitions are sterically forbidden. For $\Lambda \geq (\Lambda_{\text{T}} = 0.4142)$, the cluster unlocks and MFPT rapidly decreases with increasing Λ as the free volume available to the halo particles increased and the transition free energy barrier decreases (cf. Figure 5.4). The MFPT approaches an approximate asymptotic limit at $\Lambda > (\Lambda_{\text{U}} = 0.5361)$ corresponding to a central particle so large that the motions of the halo particles are largely decorrelated and transitions are

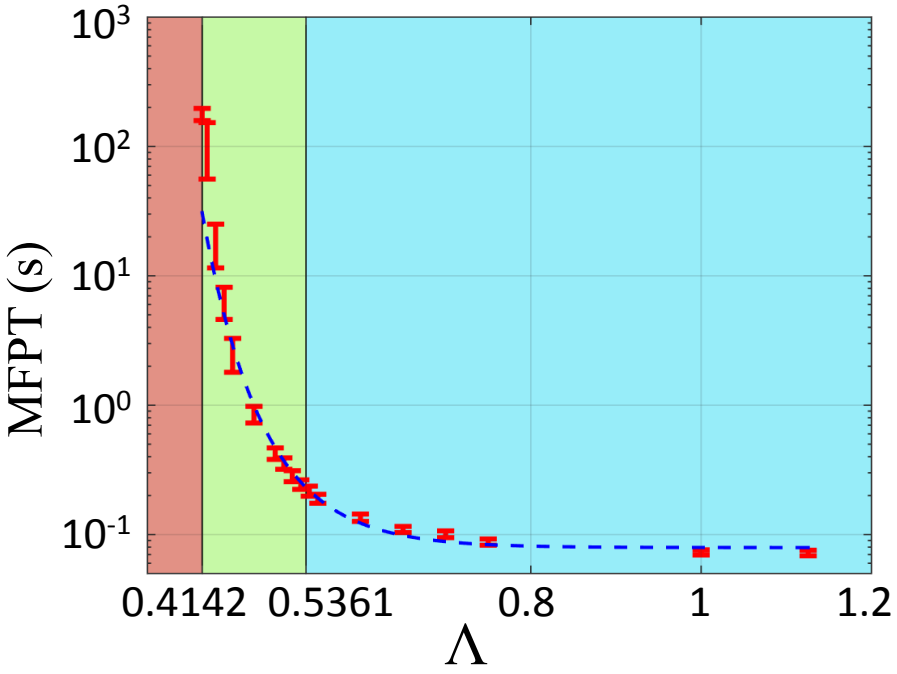

Figure 5.5: Mean first passage times (MFPT) for the N=4 digital colloid as a function of Λ. Errorbars denote 95% confidence intervals on the mean value computed from the observed distribution of first passage times. The blue dashed-line corresponds to a shifted exponential of the form $\ln(\text{MFPT}) = B_0 \exp(-B_1\Lambda) + B_2$, with parameters $\{B_0 = (2.03 \pm 0.91) \times 10^3$, $B_1 = (14.08 \pm 0.92)$, $B_2 = (-2.53 \pm 0.04)\}$ and an adjusted $R^2 = 0.97$. Best fit parameters were computed by weighted least squares regression in which each MFPT measurement is weighted in inverse proportion to its variance to confront the observed heteroskedasticity in the data due to elevated uncertainties in the low-Λ regime where bit state transitions are rare events [159]. $\Gamma = 1/\text{MFPT}$ defines the transition rate from one chiral bit state to the other.

effectively barrierless. The escape rate $\Gamma = 1/\text{MFPT}$ defines the transition rate from one bit state to the other [62] and is a critical design variable in the practical realization of digital colloids for information storage.

5.2.2 N=6 (30-state) digital colloids

Using an analogous approach, we conducted Brownian dynamics simulations of an N=6 digital colloid for $\Lambda = \{0.4142, 0.5100, 0.5275, 0.5500, 0.5750, 0.6000, 0.6500\}$, again holding the halo particle size fixed and varying the center particle diameter. There are three regimes

of Λ: (I) $(\Lambda_{\mathrm{SC}} \approx 0.4142) \leq \Lambda < (\Lambda_{\mathrm{T}} = 0.5275)$ where the digital colloid configuration is effectively locked into a particular octahedral bit state configuration, and halo particle transitions between bit states are sterically forbidden, (II) $(\Lambda_{\mathrm{T}} = 0.5275) \leq \Lambda < (\Lambda_{\mathrm{U}} = 0.7021)$ where the configuration becomes unlocked as halo particles are able to collectively transition between bit states, and (III) $\Lambda \geq (\Lambda_{\mathrm{U}} = 0.7021)$ where transitions between bit states are effectively barrierless, and the digital colloid configuration is in constant flux between states. The spherical code diameter ratio $\Lambda_{\mathrm{SC}} \approx 0.4142$ and unlocking transition threshold $\Lambda_{\mathrm{T}} = 0.5275$ were previously reported in Ref. [129] for the effective hard sphere mapping. The barrierless transition threshold $\Lambda_{\mathrm{U}} = 0.7021$ is defined as the value of Λ at which the (extrapolated) free energy barrier for bit state transitions drops to 1 $k_B T$ (cf. Figure 5.8a).

We extract from our simulations 2×10^6 microstates saved every 500 time steps for each value of Λ and compile these into a composite library $\mathcal{L}(N = 6, \Lambda = \{0.4142, 0.5100, 0.5275, 0.5500, 0.5750, 0.6000, 0.6500\})$ comprising 1.4×10^7 microstates. We extract a restricted set of 1,932 representative microstates spanning the 110 prototypical cluster architectures observed in the simulations, and apply diffusion maps employing a soft-thresholding bandwidth of $\epsilon = \exp(2)$ [77]. Using the L-method we identify a gap in the eigenvalue spectrum above λ_4 [108], prompting construction of a three-dimensional embedding into the top three non-trivial diffusion map eigenvectors (Ψ_2, Ψ_3, Ψ_4). We identify three collective variables to parameterize the intrinsic manifold of the N=6 system compared to only two for the N=4 case, reflecting the richer configurational dynamics available to the larger system. The remaining (1.4×10^7-1,932) configurations were projected into this reduced embedding via the Nyström extension.

Morphology and stability. We present in Figure 5.6 the three-dimensional diffusion map embeddings for all seven values of Λ, constructed by projecting the 2×10^6 microstates recorded from each simulation into (Ψ_2, Ψ_3, Ψ_4). We also report the associated free energy landscapes $F(\Psi_2, \Psi_3, \Psi_4)$ computed from histograms over the low-dimensional projections.

Rotating movies of these figures are provided in the supplemental information of Ref. [158].

Our diffusion map embeddings treat all halo particles as indistinguishable, collapsing together the structurally identical $(N!/\Upsilon_N) = 30$ bit states within the intrinsic manifold spanned by (Ψ_2, Ψ_3, Ψ_4). In the case of N=4 we were able to distinguish the two chiral bit states by augmenting our low-dimensional projection with the signed volume V of the parallelepiped mapped out by the halo particles. For the N=6 case, no simple order parameters are available to separate out the 30 rotationally distinguishable bit states within our low dimensional embedding. Accordingly, we do not augment our embeddings but appreciate – by virtue of the structural equivalence of all bit states – that the low-dimensional projections and free energy surfaces pertain equally to all bit states. The connectivity graph illustrating the bit states that are mutually accessible by single collective rearrangement events of the halo particles are illustrated in Figure 5.7.

To gain insight into the physical interpretation of the diffusion map variables, we project representative microstates onto the low-dimensional manifolds in Figure 5.6 and color each microstate according to the $L_{1,1}$ norm between its normalized halo particle pairwise distances matrix and that of an idealized octahedron $||\chi' - \chi'_{\text{oct}}||$ (cf. Section 5.1.2). The collective variable Ψ_2 is well-correlated with $||\chi' - \chi'_{\text{oct}}||$ indicating that it provides a measure of the octahedral character of the digital colloid architecture. The minimum value of $||\chi' - \chi'_{\text{oct}}|| = 0$ is found in the region of $(\Psi_2 \approx 0.05, \Psi_3 \approx 0.03, \Psi_4 \approx -0.03)$ where the digital colloid adopts an idealized octahedral geometry. Each of the low-dimensional manifolds in Figure 5.6 is funnel-shaped, with the narrow tip containing the transition state ensemble and wide base corresponding to the "rattling" of halo particles about a particular stable bit state. The size of the tip of the funnel increases with Λ as the increased free volume accessible to the halo particles opens access to a greater diversity of transition state configurations.

At $\Lambda = (\Lambda_{\text{SC}} \approx 0.4142)$ (Figure 5.6a,b) – corresponding to the minimum diameter ratio for which effective hard sphere halo particles can exist on the surface of the central particle without overlapping [129, 136] – the digital colloid is confined to a small set of possible

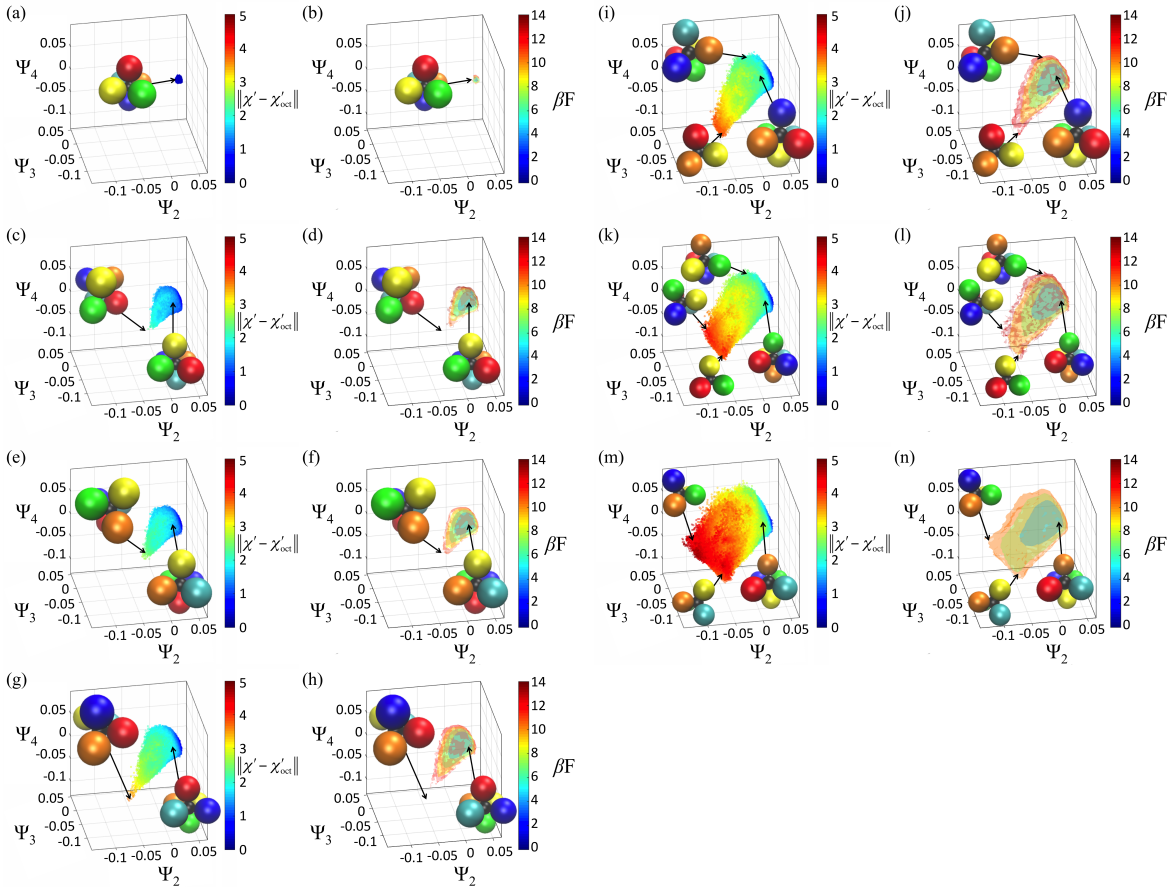

Figure 5.6: Diffusion map embeddings and free energy surfaces for the N=6 octahedral digital colloid as a function of Λ. Embeddings are constructed in the top three non-trivial eigenvectors discovered by diffusion maps corresponding to the slowest collective modes of the digital colloid dynamical rearrangements (Ψ_2, Ψ_3, Ψ_4). In each pair of panels we present on the left the low-dimensional projection of the $2{\times}10^6$ microstates harvested from the Brownian dynamics simulation performed at a particular value of Λ into the intrinsic manifold, and on the right the free energy surface over the intrinsic manifold $F(\Psi_2, \Psi_3, \Psi_4)$ computed by application of Equation 5.4 employing rectilinear histogram bins of size $[\Delta\Psi_2, \Delta\Psi_3, \Delta\Psi_4] = [0.005, 0.005, 0.005]$. (a,b) $\Lambda = 0.4142$, (c,d) $\Lambda = 0.5100$, (e,f) $\Lambda = 0.5275$, (g,h) $\Lambda = 0.5500$, (i,j) $\Lambda = 0.5750$, (k,l) $\Lambda = 0.6000$, (m,n) $\Lambda = 0.6500$. Points in the diffusion map embedding are colored by the $L_{1,1}$ norm between the normalized halo particle pairwise distances matrix of the corresponding microstate and that of an idealized octahedron $||\chi' - \chi'_{\text{oct}}||$. Isosurfaces are plotted at $\beta F = \{0, 2, 4, 6, 8, 10, 12, 14\}$, with the arbitrary zero of free energy defined by the most populated voxel of the embedding. Representative microstates have been projected over the embeddings to illustrate the halo particle configurations in each region of the intrinsic manifold. The viewing angles of the triangular prism configurations within the transition state ensemble were selected to emphasize the stacking of the two triangular layers of halo particles such that those closer to the viewer eclipse from view those that are further away.

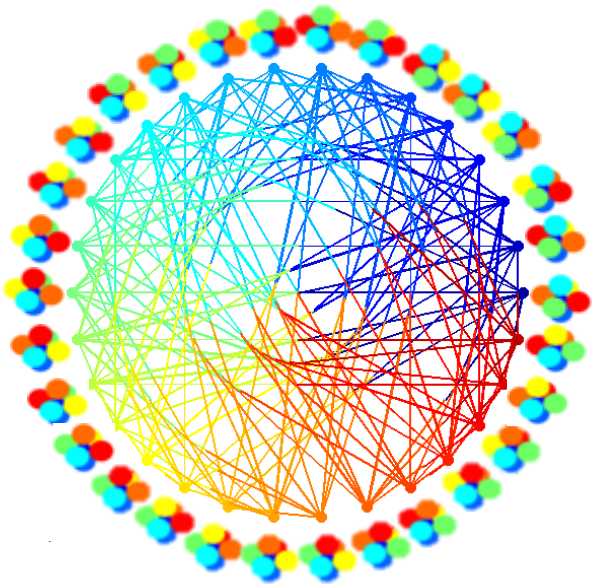

Figure 5.7: Bit state transition map for the N=6 digital colloid illustrating the 30 rotationally distinguishable bit states as nodes around the exterior of graph and structural transition events linking bit states as edges through the interior. Nodes and edges are color coded to aid in interpretation. Each bit state is able to access eight others through a single halo particle collective transition event. The diameter of the transition network is such that a maximum of three transition events are required to transition between any pair of bit states.

configurations localized around the ideal octahedron. At $(\Lambda = 0.5100) < (\Lambda_T = 0.5275)$ (Figure 5.6c,d), the digital colloid remains effectively locked in a single bit state, but the increased free volume permits the halo particles to rattle around around the ideal octahedron and fill a greater volume of the intrinsic manifold.

At the unlocking threshold of $\Lambda = (\Lambda_T = 0.5275)$ (Figure 5.6e,f), a structure very close to the triangular prism transition state between octahedral bit states emerges at $(\Psi_2 \approx -0.03, \Psi_3 \approx -0.03, \Psi_4 \approx -0.07)$ [136]. Nevertheless, bit state transitions remain sterically disfavored and – in line with Figure SI-I-3 in Ref. [129] – no transition events are observed over the course of our simulations.

For $(\Lambda = 0.5500) > (\Lambda_T = 0.5275)$ (Figure 5.6g-h), there is sufficient free volume for the halo particles to realize the triangular prism transition structure, and we observed multiple bit state transitions over the course of our calculations. The free energy surface develops

a funnel-like structure with the caged octahedral structures occupying a broad low-free energy region at the bottom of the funnel-shaped intrinsic manifold, and the triangular prism transition state occupying a small high-free energy region at the narrow end of the funnel. We define microstates as belonging to the transition state ensemble by thresholding the $L_{1,1}$ norm between the normalized halo particle pairwise distance matrix and that of the idealized triangular prism, given as $||\chi' - \chi'_{\text{prism}}|| < 1.75$. These configurations possess an average 5% deviation in the normalized pairwise distances matrix away from that of the idealized triangular prism. Productive transitions between bit states occur when the digital colloid enters the transition state and the halo particles undergo a collective rearrangement into a new rotationally distinguishable configuration (cf. Figure 5.7). The free energy barrier between the bottom of the octahedral free energy well and the transition state is $\Delta(\beta F) = (8.22 \pm 0.17)$.

At larger values of Λ (Figure 5.6i-n), the volume of the intrinsic manifold increases with the elevated free volume available to the halo particles. The transition state ensemble becomes markedly enlarged since the two planar layers of the triangular prism are able to move more freely over the center particle surface, leading to an expansion of the intrinsic manifold toward ($\Psi_2 \approx -0.10, \Psi_3 \approx 0.00, \Psi_4 \approx -0.05$) due to a greater diversity of transition structures. There is a commensurate decrease in the transition barrier height from $\Delta(\beta F) = (5.52 \pm 0.07)$ at $\Lambda = 0.5750$, to $\Delta(\beta F) = (3.99 \pm 0.06)$ at $\Lambda = 0.6000$, to $\Delta(\beta F) = (2.14 \pm 0.04)$ at $\Lambda = 0.6500$.

We report the dependence of the transition state free energy barrier as a function of Λ in Figure 5.8a. An exponential fit of the form $\Delta(\beta F) = C_0 \exp(-C_1 \Lambda)$ provides an excellent fit to the data, with best fit parameters $\{C_0 = (1.41 \pm 0.58) \times 10^4, C_1 = (13.60 \pm 0.70)\}$ and an adjusted $R^2 = 0.99$. In the next section, we will use this dependence to design of the digital colloids as information storage elements that have sufficiently low free energy barriers so as to be writable (i.e., their bit state can be changed by doing external work) but sufficiently high to be stable to thermally-activated spontaneous changes in the bit state.

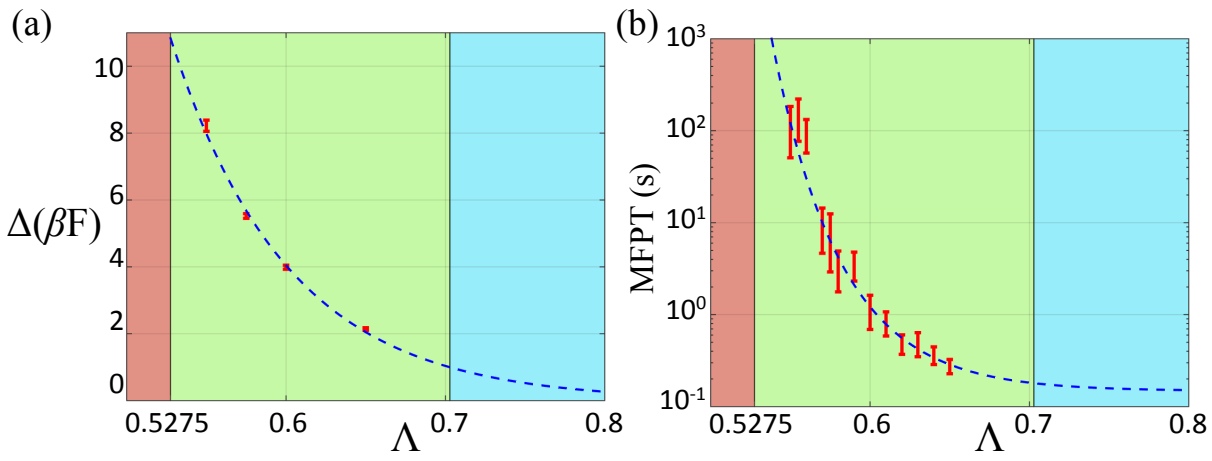

Figure 5.8: Free energy barriers for bit state transitions and mean first passage time as a function of Λ for the N=6 digital colloid. (a) Free energy barrier height $\Delta(\beta F)$ computed as the free energy difference between the global minimum of the free energy surface and the minimum free energy within the transition state region defined by the voxels containing microstates with $||\chi' - \chi'_{\text{prism}}|| < 1.75$, where χ'_{prism} is the normalized halo pairwise distances matrix for the idealized triangular prism transition state structure. This threshold identifies microstates possessing an average 5% deviation away from the normalized distance matrix for the idealized triangular prism. Error bars correspond to 95% confidence bounds computed by 10 rounds of bootstrapping. The blue dashed-line corresponds to an exponential of the form $\Delta(\beta F) = C_0 \exp(-C_1 \Lambda)$ with parameters $\{C_0 = (1.41 \pm 0.58) \times 10^4$, $C_1 = (13.60 \pm 0.70)\}$ and an adjusted $R^2 = 0.99$. Best fit parameters were computed by weighted least squares regression in which we confronted the observed heteroskedasticity in the data by weighting each free energy measurement in inverse proportion to its variance [159]. The colored regions distinguish the different regimes of Λ: $(\Lambda_{\text{SC}} \approx 0.4142) \leq \Lambda < (\Lambda_{\text{T}} = 0.5275)$ (red, locked), $(\Lambda_{\text{T}} = 0.5275) \leq \Lambda < (\Lambda_{\text{U}} = 0.7021)$ (green, unlocked), and $\Lambda \geq (\Lambda_{\text{U}} = 0.7021)$ (blue, barrierless transitions).$\Lambda_{\text{T}} = 0.5275$ defines the unlocking transition at which there is sufficient free volume for the halo particles to transition between bit states through the square planar transition state. $\Lambda_{\text{U}} = 0.7021$ defines the (extrapolated) transition to effectively unconstrained barrierless transitions between bit states where $\Delta(\beta F) = 1$. (b) Mean first passage time computed as the average dwell time within a bit state before transitioning to a new bit state by a collective structural rearrangement of the halo particles. Errorbars denote 95% confidence intervals on the mean value computed from the observed distribution of first passage times. The blue dashed-line corresponds to a shifted exponential of the form $\ln(\text{MFPT}) = B_0 \exp(-B_1 \Lambda) + B_2$, with parameters $\{B_0 = (2.30 \pm 0.16) \times 10^6$, $B_1 = (23.17 \pm 0.12)$, $B_2 = (-1.91 \pm 0.08)\}$ and an adjusted $R^2 = 0.93$ Best fit parameters were computed by weighted least squares regression in which each MFPT measurement is weighted in inverse proportion to its variance [159]. $\Gamma = 1/\text{MFPT}$ is the escape rate from any particular bit state to any one of eight other rotationally distinguishable bit states accessible by a single halo particle rearrangement event (Figure 5.7).

Kinetics. We present in Figure 5.8b the MFPT as a function of Λ. MFPT calculations were conducted for $\Lambda = \{0.5480, 0.5490, 0.5500, 0.5550, 0.5600, 0.5700, 0.5750, 0.5800, 0.5900, 0.6000, 0.6100, 0.6200, 0.6300, 0.6400, 0.6500\}$. The MFPT corresponds to the mean residence time of the digital colloid within a bit state before it makes a transition to one of the eight other bit states accessible by a single collective rearrangement of the halo particles (Figure S1 in the ESI). To eliminate artificial depression of the MFPT due to recrossing events, we define the core region of a bit state to be that region of the intrinsic manifold containing configurations possessing a halo particle adjacency matrix equivalent to that of the ideal octahedron. A transition is defined when the digital colloid adjacency matrix departs from the octahedral architecture corresponding to one rotationally distinguishable bit state then reforms the octahedral adjacency matrix in different bit state. An illustration of a productive transition event for $\Lambda = 0.5750$ is illustrated in Movie S3 of the ESI, where we simultaneously visualize the digital colloid configuration, follow its location on the low dimensional manifold, and map the transition between a pair of the 30 rotationally distinguishable bit states.

A shifted exponential of the form $\ln(\text{MFPT}) = B_0 \exp(-B_1 \Lambda) + B_2$ provides a good fit to the data, with best fit parameters $\{B_0 = (2.30 \pm 0.16) \times 10^6,\ B_1 = (23.17 \pm 0.12),\ B_2 = (-1.91 \pm 0.08)\}$ and an adjusted $R^2 = 0.93$. In the effectively locked region $\Lambda < (\Lambda_{\text{T}} = 0.5275)$ the MFPT is undefined, before dropping steeply beyond the unlocking threshold and attaining an approximate plateau at $\Lambda > (\Lambda_{\text{U}} = 0.7021)$ where transitions become effectively barrierless. The escape rate $\Gamma = 1/\text{MFPT}$ quantifies the volatility of a digital colloid memory storage element due to thermally-driven bit state flips. In the next section, we will combine this design variable with the transition free energy barrier to design N=6 digital colloid memory elements.

5.2.3 Rational design of N=6 digital colloid memory storage elements

We now proceed to use the calculated dependencies of the transition barrier height $\Delta(\beta F)$ and escape rate Γ on Λ to rationally design a N=6 digital colloid with desired memory volatility and/or actuation free energy. In Figure 5.9 we present a parametric plot of the escape rate $\Gamma = 1/\text{MFPT}$ against the transition barrier height $\Delta(\beta F)$ for the four diameter ratios at which bit state transitions were observed $\Lambda = \{0.5500, 0.5750, 0.6000, 0.6500\}$. We may interpret the transition barrier height as the reversible work required to actuate a halo particle rearrangement and intentionally write a new bit state into the digital colloid. The escape rate can be conceived as the rate at which errors are introduced due to thermally-activated spontaneous bit state transitions. An ideal storage medium would be both non-volatile and cheap to address, implying a low write free energy and a low error rate. Since the transition barrier height controls both of these properties, they are competing design constraints and our design objective becomes to identify the value of Λ that minimizes the write free energy while maintaining the error rate below a user-specified tolerance. As an illustrative example, we consider the storage of a short text block for the period of one hour, and illustrate the tradeoff between the expected error rate and write free energy. Our analysis indicates that relatively large transition barriers are required to preserve data integrity over any significant time period. Determining the tradeoff between volatility and ease of writing will depend largely on the specifics of the system, but this approach can help guide the design process by imposing the engineering requirements of the write element and intended storage duration.

5.3 Conclusions

We show how to use low-dimensional embeddings to characterize the stability and dynamical transition pathways for digital colloids. By applying diffusion maps to simulation-generated

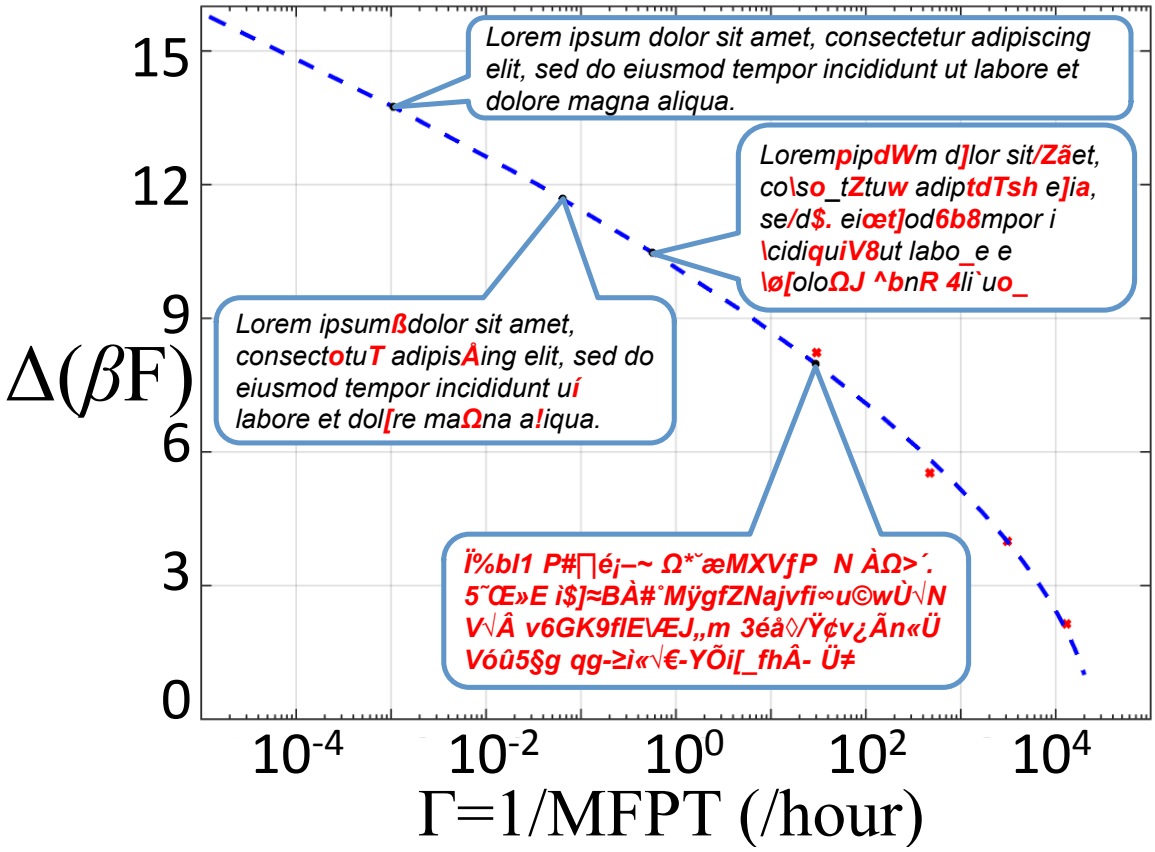

Figure 5.9: Rational design of a N=6 digital colloid with tailored write free energy and memory volatility. Red points correspond to the calculated transition barrier heights $\Delta(\beta F)$ and transition rates $\Gamma = 1/\text{MFPT}$ for the four N=6 digital colloid architectures with $\Lambda = \{0.5500, 0.5750, 0.6000, 0.6500\}$. The dashed blue line is a parametric fit of the best fit shifted exponential for the MFPT and the best fit exponential for $\Delta(\beta F)$ (cf. Figure 5.8) constructed by eliminating Λ to obtain an expression for $\Delta(\beta F)$ as a function of Γ. The ratio of the coefficients B_1 and C_1 of Λ in the two best fit exponentials controls the nonlinearity of the parametric fit. At a ratio of unity, the parametric fit corresponds to Arrhenius behavior and the dashed blue line would appear a straight line in the semi-logarithmic axes. The actual ratio is $B_1/C_1 = (1.70 \pm 0.09)$ leading to non-Arrhenius behavior and the observed non-linearity of the dashed blue curve. $\Delta(\beta F)$ is the reversible work required to actuate a halo particle rearrangement and write a new bit state into the digital colloid. Γ is the expected rate at which errors are introduced due to thermally-activated bit state transitions. The lower the write free energy, the higher the error rate. The design problem is to minimize the work required to write to the digital colloid elements while maintaining a the error rate above a particular error tolerance threshold. As a simple example, the overlaid text boxes illustrate the information storage fidelity of a short text block over a one hour duration. A system of 246 N=6 digital colloids would be required to encode this text using two digital colloids per 8-bit ASCII character. Red text is illustrative of the expected number of errors due to thermally-activated bit state transitions at the end of one hour of storage.

trajectories of the digital colloid dynamics, we discover a nonlinear projections of the digital colloid dynamics into low-dimensional embeddings. These projections of the dynamics into a low-dimensional space reveal the metastable bit states and transition pathways between them. The free energy surfaces supported by these low-dimensional embeddings quantify the stability of the bit states and height of the transition barriers for bit state interconversions as a measure of the reversible work required to write a new bit state into the digital colloid. The low-dimensional embeddings also reveal the diversity of morphologies within the metastable bit state minima and transition state ensemble, and a means to robustly identify transitions between bit states. Mean first passage times calculated from our simulations provide a measure of the average dwell time within a bit state, and a measure of memory volatility and expected rates of memory degradation due to thermally-activated bit state transitions.

We apply our method to the N=4 and N=6 digital colloids capable of storing 0.125 bytes and 0.613 bytes, respectively. Using our calculated barrier heights and escape rates for the N=6 system, we calculate the tradeoff between the reversible work required to write a bit state change and the memory degradation rate due to thermal fluctuations. The results of this calculation guide the rational design of the relative halo and central particle diameters for a memory storage application.

The double-exponential dependence of mean first passage times on Λ shows that rearrangement kinetics of digital colloids are extremely sensitive to Λ near the locking transition. This fact highlights opportunities for designing digital colloids that can "lock" and "unlock" in response to relatively small changes in the central particle size, and also provides guidelines for manufacturing digital colloids that satisfy long-term data storage requirements. Examples of N=4 digital colloids have been realized by Grier, Pine and coworkers using holographic optical tweezers [129], but it remains a challenge to produce larger clusters and fabricate them at scale. Based on the findings of this work, we anticipate next steps for manufacturing bulk quantities of digital colloids will depend on controlling the monodispersity of central particles and developing mechanisms for shrinking and swelling the central particles

controllably. Moreover, robust and scalable methods to read, store, and write information to the colloids must be developed before this can be used as a practical information storage substrate. Techniques based on DNA functionalization [160], FRET barcoding [133], and swellable central particles [161] have been suggested, and this remains an area of active research. We anticipate that the mutually beneficial feedback between simulation, machine learning-enabled data analysis, and advanced experimental synthesis and imaging techniques will improve our understanding and control of this novel and potentially ultra-high capacity information storage medium.

Chapter 6

Accelerating diffusion maps for out-of-sample embedding

Practical application of diffusion maps typically involves two distinct but related operations: (i) analysis of a high-dimensional dataset in $\mathcal{R}^K$ to discover and define a low-dimensional projection in $\mathcal{R}^k$ where $k < K$ and (ii) projection of new out-of-sample points into the low-dimensional manifold. Discovery of the manifold requires calculation of pairwise distances between all data points to construct a Markov matrix over the high-dimensional data, and subsequent diagonalization of this matrix to perform a spectral decomposition of the corresponding random walk [76, 162, 163]. This eigendecomposition yields an ordered series of increasingly faster relaxing modes of the random walk, and the identification of a gap in the eigenvalue spectrum of implied time scales informs the effective dimensionality of the underlying low-dimensional manifold and collective coordinates with which to parametrize it [56, 59, 60, 75, 76, 164]. Exact calculation of all pairwise distances is of complexity $\mathcal{O}(N^2)$, although it is possible to exploit the exponential decay in the hopping probabilities to threshold these matrix dements to zero and to avoid calculation of all distance pairs using clustering or divide and conquer approaches [165]. Diagonalization of the N-by-N matrix has complexity $\mathcal{O}(N^3)$ [166], but the typically sparse nature of the Markov matrix admits sparse Lanczos algorithms that reduce the complexity to $\mathcal{O}(N^2 + NE_{nz})$, where E_{nz} is the number of non-zero matrix elements [163, 167, 168]. Calculation of only the top $l \ll N$ eigen-

This chapter is based on work to appear in:

Andrew W. Long and Andrew L. Ferguson, "Landmark diffusion maps (L-dMaps): Accelerated manifold learning out-of-sample extension", *Applied and Computational Harmonic Analysis* (in press, 2017).

vectors can further reduce the cost to $\mathcal{O}(lN + lE_{nz})$ [163, 167]. The overall complexity of the discovery of the nonlinear low-dimensional projection is then $\mathcal{O}(N^2 + lN + lE_{nz}) \sim \mathcal{O}(N^2)$.

Projection of out-of-sample points into the nonlinear manifold is complicated by the unavailability of an explicit transformation matrix for the low-dimensional projection [56]. Naïvely, one may augment the original data with the N_{new} samples and diagonalize the augmented system, which is an exact but exceedingly expensive operation to perform for each new sample. Accordingly, a number of approximate interpolation techniques have been proposed [82], including principal component analysis-based approaches [169], Laplacian pyramids [170], and the Nyström extension [78–80]. The Nyström extension is perhaps the simplest and most widely used and scales as $\mathcal{O}(N)$, requiring the calculation of pairwise distances with the N points constituting the low-dimensional manifold. Linear scaling with the size of the original dataset can be prohibitively costly for online dimensionality reduction applications to high-velocity and/or high-volume streaming data, where fast and efficient embedding of new data points is of paramount importance. For example, in online threat or anomaly detection where excursions of the system into unfavorable regions of the nonlinear manifold must be quickly recognized in order to take corrective action [171], in robotic motion planning where movements are generated based on localized paths through a low-dimensional manifold to maintain kinematic admissibility while navigating obstacles [172, 173], and in parallel replica dynamics [174] or forward flux sampling simulations [175, 176] of biomolecular folding where departures from a particular region of the manifold can be used to robustly and rapidly identify conformational changes in any one of the simulation replicas and permit responsive reinitialization of the replicas to make maximally efficient use of computational resources.

To reduce the computational complexity of the application of diffusion maps to streaming data we propose a controlled approximation based on the identification of a subset of $M \ll N$ "landmark" data points with which to construct the original manifold and embed new data. Reducing the number of points participating in these operations can offer substantial

computational savings, and the degree of approximation can be controlled and tuned by the number and location of the landmarks. Our approach is inspired by and analogous to the landmark Isomap (L-Isomap) adaptation of the original Isomap nonlinear manifold learning approach due to Tenenbaum, de Silva, and Langford [53, 177], which has demonstrated robust landscape recovery and computational savings considering small numbers of randomly selected landmark points. Silva *et al.* subsequently introduced a systematic means to select landmarks based on L_1-regularized minimization of a least-squares objective function [178]. As observed by de Silva and Tenenbaum [177], the underlying principle of this approach is analogous to global positioning using local distances, whereby a point can be uniquely located within the manifold given sufficient distance measurements to points distributed over its surface [179]. In analogy with this work, we term our approach the landmark diffusion maps (L-dMaps).

It is the purpose of this chapter to introduce L-dMaps, in which the selection of $M \ll N$ landmark points reduces the computational complexity of the out-of-sample projection of a new data point from $\mathcal{O}(N)$ to $\mathcal{O}(M)$ offering speedups $S \propto N/M$, which can be a substantial factor when the landmarks constitute a small fraction of the data points constituting the manifold. The use of landmarks also substantially reduces the memory requirements, leading to savings in both CPU and RAM requirements that enable applications of diffusion maps to higher volume and velocity streaming data than is currently possible.

In Section 6.1, we introduce the computational and algorithmic details of our L-dMaps approach along with theoretical error bounds on its fidelity relative to diffusion maps applied to the full dataset. In Section 6.2, we demonstrate and analyze the accuracy and performance of L-dMaps on three test systems – the Swiss roll, molecular simulations of a $C_{24}H_{50}$ polymer chain, and biomolecular simulations of alanine dipeptide – in which we report up to 50-fold speedups in out-of-sample extension with less than 4% errors in manifold reconstruction fidelity relative to those calculated by dMaps applied to the full dataset. In Section 6.3 we close with an appraisal of our approach and its applications, and an outlook for future work.

6.1 Materials and methods

We have previously described diffusion map dimensionality reduction and Nyström extension in Chapter 2. Now we introduce landmark diffusion maps (L-dMaps) presenting two algorithms for systematic identification of landmark points – one fully automated spanning tree approach, and one based on k-medoids that can be tuned to achieve specific error tolerances – and the subsequent use of these landmarks to perform nonlinear manifold discovery and Nyström projection of new data. Next, we develop theoretical estimates of L-dMaps error bounds based on a first-order perturbation expansion in the errors introduced by the use of landmarks compared to consideration of the full dataset. Finally, we detail the three datasets upon which we demonstrate and validate our approach: the Swiss roll, molecular simulations of a $C_{24}H_{50}$ polymer chain, and biomolecular simulations of alanine dipeptide.

6.1.1 Landmark diffusion maps (L-dMaps)

The application of diffusion maps to the online embedding of streaming data is limited by the $\mathcal{O}(N)$ computational complexity of the out-of-sample extension that requires the calculation of pairwise distances of each new data point with the N points defining the embedding. Here we propose landmark diffusion maps (L-dMaps) that employs a subset of $M \ll N$ points providing adequate support for discovery and construction of the low-dimensional embedding to reduce this complexity to $\mathcal{O}(M)$. In this way, we trade-off errors in the embedding of new data with projection speedups that scale in inverse proportion to the number of landmarks M. We quantify the reconstruction error introduced by the landmarking procedure, and demonstrate that these errors can be made arbitrarily small by selection of sufficiently many landmark points. The use of landmarks has previously been demonstrated in the L-Isomap variant of the Isomap dimensionality reduction technique to offer substantial gains in computational efficiency [177].

Landmark selection

Landmarking can be conceived as a form of lossy compression that represents localized groups of points in the high-dimensional feature space by attributing them to a central representative landmark point. Provided the landmarks are sufficiently well distributed over the intrinsic manifold mapped out by the data in the high-dimensional space, then the pairwise distances between landmarks to a new out-of-sample data point provide sufficient distance constraints to accurately embed the new point onto the manifold [177, 179]. The original L-Isomap algorithm proposed landmarks be selected randomly [177], and a subsequent sophistication by Silva *et al.* proposed a selection procedure based on L_1-regularized minimization of a least-squares objective function [178]. In this work, we propose two efficient and systematic approaches to selection: a pruned spanning tree (PST) approach that offers an automated means to select landmarks, and a k-medoids approach that allows the user to tune the number of landmarks to trade-off speed and embedding fidelity to achieve a particular error tolerance. Both approaches require pre-computation of the N-by-N pairwise distances matrix, making them expensive for large datasets [178]. However, it is the primary goal of this work to select good landmarks for the rapid and efficient embedding of streaming data into an existing manifold, so the high one-time overhead associated with their selection is of secondary importance relative to optimal landmark identification for subsequent online performance.

Pruned spanning tree (PST) landmark selection. The square root of the soft-thresholding bandwidth $\sqrt{\epsilon}$ employed by diffusion maps defines the characteristic step size of the random walk over the high dimensional data (Equation 2.2) [55]. In order to reliably construct a low-dimensional embedding, the graph formed by applying this neighborhood threshold to the pairwise distance matrix must be fully connected to assure that no point is unreachable from any other (i.e., the Markov matrix $\mathbf{M}$ is irreducible) [56]. This assures that a single connected random walk can be formed over the data, and that the diffusion

map will discover a single unified intrinsic manifold as opposed to a series of disconnected manifolds each containing locally connected subsets of the data. This connectivity criterion imposes two requirements on the selection of landmarks $\{\vec{z}_i\}_{i=1}^{M} \in \mathcal{R}^K$ as a subset of the data points $\{\vec{x}_i\}_{i=1}^{N} \in \mathcal{R}^K$: (i) all N points are within a $\sqrt{\epsilon}$ neighborhood of (i.e., covered by) a landmark,

$$\forall \vec{x}_i, \exists \vec{z}_j \mid ||\vec{x}_i - \vec{z}_j|| \leq \sqrt{\epsilon}, \tag{6.1}$$

and (ii) the graph of pairwise distances over the landmarks is fully connected, with each landmark point within a distance of $\sqrt{\epsilon}$ of at least one other,

$$\forall \vec{z}_i, \exists \vec{z}_{j \neq i} \mid ||\vec{z}_i - \vec{z}_j|| \leq \sqrt{\epsilon}. \tag{6.2}$$

In practice, a threshold of a few multiples of $\sqrt{\epsilon}$ may be sufficient to maintain coverage and connectivity.

These coverage and connectivity conditions motivate a landmark selection procedure based on spanning trees of the pairwise distances matrix $\mathbf{d}$ that naturally enforces both of these constraints and identifies landmarks that ensure out-of-sample points residing within the manifold can be embedded within a neighborhood $\sqrt{\epsilon}$ of a landmark point. Residing within the characteristic step size of the random walk, this condition is expected to produce accurate interpolative out-of-sample extensions using the Nyström extension. As described above, extrapolative extensions are expected to perform poorly for distances greater than $\sqrt{\epsilon}$ [56, 82, 83]. First, we form the binary adjacency matrix $\mathbf{G}$ by hard-thresholding the N-by-N pairwise distances matrix $\mathbf{d}$ (Equation 2.1),

$$G_{ij} = \begin{cases} 1 & \text{if } d_{ij} \leq \sqrt{\epsilon}, i \neq j \\ 0 & \text{otherwise} \end{cases}. \tag{6.3}$$

The binary adjacency matrix defines a new graph in which two data points $\vec{x}_i$ and $\vec{x}_j$ are

connected if and only if $G_{ij} = 1$. Next, we seek the minimal subset of edges that contains no cycles and connects all nodes in the graph, which is equivalent to identifying a spanning tree representation of the graph $\mathbf{T}$ that may be determined in many ways [180]. We elect to use Prim's algorithm [181], which randomly selects a root node then recursively adds edges between tree nodes and unassigned nodes until all nodes are incorporated into the tree. As the edge weights of $\mathbf{G}$ are either 0 or 1, Prim's algorithm at each step randomly selects an edge from $\mathbf{G}$ connecting an unassigned node to a node in $\mathbf{T}$. By only creating new connections between tree nodes and non-tree nodes, this method guarantees that $\mathbf{T}$ is cycle-free and, provided that $\mathbf{G}$ is connected, is a spanning tree of $\mathbf{G}$. Finally, we recognize that each leaf node lies within $\sqrt{\epsilon}$ of their parent, meaning that all leaves of the tree can be pruned, with the remaining nodes comprising a pruned spanning tree (PST) defining a set of landmarks $\{\vec{z}_i\}$ satisfying both the covering (Equation 6.1) and connectivity (Equation 6.2) conditions. We summarize PST landmark identification procedure in Algorithm 1.

Algorithm 1: PST landmark selection

Input: $\{\vec{x}_i\}_{i=1}^N$, $\mathbf{G} = (\mathbf{V_G}, \mathbf{E_G})$
Initialize tree $\mathbf{T} = (\mathbf{V_T}, \mathbf{E_T})$ by selecting a random node i, $\mathbf{V_T} = \{i\}, \mathbf{E_T} = \emptyset$
Construct the spanning tree:
while $\mathbf{V_T} \neq \mathbf{V_G}$ do
  Gather set of all edges $\mathbf{E_N}$ between tree and unassigned nodes:
    $\mathbf{E_N} = \{uv : u \in \mathbf{V_T}, v \in \mathbf{V_G} \backslash \mathbf{V_T}, uv \in \mathbf{E_G}\}$
  Randomly add edge $mn \in \mathbf{E_N}$ to $\mathbf{T}$:
    $\mathbf{V_T} = \mathbf{V_T} \cup \{n\}, \mathbf{E_T} = \mathbf{E_T} \cup \{mn\}$
end while
Identify leaf nodes $\mathbf{V_L}$ of $\mathbf{T}$ (nodes of degree 1 in $\mathbf{T}$):
  $\mathbf{V_L} = \{u : u \in \mathbf{V_T}, \deg(u) = 1\}$
Select all non-leaf nodes:
  $\{\vec{z}\} = \{\vec{x}_i : i \in \mathbf{V_T} \backslash \mathbf{V_L}\}$
Output: $\{\vec{z}\} \equiv$ landmarks

K-medoid landmark selection. Growing and pruning a spanning tree offers an automated means to identify landmarks that ensure any out-of-sample point can be interpolatively embedded within a $\sqrt{\epsilon}$ neighborhood of a landmark. This procedure is expected to

offer good reconstruction accuracy, but the error tolerance is not directly controlled by the user. Accordingly, we introduce a second approach to landmark selection that allows the user to tune the number of landmark points to trade-off computational efficiency against embedding accuracy in the Nyström extension to achieve a particular runtime target or error tolerance relative to the use of all N data points. Specifically, we partition the data into a set of M distinct clusters, and define landmarks within each of these clusters to achieve pseudo-optimal coverage of the intrinsic manifold for a particular number of landmark points. Numerous partitioning techniques are available, including spectral clustering [182], affinity propagation [183], and agglomerative hierarchical clustering [184]. We use the well-known k-medoids algorithm, using Voronoi iteration to update and select medoid points [185]. Compared to k-means clustering, k-medoids possesses the useful attribute that cluster prototypes are selected as medoids within the data points constituting the cluster as opposed to as linear combinations defining the cluster mean. We select the initial set of landmarks randomly from the pool of all samples, although we note that alternate seeding methods exist such as k-means++ [186]. We summarize the k-medoids landmark selection in Algorithm 2.

Algorithm 2: K-medoid landmark selection

Input: $\{\vec{x}_i\}_{i=1}^N$, M, maxItr
Randomly select initial landmarks $\{\vec{z}_j^{(0)}\}_{j=1}^M \subseteq \{\vec{x}_i\}_{i=1}^N$
t = 0
do
  Assign points to clusters:
    $S_i^{(t)} = \{\vec{x}_j : ||\vec{x}_j - \vec{z}_i^{(t)}|| \leq ||\vec{x}_j - \vec{z}_m^{(t)}|| \text{ for all } m = 1, \ldots, M\}$
  Update cluster medoid:
    $\vec{z}_i^{(t+1)} = \arg\min_{\vec{x}_m \in S_i^{(t)}} \sum_{\vec{x}_j \in S_i^{(t)}} ||\vec{x}_m - \vec{x}_j||$
  t = t+1
while $\{\vec{z}^{(t)}\} \neq \{\vec{z}^{(t-1)}\})$ and (t < maxItr)
Output: $\{\vec{z}^{(t)}\} \equiv$ landmarks

Landmark intrinsic manifold discovery

The primary purpose of landmark identification is to define an ensemble of M supports for the efficient out-of-sample extension projection of streaming data. The nonlinear manifold can be defined by applying diffusion maps to all N data points. The expensive $\mathcal{O}(N^2)$ calculation of the pairwise distances matrix $\mathbf{d}$ has already been performed for the purposes of landmark identification, leaving only a relatively cheap $\mathcal{O}(lN + lE_{nz})$ calculation of the top l eigenvectors where E_{nz} is the number of non-zero elements in the matrix [163, 167, 168]. Nevertheless, having identified these landmarks, additional computational savings may be achieved by constructing the manifold using only the M landmarks.

Naïve application of diffusion maps to the M landmarks will yield a poor reconstruction of the original manifold since these landmark points do not preserve the density distribution of the N original points over the high-dimensional feature space. A previous study proposed a means to efficiently apply diffusion maps to datasets containing multiple copies of each point in the context of recovering nonlinear manifolds from biased data [83]. We adapt this approach to apply diffusion maps to only the landmark points while approximately maintaining the density distribution of the full dataset. Given a set of landmark points $\{\vec{z}_i\}_{i=1}^{M}$ we may characterize the local density of points in the high-dimensional space around each landmark by counting the number of data points residing within the Voronoi volume of each landmark point $\vec{z}_i$ defined by the set,

$$S_i = \{\vec{x}_j : ||\vec{x}_j - \vec{z}_i|| \leq ||\vec{x}_j - \vec{z}_m|| \text{ for all } m = 1, \ldots, M\}. \tag{6.4}$$

Following Ref. 83, we now apply diffusion maps to the M landmark points each weighted by a multiplicity $c_i = |S_i|$. Mathematically, this corresponds to solving the M-by-M eigenvalue problem analogous to that in Equation 2.6 of Section 2.1,

$$\tilde{\mathbf{M}}\tilde{\mathbf{C}}\tilde{\mathbf{\Psi}} = \tilde{\mathbf{\Psi}}\tilde{\mathbf{\Lambda}}, \tag{6.5}$$

where $\tilde{\mathbf{M}} = \tilde{\mathbf{D}}^{-1}\tilde{\mathbf{A}}$, the elements of $\tilde{\mathbf{A}}$ are given by,

$$\tilde{A}_{ij} = \exp\left(-\frac{||\vec{z}_i - \vec{z}_j||^2}{2\epsilon}\right), \tag{6.6}$$

defining the unnormalized hopping probability between landmark points $\vec{z}_i$ and $\vec{z}_j$, $\tilde{\mathbf{C}}$ is a diagonal matrix containing the multiplicity of each landmark point,

$$\tilde{C}_{ii} = c_i = |S_i|, \tag{6.7}$$

$\tilde{\mathbf{D}}$ is a diagonal matrix with elements,

$$\tilde{D}_{ii} = \sum_{j=1}^{M} \tilde{A}_{ij}\tilde{C}_{jj}, \tag{6.8}$$

and $\tilde{\mathbf{\Lambda}}$ is a diagonal matrix holding the eigenvalues $\{\tilde{\lambda}_i\}_{i=1}^M$ in non-ascending order, and $\tilde{\mathbf{\Psi}} = \{\vec{\tilde{\psi}}_i\}_{i=1}^M$ is the matrix of right column eigenvectors. It can be shown that by enforcing the normalization condition $\tilde{\mathbf{C}}\vec{\tilde{\psi}}_i \cdot \vec{\tilde{\psi}}_i = 1$ on the eigenvectors, that the diffusion map embedding,

$$\vec{z}_i \to \{\vec{\tilde{\psi}}_2(i), \vec{\tilde{\psi}}_3(i), \ldots, \vec{\tilde{\psi}}_{k+1}(i)\}, \tag{6.9}$$

is precisely that which would be obtained from applying diffusion maps to an ensemble of points in which each landmark point $\vec{z}_i$ is replicated c_i times, and the M non-zero eigenvalues $\{\lambda_i\}_{i=1}^M$ are identical to $\{\tilde{\lambda}_i\}_{i=1}^M$ [83].

The net result of this procedure is that we can define the intrinsic manifold by considering only the landmark points and diagonalizing a M-by-M matrix as opposed to a N-by-N matrix with an attendant reduction in computational complexity from $\mathcal{O}(lN + lE_{nz})$ to $\mathcal{O}(lM + lE_{nz})$. The diffusion mapping in Equation 6.9 defines a reduced M-point intrinsic manifold that can be considered a lossy compression of the complete N-point manifold, and which can be stored in a smaller memory footprint [177]. For large datasets, the compu-

tational and memory savings associated with calculation and storage of this manifold can be significant. Although not necessary, if desired the $(N - M)$ non-landmark points can be projected into the intrinsic manifold using the landmark Nyström extension described in the next section. This is also precisely the procedure that will be used to perform out-of-sample embeddings of new data points not contained within the original N data points.

Geometrically, the approximation we make in formulating the reduced eigenvalue problem is that all points within the Voronoi cell of a landmark point are equivalent to the landmark point itself, weighting each landmark point according to the number of points inside its Voronoi volume. This is a good assumption provided that the variation between the points within each Voronoi volume is small relative to the variation over the rest of the high-dimensional space, and becomes exact in the limit that every point is treated as a landmark (i.e., $M = N$). In Section 6.1.2 we place theoretical bounds on the errors introduced by this approximation in the nonlinear projection of new out-of-sample points onto the intrinsic manifold relative to that which would have been computed by explicitly considering all N points using the original diffusion map.

Landmark Nyström extension

The heart of our L-dMaps approach is the nonlinear projection of new out-of-sample points using the reduced manifold defined by the M landmark points as opposed to the full N-point manifold. Nyström embeddings of new points $\vec{x}_{\text{new}}$ over the reduced manifold proceed in an analogous manner to that detailed in Section 2.1.1, but now considering only the landmark points. Specifically, we compute the distance of the new point to all landmarks $\{\vec{z}_j\}_{j=1}^{M}$ to compute elements $\tilde{A}_{\text{new},j} = \exp\left(-\frac{||\vec{x}_{\text{new}} - \vec{z}_j||^2}{2\epsilon}\right)$ with which to augment the $\tilde{\mathbf{M}}$ matrix with an additional row with elements $\tilde{M}_{\text{new},j} = \left(\sum_{j=1}^{M} \tilde{A}_{\text{new},j}\tilde{C}_{jj}\right)^{-1} \tilde{A}_{\text{new},j}$. The projected coordinates of the new point onto the k-dimensional reduced intrinsic manifold defined by

the top $l = 2 \ldots (k+1)$ non-trivial eigenvectors of $\tilde{\mathbf{M}}$ is,

$$\vec{\tilde{\psi}}_l(\text{new}) = \frac{1}{\tilde{\lambda}_l} \sum_{j=1}^{M} \tilde{M}_{\text{new},j} \tilde{C}_{jj} \vec{\tilde{\psi}}_l(j). \tag{6.10}$$

This landmark form of the Nyström extension reduces the computational complexity from $\mathcal{O}(N)$ to $\mathcal{O}(M)$ by reducing both the number of distance computations and the size of the matrix-vector multiplication. The attendant runtime speedup $S \propto N/M$ can be substantial for $M \ll N$, offering accelerations to permit the application of diffusion map out-of-sample extension to higher volume and higher velocity streaming data than is currently possible.

6.1.2 Landmark error estimation

The diffusion mapping in Equation 6.9 defines a reduced intrinsic manifold comprising the $M \ll N$ landmark points that we subsequently use to perform efficient landmark Nyström projections of out-of-sample data using Equation 6.10. As detailed in Section 6.1.1 the k leading eigenvectors $\{\vec{\psi}_i'\}_{i=2}^{k+1}$ defining the intrinsic manifold come from the solution of a N-by-N eigenvalue problem in which each landmark point is weighted by the number of points falling in its Voronoi volume $c_i = |S_i|$, that we solve efficiently and exactly by mapping it to the reduced M-by-M eigenvalue problem in Equation 6.5 [83]. The approximation we make in formulating this eigenvalue problem is to consider each point in the Voroni volume of each landmark point as identical to the landmark itself. Were we not to make the landmark approximation, we would be forced to solve a different N-by-N eigenvalue problem explicitly treating all N points using the original diffusion map with k leading eigenvectors $\{\vec{\psi}_i\}_{i=2}^{k+1}$. In using $M \ll N$ landmarks we massively accelerate the out-of-sample embedding of new points, but the penalty we pay is that the resulting intrinsic manifold we discover is not exactly equivalent to that which would be discovered by the original diffusion map in the limit $M \to N$. In this section we estimate the errors in manifold reconstruction introduced by the landmarking procedure by developing approximate analytical expressions for the

discrepancy between the landmark $\{\vec{\psi}'_i\}_{i=2}^{k+1}$ and true $\{\vec{\psi}_i\}_{i=2}^{k+1}$ eigenvectors parameterizing the intrinsic manifold.

We formulate our approximate landmark eigenvalue problem by collapsing the set of points $S_k = \{\vec{x}_j : ||\vec{x}_j - \vec{z}_k|| \leq ||\vec{x}_j - \vec{z}_m|| \text{ for all } m = 1, \ldots, M\}$ within the Voronoi volume of each landmark point $\{\vec{z}_k\}_{k=1}^{M}$ onto the landmark itself. This amounts to perturbing each data point $\vec{x}_i$ in the high dimensional space by a vector $\vec{\Delta}_i = \vec{z}_\gamma - \vec{x}_i$ where $\vec{z}_\gamma$ is the landmark point within the Voronoi volume of which $\vec{x}_i$ falls. The elements of the N-by-N pairwise distance matrix between are correspondingly perturbed from $d_{ij} = ||\vec{x}_i - \vec{x}_j||$ to $d'_{ij} = ||(\vec{x}_i + \vec{\Delta}_i) - (\vec{x}_j + \vec{\Delta}_j)||$. This introduces perturbations $\delta_{ij} = d'_{ij} - d_{ij}$ into the pairwise distances, the precise form of which depends on the choice of distance metric $||.||$. By propagating these differences through the eigenvalue problem formulated by the original diffusion map over the true (unshifted) locations of the N points as a first-order perturbation expansion, we will develop analytical approximations valid in the limit of small perturbations (i.e., sufficiently many landmark points) for the corresponding perturbations in the eigenvalues and eigenvectors introduced by our landmarking procedure. We observe that for a given choice of landmark points and distance metric, the elements δ_{ij} are explicitly available, allowing is to use our terminal expressions to predict the errors introduced for a particular choice of landmarks. In Section 6.2.1 we will validate our analytical predictions against errors calculated by explicit numerical solution of the full and landmark eigenvalue problems.

We first show how to compute the perturbations in our kernel matrix $\delta\mathbf{A}$ and diagonal row sum matrix $\delta\mathbf{D}$ as a function of the pairwise distance perturbations δ_{ij}, from which we estimate perturbations in the Markov matrix $\delta\mathbf{M}$ using this expression. We then use these values to develop analytical approximations for the perturbations to the eigenvalues $\delta\mathbf{\Lambda}$ and eigenvectors $\delta\mathbf{\Psi}$ due to the landmark approximation. The perturbation analysis of the eigenvalue problem presented below follows a similar development to that developed by Deif [187].

Starting from the full diffusion map eigenvalue problem over the original data $\mathbf{M\Psi} = \mathbf{\Psi\Lambda}$

(Equation 2.6), we define the perturbed eigenvalue problem under the perturbation in the pairwise distances matrix as,

$$\begin{aligned} & \mathbf{M}'\mathbf{\Psi}' = \mathbf{\Psi}'\mathbf{\Lambda}' \\ \Rightarrow & (\mathbf{M} + \delta\mathbf{M})(\mathbf{\Psi} + \delta\mathbf{\Psi}) = (\mathbf{\Psi} + \delta\mathbf{\Psi})(\mathbf{\Lambda} + \delta\mathbf{\Lambda}), \end{aligned} \tag{6.11}$$

and where from Equation 2.4,

$$\begin{aligned} \mathbf{M} + \delta\mathbf{M} &= (\mathbf{D} + \delta\mathbf{D})^{-1}(\mathbf{A} + \delta\mathbf{A}) \\ &= (\mathbf{D}^{-1} - \delta\mathbf{D}\mathbf{D}^{-2})(\mathbf{A} + \delta\mathbf{A}) + \mathcal{O}(\delta\mathbf{D}^2) \\ &= \mathbf{D}^{-1}\mathbf{A} + \mathbf{D}^{-1}\delta\mathbf{A} - \delta\mathbf{D}\mathbf{D}^{-2}\mathbf{A} + \mathcal{O}(\delta\mathbf{D}^2, \delta\mathbf{D}\delta\mathbf{A}) \\ &= \mathbf{M} + \mathbf{D}^{-1}\delta\mathbf{A} - \delta\mathbf{D}\mathbf{D}^{-2}\mathbf{A} + \mathcal{O}(\delta\mathbf{D}^2, \delta\mathbf{D}\delta\mathbf{A}) \\ \Rightarrow \delta\mathbf{M} &= \mathbf{M}' - \mathbf{M} \\ &= \mathbf{D}^{-1}\delta\mathbf{A} - \delta\mathbf{D}\mathbf{D}^{-2}\mathbf{A} + \mathcal{O}(\delta\mathbf{D}^2, \delta\mathbf{D}\delta\mathbf{A}) \end{aligned} \tag{6.12}$$

where in going from the first line to the second we have employed the Maclaurin expansion,

$$(D_{ii} + \delta D_{ii})^{-1} = \frac{1}{D_{ii}} - \frac{\delta D_{ii}}{D_{ii}^2} + \mathcal{O}(\delta D_{ii}^2), \tag{6.13}$$

and Equation 2.4 in going from the third to the fourth. The perturbations in the elements of the Markov matrix $\delta\mathbf{M}$ may then be estimated to first order in the perturbations as,

$$\delta M_{ij} = \frac{\delta A_{ij}}{D_{ii}} - \frac{\delta D_{ii}}{D_{ii}^2} A_{ij}. \tag{6.14}$$

To estimate the $\delta\mathbf{A}$ and $\delta\mathbf{D}$ required by this expression as a function of the perturbations in the pairwise distances δ_{ij}, we commence from the expression for the elements of $\mathbf{A}'$ keeping

terms in δ_{ij} to first order,

$$\begin{aligned} A'_{ij} &= \exp\left(-\frac{(d_{ij}+\delta_{ij})^2}{2\epsilon}\right) \\ &= \exp\left(-\frac{d_{ij}^2}{2\epsilon}\right)\exp\left(-\frac{d_{ij}\delta_{ij}}{\epsilon}\right)\exp\left(-\frac{\delta_{ij}^2}{2\epsilon}\right) \\ &= A_{ij}\left(1-\frac{d_{ij}\delta_{ij}}{\epsilon}\right)+\mathcal{O}(\delta_{ij}^2), \end{aligned} \tag{6.15}$$

from which the perturbations in A_{ij} follow as,

$$\begin{aligned} \delta A_{ij} &= A'_{ij} - A_{ij} \\ &= \left(-\frac{d_{ij}\delta_{ij}}{\epsilon}\right)A_{ij}+\mathcal{O}(\delta_{ij}^2). \end{aligned} \tag{6.16}$$

The elements of the diagonal $\mathbf{D}'$ and $\mathbf{D}$ matrices are computed from the $\mathbf{A}'$ and $\mathbf{A}$ row sums respectively, from which the perturbations in D_{ii} follow immediately as,

$$\begin{aligned} \delta D_{ii} &= D'_{ii} - D_{ii} \\ &= \sum_{j=1}^{N} A'_{ij} - \sum_{j=1}^{N} A_{ij} \\ &= \sum_{j=1}^{N}\left[A_{ij}\left(1-\frac{d_{ij}\delta_{ij}}{\epsilon}\right)-A_{ij}\right]+\mathcal{O}(\delta_{ij}^2) \\ &= \sum_{j=1}^{N}\left(-\frac{d_{ij}\delta_{ij}}{\epsilon}\right)A_{ij}+\mathcal{O}(\delta_{ij}^2) \end{aligned} \tag{6.17}$$

Using Equation 6.14 we now estimate the corresponding perturbations in the eigenvalues and eigenvectors. Expanding the perturbed eigenvalue problem in Equation 6.11 and keeping terms to first order in the perturbations yields,

$$\begin{aligned} &\mathbf{M}\boldsymbol{\Psi}+\mathbf{M}\delta\boldsymbol{\Psi}+\delta\mathbf{M}\boldsymbol{\Psi} = \boldsymbol{\Psi}\boldsymbol{\Lambda}+\boldsymbol{\Psi}\delta\boldsymbol{\Lambda}+\delta\boldsymbol{\Psi}\boldsymbol{\Lambda} \\ \Rightarrow\ &\mathbf{M}\delta\boldsymbol{\Psi}+\delta\mathbf{M}\boldsymbol{\Psi} = \boldsymbol{\Psi}\delta\boldsymbol{\Lambda}+\delta\boldsymbol{\Psi}\boldsymbol{\Lambda}, \end{aligned} \tag{6.18}$$

and where in going from the first to the second line we have canceled the first term on each side using original eigenvalue problem $\mathbf{M}\mathbf{\Psi} = \mathbf{\Psi}\mathbf{\Lambda}$ (Equation 2.6). Treating the unperturbed eigenvectors $\mathbf{\Psi} = \{\vec{\psi}_i\}_{i=1}^N$ as an orthonormal basis, we expand the perturbations to each eigenvector in this basis as,

$$\delta\vec{\psi}_i = \sum_{j=1}^{N} \alpha_j^{(i)} \vec{\psi}_j, \tag{6.19}$$

where $\{\alpha_j^{(i)}\}_{j=1}^N$ are the expansion coefficients for the perturbation to the i^{th} eigenvector $\delta\vec{\psi}_i = \vec{\psi}_i' - \vec{\psi}_i$.

To solve for the perturbation to the i^{th} eigenvalue $\delta\lambda_i$ we restrict the perturbed eigenvalue problem in Equation 6.18 to the particular eigenvalue/eigenvector pair $\{\lambda_i, \vec{\psi}_i\}$ and their corresponding perturbations $\{\delta\lambda_i, \delta\vec{\psi}_i\}$ by extracting the i^{th} column, left multiplying each side by $\vec{\psi}_i^T$, and substituting in our expansion for $\delta\vec{\psi}_i$,

$$\begin{aligned}
&\vec{\psi}_i^T \left(\mathbf{M}\delta\vec{\psi}_i + \delta\mathbf{M}\vec{\psi}_i\right) = \vec{\psi}_i^T \left(\vec{\psi}_i\delta\lambda_i + \delta\vec{\psi}_i\lambda_i\right) \\
\Rightarrow\ &\vec{\psi}_i^T\mathbf{M}\left(\sum_{j=1}^{N}\alpha_j^{(i)}\vec{\psi}_j\right) + \vec{\psi}_i^T\delta\mathbf{M}\vec{\psi}_i = \vec{\psi}_i^T\vec{\psi}_i\delta\lambda_i + \vec{\psi}_i^T\left(\sum_{j=1}^{N}\alpha_j^{(i)}\vec{\psi}_j\right)\lambda_i \\
\Rightarrow\ &\sum_{j=1}^{N}\alpha_j^{(i)}\vec{\psi}_i^T\mathbf{M}\vec{\psi}_j + \vec{\psi}_i^T\delta\mathbf{M}\vec{\psi}_i = \delta\lambda_i + \lambda_i\sum_{j=1}^{N}\alpha_j^{(i)}\vec{\psi}_i^T\vec{\psi}_j \\
\Rightarrow\ &\sum_{j=1}^{N}\alpha_j^{(i)}\lambda_j\vec{\psi}_i^T\vec{\psi}_j + \vec{\psi}_i^T\delta\mathbf{M}\vec{\psi}_i = \delta\lambda_i + \lambda_i\alpha_i^{(i)} \\
\Rightarrow\ &\alpha_i^{(i)}\lambda_i + \vec{\psi}_i^T\delta\mathbf{M}\vec{\psi}_i = \delta\lambda_i + \lambda_i\alpha_i^{(i)} \\
\Rightarrow\ &\delta\lambda_i = \vec{\psi}_i^T\delta\mathbf{M}\vec{\psi}_i \\
&\qquad = \vec{\psi}_i^T(\mathbf{D}^{-1}\delta\mathbf{A} - \delta\mathbf{D}\mathbf{D}^{-2}\mathbf{A})\vec{\psi}_i
\end{aligned} \tag{6.20}$$

where we have exploited the orthonormality of the eigenvectors, in going from the third line to the fourth used the original eigenvalue problem in Equation 2.6 to make the substitution $\mathbf{M}\vec{\psi}_j = \lambda_j\vec{\psi}_j$, and used Equation 6.12 to go from the penultimate to ultimate line.

Using a similar procedure we develop expressions for the expansion coefficients $\{\alpha_j^{(i)}\}_{j=1}^N$

that we combine with Equation 6.19 to estimate perturbations in the eigenvectors. To compute $\alpha_l^{(i)}$ for $l \neq i$, we again extract the i^{th} column of the perturbed eigenvalue problem in Equation 6.18 but this time left multiply by $\vec{\psi}_l^T$,

$$\begin{aligned}
&\sum_{j=1}^{N} \alpha_j^{(i)} \vec{\psi}_l^T \mathbf{M} \vec{\psi}_j + \vec{\psi}_l^T \delta\mathbf{M} \vec{\psi}_i = \vec{\psi}_l^T \vec{\psi}_i \delta\lambda_i + \lambda_i \sum_{j=1}^{N} \alpha_j^{(i)} \vec{\psi}_l^T \vec{\psi}_j \\
\Rightarrow &\sum_{j=1}^{N} \alpha_j^{(i)} \lambda_j \vec{\psi}_l^T \vec{\psi}_j + \vec{\psi}_l^T \delta\mathbf{M} \vec{\psi}_i = \lambda_i \sum_{j=1}^{N} \alpha_j^{(i)} \vec{\psi}_l^T \vec{\psi}_j \\
\Rightarrow \alpha_l^{(i)} &= \frac{\vec{\psi}_l^T \delta\mathbf{M} \vec{\psi}_i}{\lambda_i - \lambda_l} \\
&= \frac{\vec{\psi}_l^T (\mathbf{D}^{-1}\delta\mathbf{A} - \delta\mathbf{D}\mathbf{D}^{-2}\mathbf{A}) \vec{\psi}_i}{\lambda_i - \lambda_l}, \quad l \neq i.
\end{aligned} \tag{6.21}$$

With the $\alpha_l^{(i)}$ for $l \neq i$ in hand, we recover $\alpha_i^{(i)}$ by enforcing normalization of the perturbed eigenvectors $\vec{\psi}_i' = \vec{\psi}_i + \delta\vec{\psi}_i$,

$$\begin{aligned}
&\vec{\psi}_i'^T \vec{\psi}_i' = 1 \\
\Rightarrow &(\vec{\psi}_i + \delta\vec{\psi}_i)^T (\vec{\psi}_i + \delta\vec{\psi}_i) = 1 \\
\Rightarrow &\vec{\psi}_i^T \vec{\psi}_i + 2\vec{\psi}_i^T \delta\vec{\psi}_i + \delta\vec{\psi}_i^T \delta\vec{\psi}_i = 1 \\
\Rightarrow &2\vec{\psi}_i^T \left(\sum_{j=1}^{N} \alpha_j^{(i)} \vec{\psi}_j \right) + \left(\sum_{j=1}^{N} \alpha_j^{(i)} \vec{\psi}_j \right)^T \left(\sum_{l=1}^{N} \alpha_l^{(i)} \vec{\psi}_l \right) = 0 \\
\Rightarrow &2 \sum_{j=1}^{N} \alpha_j^{(i)} \vec{\psi}_i^T \vec{\psi}_j + \sum_{j=1}^{N} \sum_{l=1}^{N} \alpha_j^{(i)} \alpha_l^{(i)} \vec{\psi}_j^T \vec{\psi}_l = 0 \\
\Rightarrow &2\alpha_i^{(i)} + \sum_{l=1}^{N} \left(\alpha_l^{(i)} \right)^2 = 0 \\
\Rightarrow &\left(\alpha_i^{(i)} \right)^2 + 2\alpha_i^{(i)} + \sum_{\substack{l=1 \\ l \neq i}}^{N} \left(\alpha_l^{(i)} \right)^2 = 0 \\
\Rightarrow &\alpha_i^{(i)} = -1 + \sqrt{1 - \sum_{\substack{l=1 \\ l \neq i}}^{N} \left(\alpha_l^{(i)} \right)^2}
\end{aligned} \tag{6.22}$$

where we have appealed to the orthonormality of the eigenvectors $\{\vec{\psi}_i\}_{i=1}^N$ and in the last line solved the quadratic in $\alpha_i^{(i)}$ by completing the square and taking the positive root that corresponds to shrinking of the perturbed eigenvector along $\vec{\psi}_i$ to maintain normalization while preserving its original sense. Finally, we restrict our perturbative analysis (Equations 6.19 and 6.20) to the subspace spanned by the top $l = 2 \ldots (k+1)$ non-trivial eigenvalues $\{\lambda_i\}_{i=2}^{k+1}$ and eigenvectors $\{\vec{\psi}_i\}_{i=2}^{k+1}$ such that we model only the perturbations within the k-dimensional subspace containing the intrinsic manifold.

The result of our analysis is a first-order perturbative expression for the errors introduced by the landmarking procedure in the eigenvalues (Equation 6.20) and eigenvectors (Equations 6.19, 6.21, and 6.22) from our landmarking procedure. In Section 6.2.1 we demonstrate that for sufficiently small perturbations in the pairwise distances δ_{ij} (i.e., sufficiently many landmark points) that these perturbative analytical predictions are in good agreement with errors calculated by explicit numerical solutions of the full and landmark eigenvalue problems.

6.1.3 Datasets

We demonstrate and benchmark the proposed L-dMaps approach in applications to three datasets: the Swiss roll, molecular simulations of a $C_{24}H_{50}$ polymer chain, and biomolecular simulations of alanine dipeptide (Figure 6.1).

Swiss roll. The "Swiss roll" – a 2D surface rolled into 3D space – is a canonical test system for nonlinear dimensionality reduction techniques [53, 56]. We illustrate in Figure 6.1a the 20,000-point Swiss roll dataset employed by Tenenbaum *et al.* in their introduction of the Isomap algorithm [53] and available for free public download from `http://isomap.stanford.edu/datasets.html`. In applying (landmark) diffusion maps to these data, distances between points are measured using Euclidean distances computed by MATLAB's L2-norm function.

Molecular simulations of a $C_{24}H_{50}$ *n*-alkane chain. Hydrophobic polymer chains

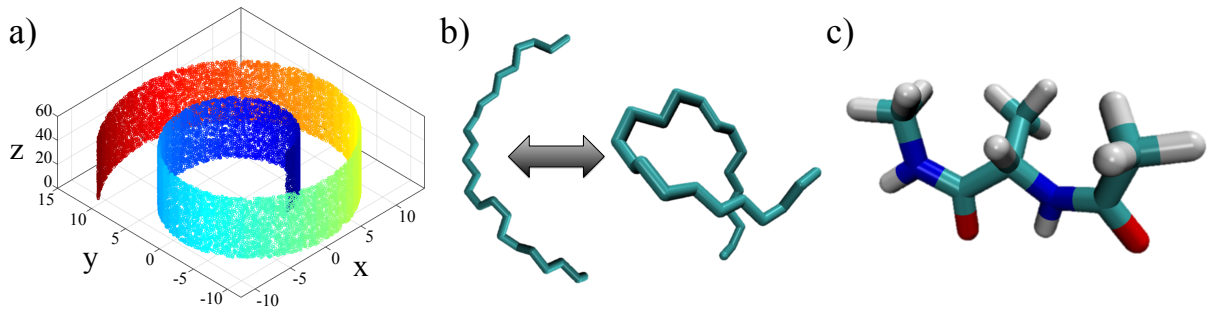

Figure 6.1: The three systems to which L-dMaps was validated and benchmarked. (a) The Swiss roll, a 2D surface embedded in 3D space that is a canonical test system for nonlinear dimensionality reduction approaches [53]. (b) Molecular dynamics simulations of a $C_{24}H_{50}$ *n*-alkane chain in water to which diffusion maps have previously been applied to discover hydrophobic collapse pathways [55, 188]. (c) Molecular dynamics simulations of alanine dipeptide – the "hydrogen atom of protein folding" – is the canonical test system for validating and benchmarking manifold learning, transition sampling, and metastable basin finding techniques in biomolecular simulation [49, 51, 73, 83, 107, 189–191].

in water possess rich conformational dynamics, and serve as prototypical models for hydrophobic folding that we have previously studied using diffusion maps to determine collapse pathways [55] and reconstruct folding funnels from low-dimensional time series [188]. We consider a molecular dynamics trajectory of a $C_{24}H_{50}$ *n*-alkane chain in water reported in Ref. [188]. Simulations were conducted in the GROMACS 4.6 simulation suite [192] at 298 K and 1 bar employing the TraPPE potential [193] for the chain that treats each CH_2 and CH_3 group as a single united atom, and the SPC water model [194]. This dataset comprises 10,000 chain configurations harvested over the course of a 100 ns simulation represented as 72-dimensional vectors corresponding to the Cartesian coordinates of the 24 united atoms. Distances between chains are computed as the rotationally and translationally minimized root-mean-square deviation (RMSD), calculated using the GROMACS *g_rms* tool (`http://manual.gromacs.org/archive/4.6.3/online/g_rms.html`).

Molecular simulations of alanine dipeptide. Finally, we study a molecular dynamics simulation trajectory of alanine dipeptide in water previously reported in Ref. [83]. The "hydrogen atom of protein folding", this peptide is a standard test system for new simulation

and analysis methods in biomolecular simulation [49, 51, 73, 83, 107, 189–191]. Unbiased molecular dynamics simulations were conducted in the Gromacs 4.0.2 suite [192] at 298 K and 1 bar modeling the peptide using the OPLS-AA/L force field [195, 196] and the TIP3P water model [197]. The dataset comprises 25,001 snapshots of the peptide collected over the course of a 50 ns simulation represented as 66-dimensional vectors comprising the Cartesian coordinates of the 22 atoms of the peptide. Distances between snapshots were again measured as the rotationally and translationally minimized RMSD calculated using the GROMACS *g_rms* tool.

6.2 Results and discussion

The principal goal of L-dMaps is to accelerate out-of-sample extension by considering only a subset $M \ll N$ of landmark points at the expense of the fidelity of the nonlinear embedding relative to that which would have been achieved using all N samples. First, we quantify the accuracy of L-dMaps nonlinear embeddings for both PST and k-medoid landmark selection strategies for the three datasets considered, and compare calculated errors with those estimated from our analytical expressions. Second, we benchmark the speedup and performance of L-dMaps for out-of-sample projection of new data.

6.2.1 Landmark diffusion map accuracy

We numerically quantify the accuracy of L-dMaps manifold reconstruction for each of the three datasets using 5-fold cross validation, where we randomly split the data into five equal partitions and consider each partition in turn as the test set and the balance as the training set. We perform a full diffusion map embedding of the training partition to compute the "true" diffusion map embedding of the complete training partition $\mathbf{\Psi}_{\text{train}}$ using Equation 2.6. We then use the embedding of the training data onto the intrinsic manifold to perform the Nyström out-of-sample extension projection of the test data onto the manifold using

Equation 2.8 to generate their "true" images $\mathbf{\Psi}_{\text{test}}$.

We assess the fidelity of the nonlinear projections of the training data generated by our landmarking approach by taking the ensemble of training data and defining M landmarks using the PST and k-medoids selection criteria. We then compute the nonlinear embedding of these landmarks onto the intrinsic manifold by solving the reduced eigenvalue problem in Equation 6.5 and projecting in the remainder of the training data (i.e., the $(N - M)$ non-landmark points) using the landmark Nyström extension in Equation 6.10. This defines a landmark projection of the training data $\mathbf{\Psi}'_{\text{train}}$. Finally, we use the landmark Nyström extension again to project in the test partition to generate the landmark embedding of the test data $\mathbf{\Psi}'_{\text{test}}$.

To compare the fidelity of the landmark embedding we define a normalized percentage deviation between the true and landmark embeddings of each point as,

$$\zeta(i) = 100 \times \sqrt{\sum_{l=2}^{k+1} \left[\frac{\vec{\psi}'_l(i) - \vec{\psi}_l(i)}{\text{range}(\vec{\psi}_l)} \right]^2}, \tag{6.23}$$

where $\vec{\psi}_l(i)$ and $\vec{\psi}'_l(i)$ are the true and landmark embeddings of data point i into the l^{th} component of the nonlinear embedding into the k-dimensional intrinsic manifold spanned by the top k non-trivial eigenvectors, $\text{range}(\vec{\psi}_l) = \max(\vec{\psi}_l(i)) - \min(\vec{\psi}_l(i))$ is the linear span of dimension l, and the dimensionality k is determined by a gap in the eigenvalue spectrum at eigenvalue λ_{k+1}. The dimensionality of the intrinsic manifolds for the Swiss roll, $C_{24}H_{50}$ chain, and alanine dipeptide have previously been determined to be 2, 4, and 2, respectively [53, 83, 188]. We then compute the root mean squared (RMS) normalized percentage error as,

$$Z = \sqrt{\frac{1}{P} \sum_{i=1}^{P} (\zeta(i))^2}, \tag{6.24}$$

where P is the number of points constituting either the training or test partition.

We illustrate in Figure 6.2 the true and landmark embeddings of the training $\{\mathbf{\Psi}_{\text{train}}, \mathbf{\Psi}'_{\text{train}}\}$

and test $\{\boldsymbol{\Psi}_{\text{test}}, \boldsymbol{\Psi}'_{\text{test}}\}$ data for the Swiss roll dataset, where we selected from the ensemble of $N_{\text{train}} = 16{,}000$ points in the training partition a set of $M = 4{,}513$ landmarks using the PST algorithm. The maximum normalized percentage deviation of any one point in either the training or test data using this set of landmarks is less than 3.2%, and the RMS errors are $Z_{\text{train}} = 0.643\%$ and $Z_{\text{test}} = 0.632\%$. This demonstrates that using only 28% of the training set as landmarks, we can reconstruct a high-fidelity embedding with average normalized percentage errors per point of less than 1%.

We present in Table 6.1 the results of our error analysis for the three datasets using the PST and k-medoids landmark selection strategies at the smallest value of the kernel bandwidth ϵ supporting a fully connected random walk over the data (cf. Equation 2.2). This value of ϵ maximally preserves the fine-grained details of the manifold; we consider larger bandwidths below. For each of the three datasets we observe high-fidelity embeddings using relatively small fractions of the data as landmarks. For the Swiss roll, $\sim$30% of the data are required to achieve a $\sim$2.5% reconstruction error. Due to the approximately constant density of points over the manifold, further reductions provide too few points to support accurate embeddings. For the $C_{24}H_{50}$ n-alkane chain and alanine dipeptide, the existence of an underlying energy potential produces large spatial variations in the density over the manifold, which is exploited by our density weighted landmark diffusion map (Equations 6.5 and 6.10) to place landmarks approximately uniformly over the manifold and eliminate large numbers of points in the high density regions without substantial loss of accuracy. For $C_{24}H_{50}$, PST landmarks constituting 1.19% of the training data attain a RMS reconstruction error of $\sim$8%, and k-medoids landmarks comprising 3.75% of the data achieve a reconstruction error of $\sim$3%. For alanine dipeptide, landmark selection using the PST selection policy achieves a $\sim$1% error rate using only 1.75% of the training points, whereas k-medoids requires more than 5% of the data to achieve that same level of accuracy.

To further explore the relative performance of the PST and k-medoids landmark selection approaches on the three datasets we conducted a parametric analysis of the error rates for the

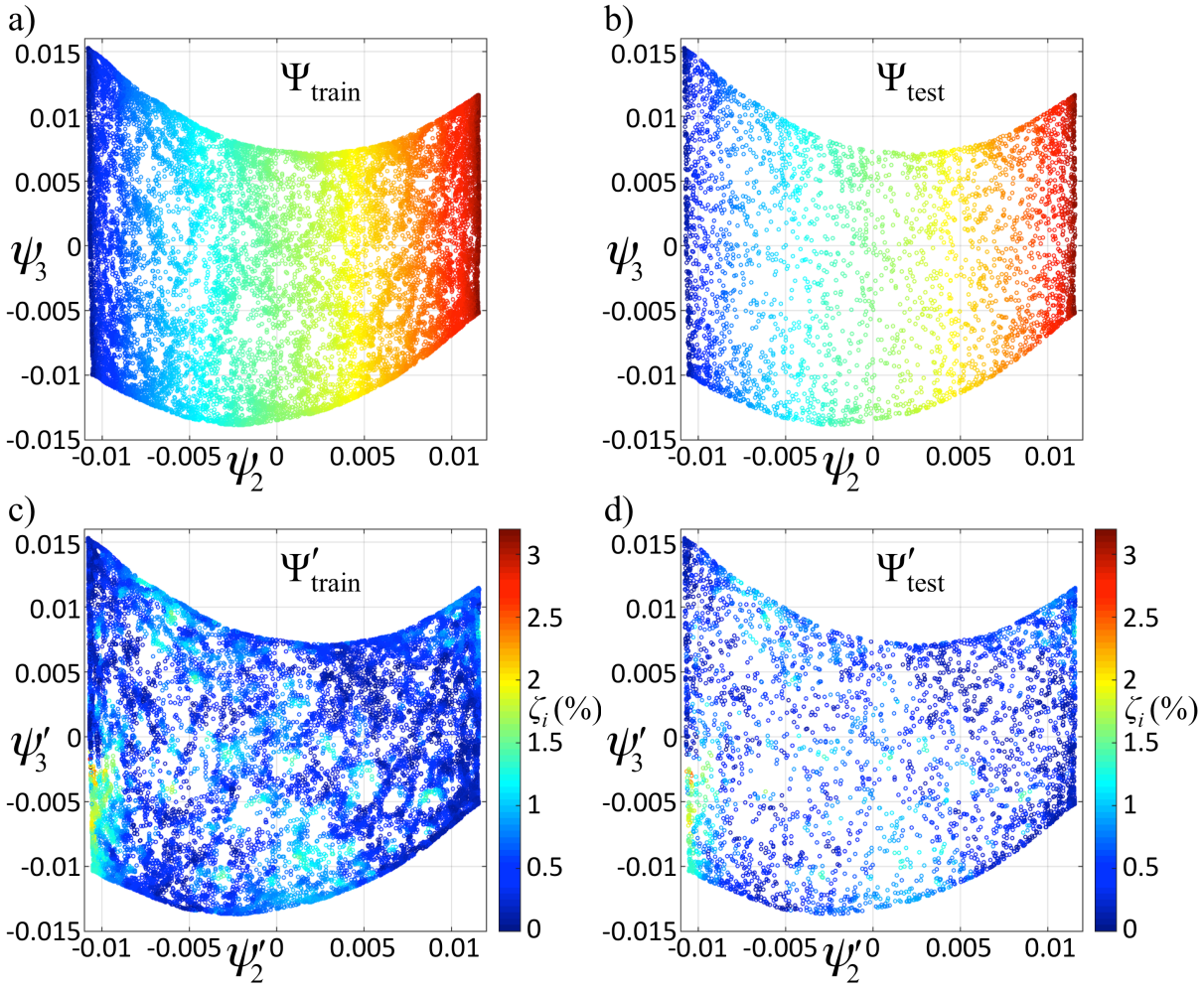

Figure 6.2: Landmark error estimates for the $N = 20{,}000$ point Swiss roll dataset split into a 80% training ($N_{\text{train}} = 16{,}000$) and 20% test ($N_{\text{test}} = 4000$) partitions. (a) Application of the original diffusion map to the full $N_{\text{train}} = 16{,}000$ training partition yields the 2D embedding $\boldsymbol{\Psi}_{\text{train}} = \{\vec{\psi}_{2,\text{train}}, \vec{\psi}_{3,\text{train}}\}$. (b) Nyström out-of-sample extension of the $N_{\text{test}} = 4000$ test points using the full embedding of the training data yields the 2D embedding $\boldsymbol{\Psi}_{\text{test}} = \{\vec{\psi}_{2,\text{test}}, \vec{\psi}_{3,\text{test}}\}$. (c) $M = 4{,}513$ landmarks were selected from the $N_{\text{train}} = 16{,}000$ training points using the pruned spanning tree (PST) approach and used to define a landmark approximation to the intrinsic manifold into which the remaining $(N_{\text{train}} - M) = 11{,}487$ training points were embedded $\boldsymbol{\Psi}'_{\text{train}} = \{\vec{\psi}'_{2,\text{train}}, \vec{\psi}'_{3,\text{train}}\}$. (d) Landmark Nyström projection of the $N_{\text{test}} = 4000$ test points into $\boldsymbol{\Psi}'_{\text{test}} = \{\vec{\psi}'_{2,\text{test}}, \vec{\psi}'_{3,\text{test}}\}$. Points are colored in panels (a,b) by their position along the spiral of the roll as illustrated in Figure 6.1a, and in panels (c,d) by the normalized percentage deviation in the projection $\zeta(i)$ defined by Eqn 6.23.

two policies at a variety of kernel bandwidths ϵ. Small ϵ values better resolve the fine-grained features of the manifold but require large numbers of landmark points to permit accurate

	Swiss roll ($N_{\mathbf{train}} = 16000$, $N_{\mathbf{test}} = 4000$, $\epsilon = 1$)			
Method	M	M / $N_{\text{train}}(\%)$	$Z_{\text{train}}(\%)$	$Z_{\text{test}}(\%)$
PST	4551.0 (25.5)	28.44 (0.16)	2.42 (1.94)	2.43 (1.95)
K-medoid	2000	12.50	13.43 (13.41)	13.37 (13.30)
	4000	25.00	3.74 (3.15)	3.75 (3.15)
	8000	50.00	1.22 (1.05)	1.22 (1.04)
	$\mathbf{C_{24}H_{50}}$ ($N_{\mathbf{train}} = 8000$, $N_{\mathbf{test}} = 2000$, $\epsilon = 2.87 \times 10^{-2}$)			
Method	M	M / $N_{\text{train}}(\%)$	$Z_{\text{train}}(\%)$	$Z_{\text{test}}(\%)$
PST	95.2 (2.6)	1.19 (0.03)	7.85 (3.44)	8.48 (3.56)
K-medoid	50	0.63	9.97 (2.86)	10.65 (2.93)
	100	1.25	5.38 (1.23)	5.76 (1.47)
	300	3.75	3.19 (0.53)	3.49 (0.65)
	Alanine dipeptide ($N_{\mathbf{train}} = 20000$, $N_{\mathbf{test}} = 5000$, $\epsilon = 1.06 \times 10^{-3}$)			
Method	M	M / $N_{\text{train}}(\%)$	$Z_{\text{train}}(\%)$	$Z_{\text{test}}(\%)$
PST	347.2 (8.4)	1.74 (0.04)	0.88 (0.26)	0.94 (0.30)
K-medoid	200	1.00	5.93 (2.81)	6.31 (3.04)
	400	2.00	2.92 (0.92)	3.05 (0.84)
	1000	5.00	1.43 (0.57)	1.50 (0.60)

Table 6.1: Root mean squared normalized percentage errors in the landmark nonlinear embeddings Z for the PST and k-medoids landmark selection algorithms over the training and test partitions of the Swiss roll, $C_{24}H_{50}$, and alanine dipeptide datasets. In each case the smallest value of ϵ supporting a fully connected random walk was employed in the kernel bandwidth. We report the mean and standard deviation of Z_{train} and Z_{test} estimated from 5-fold cross validation. For the PST landmark selection policy, we also report the mean and standard deviation in the number and percentage of landmark points.

interpolative embeddings of out-of-sample points by covering the manifold in overlapping $\sqrt{\epsilon}$ volumes. Large ϵ values sacrifice accurate representations of the details of the manifold, but permit the use of fewer landmark points. The PST selection procedure does not offer a means to directly tune the number of landmarks selected, which is controlled by ϵ used in construction of the spanning tree to ensure coverage and connectivity of the full dataset. The k-medoids policy permits the user to directly control the error to within a specified threshold by modulating the number of landmarks M. We present the results of our analysis in Figure 6.3. The PST approach achieves better accuracy than k-medoids for the same number of landmarks, offering a good approach for automated landmark selection. The k-medoids error, however, can be tuned over a large range by adaptively choosing an appropriate number of

landmark points.

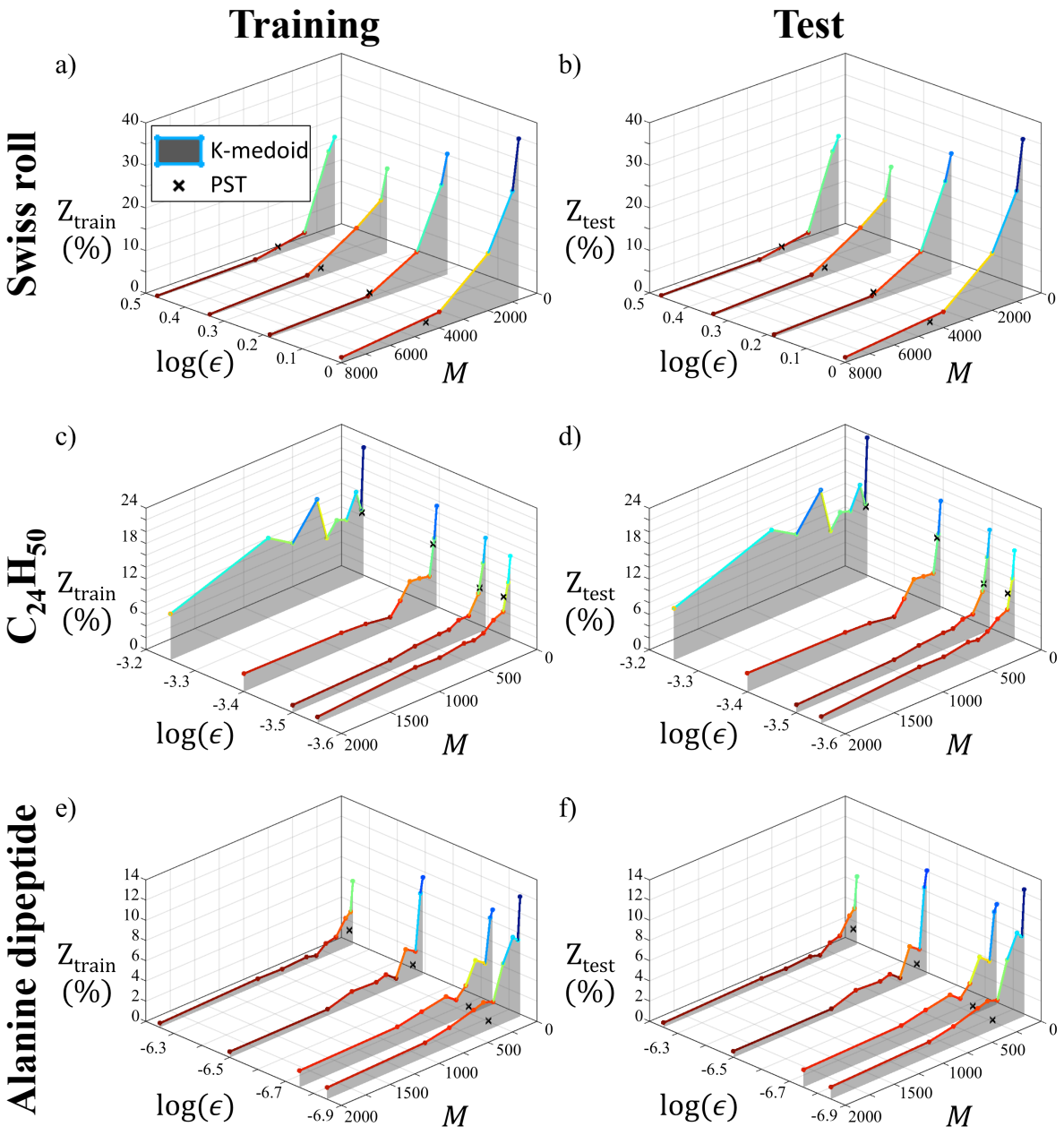

Figure 6.3: Root mean squared normalized percentage errors in the landmark nonlinear embeddings Z as a function of the PST (black crosses) or k-medoids (waterfall lines) landmark selection algorithm and kernel bandwidth ϵ for the training and test partitions of the (a,b) Swiss roll, (c,d) $C_{24}H_{50}$, and (e,f) alanine dipeptide datasets. For the PST algorithm the number of landmarks M is automatically selected as a function of ϵ, whereas this is a user-defined adjustable parameter for the k-medoids approach. We plot the mean Z_{train} and Z_{test} estimated from 5-fold cross validation.

To make contact with our analytical error estimates developed in Section 6.1.2, we present in Figure 6.4 a parity plot of the discrepancies in the embedding of the $i = 1, \ldots, N_{\text{train}}$ training points between the full and landmark embeddings,

$$\begin{aligned}\sigma(i) &= |||[\vec{\psi}'_{2,\text{train}}(i), \vec{\psi}'_{3,\text{train}}(i), \ldots, \vec{\psi}'_{k+1,\text{train}}(i)] - [\vec{\psi}_{2,\text{train}}(i), \vec{\psi}_{3,\text{train}}(i), \ldots, \vec{\psi}_{k+1,\text{train}}(i)]||| \\ &= |||[\delta\vec{\psi}_{2,\text{train}}(i), \delta\vec{\psi}_{3,\text{train}}(i), \ldots, \delta\vec{\psi}_{k+1,\text{train}}(i)]||| \\ &= \sqrt{\sum_{l=2}^{k+1} \left(\delta\vec{\psi}_{l,\text{train}}(i)\right)^2}, \end{aligned} \tag{6.25}$$

predicted from our analytical first-order perturbative expressions $\sigma_{\text{pred}}(i)$ (Equations 6.19, 6.21, and 6.22) and calculated directly from our numerical computations $\sigma_{\text{expt}}(i)$. We collate data from the k-medoids landmark selection process at all numbers of landmarks M with the ϵ bandwidths provided in Table 6.1; perfect prediction would correspond to all points lying along the diagonal. The experimental and predicted errors show quite good agreement for large values of M where the first-order perturbation expansion is a good approximation and the number of landmarks M is such that the characteristic distance between them is on the order of $\sqrt{\epsilon}$. The agreement deteriorates for small numbers of landmarks where there are too few supports covering the manifold to admit an accurate perturbative treatment. In the large-M / small-error regime where the perturbative treatment is accurate, the analytical error expressions can be used to predictively identify landmark selections to achieve a specified error tolerance.

6.2.2 Out-of-sample extension speedup

In Figure 6.5 we present as a function of the number of landmarks M the measured speedups $S(M) = t_{\text{full}}/t_{\text{landmark}}(M)$ for the k-medoids landmark selection data presented in Figure 6.3 at the ϵ values given in Table 6.1. t_{full} is the measured execution time for the Nyström embedding of the N_{test} training points using the locations of all N_{train} training points com-

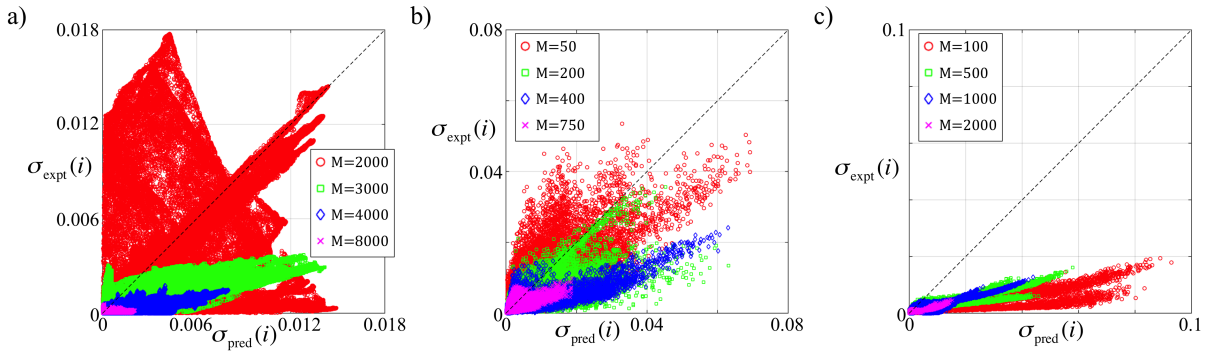

Figure 6.4: Comparison of the predicted $\sigma_{\text{pred}}(i)$ and calculated $\sigma_{\text{expt}}(i)$ errors in the discrepancy of the embedding locations of the training data under the full and landmark embeddings for the (a) Swiss roll, (b) $C_{24}H_{50}$ n-alkane chain, and (c) alanine dipeptide datasets.

puted using the full diffusion map, and $t_{\text{landmark}}(M)$ is the runtime for the landmark Nyström embedding using $M < N_{\text{train}}$ landmark points. All calculations were performed on an Intel i7-3930 3.2GHz PC with 32GB of RAM, with landmark selection and diffusion mapping performed in MATLAB and distances computed as described in Section 6.1.3.

For each of the three systems studied, we observe large accelerations in runtime as we decrease the number of landmarks employed. In the case of $C_{24}H_{50}$ and alanine dipeptide, we observe excellent agreement with the theoretically predicted $S \propto N_{\text{train}}/M$. Selecting $M/N_{\text{train}} \approx 4\%$ for $C_{24}H_{50}$ and $M/N_{\text{train}} \approx 2\%$ for alanine dipeptide, we achieve 25-fold and 50-fold accelerations in the out-of-sample embedding runtime, respectively, while incurring only $\sim$3% errors in the embedding accuracy (Table 6.1). Reduced accelerations and deviation from the expected scaling relation are observed for the Swiss roll dataset due to the very low cost of the Euclidean pairwise distance computation, which leaves these calculations dominated by computational overhead as opposed to the computational load of the pairwise distance and Nyström calculations. Nevertheless, we still achieve a two-fold acceleration in runtime for $M/N_{\text{train}} \approx 25\%$ with a $\sim$4% embedding error (Table 6.1). Using landmark diffusion maps can thus drastically reduce the out-of-sample restriction time, with particular efficacy in embedding samples with computationally expensive distance measures.

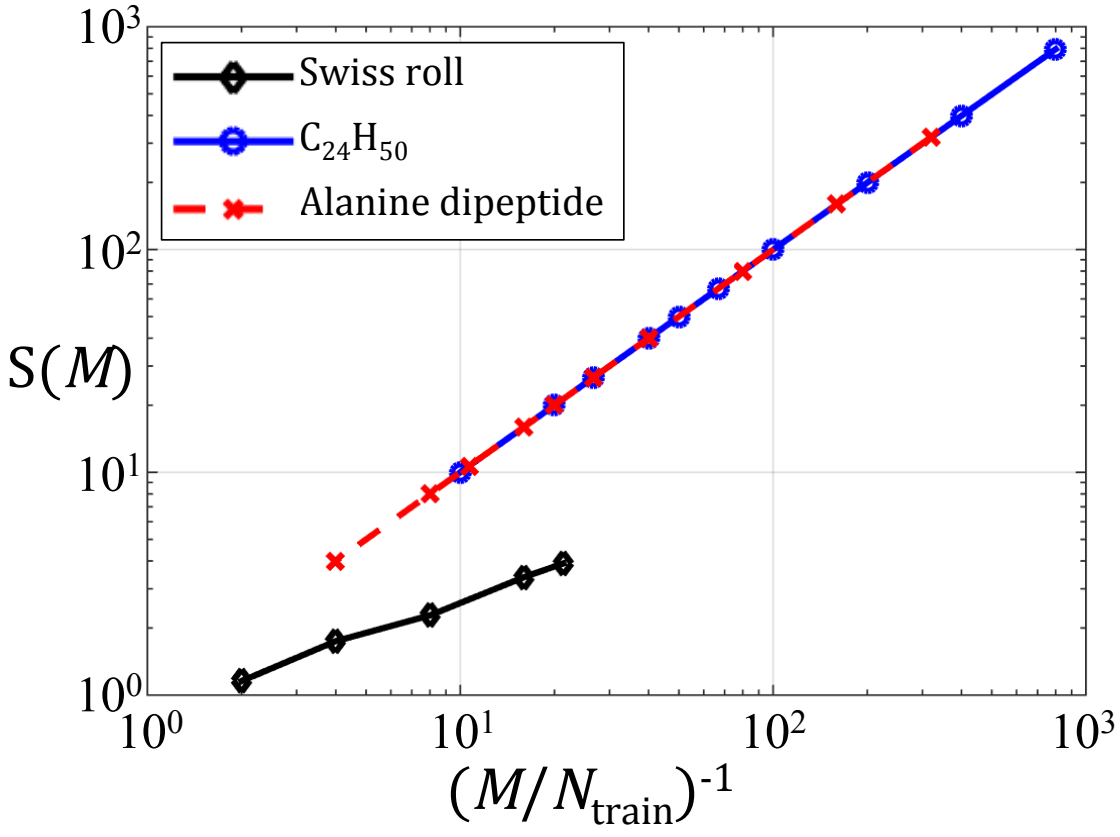

Figure 6.5: Speedup $S(M) = t_{\text{full}}/t_{\text{landmark}}(M)$ in the embedding of the N_{test} test points using a landmark Nyström embedding over M landmark points relative to a full embedding over all N_{train} points for each of the three datasets. Timings include both the computation of pairwise distances to the out-of-sample point and the Nyström projection procedure.

6.3 Conclusions

We have introduced a new technique to accelerate the nonlinear embedding of out-of-sample data into low-dimensional manifolds discovered by diffusion maps using an approach based on the identification of landmark points over which to perform the embedding. In analogy with the landmark Isomap (L-Isomap) algorithm [53, 177], we term our approach landmark diffusion maps (L-dMaps). By identifying with the N data points a small number of $M \ll N$ landmarks to support the calculation of out-of-sample embeddings, we massively reduce the computational cost associated with this operation to achieve theoretical speedups $S \propto N/M$.

We have validated the accuracy and benchmarked the performance of L-dMaps against three datasets: the Swiss roll, molecular simulations of a $C_{24}H_{50}$ polymer chain, and biomolecular simulations of alanine dipeptide. These numerical tests demonstrated the capacity of our approach to achieve up to 50-fold speedups in out-of-sample embeddings with less than 4% errors in the embedding fidelity for molecular systems. L-dMaps enables the use of diffusion maps for rapid online embedding of high-volume and high-velocity streaming data, and is expected to be particularly valuable in applications where runtime performance is critical or rapid projection of new data points is paramount, such as in threat detection, anomaly recognition, and high-throughput online monitoring or analysis.

We observe that further accelerations to L-dMaps may be achieved using efficient algorithms to eliminate the need to compute all M pairwise distances between the new out-of-sample point and the landmarks. For example the recently proposed Fast Library for Approximate Nearest Neighbors (FLANN) [198] uses a tree-search to perform a radial k-nearest neighbors search, and has been previously employed in the construction of sparse diffusion maps [199]. These techniques may also prove valuable in eliminating the need to compute the N-by-N pairwise distances matrix required for landmark identification, the storage and analysis of which can prove prohibitive for large datasets. Techniques such as FLANN provides a means to efficiently construct sparse approximations to the kernel matrix $\mathbf{A}$ in which small hopping probabilities associated with large distances below a user-defined tolerance are thresholded to zero. Accordingly, we foresee combining approximate nearest neighbor distance computations, sparse matrix representations, and landmark embedding procedures as a fruitful area for future development of fast and efficient out-of-sample nonlinear embedding approaches.

Chapter 7

Inverse design via landscape engineering

Many-body diffusion maps systematically identify the low-dimensional pathways driving building block aggregation phenomena, however this framework does not immediately permit extracting thermodynamic information of the self-assembly process. To capture both the thermodynamic stability and kinetic accessibility of self-assembly, we wish to compute the free energy inside the low-dimensional kinetic landscape furnished by the diffusion map. To achieve this, we propose a biased hybrid Monte Carlo scheme [200–202] directly in the diffusion map coordinate space allowing for rapid sampling and exploration of the configurational phase space of cluster aggregation.

Having an integrated model for the kinetic accessibility and thermodynamic stability of self-assembly, we rationally engineer building block architecture by sculpting the free energy landscape to achieve robust aggregation of a desired structure. We cast this sculpting procedure as an optimization problem to maximize the stability of a desired target aggregate as a function of tunable building block anisotropic interactions. Many optimization techniques are possible for this problem, from gradient descent [203], to swarm approaches [204] and genetic algorithms [205] . In this study we employ the covariance matrix adaptation evolutionary strategy (CMA-ES) technique [206, 207] that has previously been used in the design of substrates to direct the assembly of lamella patterned block copolymers [208, 209].

In this chapter we study the self-assembly of a class of double annular ring patchy colloids

This chapter is based on work in preparation:

Andrew W. Long and Andrew L. Ferguson, "Rational design of patchy colloids via landscape engineering", (in preparation 2017).

[9], seeking to optimize their structure to improve the yield and monodispersity of polyhedral aggregates. We propose a combined machine learning and molecular simulation framework to manipulate patchy colloid structures, and we highlight this technique on two systems: increased assembly propensity of icosahedron from an expert-directed starting configuration, and the optimization of octahedral generating patchy colloids from a poor initial guess. In both cases we show that the technique rapidly converges colloid architecture to reach a desired target structure. This technique is directly extensible to more complex assembly systems and user-defined fitness functions, opening the door to automated data-driven inverse design of novel self-assembled structures.

7.1 Patchy colloid model

In this work, we utilize the double ring patchy colloid model proposed by Glotzer et al. in Ref. 9, and previously studied via diffusion mapping in Chapter 3. For this model, the surface of a spherical colloidal particle (type A) is decorated with two annular rings of smaller spheres (types B and C), as portrayed in Figure 7.1. The diameter of these three species is chosen as $\sigma_A = 5\sigma$, $\sigma_B = \sigma_C = \sigma$. For a given polar angle ϕ, we generate a ring as the maximal non-overlapping arrangement of patch spheres over the central sphere. After generating rings at ϕ_B, ϕ_C, we rotate the C-ring around it's central axis to minimize the overlap between patch particles in the B- and C-rings. These rings are then rigidly constrained to the surface of the central A-sphere, neglecting all intraparticle interactions.

Colloidal interactions are determined by the patchy rings, enabling a rich diversity of interactions built up from spherically symmetric potentials [9, 34]. Interactions between B-B and C-C patches are given by the Lennard-Jones potential

$$U_{\mathrm{LJ}}^{ii}(r) = 4\varepsilon_i \left[\left(\frac{\sigma_i}{r}\right)^{12} - \left(\frac{\sigma_i}{r}\right)^{6} \right], \tag{7.1}$$

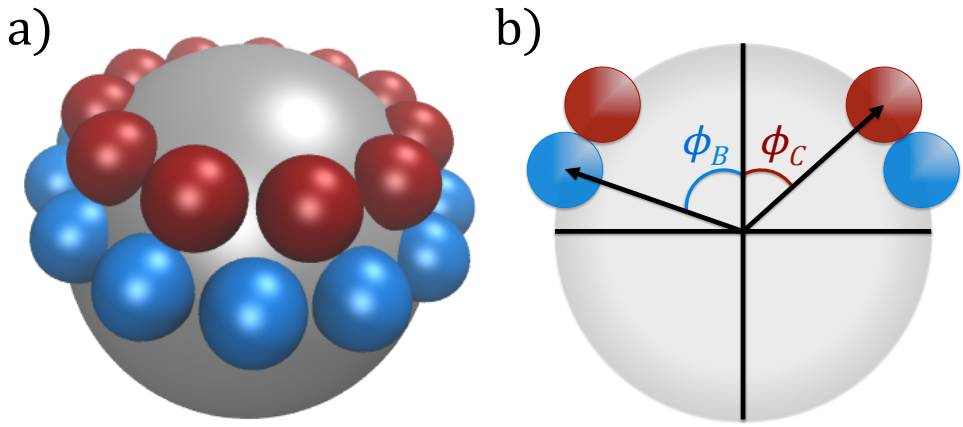

Figure 7.1: Double annular ring patchy colloid model used in this study. (a) A central particle of type A (silver) is decorated with two rings of types B (blue) and C (red), visualized in VMD [96]. (b) The height of these coaxial rings are determined by the polar angle (ϕ_B, ϕ_C). For each ring, we compute the maximal number of non-overlapping patch particles for this given height and evenly distribute these patches around the central particle surface.

where σ_i and ε_i are the diameter and energy well depth, respectively, for particle type i, and r is the interparticle separation. All other interactions, A–X where X$\in$ {A,B,C} and B–C, are given by a surface shifted Weeks-Chandler-Andersen (WCA) potential to model excluded volume effects [97],

$$U_{WCA}^{ij}(r) = \begin{cases} 4\varepsilon_{ij}\left[\left(\frac{\sigma}{r-\Delta}\right)^{12} - \left(\frac{\sigma}{r-\Delta}\right)^{6}\right] + \varepsilon, & r < 2^{(1/6)}\sigma + \Delta \\ 0, & r \geq 2^{(1/6)}\sigma + \Delta \end{cases}, \tag{7.2}$$

where $\varepsilon_{ij} = \sqrt{\varepsilon_i \varepsilon_j}$ is defined by the Berthelot mixing rule [98], and $\Delta_{ij} = (\sigma_i + \sigma_j)/2 - \sigma$ shifts the potential to act between particle surfaces [210].

For this study, colloid structure is optimized to improve the yield of a target self-assembled aggregate by optimization of the polar angles, (ϕ_B, ϕ_C). Previous studies of this patchy colloid model have shown that manipulation of the polar angles induces self-assembly of a variety of different polyhedral architecture [9, 125]. Since the number of particles N_i

in a ring may change with varying ϕ_i due to geometric constraints on how many particles can occupy an annular ring, we must redistribute the sum of the particle Lennard-Jones ε_i parameters such that the total interaction strength $E_i = N_i\varepsilon_i$ is conserved for each particle type $i = \{B, C\}$.

Following Chapter 3, simulations are performed in dimensionless units, with $\sigma = \sigma_B = \sigma_C = 1$, $\sigma_A = 5$, $\epsilon = \epsilon_A = 1$, $E_B = N_B\varepsilon_B = 14$ and $E_C = N_C\varepsilon_C = 11$, and $m = m_A = m_B = m_C = 1$. For these parameters, $\Delta_{AA} = 4$, $\Delta_{AB} = \Delta_{AC} = 2$, and $\Delta_{BC} = 0$, such that A overlaps are effectively forbidden and the particles interact primarily by specific surface interactions between the B and C rings. We use the dimensionless mapping previously defined in Chapter 3 to map our dimensionless simulations to real units. We consider particles of size $\sigma_A = 5\sigma = 1\mu m$, with the density $\rho_A = 1\text{g/cm}^3$, and an energy scale of $\varepsilon = 1k_\text{B}T$ at $T = 298K$. The real temperature is given as $T = \varepsilon T^*/k_\text{B}$ and real time is given by $t = t^*\sqrt{m\sigma^2/\varepsilon}$. Our simulations are run at $T^* = 0.8$, giving a real temperature of $238.4K$, with a time step of $dt^* = 5 \times 10^{-3}$ which yields a real unit time step of $dt = 0.36\mu s$.

7.2 Landscape engineering for patchy colloid design

We employ an evolutionary strategy for building block design by iterative evolution of the underlying free energy landscape for self-assembly, presented in Figure 7.2. Given an initial ensemble of building block designs, we conduct Langevin dynamics simulations of the self-assembly of each particle design and apply diffusion maps to construct a low-dimensional parameterization of the accessible configurational space[125, 158]. We then perform enhanced sampling over the low-dimensional landscape to compute the free energy landscape for each particle design, compute the relative stability of the target self-assembled aggregate, and assign a fitness to each design. We then analyze the relative fitnesses of the swarm of intitial particle designs using CMA-ES to predictively design a new generation of particle designs predicted to possess higher fitness. We loop through a three-step process - unbiased

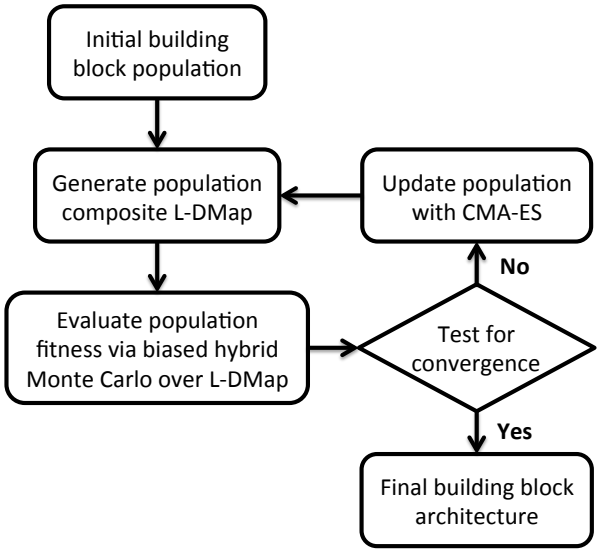

Figure 7.2: Evolutionary landscape engineering procedure for building block design. For each generation, we compute a population-wide low-dimensional representation of the self-assembly phase space via L-dMaps. We evaluate fitness for each building block architecture (genotype) as variations on the underlying free energy landscape over the L-dMap space. Population updates are performed using the covariance matrix adaptation evolutionary strategy (CMA-ES) until the building block design converges to a stable optimum.

sampling, composite diffusion map and enhanced sampling in the low-dimensional space, CMA-ES update of the particle design – until the CMA-ES approach converges to a stable optimal building block design.

7.2.1 Unbiased sampling of building block population

Given a population of P candidate building blocks with slightly different (ϕ_B, ϕ_C) polar angles, we need to understand of the range of accessible morphologies to these building block designs in order to generate a map of the aggregation process. To do this, we employ Langevin dynamics simulations in HOOMD-blue[99, 145] v2.1.2 employing a rigid-body model of the patchy colloids.[100] Simulations were performed in a cubic box with periodic boundary conditions in all dimensions. We initialized all unbiased simulations in the following manner. A random initial configuration was generated by decorating a $4 \times 4 \times 4$ cubic

lattice with monomers and evolving this system at high temperature ($T^* = 1.0$) with only WCA interactions active. The box dimensions are initialized to yield a volume fraction of $\phi = 0.006$ ($L = 105.04\sigma$), after which the box is shrunk to achieve the target volume fraction of $\phi = 0.05$ ($L = 52.52\sigma$) over 10^4 time steps with $dt^* = 10^{-4}$. During this shrinking process, the particle positions are scaled with the box dimensions. Upon reaching the terminal box size, the system is run for an additional 10^4 time steps at $dt^* = 10^{-3}$ and $T^* = 1.0$ to randomize the starting configuration inside the new box dimensions.

After this initialization procedure, we run Langevin dynamics simulations using the potentials described in Section 7.1 at $T^* = 0.8$ for 2.5×10^6 time steps with $dt^* = 5 \times 10^{-3}$, with diameter-scaled dampening coefficients $\gamma_i = \lambda\sigma_i$, where we select in our dimensionless units $\lambda = 1$. We sample configurations every 250 time steps, yielding 10^4 snapshots per trajectory. For each of the P building blocks we perform three independent runs to provide a representative sample of the accessible structures of a given building block over which to build a set of low-dimensional descriptors using diffusion maps. In this work we employ P=9-10 as a balance between good exploration of the building block design space and the computational burden associated with the simulation and analysis of each generation of the optimization loop.

7.2.2 Population composite landmark diffusion map

In this work, we employ the many-body diffusion map approach presented in Chapter 2 to identify the low-dimensional manifold containing the self-assembly dynamics. The primary requirement to apply diffusion maps to the problem of assembly is a measure of similarity between cluster aggregates. Due to the fungible nature of identical particles in our simulation, we require a technique that can handle the factorial growth of possible particle labelings in an efficient way. We have proposed the use of a graph-based distance measure, reducing the particles in an aggregate to nodes and distances between particles as edges of the graph. To find the distance, $\mathbf{d}(\mathbf{G}_i, \mathbf{G}_j)$, between two aggregates with corresponding graphs $\mathbf{G}_i$ and

$\mathbf{G}_j$ we identify the pseudo-optimal permutation, $\mathbf{H}$, that minimizes the $L_{1,1}$ norm between them given as

$$\mathbf{d}\left(\mathbf{G}_i, \mathbf{G}_j\right) = \min_{\mathbf{H}} \frac{\sum_k \sum_l |(\mathbf{H}^T \mathbf{G}_i \mathbf{H})(k,l) - \mathbf{G}_j(k,l)|}{|\mathbf{G}_j|(|\mathbf{G}_j| - 1)}. \tag{7.3}$$

where $|\mathbf{G}_j|$ corresponds to the number of nodes in graph $\mathbf{G}_j$. The solution to this problem is in general NP-complete [126], necessitating the use of greedy techniques. As described in Section 2.2.3, we employ a tree-based alignment procedure with IsoRank [85] node-alignment scores as a selection heuristic at each node of the tree, with a branching factor $k = 2$. For the matching of different sized graphs, we extend the smaller graph to be of the same shape as the larger graph via the addition of ghost nodes [125]. To handle the disparity between graph sizes, we normalize the distance by the number of non-diagonal elements in the larger graph's matrix representation. C++ and python codes for this graph alignment procedure, alongside our diffusion map codes, are published at `https://github.com/awlong/DiffusionMap`.

Due to the computational complexity of graph matching as a distance measure, we utilize the recently developed landmark diffusion map (L-dMap) algorithm [211] to improve the runtime for out-of-sample embedding. Here we provide the key methodological details for L-dMaps, the full details of this method are presented in Chapter 6. Having sampled a set of aggregates, $\{\mathbf{x}_i\}_{i=1}^N$, we compute the $N \times N$ pairwise distance matrix $\mathbf{d}_{ij}$ between pairs of aggregates via Equation 7.3. We identify a subset of M aggregates, $\{\mathbf{z}_j\}_{j=1}^M \subseteq \{\mathbf{x}_i\}_{i=1}^N$, to serve as landmark points via k-medoids clustering [185], with corresponding landmark multiplicities $\{\mathbf{c}_j\}_{j=1}^M$ given by the number of points $\mathbf{x}$ within the Voronoi volume surrounding each landmark $\{\mathbf{z}_j\}_{j=1}^M$.

Having selected a set of landmark aggregates, we compute a reduced $M \times M$ form of the diffusion map analogous to Equation 2.6. We compute the unnormalized hopping probability $\tilde{\mathbf{A}}_{ij}$ between landmarks as

$$\tilde{\mathbf{A}}_{ij} = \exp\left(-\frac{\mathbf{d}\left(\mathbf{z}_i, \mathbf{z}_j\right)^2}{2\varepsilon}\right). \tag{7.4}$$

We define the diagonal multiplicity matrix $\tilde{\mathbf{C}}_{ii} = \mathbf{c}_i$ to approximate the local density of

points given in the full data set. The normalized Markov matrix for this reduced problem is given by $\tilde{\mathbf{M}} = \tilde{\mathbf{D}}^{-1}\tilde{\mathbf{A}}$ where $\tilde{\mathbf{D}}$ is the diagonal matrix

$$\tilde{\mathbf{D}}_{ii} = \sum_{j=1}^{M} \tilde{\mathbf{A}}_{ij}\tilde{\mathbf{C}}_{jj}. \tag{7.5}$$

The collective variables spanning the low-dimensional intrinsic manifold are then given by the solution of the eigenvalue problem $\tilde{\mathbf{M}}\tilde{\mathbf{C}}\tilde{\mathbf{\Psi}} = \tilde{\mathbf{\Psi}}\tilde{\mathbf{\Lambda}}$. By enforcing the normalization condition $\tilde{\mathbf{C}}\vec{\tilde{\Psi}}_i \cdot \vec{\tilde{\Psi}}_i = 1$, it can be shown that the diffusion map embedding,

$$\text{cluster}_i \rightarrow \{\vec{\tilde{\Psi}}_2(i), \vec{\tilde{\Psi}}_3(i), \ldots, \vec{\tilde{\Psi}}_{k+1}(i)\}, \tag{7.6}$$

is precisely the embedding garnered from diffusion mapping of an ensemble of landmark points where each landmark $\mathbf{z}_i$ is reproduced $\mathbf{c}_i$ times, and the corresponding M non-zero eigenvalues are identical, $\{\tilde{\lambda}_i\}_{i=1}^{M} = \{\lambda_i\}_{i=1}^{M}$ [83]. In this work, we treat $\{\vec{\Psi}_i\}_{i=1}^{M}$ as the set of eigenvectors satisfying this normalization condition. Generating a single composite diffusion map space allows for direct comparison between building blocks over a consistent basis set, as opposed to generating unique diffusion map landscapes for each building block design. In this way, we are able to directly probe the impact that building block architecture has on the self-assembly landscape for all building block designs within a generation.

7.2.3 Sampling free energy over L-dMap space

Having developed a set of collective coordinates $\{\vec{\Psi}\}$ providing a low-dimensional parameterization of the configurational space in which assembly proceeds, we are interested in computing the free energy landscape over this space. Theoretically we can recover the free energy landscape from a prolonged unbiased simulation, approximating the probability density function $P(\vec{\Psi})$ and free energies as $\beta F(\vec{\Psi}) = -\ln P(\vec{\Psi}) + C$, where we use F to denote the Helmholtz free energy, $\beta = \frac{1}{k_{\mathrm{B}}T}$, and C is an arbitrary additive constant. This process,

although consistent in the infinite time horizon, suffers from poor sampling of rugged landscapes, due to kinetic trapping behind high free energy barriers. We confront this difficulty by conducting accelerated sampling in the space of the diffusion map collective coordinates.

Efficient sampling along reaction coordinates is a problem of intense interest in the molecular simulation community, with a variety of developments in recent years. For systems where the reaction coordinates are constructed as analytical functions of the atomic coordinates, biasing forces can be derived to localize systems in particular regions of the reaction coordinate space within molecular or Langevin dynamics simulations [212–215]. In the case of our low-dimensional diffusion map manifold, we lack such a functional mapping between atomic and reaction coordinates and so instead implement Monte Carlo sampling, whereby we can apply a biasing potential to localize sampling in regions of the reaction coordinate space by accepting or rejecting trial moves in configurational space. We observe that a small number of techniques have very recently been proposed to compute biasing forces in the low-dimensional projections lacking an explicit functional mapping [216–219], but these approaches employ nearest-neighbor embeddings or basis function expansions to furnish only approximate biasing forces.

In this work, we employ umbrella sampling [220] employing a harmonic restraining potential α in the low-dimensional collective coordinates given by,

$$\alpha(\vec{\Psi}, \vec{\Psi}^*) = \frac{1}{2} \sum_{j=1}^{k} \kappa_j \left(\Psi_j - \Psi_j^* \right)^2 , \tag{7.7}$$

where $\vec{\Psi}^*$ is a k-dimensional harmonic center, and κ_j is the strength of the harmonic constraint in the j^{th} dimension. Trial moves are proposed using a hybrid Monte Carlo (HMC) approach [200], where moves are generated using a short molecular dynamics simulation in the microcanonical ensemble. As the particles studied are strongly attractive, single-particle Metropolis Monte Carlo strategies will yield a critical slowing phenomena as aggregation occurs, with overly deflated acceptance probabilities due to an exponential dependence on

the change in potential energy when moving a single particle.[221] For each HMC step, translational and rotational velocities are randomly sampled from the Maxwell-Boltzmann distribution with scaling to impose zero net momentum. Particle positions are evolved using an NVE integrator, which in HOOMD is implemented using the Velocity-Verlet algorithm [100]. The use of an NVE integrator ensures that the proposed move is reversible. Upon completing a series of NVE integration steps, the system energy is given by the Hamiltonian $H(q,p) = U(q) + K(p)$, where $U(q)$ is the potential energy for the system with particles at locations q, and $K(p)$ is the kinetic energy of the system with momenta p. Acceptance of this HMC step from the initial state (q_i, p_i) to the trial state (q_{i+1}, p_{i+1}) is then determined by a Metropolis criterion,

$$\text{acc}\left((q_i,p_i) \rightarrow (q_{i+1},p_{i+1})\right) = \min\left(1, \frac{\exp[-\beta H(q_{i+1},p_{i+1})]}{\exp[-\beta H(q_i,p_i)]}\right) \tag{7.8}$$

The benefits of HMC sampling are that it is able to rapidly sample system configurations, avoiding the low acceptance ratios of non-cluster based moves, and it is easily implemented using standard molecular dynamics packages.

Given a Hamiltonian for the system $H(q,p)$, the biased acceptance criterion in going from state $(q_i, p_i, \vec{\Psi}_i)$ to $(q_{i+1}, p_{i+1}, \vec{\Psi}_{i+1})$ in the presence of an umbrella restraining potential centered on $\vec{\Psi}^*$ is given as,

$$\text{acc}\left((q_i,p_i,\vec{\Psi}_i) \rightarrow (q_{i+1},p_{i+1},\vec{\Psi}_{i+1})\right) = \min\left(1, \frac{\exp[-\beta H(q_{i+1},p_{i+1}) - \beta\alpha(\vec{\Psi}_{i+1},\vec{\Psi}^*)]}{\exp[-\beta H(q_i,p_i) - \beta\alpha(\vec{\Psi}_i,\vec{\Psi}^*)]}\right). \tag{7.9}$$

At the beginning of our HMC simulation, we tag a single colloid for which the aggregation state is tracked throughout biasing to identify a snapshot's location in diffusion map space, $\vec{\Psi}$. In this way, we are biasing the self-assembly of a particular aggregate in a sea of colloids evolving according to the unbiased system Hamiltonian. We note that traditional Monte

Carlo techniques involving cluster moves could also be employed for these types of simulations [221, 222], however for these cases a multiple time-stepping method might prove best to limit the number of calls to the expensive biasing potential [223].

Having defined our sampling technique, we require a method to efficiently place umbrella restraining potentials over the low-dimensional our diffusion map landscape to provide good sampling of the intrinsic manifold. Here we utilize Lloyd's algorithm [224] to evenly partition the convex hull encompassing the embedding of our unbiased simulation data into the intrinsic manifold to define a series of evenly distributed centers in the landscape. For our initial sampling pass, we generate 80 centers inside the convex hull. As our landscapes are typically not convex, we exclude centers outside of a skin depth of our landscape, which we define to be $\delta = 0.005$. We bin the points of the convex hull onto a 50×50 grid, adding each filled grid location to our set of biasing centers to effectively smooth the hull boundary shape and remove noise from the boundary due to sampling. This set of centers defined by Lloyd's algorithm and these hull points, typically an even distribution, serve as an initial series of umbrella sampling windows. Subsequent runs are performed as needed to improve coverage of undersampled regions of the manifold.

For each umbrella sampling simulation, we start from a previous simulation snapshot that is located closest to the umbrella window in (Ψ_2, Ψ_3) space. We freeze the configuration of the cluster attached to the tagged particle and disassociate the remaining particles in the box using the fast inertial relaxation engine (FIRE) algorithm [225] with purely WCA interactions between particles and a time step of $dt^* = 10^{-5}$ until the system energy has converged to within a tolerance of $0.1 k_\mathrm{B} T$. After this initialization, we unfreeze the tagged cluster and allow the system to evolve using the hybrid Monte Carlo approach as described above. For each Monte Carlo step, we log the starting location in the diffusion map space, as well as the system kinetic and potential energies. Trial moves are proposed via short molecular dynamics runs at $T^* = 0.8$ for 250 steps at $dt^* = 5 \times 10^{-3}$. Upon completing this step, we calculate the diffusion map coordinates for the tagged cluster. We use the harmonic

biasing potential given in Equation 7.7 with $\kappa = \kappa_i = \kappa_j = 1250 k_{\mathrm{B}}T$ over the dimensionless diffusion map coordinate space. We accept or reject trial moves via Equation 7.9, where we observe approximately 30-40% move acceptance using these conditions. We perform 1.6×10^4 Monte Carlo steps in this fashion, allowing for equilibration to these biasing conditions by running first for 8×10^3 steps, followed by data collection for the remaining 8×10^3 steps.

Having conducted the ensemble of biased umbrella sampling runs over the manifold, we patch together the biased probability distributions to estimate the maximum likelihood unbiased free energy landscape $\beta F(\vec{\Psi})$ using the BayesWHAM algorithm presented in Ref. [226]. This approach is a Bayesian implementation of the weighted histogram analysis method (WHAM) [110] that enables a statistically optimal estimation of the free energy landscape, and provides a clear method of evaluating uncertainty in estimates. This landscape allows us to determine the fitness of each building block design within the generation and deploy an optimization strategy to rationally sculpt the landscape to favor the target self-assembled aggregate.

Building block optimization via CMA-ES

Having captured the self-assembly free energy landscape for a population of colloids, we wish to measure some feature on the landscape to serve as a fitness metric over which to optimize. A variety of choices can be made in deriving the fitness of our species, such as binding polynomial estimates of the formation rate [227] or string methods to minimize the reaction path between monomers and our desired aggregate [228–230]. In this work, we choose a simple measure of fitness as the free energy gap between the desired aggregate and the most stable competing structure. The goal of this fitness metric is to stabilize our desired self-assembled state over other possible assembled aggregates. We simplify this further by binning regions of the free energy landscape to their inherent structure [231], the nearest local free energy minima to which a downhill trajectory would reside. This reduces the noise in our estimates, focusing instead on the metastable free energy wells in our system.

Having developed a measure of fitness for each building block architecture in a generation, we now seek to integrate information about these building blocks to perform data-driven predictive design of a subsequent generation of building blocks. Many possible optimization techniques exist, from gradient descent [203] techniques to swarm techniques [232] to evolutionary strategies [206]. Here we use the covariance matrix adaptation evolutionary strategy (CMA-ES) [206, 207], as an evolutionary strategy to direct our building block designs towards those of improving fitness. For each generation, CMA-ES selects the top μ samples from our population and uses their locations in feature space to update the estimate of the covariance matrix $\mathbf{C}$ and the step size in feature space, σ. The full details of this adaptation procedure for the covariance matrix and step size are given in Ref. 207. Having updated our covariance matrix and step size we compute a new population of N building block designs in iteration $i+1$ as

$$\vec{x}_{i+1} = \langle \vec{x}_i \rangle_\mu + \sigma \mathcal{N}(0, \mathbf{C}), \tag{7.10}$$

where $\langle \vec{x}_i \rangle_\mu$ is the mean of the i-th generation's top μ candidate structures, and $\mathcal{N}(0, \mathbf{C})$ is the multi-dimensional normal distribution with mean 0 and covariance $\mathbf{C}$. Given this new generation of building blocks, we check for convergence on the distribution of samples in the polar angle feature space, cutting off when the standard deviation in a generation is $< 1^\circ$ in each of ϕ_B, ϕ_C. If not yet converged, we continue through the full process again, performing unbiased Langevin dynamics simulations for the new generation, applying diffusion maps and conducting umbrella sampling to determine free energy surfaces, and conducting another round of CMA-ES. In this way, we devise a data-driven optimization framework able to iteratively converge to a desired building block architecture. Since this approach proceeds by engineering features of the underlying free energy landscape to maximize a building block fitness metric, we term this approach "landscape engineering".

7.3 Expert-directed optimization of patchy icosahedral formation

From previous study of this system [9, 125], icosahedra form from a double-ring patchy colloid with polar angles $(\phi_B^0, \phi_C^0), = (70.6°, 49.0°)$. While this patchy colloid model has proven to stably form icosahedra, we wished to probe the effectiveness of landscape engineering to improve patchy colloid architecture over an expert design with the polar rings placed to maximize contact between the sticky patches within an idealized icosahedral aggregate.

7.3.1 Data-driven inverse design

We start our optimization procedure with a 3×3 grid of $N = 9$ initial configurations in (ϕ_B, ϕ_C) space around the center (ϕ_B^0, ϕ_C^0), with spacing $\pm 5°$ in each dimension, $\{(\phi_B^1, \phi_C^1)\} = \{(\phi_B^0, \phi_C^0), (\phi_B^0 \pm 5°, \phi_C^0 \pm 5°)\}$. For each architecture, we run three unbiased simulations with differing random seeds to sample the variety of aggregate structures that can be formed. We perform a two-stage landmarking procedure to identify representative cluster topologies. First, for each architecture we generate $K = 400$ landmarks from data accumulated from these three unbiased simulations. Next, we aggregate these landmark points across all architectures and perform another round of landmark selection, resulting in a set of $K = 400$ composite landmarks spanning the aggregates sampled by all nine architectures.

We utilize these $K = 400$ composite landmarks to generate the composite L-dMap characterizing the configurational self-assembly space of our population of colloid structures. In each case a gap in the eigenvalue spectrum informs a two-dimensional embedding into the leading eigenvectors (Ψ_2, Ψ_3). We observe that these eigenvectors emerge from an application of diffusion maps to the ensemble of structures explored in the unbiased simulation runs, and so differ between generations. Using the hybrid Monte Carlo approach discussed in Section 7.2.3, we perform umbrella sampling for each colloid architecture to sample over this landscape. Having sampled across these different umbrella windows, we reconstruct the

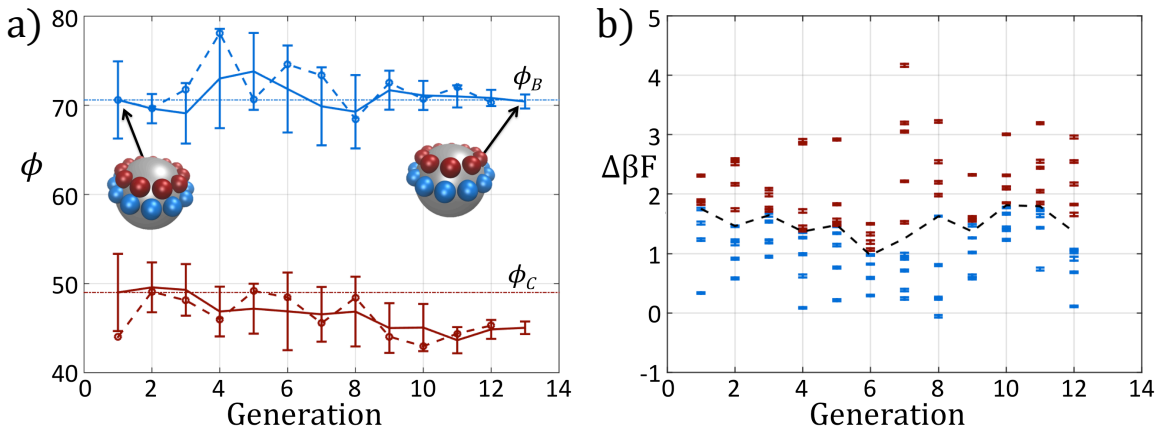

Figure 7.3: Optimization results for an icosahedron-forming patchy colloid via landscape engineering. (a) The distribution of polar angles for each generation of the optimization procedure. In solid blue (red) we show the mean polar angle ϕ_B (ϕ_C), along with the standard deviation in angles within each generation. The colored blue and red dashed lines, with corresponding circular markers, correspond to the fittest member of each generation. The horizontal dashed-dot lines correspond to the polar angles of the initial expert designed architecture $(\phi_B, \phi_C) = (70.6°, 49°)$ based on the optimal alignment of patches within an idealized icosahedral cluster. (b) The fitness $\Delta\beta F$ of each candidate in each generation. Here we color in blue the top $\mu = \lfloor N/2 \rfloor$ candidates from each generation which are used to adapt the covariance matrix in CMA-ES. The remaining samples that are neglected in red. The black dashed line indicates the boundary between these subsets.

free energy landscape for self-assembly using the Bayes WHAM technique [226]. Finally, we compute the inherent structures over the free energy landscape for each colloid to find free energy wells representing the locally stable cluster structures. We compute the fitness of each landscape as the difference between our desired icosahedral structure and the free energy well of the most stable competing aggregate, $\Delta\beta F = \beta F_{\text{icos}} - \beta F_{\text{min}\neq\text{icos}}$.

Employing $\Delta\beta F$ as a measure of the fitness of each colloidal architecture, we pass these fitness values to the CMA-ES algorithm, which selects the top $\mu = \lfloor N/2 \rfloor$ candidates over which to perform data-driven predictive design of the next generation of candidate architectures. We start the optimization procedure with covariance matrix $C = \mathbf{I}$, step size $\sigma = 5°$ and evolution paths $\vec{p}_C = \vec{p}_\sigma = \vec{0}$. The CMA-ES algorithm updates the covariance matrix and evolution paths, providing the distribution from which to draw new colloid architectures. We impose no restrictions on the range of allowable polar angles for either

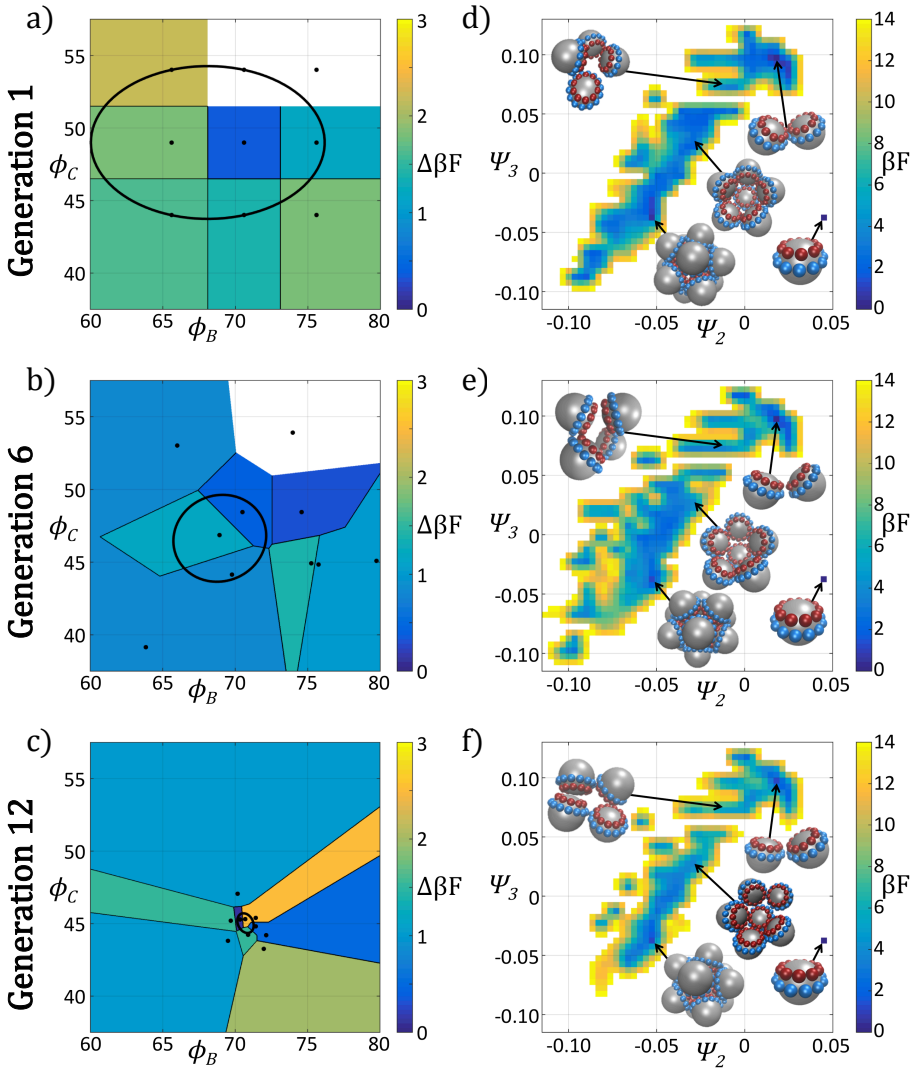

Figure 7.4: Plots of the polar angles of each member of the generation and free energy landscapes in generations 1, 6, and 12 of the optimization procedure. In (a)-(c) we illustrate the polar angles (ϕ_B, ϕ_C) of each of the N members in each of the three generations, where $N = 9$ in generation 1 and $N = 10$ in generations 6 and 12. We partition the design space spanned by the two polar angles using a Voronoi tessellation that demarcates the regions of space closer to each candidate than any other. We color each Voronoi cell by the fitness $\Delta\beta F$ of that candidate. The ellipse drawn in each of (a)-(c) corresponds to the current covariance matrix after running the new population through the CMA-ES optimizer. In (d)-(f) we present the self-assembly free energy landscapes for the fittest candidate in the generation projected in the top two collective variables furnished by the diffusion map (Ψ_2, Ψ_3). To permit comparisons between the landscapes computed for each generation, we construct composite diffusion map embeddings over the three systems so the collective variables (Ψ_2, Ψ_3) are identical between the three systems. The arbitrary zero of the free energy in each system is specified by asserting that the monomer has $\beta F = 0$. In each case we illustrate the locations in the low-dimensional embeddings corresponding to the monomer, icosahedral target aggregate, half-icosahedron, tetramer, and dimer.

ring, allowing for overlap or reordering of the top and bottom rings. Using Equation 7.10, we draw N=10 samples from this distribution to construct the next generation of colloidal architectures $\{(\phi_B^2, \phi_C^2)_i\}_{i=1}^{10}$ predicted by CMA-ES to have improved fitness (i.e., enhanced stability of the target icosahedral aggregate). We continue iterating until the distribution of new configurations is sufficiently small – less than 1° in $\{(\phi_B^n, \phi_C^n)\}$ – at which point we declare the optimization procedure to have converged. The fittest candidate within this terminal generation represents the optimal design produced by our procedure.

We present the sample paths of our data-driven optimization procedure in Figure 7.3. Looking at the distribution of polar angles over generations, shown in Figure 7.3a, we observe that the optimization procedure fluctuates around the expert-derived polar angles for several generations, but after four generations the interior polar angle ϕ_C deviates from our expert-derived value by moving closer to the particle zenith. At the end of 12 generations our optimization converges and we arrive at a final population with a standard deviation of less than 1° around the mean of $(\phi_B, \phi_C) = (70.7°, 45.0°)$. This optimization procedure promoted the use of a building block with inner polar angle ϕ_C shifted 4° towards the zenith from the initial expert system, meanwhile proposing a negligible deviation in ϕ_B.

In Figure 7.3b we show the fitnesses of each candidate in each generation. In the early stages of the optimization procedure, the fitness metric $\Delta\beta F$ cannot be directly compared between generations since the underlying free energy surface is parameterized by different collective variables $\{\Psi_2, \Psi_3\}$. However, the CMA-ES procedure acts *within* a single generation, and so identifies the top candidates and proposes a predictive optimization step within a unified fitness basis. In the latter stages of the optimization as the particle designs converge, the fitness metrics do become comparable since the particle designs converge and the basis vectors stabilize between generations.

In Figure 7.4 we show the ensemble of colloidal architectures in generations 1, 6, and 12 of the optimization process (panels a-c), and free energy surfaces showing the stability of the various competing self-assembled aggregates for the fittest candidate in each generation (d-f).

Figures 7.4a-c show that the fitness landscape in the design space of the two polar angles is quite rugged. Nevertheless, the CMA-ES is able to ably handle this rugged topography and the covariance matrix shrinks and converges to the optimum design over the course of the 12 generations. This reduction in the search space eventually leads to a converged particle geometry of $(\phi_B, \phi_C) = (70.7°, 45.0°)$. Figures 7.4d-f show the modulation of the underlying free energy landscape imposed by CMA-ES optimization of the polar angles. Using the fittest colloid structure for each generation from the CMA-ES optimizer, we construct a single composite diffusion map to enable inter-generational landscape comparison. We utilize the same landmarking strategy described above to allow for computationally efficient embedding of points in the diffusion map space, and free energy landscapes for each generation's building block are constructed using the procedure described in Section 7.2.3.

The first generation in Figure 7.4d shows that the primary mechanism for icosahedral formation is through a single energy valley from $(\Psi_2, \Psi_3) = (-0.025, 0.050) \rightarrow (-0.055, -0.040)$ with $\Delta F \approx -1 k_{\mathrm{B}} T$ along this pathway, connecting small assembled aggregates to the icosahedron. This assembly pathway has been previously described in Refs. [35, 43, 125], as the monomeric addition pathway describing the sequential locking of new colloids into the aggregate structure. There exists at the icosahedron state a small energy well, serving as a metastable state for the assembly process at free energy of $F_{\mathrm{icos}} = 0.4 k_{\mathrm{B}} T$ with respect to the monomer free energy. The assembly of larger aggregates proceeds via attachment to the icosahedral surface, or via formation of a misassembled icosahedron, as observed by the low-free energy pathway leading to large aggregates at $(\Psi_2, \Psi_3) = (-0.100, -0.100)$.

The optimization procedure leads to structural shifts in the free energy landscape across generations. By generation 6 the stability of small sized clusters is reduced, leading to a widening and flattening of the free energy valley observed in the first generation. The volume of configuration space marking the transition between small and large cluster regimes, located at $(\Psi_2, \Psi_3) \approx (-0.025, 0.060)$, is expanded, making the formation of these larger clusters easier. The formation of aggregates larger than the icosahedron is disfavored, as il-

lustrated by elevation of the free energy of the pathway towards $(\Psi_2, \Psi_3) = (-0.043, -0.075)$. Interestingly, the free energy of the target icosahedron relative to the monomer has actually increased relative to generation 1, raised slightly to $F_{\text{icos}} = 1.2k_{\text{B}}T$, corresponding to an increase of $0.8k_{\text{B}}T$. This initial decrease in fitness is due to exploration of the design space by CMA-ES with a rather large covariance matrix prior to tightening of this distribution and convergence to an optimal design in the latter stages of the process.

Continuing the optimization procedure through generation 12, we observe a marked improvement in landscape features. The monomeric-assembly valley has narrowed from generation 6 and the landscape has been further tilted to drive assembly from small clusters to the icosahedron, reaching $F_{\text{icos}} = 1.1k_{\text{B}}T$. Upon transitioning over the small cluster barrier regime, assembly occurs downhill to the icosahedral sink state that serves as a local minimum, competing with the dimer state existing at $F_{\text{dimer}} = 0k_{\text{B}}T$, which has increased in energy by $0.6k_{\text{B}}T$ from generation 6 to 12. Dynamic simulations also reveal that the icosahedra are strongly kinetically stabilized (Section 7.3.2), wherein once formed we never observe icosahedron dissociation on the time scale of our simulations. Furthermore, large aggregates populating the lower left corner of the intrinsic manifold have been destabilized, leading to fewer misassembled massive clusters. Moreover, the smooth character of the free energy surface around the icosahedron means that those defective aggregates that do form can easily tumble down into the icosahedral minimum, providing this target structure with a large basin of attraction in configurational space.

In sum, using only the simple fitness measure of relative stability for the desired icosahedral configuration, our data-driven design strategy has effected drastic changes to the landscape. As illustrated in Figure 7.3a, ϕ_B remains unchanged from the initial architecture, and by decreasing ϕ_C by only $4°$, our optimal design has destabilized the formation of large aggregates by disfavoring promiscuous bonding between particles and enlarged the basin of attraction for the desired icosahedral target.

7.3.2 Validation of optimal design

Our landscape engineering strategy sought to optimize the thermodynamic stability of the target icosahedral aggregate by sculpting the underlying self-assembly free energy landscape. Optimization of this simple fitness metric does not appeal to any kinetic concerns, and it is possible that although the icosahedron is a local free energy minimum, that assembly may become kinetically trapped in an undesired trap state. To provide an independent validation that the optimized architecture really does lead to improved assembly characteristics, we compare the yield of icosahedral capsids formed for our optimized building block against the expert building block in Figure 7.5. For each system, we perform 10 independent Langevin dynamics simulations containing 125 randomly positioned colloidal building blocks for 10^7 time steps (3.6 seconds under our real unit mapping defined in Section 7.1). Every 250 time steps we count the number of icosahedral capsids that exist in the simulation. Over the course of these calculations we observe an increase in average yield from the expert design with 4.7 ± 0.5 capsids formed to 6.8 ± 0.6 capsids formed for the optimized building block. Modeling assembly using first order reaction kinetics, we can extract effective rate constants for the incorporation of particles into icosahedral aggregates for each of the two building block designs. For each system, we compute the fraction of monomers belonging to icosahedron as a function of time, $f(t)$, and fit the first-order kinetics $f(t) = 1 - e^{-kt}$, where k is the rate constant for aggregation and t is the time. Using this functional fit, we can assess the rate of icosahedral formation between the two systems, with $k_{\text{exp}} = 0.21 \pm 0.03/s$ and $k_{\text{opt}} = 0.37 \pm 0.03/s$, where the uncertainty corresponds to a 95% confidence interval. This analysis reveals that our optimized building block that was designed purely on the basis of thermodynamic stability leads to 76% improvement in aggregation rate.

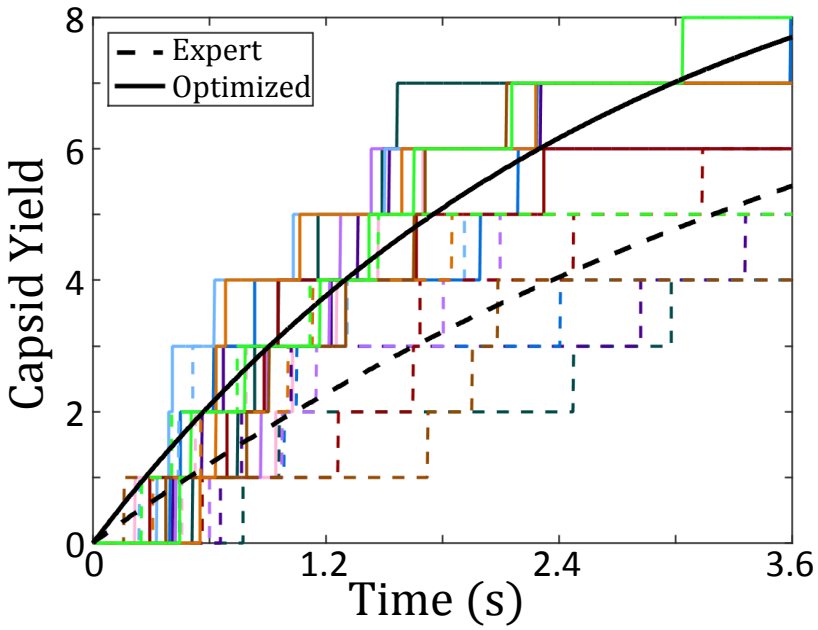

Figure 7.5: Icosahedral capsid yield as a function of time for the original and optimized building block architectures. Each color corresponds to an individual simulation, with dashed lines being the expert-derived system and solid lines as the optimized building block. Black lines correspond to fits of the capsid formation process as a first-order reaction of the form $f(t) = 1 - e^{-kt}$ where $f(t)$ is the fraction of colloidal particles that exist within icosahedral aggregates and k is the effective first order rate constant. The rate constant for the initial expert designed building block is $k_{\text{exp}} = 0.21 \pm 0.03/s$ whereas that for the optimal design discovered by our inverse design protocol is 76% larger at $k_{\text{opt}} = 0.37 \pm 0.03/s$.

7.3.3 Analysis

This building block design platform is capable of significant improvement in the assembly of icosahedral aggregates when seeded by an expert configuration. By manipulating the free energy landscape for self-assembly, the procedure is able to systematically tilt and shrink the primary pathway driving assembly from small aggregate clusters to icosahedra, stabilizing and favoring the assembly of these target aggregates and destabilizing competing structures. Despite performing design based on an exclusively thermodynamic fitness metric, there is also a 76% improvement in yield as compared to the expert-designed system. This result demonstrates the pitfalls in utilizing expert knowledge in building block design, since the many-body collective dynamics can be highly unintuitive and rugged underlying assembly

landscapes mean that small changes to the particle design can have a large impact on the assembly behavior. Data-driven inverse design techniques can exploit expert knowledge as a good initial candidate and use this initial guess to design self-assembling building blocks with greatly improved assembly behavior.

7.4 Octahedral building block optimization from a poor initial configuration

Having shown the effectiveness of this technique in improving the design of icosahedral forming building blocks around an expert-guided starting configuration, we sought to validate this method by considering the optimization of a structure far from the starting configuration. In this system, we use the final building block architecture for icosahedra above, $(\phi_B, \phi_C) = (70.7°, 45.0°)$, as a starting point for the optimization of target octahedral structures. This new structure shares a similar hollow structure to the icosahedron, but previous studies have shown that the polar angles required to stabilize octahedra are quite different with polar angles based on the optimal geometric alignment of particles in an idealized octahedral aggregate of $\phi_B = 50.7°, \phi_C = 39.3°$[9].

7.4.1 Data-driven inverse design

We start with an identity covariance matrix, $\mathbf{C} = I_2$ and $\sigma = 5°$, and generate a set of new configurations around this start point using Equation 7.10. We use the same update, landmarking, and sampling procedures as described in Section 7.3, modifying the fitness measure now to be for the relative octahedral free energy, $\Delta\beta F = \beta F_{\text{oct}} - \beta F_{\text{min}\neq\text{oct}}$. In this case, our initial candidate architecture is such a poor guess that it does not form any target octahedra over the course of our unbiased or biased calculations. Despite this lack of direct sampling, the landscape engineering approach readily predicts the location of the

octahedral structure by Nyström extension (Chapter 2.1.1) of the idealized octahedron onto the diffusion map manifold, providing a means of approximating the free energy of the octahedral aggregate with which we measure building block fitness. We observe convergence in the polar angles after 12 generations, yielding a 13th generation with a standard deviation of $< 1°$ in both polar angles prompting the termination of this optimization procedure.

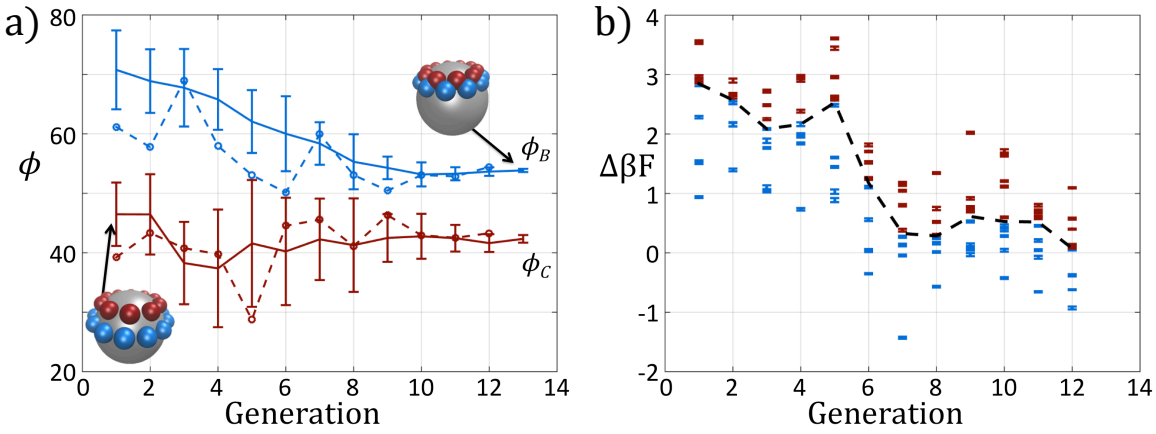

Figure 7.6: Optimization results for an octahedron-forming patchy colloid via landscape engineering. (a) The distribution of polar angles for each generation of the optimization procedure. In solid blue (red) we show the mean polar angle ϕ_B (ϕ_C), along with the standard deviation in angles within each generation. The blue and red dashed lines, with corresponding circular markers, correspond to the fittest member of each generation. (b) The fitness $\Delta\beta F$ of each candidate in each generation. Here we color in blue the top $\mu = \lfloor N/2 \rfloor = 5$ candidates from each generation which are used to adapt the covariance matrix in CMA-ES. The remaining samples that are neglected in red. The black dashed line indicates the boundary between these subsets.

We present the results of this optimization of polar angles for octahedral forming patchy colloids in Figure 7.6. We see a steady decline in the exterior ring angle ϕ_B through 8 generations of this optimization scheme, eventually converging around $\phi_B = 53.7°$. Meanwhile the interior polar angle stays roughly constant, oscillating around it's starting position until stabilizing at $\phi_C = 42.0°$ during the final iteration. We can see that this procedure only takes 12 completed generations to fully converge, having only attempted 120 unique building block architectures in this 2D feature space to yield a finalized design. The optimized colloid design conforms to our expectations, as the polar angles should go down to achieve the 90°

angle between vertices of an octahedron.

We observe a marked improvement in the free energy profile over generations compared to the expert-direct optimization from the previous section. As illustrated in Figure 7.6b the fitness of the first five generations remains rather flat, before the relative stability of the desired octahedron improves precipitously between generations 5 and 7 by 3 kT. The fitness remains approximately stable for the remainder of the optimization course.

The trends in fitness over the optimization course are explained by the behavior of the CMA-ES algorithm in each generation. We show in Figures 7.7a-c an initial large increase in the covariance matrix as the optimization algorithm expands its search area of the rugged design space between generations 1 and 6, followed by shrinking and convergence to the optimum design by generation 12. The structure of the free energy landscape changes quite dramatically over this optimization procedure as illustrated in Figure 7.7d-f. For the initial configuration in generation 1 (Figure 7.7d), we observe a free energy well in this low-dimensional landscape around the icosahedral configuration at $(\Psi_2, \Psi_3) \approx (0.042, 0.045)$, with a valley in the free energy landscape connecting monomers to pentamer and hexamer configurations. There exists a barrier to nucleation of structures above this hexameric regime, which when crossed leads to a valley of connected states driving towards the icosahedral configuration.

By generation 6, shown in Figure 7.7e, the shape of the landscape has adapted to reduce icosahedral stability. The location of the icosahedral configuration now exists as a high-energy state on the boundary of the landscape. This reduction in icosahedral stability comes with an increase in stability for the now formed octahedral well around $(\Psi_2, \Psi_3) \approx (0.025, 0.012)$, with the free energy with respect to the monomer state decreasing from $F_{\text{oct}} = 6.2k_{\text{B}}T \rightarrow 2.1k_{\text{B}}T$. Due to the decrease in polar angles of the inner ring, shifting from $\phi_B = 45.0^\circ \rightarrow 41.1^\circ$, we observe a greater stability of the dimer state due to face-to-face interactions between particle C rings. This dimer stability enables the formation of dimer chains, with dimers interlocking at 90° angles mediated by the exterior particle B rings,

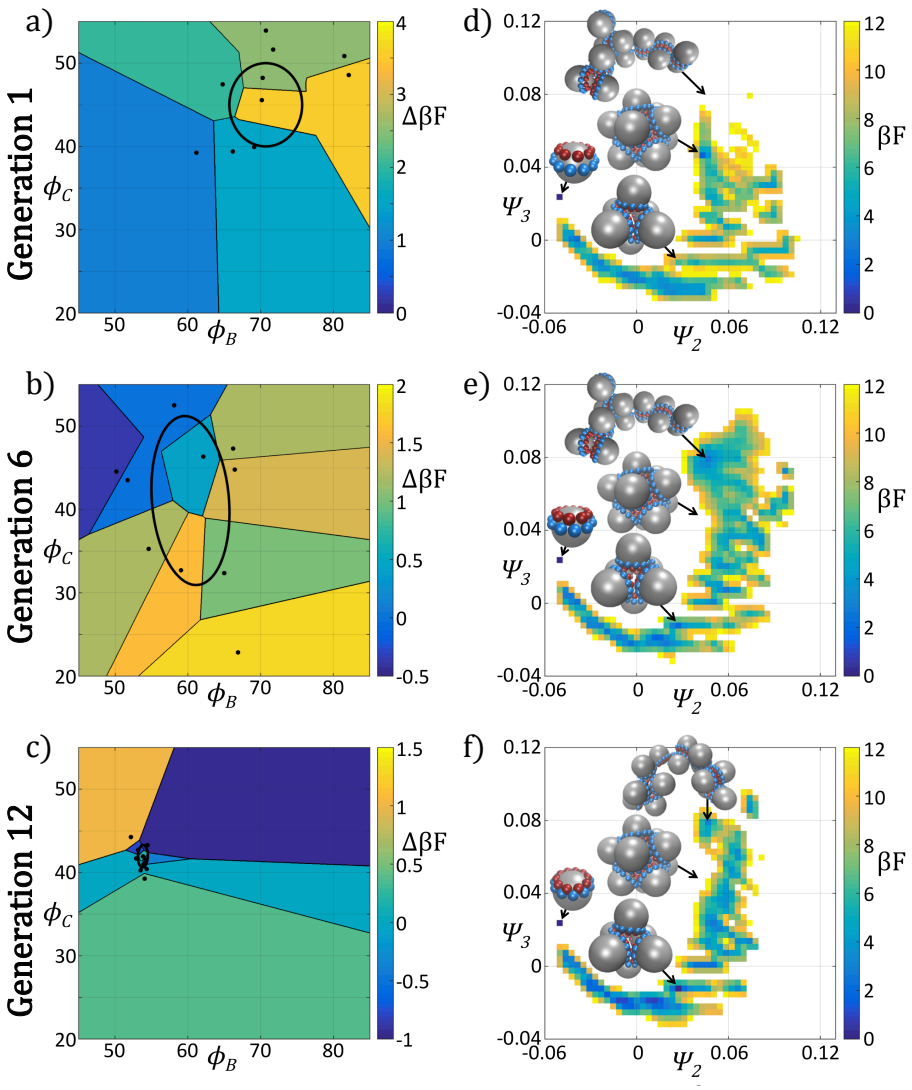

Figure 7.7: Plots of the polar angles of each member of the generation and free energy landscapes in generations 1, 6, and 12 of the optimization procedure. In (a)-(c) we illustrate the polar angles (ϕ_B, ϕ_C) of each of the $N = 10$ members in each of the three generations. We partition the design space spanned by the two polar angles using a Voronoi tessellation that demarcates the regions of space closer to each candidate than any other. We color each Voronoi cell by the fitness $\Delta\beta F$ of that candidate. The ellipse drawn in each of (a)-(c) corresponds to the current covariance matrix after running the new population through the CMA-ES optimizer. In (d)-(f) we present the self-assembly free energy landscapes for the fittest candidate in the generated projected in the top two collective variables (Ψ_2, Ψ_3) furnished by the diffusion map. To permit comparisons between the landscapes computed for each generation, we construct composite diffusion map embeddings over the three systems so the collective variables (Ψ_2, Ψ_3) are identical between the three systems. The arbitrary zero of the free energy in each system is specified by asserting that the monomer has $\beta F = 0$. In each case we illustrate the locations in the low-dimensional embeddings corresponding to the monomer, octahedral target aggregate, icosahedral aggregate, and dimer chains.

which we observe as an opening up of the landscape in the $\Psi_3 > 0.04$ region.

Continued optimization leads to a reduction of the dimer stability, and a subsequent reduction in chain formation as observed in Figure 7.7f at generation 12. By increasing the interior angle now to $\phi_C = 42°$, the face-to-face interaction is now less stable due to an increased protrusion of the central particle surface through the patch ring. The shifting landscape now has completely destabilized the icosahedral configuration, evidenced by a noticeable gap at the icosahedral location. Meanwhile the well around the octahedral state becomes deeper as compared to previous generations, reaching below the monomer free energy at $F_{\text{oct}} = -0.01 k_{\text{B}}T$, while the pentamer state also becomes markedly more stable as a pivotal transition state for octahedral formation. Using only a simple measure of relative structural stability as fitness, this optimization procedure is able to sculpt the structure of the free energy landscape structure, filling in the sinks and troughs around undesirable aggregation states and deepening the wells and basin of attraction of the desired configuration.

7.4.2 Validation of optimal design

Having developed a new building block architecture from our design framework, we validate its ability to form octahedral aggregates by conducting 10 independent Langevin dynamics simulations on a system of 125 randomly positioned colloidal building blocks for 10^7 time steps (3.6 seconds). Every 250 time steps we count the number of octahedral capsids that exist in the simulation. We present our results in Figure 7.8. This new structure readily forms octahedral capsids, with an average yield of 13.3 ± 2.2 octahedra over the course of the simulation runs. This constitutes a greater than 60% yield of monomers into target octahedra. The initial building block design optimized to assemble icosahedra did not form a single octahedron in any of the simulations. Fitting a first order reaction to the octahedral aggregation data yields a rate constant for formation of $k = 0.39 \pm 0.07/s$. In a relatively few number of generations, our optimization approach is able to take an initial poor starting

structure and identify a building block architecture that will preferentially form octahedra with a high degree of specificity and yield. This result is made more impressive as the starting configuration used in the optimization framework does not sample an octahedral aggregate.

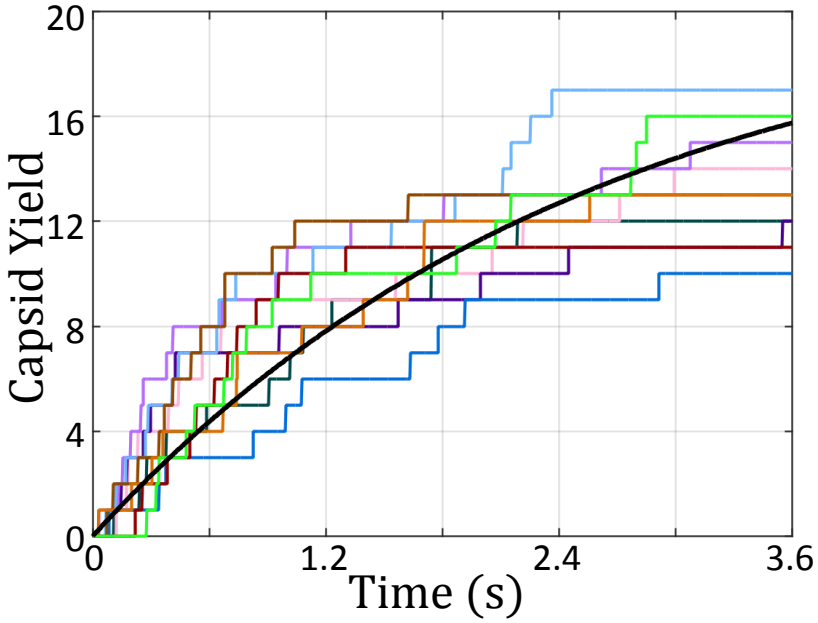

Figure 7.8: Octahedral capsid yield for the optimized colloidal building block. Each color corresponds to an individual simulation, with the black line corresponding to a first-order kinetic fit of the capsid formation process of the form $f(t) = 1 - e^{-kt}$ where $f(t)$ is the fraction of colloidal particles that exist within an octahedral aggregate is k is the effective first order rate constant. The rate constant for the optimized octahedral building block is $k = 0.39 \pm 0.07/s$.

7.4.3 Analysis

This technique is powerful because it can direct the optimization of building blocks even in circumstances where the desired aggregate is not observed. Nevertheless, the CMA-ES procedure is capable of expanding the search space to push the optimization towards the desired structure, ultimately resolving it within the sampling procedure and then rapidly converging to an optimized building block design. Although we have shown our procedure to

perform well from a poor initial design, by leveraging domain specific knowledge on building block geometry and interactions, this technique may be better seeded to reduce the number of generations or improve further upon the expert-designed system. It is at this crossroads that we believe this framework will be best utilized, enhancing the yield or monodispersity of self-assembled systems.

7.5 Conclusion

We have demonstrated a novel building block design framework by engineering the free energy landscape for self-assembly of a desired aggregate, and have tested its efficacy in the design of patchy colloids to form hollow capsid structures. Many-body diffusion map dimensionality reduction enables the reconstruction of the low-dimensional intrinsic manifold for self-assembly, providing a reduced set of collective order parameters that describe the self-assembly dynamics. Hybrid Monte Carlo is employed to sample directly in the low-dimensional diffusion map space, and by biased umbrella sampling we can construct free energy surfaces over our assembly landscapes. These free energy landscapes capture the key thermodynamic and kinetic details driving self-assembly behavior. By sampling the free energy landscape for a variety of different building blocks, we are able to understand how properties of the building block geometry affect features of the energy landscape. Ultimately, by applying optimization algorithms we perform data-driven inverse design to sculpt the free energy landscape to favor particular target aggregates and identify promising building block structures capable of robust self-assembly of a desired aggregate.

We test this design platform in the formation of icosahedral and octahedral clusters from a double ring patchy colloid model. The design process, having started with the expert-defined colloid configuration, proposed a new patchy colloid that showed an 76% improvement in aggregation rate. By marrying expert knowledge with building block design engines, we believe this technique will offer a useful methodology in the continued development of novel mate-

rials systems formed via bottom-up self-assembly. In an instance where expert-knowledge is lacking this technique can still suggest building blocks capable of reliably forming into a desired terminal aggregate. We start the optimization of octahedral-forming patchy colloids from our icosahedral-forming colloid, a scenario where the octahedron is highly unstable. Through continued iteration of the free energy landscape, our technique dissolves the energy pathway leading to formation of icosahedra, and develops a new energy well around the octahedral configuration. The converged building block architecture proposed by this landscape engineering platform is capable of reaching 60% yield in tests of octahedral capsid formation.

We foresee the application of machine learning techniques to continue improving the development of next generation self-assembly systems. Machine learned order parameters have been widely used to improve our understanding of the protein folding free energy landscape and folding dynamics [55, 57, 70, 188], requiring rapid exploration and sampling of the low-dimensional manifolds [83, 233]. Here we propose a novel means of sampling free energy surfaces directly in the low-dimensional self-assembly space furnished by diffusion map dimensionality reduction. While the system studied here were simulated, we have previously demonstrated the application of diffusion maps directly to particle tracking experiments of Janus colloid self-assembly [118]. Working in tandem with experiment and simulated data sources, we believe landscape engineering can provide a platform for continued improvement in the design of self-assembly systems. Moving beyond colloidal assembly, we believe this same framework can be employed in the study of molecular self-assembly – as illustrated in a recent application of many-body diffusion maps in the study of asphaltene aggregation, a primary foulant in crude oil extraction [234]. Accordingly, we envision our approach being of use in the engineering of a variety of self-assembling materials of scientific and technological importance, including organic electronics [18, 213], tissue scaffolds [235], and cell-penetrating peptides for antimicrobial therapies [12, 13].

Chapter 8

Conclusion and future work

This dissertation applies and develops nonlinear manifold learning techniques to understand and engineering self-assembling colloidal materials. Harnessing techniques from statistical mechanics, nonlinear dimensionality reduction, and graph theory, we developed a novel means to recover the low-dimensional manifold describing the structural morphology of self-assembled aggregates. We also developed technical innovations to enable application of our approach to more voluminous and higher velocity data sets than was previously possible. By combining our approach with state-of-the-art optimization techniques we establish a data-driven inverse building block design framework that sculpts the self-assembling free energy landscape to maximize the stability and yield of a desired target aggregate structure. In application of these techniques, we demonstrate the usefulness of this technique both in improving our understanding of simulated and experimental self-assembly processes, and in the manipulation of colloid architectures to improve the assembly of a target structure.

8.1 Summary of work

The first portion of this work (Chapters 2-5) we developed a new many-body diffusion map platform and tested it on a variety of systems, simulated and experimental, to highlight the effectiveness of this technique in understanding the mechanisms and pathways driving self-assembly. In Chapter 6, we turned back to the diffusion map in an attempt to improve the runtime performance for out-of-sample embedding, a problem plaguing use of diffusion maps in real-time or computationally intensive settings. In Chapter 7, we leverage these

developments to perform data-driven inverse design of polyhedral-forming patchy colloids.

In Chapter 2, we discuss the diffusion map and a many-body distance measure for self-assembly systems based on graph alignment techniques. The diffusion map, a nonlinear dimensionality reduction technique, is used extensively in the realms of biophysical simulation [55, 57, 72, 83, 188, 213]. Owing to the problems of many-body systems, namely particle fungibility and varying numbers of particles, the application of diffusion maps to self-assembly have been previously stymied. Here we propose a graph-based distance measure, owing to the effectiveness of graphs to store structural information [89]. The specific form of the distance function may vary between problems, however the general principle is to use graph alignment between cluster bonding networks to find a permutation that minimizes the distance between network architectures. This choice of distance measures enables a direct comparison between particle clusters allowing for the application of diffusion maps. This distance measure is not without faults as it is very computationally expensive. In many circumstances this can be mitigated by trading accuracy for performance to enable the application of this algorithm to large systems.

To validate and test this method's ability to extract the low-dimensional self-assembly space, we model a class of polyhedral-forming patchy colloids in Chapter 3. This model system, a double annular ring patchy colloid developed by Glotzer et al. [9], offers several simple design variables, the strength of patch interactions and the polar angles for the different patch rings, which induce large deviations in assembly character. Employing our many-body diffusion map approach, we are able to systematically infer the assembly pathway driving tetrahedral cluster aggregation and the temperature dependent mechanisms driving a deviation between tetrahedral and dimer-chain formation.

On a set of patchy colloids designed to form icosahedra, we observed two competing mechanisms for self-assembly that have been previously been demonstrated by Wilber et al. [35, 43], a monomeric-addition pathway and a budding pathway from a liquid-like aggregate. Our approach was able to validate the existence of these two pathways. By construction of a

classifier over the diffusion map space we were able to elicit out the temperature-dependent flux along each of these pathways leading to the formation of icosahedra, and provide a general design rule for the relative patch strengths that would maximize aggregate yield. This work demonstrated the capacity of our approach to reveal the microscopic mechanisms and pathways driving assembly behavior by discovering a low-dimensional description of the self-assembly phase space.

Having shown the effectiveness of this technique in simulated self-assembly, we approached the problem of experimental Janus colloid assembly in Chapter 4. Janus colloids, hemispheric patterned particles capable of being functionalized with different chemical and functional characteristics, possess rich assembly behaviors and offer an ideal computationally and experimentally-accessible model for studying particle anisotropy and external conditions on assembly behavior. Here we leveraged particle tracking techniques to analyze the two-dimensional self-assembly of a class of metallodielectric Janus colloids under an applied AC electric field.

Using our many-body diffusion map approach we were able to systematically infer the low-dimensional assembly landscape for a set of heterogeneous and homogeneous colloid mixtures. In the heterogeneous case we identified three distinct assembly regimes corresponding to dense disordered clusters, three-armed pinwheels, and extended archipelago topologies. Generating histograms over our assembly landscapes offered a means of measuring the relative stability of different aggregate morphologies. By manipulating the AC frequency, we showed that the stability of aggregation regimes could be tuned in good agreement with the physical understanding for AC field response on Janus colloids. For a homogeneous system of Janus colloids, we recovered the assembly landscape and in using this landscape suggested design rules for the experimental controls to improve the yield and specificity of different aggregation states. This effort represented the first time that machine learned order parameters and assembly landscapes had been inferred directly from experimental data.

In the study of digital colloids presented in Chapter 5, we shift from investigating the self-

assembly of distinct colloids and focus instead on the self-organization of a colloidal cluster. Digital colloids, a lock-and-key arrangement of "halo" particles able to freely move over the surface of a central particle, have been proposed as a novel means for soft information storage. Using our machine learning framework, we were able to identify and map the structural transitions between different colloidal bit states for a two-state tetrahedral and 30-state octahedral digital colloid.

Using this framework, we mapped the key engineering design challenge in the practical application of these digital colloids for data storage, the tradeoff between the work required to change the state of the particle assembly and write information and the error rate in storing information due to unintended state changes induced by thermal noise. By constructing the free energy landscape in our low-dimensional manifold we computed the relative stability of the different bit states for these digital colloids from swelling or shrinking of the central particle. We determined the error rate in information storage by calculation of the mean-first passage time between bit states. This work highlights the efficacy of this technique in the design of novel materials systems by eliciting the key physical properties necessary to experimentally realize these digital colloids.

In Chapter 6 we propose a novel extension of the diffusion map to operate on a subset of data, so-called landmark diffusion maps. By leveraging the neighborhood size used in generating the diffusion map, we can systematically identify a small set of optimally located landmark points that provides adequate coverage of the full data set. Constructing a weighted diffusion map over these landmarks allows for the high accuracy construction of the low-dimensional landscape using only a fraction of the data. We demonstrate the usefulness of this technique on the canonical Swiss roll data set and on two biophysical systems, $C_{24}H_{50}$ and alanine dipeptide, where distance computation is similarly expensive as our many-body distance measure. For the latter two systems, using our landmark procedure yields upwards of 95% reconstruction accuracy using less than 4% of the full ensemble, allowing us to realize 25- to 50-fold speedups with very little loss of accuracy. This development opens the door for

landmark diffusion maps to be used in a variety of large-scale scenarios that were previously inaccessible including high-volume and high-velocity applications in anomaly detection [236] and computer vision [237].

The culmination of this work is the building block design framework using landscape engineering presented in Chapter 7. Using landmark diffusion maps with our many-body distance measure and hybrid Monte Carlo sampling, we are able to sample the free energy directly over the low-dimensional self-assembly landscape. Applying directed evolutionary optimization techniques to ensembles of these free energy landscapes permits the rational manipulation of building block properties to sculpt features of the landscape.

We utilized this design platform in the optimization of the double ring patchy colloid model used in Chapter 3. Starting from the icosahedron-forming particle previously studied, our method converged on a patchy colloid that improved the yield of icosahedra by 45%, a marked improvement over the expert-designed colloid. By changing our objective function to optimize the stability of octahedra over icosahedra, our approach rapidly converged the free energy landscape toward octahedral formation and proposed a new particle geometry that achieved 60% yield of octahedrons. This result highlights the effectiveness of this design framework working in tandem with experts and in generating building blocks where expert knowledge is only loosely able to direct the search process.

This dissertation is focused on the development of a machine learning toolset to improve the understanding and design of colloidal building blocks that preferentially self-assemble into desired aggregates. By leveraging information from both simulation and experiment, these tools are able to extract the intrinsic self-assembly landscape, offering new insights on the microscopic mechanisms driving assembly phenomena. By mixing high performance computing techniques and improved dimensionality reduction algorithms, we are able to readily sample the free energy landscape for self-assembly, akin to the rugged energy funnels described in the "new view" of protein folding. We foresee these tools emerging as a powerful means to marry simulation, theory, and experimental data, ultimately improving the

development cycle for next generation materials fabricated via bottom up self-assembly,

8.2 Future directions

We envision several key directions based on the work established in this dissertation that we believe will prove fruitful in the application and development of machine learning applications for materials self-assembly.

The first such area of continued research should be in the validation of these techniques with experimentally realizable systems. Having previously shown the effectiveness of these techniques in the analysis of experimental Janus colloid self-assembly, an important next step is to experimentally realize a computationally designed building block to validate the efficacy of our design framework. This brings about a range of challenges, the first and most difficult of which is the concept of experimental control. Simulation trajectories offer exquisite control of the self-assembly process, able to consider idealized and monodisperse building blocks and isolate the specific factors that induce observed structural changes. Achieving the same reproducibility in experiment is far more challenging. It would be interesting to observe whether the proposed design platform is able to readily handle this added difficulty in the optimization of colloidal building blocks. Further, additional changes must be made to the optimizer to ensure that the proposed building blocks or experimental controls are feasible, requiring changes to the algorithm that impose boundary conditions on the experimental feature space and explicitly treat particle polydispersity and uncontrolled experimental variables. Thirdly, there is additional noise necessarily generated during the tracking of particle locations in experiment, with particles entering and leaving the reference frame during an experimental run. These fluctuations may require additional algorithmic developments to ensure that the sampled configurations are whole and fully observable for long periods. Finally, alternative strategies for generating free energy landscapes should be explored, such as the diffusion-map directed exploration techniques proposed by Clementi

et al. [73, 233], to improve the efficiency and efficacy of free energy landscape recovery using enhanced sampling.

The next area of potential interest in expanding on this work is in the optimization of more complex feature spaces. The work presented in Chapter 7 seeks to optimize particle geometry by modifying the two polar angles defining the location of the two patchy rings. Further optimization could be done on the interaction strengths of each patch type, leading to a 4D optimization surface in which to investigate improved building block designs. The complexity of optimizing over this higher dimensional design space will necessitate improvements to the sampling procedure, making more efficient use of computing power to generate free energy landscapes. Continued expansion of the design space could include things like changing patch size in each ring, or moving to a different patchy colloid model offering direct control of the location, size, and types of each surface patch. A simple discrete patchy colloid model has been previously studied by Wilber et al. [35, 43], where the location and size of patches could be independently manipulated to test the effect these controls had on the self-assembly of polyhedral aggregates. To be more in line with experimental fabrication of patchy colloids, it would be interesting to optimize a patchy colloid system defined by a probability distribution over the feature space. Errors in the fabrication process can lead to a polydisperse set of colloids. Testing this design framework on a class of colloids with a degree of noise in the feature space would more closely mimic the real world challenges related to self-assembly and help bolster this technique in future applications.

A third area that has already shown some promise is in taking this platform away from finite-sized aggregates and looking at the formation of colloidal crystals. A recent collaboration with the Panagiotopoulos group at Princeton has demonstrated that our technique can be employed to improve the classification of colloid topologies during crystallization well beyond current state of the art techniques [67]. The Network Graph Analysis (NGA) technique proposed in this work utilized the many-body diffusion map to identify the low-dimensional manifold describing the geometry of the bonding network for a particle in a crystal. By

forming a classifier over this manifold, we were able to readily identify the crystal structure around a colloid, including defective and surface states that were previously challenging to classify. We also provide a means of imparting relative character to these different classifications, allowing for intermediate crystallization states to be identified. Harnessing this technique alongside our design framework, we believe it possible to ultimately design particles that control the polycrystalline nature of colloidal crystals, improving their efficiency in a variety of different optoelectronic and catalytic applications [238].

A final area of interest is in adaptation from colloidal to polymeric building blocks. Peptides and proteins have been widely studied in single molecule experiments and simulation to ascertain the folding pathways driving conformational change, however the computational study of the self-assembly of these peptides is still in its infancy. General strategies have previously employed cluster size distributions, using bonding measures to try and distinguish between the different alignment regimes between peptide chains [57, 213, 239]. Alternative approaches focus on the macroscopic details of peptide self-assembly, however it has remained a challenge to investigate the microscopic mechanisms driving assembly behavior. Recently, our many-body diffusion map approach was used by Wang et al. to identify the assembly landscape for asphaltene aggregation, a foulant in the production of crude oil [234]. Structural graphs were generated using a core-core distance measure, enabling the direct application of our graph matching techniques to identify the pairwise similarity between aggregates. Alternative distance measures could be employed, such as the construction of hyper-graphs that allow for intra- and inter-molecular distances to be computed, allowing for higher resolution understanding of the structural morphology of molecular aggregates. A hierarchical approach, matching between peptides on their local structure and then matching on the global aggregate structure could also serve to better approximate similarities between aggregate morphologies. This problem can be seen as a direct expansion of the colloidal distance measure presented here, where instead of treating all colloids as identical we impart some measure of similarity between colloids into the matching procedure. These techniques

are necessarily more complicated than the distance measure used for self-assembly presented in this work, requiring more thought on the computational efficiency of computing distances between molecular aggregates. Application of these techniques to the problem of peptide self-assembly will ultimately enable the improvement of peptide architectures to preferentially assemble into desired aggregates for a host of applications across the biomedical [235], electronic [18], and structural [240] materials domains.

References

[1] Whitesides, G. M.; Boncheva, M. Beyond molecules: Self-assembly of mesoscopic and macroscopic components. *Proceedings of the National Academy of Sciences of the United States of America* **2002**, *99*, 4769–4774.

[2] Ariga, K.; Hill, J. P.; Lee, M. V.; Vinu, A.; Charvet, R.; Acharya, S. Challenges and breakthroughs in recent research on self-assembly. *Science and Technology of Advanced Materials* **2008**, *9*, 014109.

[3] Hagan, M. F.; Chandler, D. Dynamic pathways for viral capsid assembly. *Biophysical Journal* **2006**, *91*, 42 – 54.

[4] Da Poian, A. T.; Oliveira, A. C.; Silva, J. L. Cold denaturation of an icosahedral virus. The role of entropy in virus assembly. *Biochemistry* **1995**, *34*, 2672–2677.

[5] Gazit, E. Mechanisms of amyloid fibril self-assembly and inhibition. *The FEBS Journal* **2005**, *272*, 5971–5978.

[6] Chen, M. C.; Cafferty, B. J.; Mamajanov, I.; Gállego, I.; Khanam, J.; Krishnamurthy, R.; Hud, N. V. Spontaneous Prebiotic Formation of a -Ribofuranoside That Self-Assembles with a Complementary Heterocycle. *Journal of the American Chemical Society* **2014**, *136*, 5640–5646.

[7] Matson, J. B.; Zha, R. H.; Stupp, S. I. Peptide self-assembly for crafting functional biological materials. *Current Opinion in Solid State and Materials Science* **2011**, *15*, 225 – 235.

[8] Whitesides, G. M.; Grzybowski, B. Self-assembly at all scales. *Science* **2002**, *295*, 2418–2421.

[9] Zhang, Z.; Glotzer, S. C. Self-assembly of patchy particles. *Nano Letters* **2004**, *4*, 1407–1413.

[10] Steinmetz, N.; Lin, T.; Lomonossoff, G.; Johnson, J. In *Viruses and Nanotechnology*; Manchester, M., Steinmetz, N., Eds.; Curr. Top. Microbiol. Immunol.; Springer Berlin Heidelberg, 2009; Vol. 327; pp 23–58.

[11] Pawar, A. B.; Kretzschmar, I. Fabrication, assembly, and application of patchy particles. *Macromolecular Rapid Communications* **2010**, *31*, 150–168.

[12] Chen, C.; Hu, J.; Zhang, S.; Zhou, P.; Zhao, X.; Xu, H.; Zhao, X.; Yaseen, M.; Lu, J. R. Molecular mechanisms of antibacterial and antitumor actions of designed surfactant-like peptides. *Biomaterials* **2012**, *33*, 592 – 603.

[13] Chen, C.; Pan, F.; Zhang, S.; Hu, J.; Cao, M.; Wang, J.; Xu, H.; Zhao, X.; Lu, J. R. Antibacterial Activities of Short Designer Peptides: a Link between Propensity for Nanostructuring and Capacity for Membrane Destabilization. *Biomacromolecules* **2010**, *11*, 402–411, PMID: 20078032.

[14] Zhao, X.; Pan, F.; Xu, H.; Yaseen, M.; Shan, H.; Hauser, C. A. E.; Zhang, S.; Lu, J. R. Molecular self-assembly and applications of designer peptide amphiphiles. *Chemical Society Reviews* **2010**, *39*, 3480–3498.

[15] Anees, P.; Sreejith, S.; Ajayaghosh, A. Self-Assembled Near-Infrared Dye Nanoparticles as a Selective Protein Sensor by Activation of a Dormant Fluorophore. *Journal of the American Chemical Society* **2014**, *136*, 13233–13239, PMID: 25199066.

[16] Zhang, H.; Wu, R.; Chen, Z.; Liu, G.; Zhang, Z.; Jiao, Z. Self-assembly fabrication of 3D flower-like ZnO hierarchical nanostructures and their gas sensing properties. *CrystEngComm* **2012**, *14*, 1775–1782.

[17] Bian, L.; Zhu, E.; Tang, J.; Tang, W.; Zhang, F. Recent progress in the design of narrow bandgap conjugated polymers for high-efficiency organic solar cells. *Progress in Polymer Science* **2012**, *37*, 1292 – 1331, Topical Issue on Conducting Polymers.

[18] Guo, X.; Baumgarten, M.; Müllen, K. Designing -conjugated polymers for organic electronics. *Progress in Polymer Science* **2013**, *38*, 1832 – 1908, Topical issue on Conductive Polymers.

[19] Ning, H.; Mihi, A.; Geddes, J. B.; Miyake, M.; Braun, P. V. Radiative lifetime modification of LaF3:Nd nanoparticles embedded in 3D silicon photonic crystals. *Advanced Materials* **2012**, *24*, OP153–OP158.

[20] Glotzer, S. C.; Solomon, M. J. Anisotropy of building blocks and their assembly into complex structures. *Nature Materials* **2007**, *6*, 557–562.

[21] Wang, Y.; Wang, Y.; Breed, D. R.; Manoharan, V. N.; Feng, L.; Hollingsworth, A. D.; Weck, M.; Pine, D. J. Colloids with valence and specific directional bonding. *Nature* **2011**, *491*, 51–55.

[22] Sciortino, F.; Giacometti, A.; Pastore, G. Phase diagram of Janus particles. *Physical Review Letters* **2009**, *103*, 237801.

[23] Jiang, S.; Chen, Q.; Tripathy, M.; Luijten, E.; Schweizer, K. S.; Granick, S. Janus particle synthesis and assembly. *Advanced Materials* **2010**, *22*, 1060–1071.

[24] Hong, L.; Cacciuto, A.; Luijten, E.; Granick, S. Clusters of amphiphilic colloidal spheres. *Langmuir* **2008**, *24*, 621–625.

[25] Chen, Q.; Bae, S. C.; Granick, S. Directed self-assembly of a colloidal kagome lattice. *Nature* **2011**, *469*, 381–384.

[26] Walther, A.; Müller, A. H. E. Janus particles: Synthesis, self-assembly, physical properties, and applications. *Chemical Reviews* **2013**, *113*, 5194–5261, PMID: 23557169.

[27] Avvisati, G.; Vissers, T.; Dijkstra, M. Self-assembly of patchy colloidal dumbbells. *ArXiv e-prints* **2014**,

[28] Wolters, J. R.; Avvisati, G.; Hagemans, F.; Vissers, T.; Kraft, D. J.; Dijkstra, M.; Kegel, W. K. Self-assembly of "Mickey Mouse" shaped colloids into tube-like structures: experiments and simulations. *Soft Matter* **2015**, *11*, 1067–1077.

[29] Kraft, D. J.; Vlug, W. S.; van Kats, C. M.; van Blaaderen, A.; Imhof, A.; Kegel, W. K. Self-Assembly of Colloids with Liquid Protrusions. *Journal of the American Chemical Society* **2009**, *131*, 1182–1186, PMID: 19105699.

[30] Sacanna, S.; Pine, D. J. Shape-anisotropic colloids: Building blocks for complex assemblies. *Current Opinion in Colloid & Interface Science* **2011**, *16*, 96 – 105.

[31] Solomon, M. J. Directions for targeted self-assembly of anisotropic colloids from statistical thermodynamics. *Current Opinion in Colloid & Interface Science* **2011**, *16*, 158 – 167.

[32] White House Office of Science and Technology Policy, *Materials Genome Initiative for Global Competitiveness*; 2011.

[33] Jankowski, E.; Glotzer, S. C. Screening and designing patchy particles for optimized self-assembly propensity through assembly pathway engineering. *Soft Matter* **2012**, *8*, 2852–2859.

[34] Glotzer, S. C.; Solomon, M. J.; Kotov, N. A. Self-assembly: From nanoscale to microscale colloids. *AIChE Journal* **2004**, *50*, 2978–2985.

[35] Wilber, A. W.; Doye, J. P. K.; Louis, A. A.; Lewis, A. C. F. Monodisperse self-assembly in a model with protein-like interactions. *The Journal of Chemical Physics* **2009**, *131*, 175102.

[36] Whitelam, S.; Feng, E. H.; Hagan, M. F.; Geissler, P. L. The role of collective motion in examples of coarsening and self-assembly. *Soft Matter* **2009**, *5*, 1251–1262.

[37] Hemberg, M.; Yaliraki, S. N.; Barahona, M. Stochastic Kinetics of Viral Capsid Assembly Based on Detailed Protein Structures. *Biophysical Journal* **2006**, *90*, 3029 – 3042.

[38] Miller, W. L.; Cacciuto, A. Hierarchical self-assembly of asymmetric amphiphatic spherical colloidal particles. *Physical Review E* **2009**, *80*, 021404.

[39] Miller, W. L.; Cacciuto, A. Exploiting classical nucleation theory for reverse self-assembly. *The Journal of Chemical Physics* **2010**, *133*, 234108.

[40] Dill, K. A.; Chan, H. S. From Levinthal to pathways to funnels. *Nature Structural Biology* **1997**, *4*, 10 – 19.

[41] Pande, V. S.; Grosberg, A. Y.; Tanaka, T.; Rokhsar, D. S. Pathways for protein folding: is a new view needed? *Current Opinion in Structural Biology* **1998**, *8*, 68 – 79.

[42] Gruebele, M. Protein folding: the free energy surface. *Current Opinion in Structural Biology* **2002**, *12*, 161 – 168.

[43] Wilber, A. W.; Doye, J. P. K.; Louis, A. A.; Noya, E. G.; Miller, M. A.; Wong, P. Reversible self-assembly of patchy particles into monodisperse icosahedral clusters. *The Journal of Chemical Physics* **2007**, *127*, 085106.

[44] Calvo, F.; Doye, J. P. K.; Wales, D. J. Energy landscapes of colloidal clusters: thermodynamics and rearrangement mechanisms. *Nanoscale* **2012**, *4*, 1085–1100.

[45] Jr., P. E. R. A Theory of the Linear Viscoelastic Properties of Dilute Solutions of Coiling Polymers. *The Journal of Chemical Physics* **1953**, *21*, 1272–1280.

[46] Zimm, B. H. Dynamics of Polymer Molecules in Dilute Solution: Viscoelasticity, Flow Birefringence and Dielectric Loss. *The Journal of Chemical Physics* **1956**, *24*, 269–278.

[47] Jolliffe, I. T. *Principal Component Analysis*, 2nd ed.; Springer: New York, 2002.

[48] Maisuradze, G. G.; Liwo, A.; Scheraga, H. A. Principal component analysis for protein folding dynamics. *Journal of Molecular Biology* **2009**, *385*, 312 – 329.

[49] Michielssens, S.; van Erp, T. S.; Kutzner, C.; Ceulemans, A.; de Groot, B. L. Molecular dynamics in principal component space. *The Journal of Physical Chemistry B* **2012**, *116*, 8350–8354.

[50] Ceriotti, M.; Tribello, G. A.; Parrinello, M. Simplifying the representation of complex free-energy landscapes using sketch-map. *Proceedings of the National Academy of Sciences of the United States of America* **2011**, *108*, 13023–13028.

[51] Stamati, H.; Clementi, C.; Kavraki, L. E. Application of nonlinear dimensionality reduction to characterize the conformational landscape of small peptides. *Proteins: Structure, Function, and Bioinformatics* **2010**, *78*, 223–235.

[52] Plaku, E.; Stamati, H.; Clementi, C.; Kavraki, L. E. Fast and reliable analysis of molecular motion using proximity relations and dimensionality reduction. *Proteins: Structure, Function, and Bioinformatics* **2007**, *67*, 897–907.

[53] Tenenbaum, J. B.; De Silva, V.; Langford, J. C. A global geometric framework for nonlinear dimensionality reduction. *Science* **2000**, *290*, 2319–2323.

[54] Roweis, S. T.; Saul, L. K. Nonlinear dimensionality reduction by locally linear embedding. *Science* **2000**, *290*, 2323–2326.

[55] Ferguson, A. L.; Panagiotopoulos, A. Z.; Debenedetti, P. G.; Kevrekidis, I. G. Systematic determination of order parameters for chain dynamics using diffusion maps. *Proceedings of the National Academy of Sciences of the United States of America* **2010**, *107*, 13597–13602.

[56] Ferguson, A. L.; Panagiotopoulos, A. Z.; Kevrekidis, I. G.; Debenedetti, P. G. Nonlinear dimensionality reduction in molecular simulation: The diffusion map approach. *Chemical Physics Letters* **2011**, *509*, 1 – 11.

[57] Mansbach, R. A.; Ferguson, A. L. Machine learning of single molecule free energy surfaces and the impact of chemistry and environment upon structure and dynamics. *The Journal of Chemical Physics* **2015**, *142*.

[58] Rohrdanz, M. A.; Zheng, W.; Maggioni, M.; Clementi, C. Determination of reaction coordinates via locally scaled diffusion map. *The Journal of Chemical Physics* **2011**, *134*, 124116.

[59] Coifman, R. R.; Lafon, S. Diffusion maps. *Applied and Computational Harmonic Analysis* **2006**, *21*, 5–30.

[60] Coifman, R. R.; Kevrekidis, I. G.; Lafon, S.; Maggioni, M.; Nadler, B. Diffusion maps, reduction coordinates, and low dimensional representation of stochastic systems. *Multiscale Modeling and Simulation* **2008**, *7*, 842–864.

[61] Nadler, B.; Lafon, S.; Coifman, R. R.; Kevrekidis, I. G. Diffusion maps, spectral clustering and reaction coordinates of dynamical systems. *Applied and Computational Harmonic Analysis* **2006**, *21*, 113 – 127.

[62] Zwanzig, R. *Nonequilibrium Statistical Mechanics*; Oxford University Press: New York, 2001.

[63] Kabsch, W. A solution for the best rotation to relate two sets of vectors. *Acta Crystallographica Section A* **1976**, *32*, 922–923.

[64] Beltran-Villegas, D. J.; Sehgal, R. M.; Maroudas, D.; Ford, D. M.; Bevan, M. A. Colloidal cluster crystallization dynamics. *The Journal of Chemical Physics* **2012**, *137*, 134901.

[65] Doye, J. P. K.; Miller, M. A.; Wales, D. J. The double-funnel energy landscape of the 38-atom Lennard-Jones cluster. *The Journal of Chemical Physics* **1999**, *110*, 6896–6906.

[66] Bevan, M. A.; Ford, D. M.; Grover, M. A.; Shapiro, B.; Maroudas, D.; Yang, Y.; Thyagarajan, R.; Tang, X.; Sehgal, R. M. Controlling assembly of colloidal particles into structured objects: Basic strategy and a case study. *Journal of Process Control* **2015**, *27*, 64 – 75.

[67] Reinhart, W. F.; Long, A. W.; Howard, M. P.; Ferguson, A. L.; Panagiotopoulos, A. Z. Machine learning for autonomous crystal structure identification. *Soft Matter* **2017**, *13*, 4733–4745.

[68] Jankowski, E.; Glotzer, S. C. Calculation of partition functions for the self-assembly of patchy particles. *The Journal of Physical Chemistry B* **2011**, *115*, 14321–14326.

[69] Ferguson, A. L.; Zhang, S.; Dikiy, I.; Panagiotopoulos, A. Z.; Debenedetti, P. G.; Link, A. J. An experimental and computational investigation of spontaneous lasso formation in microcin J25. *Biophysical Journal* **2010**, *99*, 3056 – 3065.

[70] Das, P.; Moll, M.; Stamati, H.; Kavraki, L. E.; Clementi, C. Low-dimensional, free-energy landscapes of protein-folding reactions by nonlinear dimensionality reduction. *Proceedings of the National Academy of Sciences of the United States of America* **2006**, *103*, 9885–9890.

[71] Kentsis, A.; Gindin, T.; Mezei, M.; Osman, R. Calculation of the free energy and cooperativity of protein folding. *PLoS ONE* **2007**, *2*, e446.

[72] Zheng, W.; Rohrdanz, M. A.; Maggioni, M.; Clementi, C. Polymer reversal rate calculated via locally scaled diffusion map. *The Journal of Chemical Physics* **2011**, *134*, 144109.

[73] Zheng, W.; Rohrdanz, M. A.; Clementi, C. Rapid exploration of configuration space with diffusion-map-directed molecular dynamics. *The Journal of Physical Chemistry B* **2013**, *117*, 12769–12776.

[74] García, A. E. Large-amplitude nonlinear motions in proteins. *Physical Review Letters* **1992**, *68*, 2696–2699.

[75] Coifman, R. R.; Lafon, S.; Lee, A. B.; Maggioni, M.; Nadler, B.; Warner, F.; Zucker, S. W. Geometric diffusions as a tool for harmonic analysis and structure definition of data: Diffusion maps. *Proceedings of the National Academy of Sciences of the United States of America* **2005**, *102*, 7426–7431.

[76] Nadler, B.; Lafon, S.; Coifman, R. R.; Kevrekidis, I. G. Diffusion maps, spectral clustering and eigenfunctions of Fokker-Planck operators. *Advances in Neural Information Processing Systems 18* **2006**, 955–962.

[77] Coifman, R.; Shkolnisky, Y.; Sigworth, F.; Singer, A. Graph Laplacian tomography from unknown random projections. *IEEE Transactions on Image Processing* **2008**, *17*, 1891–1899.

[78] Fowlkes, C.; Belongie, S.; Chung, F.; Malik, J. Spectral grouping using the Nystrom method. *IEEE Transactions on Pattern Analysis and Machine Intelligence* **2004**, *26*, 214–225.

[79] Lafon, S.; Keller, Y.; Coifman, R. R. Data fusion and multicue data matching by diffusion maps. *IEEE Transactions on Pattern Analysis and Machine Intelligence* **2006**, *28*, 1784–1797.

[80] Baker, C. T. H. *The Numerical Treatment of Integral Equations*; Clarendon Press: Oxford, 1977; Vol. 13.

[81] Sonday, B. E.; Haataja, M.; Kevrekidis, I. G. Coarse-graining the dynamics of a driven interface in the presence of mobile impurities: Effective description via diffusion maps. *Physical Review E* **2009**, *80*, 031102.

[82] Bengio, Y.; Paiement, J.-F.; Vincent, P.; Delalleau, O.; Le Roux, N.; Ouimet, M. Out-of-sample extensions for LLE, Isomap, MDS, Eigenmaps, and spectral clustering. *Advances in Neural Information Processing Systems 16* **2004**, 177–184.

[83] Ferguson, A. L.; Panagiotopoulos, A. Z.; Debenedetti, P. G.; Kevrekidis, I. G. Integrating diffusion maps with umbrella sampling: Application to alanine dipeptide. *The Journal of Chemical Physics* **2011**, *134*, 135103.

[84] Keys, A. S.; Iacovella, C. R.; Glotzer, S. C. Characterizing structure through shape matching and applications to self-assembly. *Annual Review of Condensed Matter Physics* **2011**, *2*, 263–285.

[85] Singh, R.; Xu, J.; Berger, B. Global alignment of multiple protein interaction networks with application to functional orthology detection. *Proceedings of the National Academy of Sciences of the United States of America* **2008**, *105*, 12763–12768.

[86] Keys, A. S.; Iacovella, C. R.; Glotzer, S. C. Characterizing complex particle morphologies through shape matching: Descriptors, applications, and algorithms. *Journal of Computational Physics* **2011**, *230*, 6438–6463.

[87] Rubner, Y.; Tomasi, C.; Guibas, L. J. A metric for distributions with applications to image databases. IEEE Sixth International Conference on Computer Vision. 1998; pp 59–66.

[88] Littlejohn, R. G.; Reinsch, M. Gauge fields in the separation of rotations andinternal motions in the n-body problem. *Reviews of Modern Physics* **1997**, *69*, 213–276.

[89] Lauck, F.; Helms, V.; Geyer, T. Graph measures reveal fine structure of complexes forming in multiparticle simulations. *Journal of Chemical Theory and Computation* **2009**, *5*, 641–648.

[90] Conte, D.; Foggia, P.; Sansone, C.; Vento, M. Thirty years of graph matching in pattern recognition. *International Journal of Pattern Recognition and Artificial Intelligence* **2004**, *18*, 265–298.

[91] Klau, G. W. A new graph-based method for pairwise global network alignment. *BMC Bioinformatics* **2009**, *10*, S59.

[92] de la Higuera, C.; Janodet, J.-C.; Samuel, É.; Damiand, G.; Solnon, C. Polynomial algorithms for open plane graph and subgraph isomorphisms. *Theoretical Computer Science* **2013**, *498*, 76 – 99.

[93] Laub, A. J. *Matrix Analysis For Scientists And Engineers*; Society for Industrial and Applied Mathematics: Philadelphia, PA, USA, 2004.

[94] Kuhn, H. W. The Hungarian method for the assignment problem. *Naval Research Logistics Quarterly* **1955**, *2*, 83–97.

[95] Belkin, M.; Niyogi, P. Laplacian eigenmaps and spectral techniques for embedding and clustering. Advances in Neural Information Processing Systems. 2002; pp 585–591.

[96] Humphrey, W.; Dalke, A.; Schulten, K. VMD: Visual molecular dynamics. *Journal of Molecular Graphics* **1996**, *14*, 33 – 38.

[97] Weeks, J. D.; Chandler, D.; Andersen, H. C. Role of repulsive forces in determining the equilibrium structure of simple liquids. *The Journal of Chemical Physics* **1971**, *54*, 5237–5247.

[98] Berthelot, D. Sur le mélange des gaz. *Comptes Rendus Hebdomadaires des Séances de l'Académie des Sciences* **1898**, *126*, 1857–1858.

[99] Anderson, J. A.; Lorenz, C. D.; Travesset, A. General purpose molecular dynamics simulations fully implemented on graphics processing units. *Journal of Computational Physics* **2008**, *227*, 5342–5359.

[100] Nguyen, T. D.; Phillips, C. L.; Anderson, J. A.; Glotzer, S. C. Rigid body constraints realized in massively-parallel molecular dynamics on graphics processing units. *Computer Physics Communications* **2011**, *182*, 2307–2313.

[101] Miller, T. F.; Eleftheriou, M.; Pattnaik, P.; Ndirango, A.; Newns, D.; Martyna, G. J. Symplectic quaternion scheme for biophysical molecular dynamics. *The Journal of Chemical Physics* **2002**, *116*, 8649–8659.

[102] Tarjan, R. Depth-first search and linear graph algorithms. *SIAM Journal on Computing* **1972**, *1*, 146–160.

[103] Steinhardt, P. J.; Nelson, D. R.; Ronchetti, M. Bond-orientational order in liquids and glasses. *Physical Review B* **1983**, *28*, 784–805.

[104] ten Wolde, P.; Ruiz-Montero, M.; Frenkel, D. Numerical calculation of the rate of crystal nucleation in a Lennard-Jones system at moderate undercooling. *The Journal of Chemical Physics* **1996**, *104*, 9932–9947.

[105] Filion, L.; Hermes, M.; Ni, R.; Dijkstra, M. Crystal nucleation of hard spheres using molecular dynamics, umbrella sampling, and forward flux sampling: A comparison of simulation techniques. *The Journal of Chemical Physics* **2010**, *133*, 244115.

[106] Peters, B.; Trout, B. L. Obtaining reaction coordinates by likelihood maximization. *The Journal of Chemical Physics* **2006**, *125*, 054108.

[107] Ma, A.; Dinner, A. R. Automatic method for identifying reaction coordinates in complex systems. *The Journal of Physical Chemistry B* **2005**, *109*, 6769–6779.

[108] Salvador, S.; Chan, P. Determining the number of clusters/segments in hierarchical clustering/segmentation algorithms. 16th IEEE International Conference on Tools with Artificial Intelligence. 2004; pp 576–584.

[109] Laing, C. R.; Frewen, T. A.; Kevrekidis, I. G. Coarse-grained dynamics of an activity bump in a neural field model. *Nonlinearity* **2007**, *20*, 2127.

[110] Kumar, S.; Rosenberg, J. M.; Bouzida, D.; Swendsen, R. H.; Kollman, P. A. The weighted histogram analysis method for free-energy calculations on biomolecules. I. The method. *Journal of Computational Chemistry* **1992**, *13*, 1011–1021.

[111] Hormoz, S.; Brenner, M. P. Design principles for self-assembly with short-range interactions. *Proceedings of the National Academy of Sciences of the United States of America* **2011**, *108*, 5193–5198.

[112] de Gennes, P. G. Soft matter. *Reviews of Modern Physics* **1992**, *64*, 645–648.

[113] Granick, S.; Jiang, S.; Chen, Q. Janus particles. *Physics Today* **2009**, *62*, 68–69.

[114] Chen, Q.; Whitmer, J. K.; Jiang, S.; Bae, S. C.; Luijten, E.; Granick, S. Supracolloidal reaction kinetics of janus spheres. *Science* **2011**, *331*, 199–202.

[115] Walther, A.; Müller, A. H. E. Janus particles. *Soft Matter* **2008**, *4*, 663–668.

[116] Gangwal, S.; Cayre, O. J.; Velev, O. D. Dielectrophoretic assembly of metallodielectric Janus particles in AC electric fields. *Langmuir* **2008**, *24*, 13312–13320, PMID: 18973307.

[117] Gangwal, S.; Cayre, O. J.; Bazant, M. Z.; Velev, O. D. Induced-charge electrophoresis of metallodielectric particles. *Physical Review Letters* **2008**, *100*, 058302.

[118] Long, A. W.; Zhang, J.; Granick, S.; Ferguson, A. L. Machine learning assembly landscapes from particle tracking data. *Soft Matter* **2015**, *11*, 8141–8153.

[119] Atherton, T.; Kerbyson, D. Size invariant circle detection. *Image and Vision Computing* **1999**, *17*, 795 – 803.

[120] García-Sánchez, P.; Ren, Y.; Arcenegui, J. J.; Morgan, H.; Ramos, A. Alternating Current Electrokinetic Properties of Gold-Coated Microspheres. *Langmuir* **2012**, *28*, 13861–13870, PMID: 22931290.

[121] Shilov, V.; Delgado, A.; Gonzalez-Caballero, F.; Grosse, C. Thin double layer theory of the wide-frequency range dielectric dispersion of suspensions of non-conducting spherical particles including surface conductivity of the stagnant layer. *Colloids and Surfaces A: Physicochemical and Engineering Aspects* **2001**, *192*, 253 – 265.

[122] Wang, S.; Ma, F.; Zhao, H.; Wu, N. Bulk synthesis of metal–organic hybrid dimers and their propulsion under electric fields. *ACS Applied Materials & Interfaces* **2014**, *6*, 4560–4569, PMID: 24581149.

[123] Crocker, J. C.; Grier, D. G. Methods of digital video microscopy for colloidal studies. *Journal of Colloid and Interface Science* **1996**, *179*, 298 – 310.

[124] Bolhuis, P. G.; Dellago, C.; Chandler, D. Reaction coordinates of biomolecular isomerization. *Proceedings of the National Academy of Sciences of the United States of America* **2000**, *97*, 5877–5882.

[125] Long, A. W.; Ferguson, A. L. Nonlinear machine learning of patchy colloid self-assembly pathways and mechanisms. *The Journal of Physical Chemistry B* **2014**, *118*, 4228–4244.

[126] Zaslavskiy, M.; Bach, F.; Vert, J.-P. Global alignment of protein-protein interaction networks by graph matching methods. *Bioinformatics* **2009**, *25*, 1259–1267.

[127] Trau, M.; Saville, D. A.; Aksay, I. A. Assembly of Colloidal Crystals at Electrode Interfaces. *Langmuir* **1997**, *13*, 6375–6381.

[128] Ristenpart, W. D.; Aksay, I. A.; Saville, D. A. Electrohydrodynamic flow around a colloidal particle near an electrode with an oscillating potential. *Journal of Fluid Mechanics* **2007**, *575*, 83–109.

[129] Phillips, C. L.; Jankowski, E.; Krishnatreya, B. J.; Edmond, K. V.; Sacanna, S.; Grier, D. G.; Pine, D. J.; Glotzer, S. C. Digital colloids: Reconfigurable clusters as high information density elements. *Soft Matter* **2014**, *10*, 7468–7479.

[130] Sacanna, S.; Irvine, W. T. M.; Chaikin, P. M.; Pine, D. J. Lock and key colloids. *Nature* **2010**, *464*, 575–578.

[131] McGinley, J. T.; Jenkins, I.; Sinno, T.; Crocker, J. C. Assembling colloidal clusters using crystalline templates and reprogrammable DNA interactions. *Soft Matter* **2013**, *9*, 9119–9128.

[132] Wang, L.; Zhao, W.; Tan, W. Bioconjugated silica nanoparticles: Development and applications. *Nano Research* **2008**, *1*, 99–115.

[133] Wang, L.; ; Tan, W. Multicolor FRET silica nanoparticles by single wavelength excitation. *Nano Letters* **2006**, *6*, 84–88, PMID: 16402792.

[134] Sacanna, S.; Irvine, W. T. M.; Rossi, L.; Pine, D. J. Lock and key colloids through polymerization-induced buckling of monodisperse silicon oil droplets. *Soft Matter* **2011**, *7*, 1631–1634.

[135] Qian, L.; Winfree, E. Scaling up digital circuit computation with DNA strand displacement cascades. *Science* **2011**, *332*, 1196–1201.

[136] Phillips, C. L.; Jankowski, E.; Marval, M.; Glotzer, S. C. Self-assembled clusters of spheres related to spherical codes. *Physical Review E* **2012**, *86*, 041124.

[137] Melnyk, T. W.; Knop, O.; Smith, W. R. Extremal arrangements of points and unit charges on a sphere: equilibrium configurations revisited. *Canadian Journal of Chemistry* **1977**, *55*, 1745–1761.

[138] Whyte, L. Unique arrangements of points on a sphere. *The American Mathematical Monthly* **1952**, *59*, 606–611.

[139] Edmundson, J. The distribution of point charges on the surface of a sphere. *Acta Crystallographica Section A: Foundations of Crystallography* **1992**, *48*, 60–69.

[140] Tammes, R. On the Origin Number and Arrangement of the Places of Exits on the Surface of Pollengrains. *Recueil des Travaux Botaniques Neerlandais* **1930**, *27*, 1–84.

[141] Thomson, J. J. On the structure of the atom: an investigation of the stability and periods of oscillation of a number of corpuscles arranged at equal intervals around the circumference of a circle; with application of the results to the theory of atomic structure. *The London, Edinburgh, and Dublin Philosophical Magazine and Journal of Science* **1904**, *7*, 237–265.

[142] Weaire, D.; Aste, T. *The pursuit of perfect packing*; CRC Press, 2008.

[143] Sloane, N. J. A.; Hardin, R. H.; Smith, W. D. Tables of Spherical Codes, published electronically at NeilSloane.com/packings/.

[144] Phillips, C. L.; Anderson, J. A.; Glotzer, S. C. Pseudo-random number generation for Brownian Dynamics and Dissipative Particle Dynamics simulations on {GPU} devices. *Journal of Computational Physics* **2011**, *230*, 7191 – 7201.

[145] Glaser, J.; Nguyen, T. D.; Anderson, J. A.; Lui, P.; Spiga, F.; Millan, J. A.; Morse, D. C.; Glotzer, S. C. Strong scaling of general-purpose molecular dynamics simulations on {GPUs}. *Computer Physics Communications* **2015**, *192*, 97 – 107.

[146] Andersen, H. C.; Weeks, J. D.; Chandler, D. Relationship between the hard-sphere fluid and fluids with realistic repulsive forces. *Physical Review A* **1971**, *4*, 1597.

[147] Filion, L.; Ni, R.; Frenkel, D.; Dijkstra, M. Simulation of nucleation in almost hard-sphere colloids: The discrepancy between experiment and simulation persists. *The Journal of Chemical Physics* **2011**, *134*, 134901.

[148] Barker, J. A.; Henderson, D. Perturbation theory and equation of state for fluids. II. A successful theory of liquids. *The Journal of Chemical Physics* **1967**, *47*, 4714–4721.

[149] Rowlinson, J. An equation of state of gases at high temperatures and densities. *Molecular Physics* **1964**, *7*, 349–361.

[150] Rowlinson, J. The statistical mechanics of systems with steep intermolecular potentials. *Molecular Physics* **1964**, *8*, 107–115.

[151] Schlick, T. *Molecular Modeling and Simulation: An Interdisciplinary Guide*; Springer Science & Business Media, 2010.

[152] Transtrum, M. K.; Machta, B. B.; Brown, K. S.; Daniels, B. C.; Myers, C. R.; Sethna, J. P. Perspective: Sloppiness and emergent theories in physics, biology, and beyond. *The Journal of Chemical Physics* **2015**, *143*, 010901.

[153] Scholz, M.; Fraunholz, M.; Selbig, J. *Principal manifolds for data visualization and dimension reduction*; Springer, 2008; pp 44–67.

[154] Shell, M. S. *Thermodynamics and Statistical Mechanics: An Integrated Approach*; Cambridge University Press, 2015; Chapter Chapter 16.

[155] Shell, M. S. *Thermodynamics and Statistical Mechanics: An Integrated Approach*; Cambridge University Press, 2015; Chapter Chapter 21.

[156] Redner, S. *A Guide to First-Passage Processes*; Cambridge University Press, 2001.

[157] Bowman, G. R. In *An introduction to markov state models and their application to long timescale molecular simulation*; Bowman, G. R., Pande, V. S., Noé, F., Eds.; Springer Science & Business Media, 2013; Vol. 797; Chapter 2. An overview and practical guide to building Markov state models, pp 20–21.

[158] Long, A. W.; Phillips, C. L.; Jankowksi, E.; Ferguson, A. L. Nonlinear machine learning and design of reconfigurable digital colloids. *Soft Matter* **2016**, *12*, 7119–7135.

[159] Chatterjee, S.; Hadi, A. S. *Regression Analysis by Example*, 5th ed.; John Wiley & Sons: Hoboken, New Jersey, 2012.

[160] Geerts, N.; Eiser, E. DNA-functionalized colloids: Physical properties and applications. *Soft Matter* **2010**, *6*, 4647–4660.

[161] Kratz, K.; Hellweg, T.; Eimer, W. Influence of charge density on the swelling of colloidal poly(N-isopropylacrylamide-co-acrylic acid) microgels. *Colloids and Surfaces A: Physicochemical and Engineering Aspects* **2000**, *170*, 137 – 149.

[162] Pan, V. Y.; Chen, Z. Q. The complexity of the matrix eigenproblem. Proceedings of the Thirty-first Annual ACM Symposium on Theory of Computing. New York, NY, USA, 1999; pp 507–516.

[163] Hu, J.; Ferguson, A. L. Global graph matching using diffusion maps. *Intelligent Data Analysis* **2016**, *20*, 637–654.

[164] Belkin, M.; Niyogi, P. Laplacian eigenmaps for dimensionality reduction and data representation. *Neural Computation* **2003**, *15*, 1373–1396.

[165] Kao, M.-Y. *Encyclopedia of Algorithms*; Springer Science & Business Media, 2008.

[166] Golub, G.; Van Loan, C. *Matrix Computations*; Johns Hopkins Studies in the Mathematical Sciences; Johns Hopkins University Press, 2013.

[167] Bechtold, T.; Rudnyi, E. B.; Korvink, J. G. *Fast Simulation of Electro-Thermal MEMS: Efficient Dynamic Compact Models*; Springer-Verlag: Berlin, Heidelberg, Germany, 2006.

[168] Larsen, R. M. *Lanczos bidiagonalization with partial reorthogonalization*; DAIMI PB-357 Technical Report, 1998.

[169] Aizenbud, Y.; Bermanis, A.; Averbuch, A. PCA-based out-of-sample extension for dimensionality reduction. *ArXiv e-prints* **2015**,

[170] Rabin, N.; Coifman, R. R. Heterogeneous datasets representation and learning using diffusion maps and Laplacian pyramids. Proceedings of the 2012 SIAM International Conference on Data Mining. 2012; pp 189–199.

[171] Eskin, E.; Arnold, A.; Prerau, M.; Portnoy, L.; Stolfo, S. *Applications of Data Mining in Computer Security*; Springer, 2002; Vol. 6; pp 77–101.

[172] Mahoney, A.; Bross, J.; Johnson, D. Deformable robot motion planning in a reduced-dimension configuration space. 2010 IEEE International Conference on Robotics and Automation. 2010; pp 5133–5138.

[173] Chen, Y. F.; Liu, S.-Y.; Liu, M.; Miller, J.; How, J. P. Motion planning with diffusion maps. 2016 IEEE/RSJ International Conference on Intelligent Robots and Systems. 2016.

[174] Voter, A. F. Parallel replica method for dynamics of infrequent events. *Physical Review B* **1998**, *57*, R13985.

[175] Allen, R. J.; Valeriani, C.; ten Wolde, P. R. Forward flux sampling for rare event simulations. *Journal of Physics: Condensed Matter* **2009**, *21*, 463102.

[176] Escobedo, F. A.; Borrero, E. E.; Araque, J. C. Transition path sampling and forward flux sampling. Applications to biological systems. *Journal of Physics: Condensed Matter* **2009**, *21*, 333101.

[177] de Silva, V.; Tenenbaum, J. B. Global versus local methods in nonlinear dimensionality reduction. *Advances in Neural Information Processing Systems 15* **2003**, 721–728.

[178] Silva, J.; Marques, J.; Lemos, J. Selecting landmark points for sparse manifold learning. *Advances in Neural Information Processing Systems 18* **2006**, 1241–1248.

[179] Singer, A. A remark on global positioning from local distances. *Proceedings of the National Academy of Sciences of the United States of America* **2008**, *105*, 9507–9511.

[180] Cormen, T. H. *Introduction to Algorithms*; MIT Press: Cambridge, MA, 2009.

[181] Prim, R. C. Shortest connection networks and some generalizations. *The Bell System Technical Journal* **1957**, *36*, 1389–1401.

[182] Von Luxburg, U. A tutorial on spectral clustering. *Statistics and Computing* **2007**, *17*, 395–416.

[183] Frey, B. J.; Dueck, D. Clustering by passing messages between data points. *Science* **2007**, *315*, 972–976.

[184] Day, W. H.; Edelsbrunner, H. Efficient algorithms for agglomerative hierarchical clustering methods. *Journal of Classification* **1984**, *1*, 7–24.

[185] Park, H.-S.; Jun, C.-H. A simple and fast algorithm for k-medoids clustering. *Expert Systems with Applications* **2009**, *36*, 3336 – 3341.

[186] Arthur, D.; Vassilvitskii, S. k-means++: The advantages of careful seeding. Proceedings of the 18th Annual ACM-SIAM Symposium on Discrete Algorithms. 2007; pp 1027–1035.

[187] Deif, A. S. Rigorous perturbation bounds for eigenvalues and eigenvectors of a matrix. *Journal of Computational and Applied Mathematics* **1995**, *57*, 403 – 412.

[188] Wang, J.; Ferguson, A. L. Nonlinear reconstruction of single-molecule free-energy surfaces from univariate time series. *Physical Review E* **2016**, *93*, 032412.

[189] Hummer, G.; Kevrekidis, I. G. Coarse molecular dynamics of a peptide fragment: Free energy, kinetics, and long-time dynamics computations. *The Journal of Chemical Physics* **2003**, *118*, 10762–10773.

[190] Chodera, J. D.; Swope, W. C.; Pitera, J. W.; Dill, K. A. Long-time protein folding dynamics from short-time molecular dynamics simulations. *Multiscale Modeling and Simulation* **2006**, *5*, 1214–1226.

[191] Chodera, J. D.; Singhal, N.; Pande, V. S.; Dill, K. A.; Swope, W. C. Automatic discovery of metastable states for the construction of Markov models of macromolecular conformational dynamics. *The Journal of Chemical Physics* **2007**, *126*.

[192] Van Der Spoel, D.; Lindahl, E.; Hess, B.; Groenhof, G.; Mark, A. E.; Berendsen, H. J. C. GROMACS: Fast, flexible, and free. *Journal of Computational Chemistry* **2005**, *26*, 1701–1718.

[193] Martin, M. G.; ; Siepmann, J. I. Transferable potentials for phase equilibria. 1. United-atom description of n-alkanes. *The Journal of Physical Chemistry B* **1998**, *102*, 2569–2577.

[194] Berendsen, H. J.; Postma, J. P.; van Gunsteren, W. F.; Hermans, J. *Intermolecular Forces*; Springer, 1981; pp 331–342.

[195] Jorgensen, W. L.; Chandrasekhar, J.; Madura, J. D.; Impey, R. W.; Klein, M. L. Comparison of simple potential functions for simulating liquid water. *The Journal of Chemical Physics* **1983**, *79*, 926–935.

[196] Kaminski, G. A.; Friesner, R. A.; Tirado-Rives, J.; Jorgensen, W. L. Evaluation and reparametrization of the OPLS-AA force field for proteins via comparison with accurate quantum chemical calculations on peptides. *The Journal of Physical Chemistry B* **2001**, *105*, 6474–6487.

[197] Jorgensen, W. L.; Tirado-Rives, J. The OPLS [optimized potentials for liquid simulations] potential functions for proteins, energy minimizations for crystals of cyclic peptides and crambin. *Journal of the American Chemical Society* **1988**, *110*, 1657–1666.

[198] Muja, M.; Lowe, D. G. Scalable nearest neighbor algorithms for high dimensional data. *IEEE Transactions on Pattern Analysis and Machine Intelligence* **2014**, *36*, 2227–2240.

[199] McQueen, J.; Meila, M.; VanderPlas, J.; Zhang, Z. Megaman: Scalable manifold learning in Python. *Journal of Machine Learning Research* **2016**, *17*, 1–5.

[200] Duane, S.; Kennedy, A.; Pendleton, B. J.; Roweth, D. Hybrid Monte Carlo. *Physics Letters B* **1987**, *195*, 216 – 222.

[201] Neal, R. M. In *Handbook of Markov Chain Monte Carlo*; Brooks, S., Gelmen, A., Jones, G., Meng, X.-L., Eds.; Chapman & Hall/CRC Press, 2011; Chapter 5, pp 113–162.

[202] Gonzalez, M. A.; Sanz, E.; McBride, C.; Abascal, J. L. F.; Vega, C.; Valeriani, C. Nucleation free-energy barriers with hybrid Monte-Carlo/umbrella sampling. *Physical Chemistry Chemical Physics* **2014**, *16*, 24913–24919.

[203] Boyd, S.; Vandenberghe, L. *Convex Optimization*; Cambridge University Press, 2004.

[204] Dorigo, M.; Birattari, M.; Stutzle, T. Ant Colony Optimization. *IEEE Computational Intelligence Magazine* **2006**, *1*, 28–39.

[205] Mitchell, M. *An Introduction to Genetic Algorithms*; MIT Press, 1998.

[206] Hansen, N.; Ostermeier, A. Completely derandomized self-adaptation in evolution strategies. *Evolutionary Computation* **2001**, *9*, 159–195.

[207] Hansen, N.; Müller, S. D.; Koumoutsakos, P. Reducing the time complexity of the derandomized evolution strategy with covariance matrix adaptation (CMA-ES). *Evolutionary Computation* **2003**, *11*, 1–18.

[208] Qin, J.; Khaira, G. S.; Su, Y.; Garner, G. P.; Miskin, M.; Jaeger, H. M.; de Pablo, J. J. Evolutionary pattern design for copolymer directed self-assembly. *Soft Matter* **2013**, *9*, 11467–11472.

[209] Khaira, G. S.; Qin, J.; Garner, G. P.; Xiong, S.; Wan, L.; Ruiz, R.; Jaeger, H. M.; Nealey, P. F.; de Pablo, J. J. Evolutionary optimization of directed self-assembly of triblock copolymers on chemically patterned substrates. *ACS Macro Letters* **2014**, *3*, 747–752.

[210] Glotzer Group, Shifted Lennard Jones Potential. `http://hoomd-blue.readthedocs.io/en/stable/module-md-pair.html#hoomd.md.pair.slj`.

[211] Long, A. W.; Ferguson, A. L. Landmark diffusion maps (L-dMaps): Accelerated manifold learning out-of-sample extension. *ArXiv e-prints* **2017**,

[212] Frenkel, D.; Smit, B. *Understanding molecular simulation: from algorithms to applications*, 2nd ed.; Academic Press, 2002.

[213] Thurston, B. A.; Tovar, J. D.; Ferguson, A. L. Thermodynamics, morphology, and kinetics of early-stage self-assembly of -conjugated oligopeptides. *Molecular Simulation* **2016**, *42*, 955–975.

[214] Hamelberg, D.; Mongan, J.; McCammon, J. A. Accelerated molecular dynamics: A promising and efficient simulation method for biomolecules. *The Journal of Chemical Physics* **2004**, *120*, 11919–11929.

[215] Marinelli, F.; Pietrucci, F.; Laio, A.; Piana, S. A Kinetic Model of Trp-Cage Folding from Multiple Biased Molecular Dynamics Simulations. *PLOS Computational Biology* **2009**, *5*, 1–18.

[216] Hashemian, B.; Millán, D.; Arroyo, M. Modeling and enhanced sampling of molecular systems with smooth and nonlinear data-driven collective variables. *The Journal of Chemical Physics* **2013**, *139*, 214101.

[217] Li, C.-G.; Guo, J.; Chen, G.; Nie, X.-F.; Yang, Z. A Version of Isomap with Explicit Mapping. 2006 International Conference on Machine Learning and Cybernetics. 2006; pp 3201–3206.

[218] Spiwok, V.; Králová, B. Metadynamics in the conformational space nonlinearly dimensionally reduced by Isomap. *The Journal of Chemical Physics* **2011**, *135*, 224504.

[219] Branduardi, D.; Gervasio, F. L.; Parrinello, M. From A to B in free energy space. *The Journal of Chemical Physics* **2007**, *126*, 054103.

[220] Torrie, G.; Valleau, J. Nonphysical sampling distributions in Monte Carlo free-energy estimation: Umbrella sampling. *Journal of Computational Physics* **1977**, *23*, 187 – 199.

[221] Whitelam, S.; Geissler, P. L. Avoiding unphysical kinetic traps in Monte Carlo simulations of strongly attractive particles. *The Journal of Chemical Physics* **2007**, *127*, 154101.

[222] Liu, J.; Luijten, E. Rejection-free geometric cluster algorithm for complex fluids. *Physical Review Letters* **2004**, *92*, 035504.

[223] Hetényi, B.; Bernacki, K.; Berne, B. J. Multiple "time step" Monte Carlo. *The Journal of Chemical Physics* **2002**, *117*, 8203–8207.

[224] Lloyd, S. Least squares quantization in PCM. *IEEE Transactions on Information Theory* **1982**, *28*, 129–137.

[225] Bitzek, E.; Koskinen, P.; Gähler, F.; Moseler, M.; Gumbsch, P. Structural Relaxation Made Simple. *Physical Review Letters* **2006**, *97*, 170201.

[226] Ferguson, A. L. BayesWHAM: A Bayesian approach for free energy estimation, reweighting, and uncertainty quantification in the weighted histogram analysis method. *Journal of Computational Chemistry* **2017**, *38*, 1583–1605.

[227] Schmit, J. D.; Ghosh, K.; Dill, K. What Drives Amyloid Molecules To Assemble into Oligomers and Fibrils? *Biophysical Journal* **2010**, *100*, 450–458.

[228] Peters, B.; Heyden, A.; Bell, A. T.; Chakraborty, A. A growing string method for determining transition states: Comparison to the nudged elastic band and string methods. *The Journal of Chemical Physics* **2004**, *120*, 7877–7886.

[229] Maragliano, L.; Fischer, A.; Vanden-Eijnden, E.; Ciccotti, G. String method in collective variables: Minimum free energy paths and isocommittor surfaces. *Journal of Chemical Physics* **2006**, *125*, 024106.

[230] Branduardi, D.; Faraldo-Gómez, J. D. String Method for Calculation of Minimum Free-Energy Paths in Cartesian Space in Freely Tumbling Systems. *Journal of Chemical Theory and Computation* **2013**, *9*, 4140–4154.

[231] Nakagawa, N.; Peyrard, M. The Inherent Structure Landscape of a Protein. *Proceedings of the National Academy of Sciences* **2006**, *103*, 5279–5284.

[232] Kennedy, J.; Eberhart, R. Particle swarm optimization. IEEE International Conference on Neural Networks. 1995; pp 1942–1948.

[233] Preto, J.; Clementi, C. Fast recovery of free energy landscapes via diffusion-map-directed molecular dynamics. *Physical Chemistry Chemical Physics* **2014**, *16*, 19181–19191.

[234] Wang, J.; Gayatri, M. A.; Ferguson, A. L. Mesoscale Simulation and Machine Learning of Asphaltene Aggregation Phase Behavior and Molecular Assembly Landscapes. *The Journal of Physical Chemistry B* **2017**, *121*, 4923–4944, PMID: 28418682.

[235] Zhang, S.; Gelain, F.; Zhao, X. Designer self-assembling peptide nanofiber scaffolds for 3D tissue cell cultures. *Seminars in Cancer Biology* **2005**, *15*, 413 – 420.

[236] Juvonen, A.; Sipola, T.; Hämäläinen, T. Online anomaly detection using dimensionality reduction techniques for HTTP log analysis. *Computer Networks* **2015**, *91*, 46 – 56.

[237] Gepshtein, S.; Keller, Y. Image completion by diffusion maps and spectral relaxation. *IEEE Transactions on Image Processing* **2013**, *22*, 2983–2994.

[238] Boles, M. A.; Engel, M.; Talapin, D. V. Self-Assembly of Colloidal Nanocrystals: From Intricate Structures to Functional Materials. *Chemical Reviews* **2016**, *116*, 11220–11289, PMID: 27552640.

[239] Wang, J.; Ferguson, A. L. Mesoscale Simulation of Asphaltene Aggregation. *The Journal of Physical Chemistry B* **2016**, *120*, 8016–8035, PMID: 27455391.

[240] Dehsorkhi, A.; Castelletto, V.; Hamley, I. W. Self-assembling amphiphilic peptides. *Journal of Peptide Science* **2014**, *20*, 453–467, PSC-14-0011.R1.